

Measurement of Hadron Multiplicities in Deep Inelastic Muon-Nucleon Scattering

Dissertation
zur Erlangung des Grades
"Doktor
der Naturwissenschaften"

am Fachbereich Physik, Mathematik und Informatik
der JOHANNES GUTENBERG-UNIVERSITÄT
in Mainz

NICOLAS DU FRESNE VON HOHENESCHE

geboren in Frankfurt am Main

Mainz, den 19. November 2015

Nicolas du Fresne von Hohenesche: *Measurement of Hadron Multiplicities in Deep Inelastic Muon-Nucleon Scattering*

BERICHTERSTATTER:

Prof. Dr. Eva-Maria Kabuß

Prof. Dr. Volker Büscher

TAG DER MÜNDLICHEN PRÜFUNG: 2. Juni 2016

CONTENTS

1	INTRODUCTION	1
2	THEORETICAL FRAMEWORK	5
2.1	Structure of the Nucleon	5
2.2	Hadronisation	20
2.3	Measurement of Fragmentation Functions	25
I	EXPERIMENTAL PART	29
3	THE COMPASS EXPERIMENT	31
3.1	Beam	32
3.2	Beam Telescope	34
3.3	Target Region	35
3.4	Spectrometer	38
3.5	Data Acquisition and Online-Monitoring	43
4	THE COMPASS MUON TRIGGER	47
4.1	Trigger Principles	47
4.2	Hodoscopes and Veto Detectors	50
4.3	Trigger Electronics	57
5	THE LARGE ANGLE SPECTROMETER TRIGGER (LAST)	61
5.1	Concept	61
5.2	Hodoscope H1	62
5.3	Hodoscope H2	65
5.4	Trigger Electronics	68
5.5	Performance	70
6	TRIGGER EFFICIENCY AND LUMINOSITY FROM DATA	73
6.1	Data Flow and COMPASS Analysis	73
6.2	Hodoscope and Trigger Efficiencies	75
6.3	Luminosity Determination	80
II	THE 2006 MULTIPLICITY ANALYSIS	97
7	DETERMINATION OF THE 2006 RAW MULTIPLICITIES	99
7.1	Particle Identification with the RICH	99
7.2	Data Set	105
7.3	Raw Multiplicities	107
8	CORRECTION FACTORS FOR MULTIPLICITIES	113
8.1	Monte Carlo Simulation	113
8.2	Acceptance Correction	115
8.3	Electron Contamination	122
8.4	Contamination of Exclusive Vector Mesons	125
8.5	LEPTO Extrapolation	128
9	FINAL CHARGED HADRON MULTIPLICITIES	131
9.1	Summary of the Systematic Studies	131
9.2	Final Multiplicities (h^\pm , π^\pm and K^\pm)	132
9.3	Charge Asymmetry	133
10	DETERMINATION OF QUARK FRAGMENTATION FUNCTIONS	137
10.1	Direct Extraction of Fragmentation Functions	137

10.2 COMPASS Leading-Order Fit	139
10.3 LO and NLO Parametrisations	142
11 SUMMARY AND OUTLOOK	147
III APPENDIX	149

For my family



ABSTRACT

In deep-inelastic muon-nucleon scattering, a single quark can be ejected out of the nucleon by the absorption of a high-energy photon. Such a free isolated quark has never been observed in nature. In quantum chromodynamics (QCD), coloured objects, such as a single quark, create additional quark anti-quark pairs out of the colour field and the final state comprises a jet of hadrons. The hadronisation process can be described by fragmentation functions D_q^h , the probability that a quark with the flavour q turns into a hadron of the type h . Similar to the parton distribution function, the fragmentation functions are fundamental, universal and process-independent quantities. The fragmentation functions are measured with the COMPASS spectrometer in muon-nucleon scattering. The observables are the hadron multiplicities M^h .

The COMPASS experiment consists of a two-stage magnetic spectrometer located at the M2 beam line of the Super Proton Synchrotron at CERN and uses a polarised muon beam on a nuclear fixed target. The scattered muon and the final-state hadrons are measured with a large number of tracking detectors. The identification of the hadrons is done using a ring imaging Cherenkov detector. An essential part of the spectrometer is the trigger system. It mainly consists of scintillator hodoscopes and triggers on scattered muons coming from the target. The trigger acceptance was increased towards larger four-momentum transfers Q^2 with the implementation of a new pair of hodoscopes, triggering on larger scattering angles. The trigger system is also used to determine spectrometer specific quantities such as efficiencies and luminosities. In a fixed target experiment, the luminosity is given to the incident particle flux and the target density. The flux is measured with two methods, by counting beam tracks using a true random trigger and by counting the hits in a plane of the beam telescope.

For the determination of the fragmentation functions, a measurement taken in 2006 with a 160 GeV/c muon beam impinging on an isoscalar lithium-deuterid target is used. The scattered muon and additional hadrons are measured. The hadron multiplicities M^h are the average number of hadrons per deep inelastic scattering event and are determined in a three-dimensional binning in the Bjorken scaling variable x , the relative virtual photon energy y and the hadron energy fraction z for pions, kaons and unidentified hadrons. The DIS events are selected by requiring an invariant mass W larger than $5 \text{ GeV}/c^2$, thus excluding events coming from nucleon resonances. The charged hadron multiplicities are corrected for the particle identification efficiency using real data. Further corrections, *e. g.* the spectrometer acceptance and electron/positron contamination, are determined using Monte Carlo simulations. The fragmentation functions are extracted in two ways. The first method is the direct extraction point-by-point. The second method uses a simultaneous leading-order perturbative QCD fit on π^+ and π^- multiplicities. The results are compared to existing parametrisations.

ZUSAMMENFASSUNG

In der tiefinelastischen Streuung kann ein einzelnes Quark durch die Absorption eines hochenergetischen virtuellen Photons aus einem Nukleon herausgeschlagen werden. Ein freies, isoliertes Quark wurde in der Natur aber nicht beobachtet. In der Quantenchromodynamik (QCD) erzeugen farbladungstragende Objekte, so wie ein isoliertes Quark, Quark-Antiquarkpaare aus dem Farbfeld und erzeugen einen Teilchenschauer. Der Hadronisierungsprozess kann durch die Fragmentationsfunktionen D_q^h beschrieben werden. Diese geben an, mit welcher Wahrscheinlichkeit ein Quark der Sorte q in ein Hadron des Typs h übergeht. Ähnlich wie die Partonverteilungsfunktionen $q(x)$ sind die Fragmentationsfunktionen grundlegende, allgemeingültige, prozessunabhängige Größen. Die Fragmentationsfunktionen werden mit dem COMPASS-Spektrometer in tiefinelastischer Myon-Nukleon-Streuung gemessen. Die Observable ist die geladene Hadronenmultiplizität M^h .

Das COMPASS-Experiment ist ein zweistufiges Spektrometer an der M2-Strahlführung am CERN und verwendet einen polarisierten Myonstrahl und ein sogenanntes Fixed-Target. Die gestreuten Myonen und der hadronische Endzustand werden mit einer großen Zahl an Spurdetektoren nachgewiesen. Der ringabbildende Cherenkov-Detektor RICH sorgt für die Identifikation der Hadronen. Ein wichtiger Bestandteil des Spektrometers ist das Triggersystem. Es besteht hauptsächlich aus Szintillatorrhodokopen und startet die Datennahme nach der Messung eines gestreuten Myons aus dem Target. Die Akzeptanz des Triggersystems wurde durch das Hinzufügen eines neuen Triggerhodokoppaares, welches auf große Myonstreuwinkel triggert, erweitert. Des Weiteren kann das Triggersystem dazu verwendet werden, um spektrometerspezifische Größen, wie zum Beispiel Effizienzen und Luminositäten, zu bestimmen. Die Luminosität in einem Fixed-Target-Experiment ist gleich dem Produkt aus einlaufenden Teilchenfluss und der Massenbelegung des Target-Materials. Der Teilchenfluss wird mit zwei Methoden bestimmt: einmal durch das Zählen von Strahltrajektorien, die durch einen Zufallstrigger ausgewählt werden oder durch das Zählen der Treffer in einer Ebene im Strahlteleskop des Experiments.

Die für diese Arbeit verwendeten Daten wurden 2006 mit einem 160 GeV Myonstrahl an einem isoskalaren Lithiumdeuteridtarget aufgenommen. Dabei wird das gestreute Myon sowie mindestens ein Hadron nachgewiesen. Die Hadronmultiplizität M^h ist die mittlere Anzahl von Hadronen pro tiefinelastischem Streueignis. Sie wurden in Abhängigkeit von den drei kinematischen Variablen, der Bjorken'schen SkalenvARIABLE x , der relativen Photonenergie y und der relativen Hadronenenergie z , für identifizierte Pionen, Kaonen und nichtidentifizierte Hadronen gemessen. Die tiefinelastischen Ereignisse werden durch einen Schnitt auf die invariante Masse $W > 5 \text{ GeV}/c^2$ selektiert. Dadurch werden Ereignisse, die aus Nukleonresonanzen kommen, verworfen. Die gemessenen Multiplizitäten für geladene Hadronen werden auf die Identifizierungseffizienz des RICH korrigiert. Weitere Korrekturen, unter anderem für die Spektrometerakzeptanz und die Kontamination durch Elektronen und Positronen, werden durch Monte-Carlo-Simulationen abgeschätzt. Die Fragmentationsfunktionen werden durch zwei Methoden bestimmt. Erstens, durch eine direkten Extraktion und zweitens, aus einem perturbativen QCD-Fit in führender Ordnung an die π^+ und π^- Multiplizitäten. Die Ergebnisse werden mit existierenden Parametrisierungen verglichen.

INTRODUCTION

After the discovery of the atomic nuclei with the α -Au scattering experiment, conducted by Geiger and Mardsen [1] and interpreted by Rutherford [2] in 1911, which displayed the emptiness of an atom with a point-like but dense core, the interest for a deeper understanding of the nuclei structure rose. As α -sources just have energies of a few mega electron volts (MeV), the probing resolution is a few picometers (according to the De Broglie wavelength $\lambda = \hbar/p$ with the reduced Planck constant \hbar). With additional scattering experiments, the understanding of the inner structure of the atom increased as well as the understanding of the involved forces. The electromagnetic scattering can be easily calculated using the theory of quantum electrodynamic (QED). With improving techniques and engineering, radioactive particle emitters were replaced by much more powerful accelerators for charged particles. Different types of accelerators (*e.g.* cyclotrons, synchrotrons and linear accelerators) were used to investigate the components, the constituents and the structure of everyday matter with the goal of a deeper understanding of the fundamental interactions.

The substructure of the nucleon was discovered in 1969 at SLAC [3] by scattering high energy electrons on nucleons. In this process, the electron interacts with the substructure with an exchange of a virtual photon γ^* . Theories about the substructure of hadrons were developed in 1964 by Gell-Mann [4] (“quarks”) and Zweig [5] (“aces”), describing the nucleon as system made up by three point-like constituents. Confronted with the experimental results from SLAC, Feynman [6] developed the parton model, but it became clear partons and quarks were identical, leading to the quark-parton model. Charged partons are identified as *quarks* and are fermions with a spin $\frac{1}{2}\hbar$. In the QPM, the nucleon is composed of three *valence quarks*, which hold all quantum numbers of the nucleon. In addition, the nucleon contains quark anti-quark pairs (*sea quarks*). Six different types of quarks (with the corresponding anti-quarks) were discovered. The six so-called *quark flavours* q are down (d), up (u), strange (s), charm (c), bottom (b) and top (t), and carry an electric charge Q of either $\pm 1/3$ or $\pm 2/3$. The everyday matter, such as protons and neutrons, only have up and down quarks as valence quarks. The proton consists of uud and the neutron of udd. Meanwhile the quantum chromodynamics was developed, describing the interaction between the quarks with electrically neutral partons, the so-called *gluons*. The gluons are the gauge bosons of the strong force and were discovered by the TASSO experiment [7] in 3-jet events. Hadrons are classified as baryons with three quarks (qqq) and mesons with a quark anti-quark state (q \bar{q}), although there are hints for more exotic hadronic states (glueballs and hadronic molecules). Table 1 summarises the properties of partons [8].

Partons	d	u	s	c	b	t	g
electric charge	$-\frac{1}{3}$	$+\frac{2}{3}$	$-\frac{1}{3}$	$+\frac{2}{3}$	$-\frac{1}{3}$	$+\frac{2}{3}$	0
Spin	$\frac{1}{2}$	$\frac{1}{2}$	$\frac{1}{2}$	$\frac{1}{2}$	$\frac{1}{2}$	$\frac{1}{2}$	1
Color charge	c	c	c	c	c	c	$c\bar{c}$
Mass (MeV/ c^2)	$4.8^{+0.5}_{-0.3}$	$2.3^{+0.7}_{-0.5}$	95^{+5}_{+5}	1275^{+25}_{-25}	4180^{+30}_{-30}	173070^{+52}_{-72}	0

Table 1: Summary of the quark and gluon properties.

The intrinsic momentum structure and the quark dynamics inside the nucleon are investigated using *deep inelastic scattering* (DIS) of leptons on nucleons. A quark is struck and ejected out of the nucleon. By measuring the final-state scattered lepton, the unpolarised structure function $F_1(x, Q^2)$ and $F_2(x, Q^2)$ are extracted, interpreted in the parton distribution function (PDF) $q(x)$. The PDFs describe the number density of finding a quark with the flavour q and the momentum fraction x inside the nucleon. With the access to polarised beams and polarised targets, the longitudinal spin structure $\Delta q(x)$ of the nucleons can be investigated. Polarised parton distribution functions denote the difference of the probability to find quarks with the flavour q with opposite spins and are extracted from the measured helicity spin distribution $g_1(x)$. The first polarised measurement of the nucleon structure were performed at SLAC.

In QCD, strong interacting particles are allocated *colour* charge c (r, g, b and anti-colours). A quark carries an electric charge and a colour charge c and a gluon carries colour and anti-colour at the same time. Only colourless¹ particles seem to be observable in nature (*confinement*), while within a hadron, quarks move freely. When the distance of a struck quark to the target remnant increases, quark anti-quark pairs are created by the colour field. In the very end, all quarks recombine to hadrons. Several models for the hadronisation process were formulated to explain the experimental observations. To study hadronisation, any high energy process that produces hadrons can be used. The focus of this thesis lays on the semi-inclusive deep inelastic scattering, where a scattered lepton and at least one hadron are detected in the final state. For identified hadrons, the hadronisation is described using the quark-to-hadron fragmentation function (FF) $D_q^h(z, Q^2)$. It denotes the probability that a quark with a relative hadron momentum z with the flavour q hadronises into a hadron h . The FFs also depend on the four-momentum transfer Q^2 of the scattered lepton. Similar to the PDF, the FFs are universal quantities, but while the PDFs are well determined (with high precision), the FFs are still not well measured.

An excellent facility to study the structure of the nucleon and the hadronisation process is the COMPASS spectrometer. This two-staged fixed-target experiment is located at the M2 beam line of the Super Proton Synchrotron at CERN. With its unique high energetic polarised muon beam, the large acceptance and good particle identification, it is well-suited to efficiently measure semi-inclusive deep inelastic scattering using events with identified hadrons. The COMPASS I phase (between 2002 and 2011) was dedicated to the investigation of the spin structure of the nucleon using the polarised muon beam and a polarised proton target (NH₃) or a polarised deuteron target (⁶LiD). The main physics interest of the COMPASS II phase (started in 2012) is the measurement of deep virtual Compton scattering (DVCS) for which the muon beam impinges on an unpolarised liquid hydrogen target. In parallel, semi-inclusive deep inelastic scattering is measured to extract charged hadron multiplicities on protons.

The thesis is organised as follows: the theoretical background is summarised in Chapter 2 with the main focus laying on the semi-inclusive deep inelastic scattering process and the interpretation in the quark-parton model. Furthermore, the production of hadrons from a single quark is discussed and the fragmentation functions are introduced. The DIS measurement with a polarised muon beam on a fixed-target performed with the COMPASS spectrometer is presented in Chapter 3. Here, details and principles of major detectors are described. The muon trigger system is mandatory for the data taking at COMPASS and is introduced in Chapter 4. The trigger principles and the existing trigger detectors are discussed. In Chap-

¹ a colourless object is obtained by the combination of colour and anti-colour, or the combination of all three colours

ter 5, the new trigger hodoscopes for large scattering angle are introduced and described in details. The analysis part of this thesis starts in Chapter 6, where the efficiencies of the muon trigger are calculated. The COMPASS luminosity is determined for the 2006 and 2009 data taking period using two different methods. The main analysis, the determination of the charged hadron multiplicities of the 2006 run, is divided into two parts: in Chapter 7, the data set is introduced and the raw multiplicities with event-by-event corrections determined. In Chapter 8, further corrections for the multiplicities are shown, mostly coming from Monte Carlo simulations. With all corrections applied, the final results on charged hadron multiplicities are shown and discussed in Chapter 9. The experimental results on multiplicities are used to determine the fragmentation functions in leading-order in Chapter 10. The thesis concludes with a summary of the results. In the Appendix, additional information (including supporting figures and technical drawings) is provided. The numerical values of the charged pion multiplicities are displayed in a Table.

THEORETICAL FRAMEWORK

This chapter describes the underlying theory of the physics processes investigated in this thesis. First, the inclusive deep inelastic scattering process is introduced and the experimental results are interpreted within the quark-parton model. The scattering process is extended towards semi-inclusive deep inelastic scattering, where hadronisation processes come into play. The hadronisation process is described by fragmentation functions.

2.1 STRUCTURE OF THE NUCLEON

Inelastic scattering processes with virtual photons¹ are used to probe the structure of the nucleon. In first order of Quantum Electro Dynamics (QED), the process is described by an exchange of a single virtual photon, which is delivered by a lepton ℓ scattering off the nucleon N . The final state has a scattered lepton ℓ' and a hadronic state X . Figure 1 illustrates deep inelastic scattering process of $\ell(k) + N(P) \rightarrow \ell'(k') + X(p_X)$ in the fixed target frame with the corresponding four-momentum vectors k, k', P and q . When only the scattered lepton is measured, the process is called *inclusive*. At the COMPASS experiment, the lepton is replaced by a muon hitting a fixed target nucleon, which is the laboratory frame where the momentum of the target nucleon \mathbf{P} is zero.

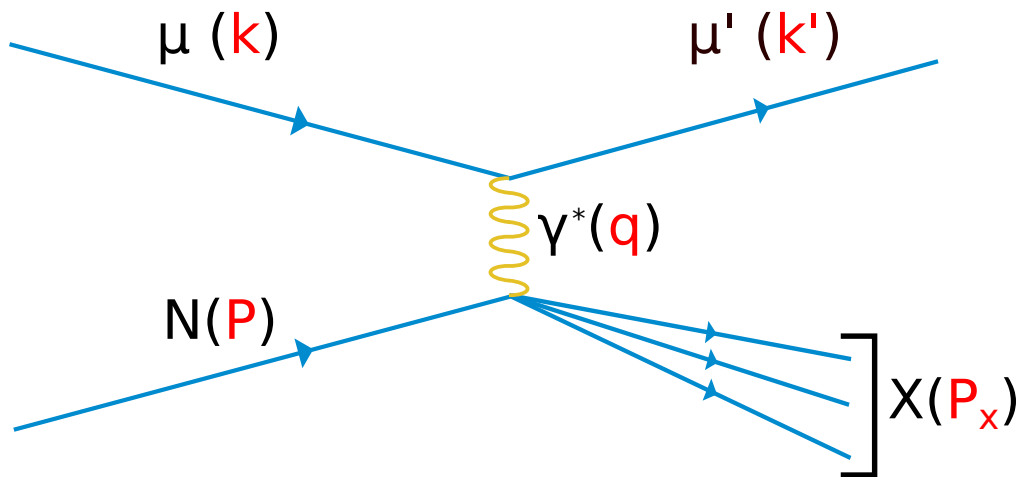


Figure 1: Kinematic of an inelastic scattering. A muon scatters off a nucleon, the final state contains a scattered lepton μ' and a hadronic state X . An one-photon exchange is assumed.

2.1.1 Kinematics of Deep-Inelastic Scattering

The DIS process is described by two independent kinematic variables. The kinematics of the inelastic scattering process are discussed according to Figure 1. The muon beam is represented by μ with the four-vector $k = (E, \mathbf{k})$. The scattered muon is shown as μ' with the

¹ Z-bosons take also part in the reaction but are suppressed

4-momentum $k' = (E', \mathbf{k}')$ with an azimuthal scattering angle θ , the resting target nucleon N with the 4-momentum $P = (M_N, 0)$ and the final hadronic state X with the total invariant mass W . The polar scattering angle ϕ has an isotropic distribution. The spin of the muon projectile is s , for the scattered muon s' and the spin of the target nucleon is S . The muon mass is m_μ . The bold variables represent the three-momentum vectors. The process is done by the exchange of a virtual photon γ . The four-vector of the photon q^2 is negative and therefore space-like. Additional kinematic variables are used to characterise the deep inelastic scattering. The most important inclusive variables are summarised below. The virtual photon, which is exchanged between the lepton and the nucleon, has the 4-momentum $q = k - k'$. Commonly, the negative squared transfer

$$Q^2 = -q^2 = -2m^2c^2 \left(\frac{EE'}{c^2} - |\mathbf{k}||\mathbf{k}'| \cos \theta \right) \stackrel{|\mathbf{k}'| \ll mc}{\simeq} -2m^2c^2 + \frac{4EE'}{c^2} \sin^2 \frac{\theta}{2} \quad (1)$$

is used. It is the virtuality of the photon and represents the scale of the interaction and the resolution of the probe. The Bjorken scaling variable x is interpreted as the elasticity of the scattering by

$$x = \frac{Q^2}{2P \cdot q}. \quad (2)$$

The energy loss of the muon or energy transfer in the laboratory system from the lepton to the nucleon is given by

$$\nu = \frac{P \cdot q}{M_N} = E - E'. \quad (3)$$

Here, E denotes the energy of the incoming muon and E' the energy of the scattered muon. Commonly, the dimensionless Lorentz-invariant energy fraction y is used.

$$y = \frac{P \cdot q}{P \cdot k} \xrightarrow{\text{fixed t.}} \frac{E - E'}{E} \quad (4)$$

The invariant mass of the hadronic final state is given by:

$$P_X^2 = (P + q)^2 \equiv W^2. \quad (5)$$

The invariant mass W is about $18 \text{ GeV}/c^2$ for the COMPASS kinematic.

$$\begin{aligned} W^2 = M_N^2 & \hat{=} x = 1 & \text{(elastic scattering)} \\ W^2 > M_N^2 & \hat{=} x < 1 & \text{(inelastic scattering)} \\ W^2 > M_{\text{resonance}}^2 & \hat{=} x < 1 & \text{(deep inelastic Scattering)} \end{aligned}$$

The lepton-nucleon scattering is called elastic when the invariant mass W is as large as the mass of the struck nucleon. With a W larger than $1 \text{ GeV}/c^2$, the process is called inelastic. With even larger invariant masses, larger than $M_{\text{resonance}}^2 > 5 \text{ GeV}^2/c^4$, the scattering is called deep inelastic (DIS). Figure 2 shows the differential cross section as a function W for different Q^2 measured at SLAC [9] for different beam energies E and for different four-momentum transfers q^2 . Above $W \approx M_N$, the structures at lower W are the nucleon resonances, which are observable up to 2.5 GeV .

2.1.2 The DIS Cross Section

The differential cross-section of the inclusive DIS process can be written as a contraction of a leptonic tensor $L_{\mu\nu}$ and a hadronic tensor $W^{\mu\nu}$.

$$\frac{d^2\sigma}{dx dQ^2} = \frac{\alpha^2 (\hbar c)^2}{Q^4} \frac{E'}{E} \cdot L_{\mu\nu} W^{\mu\nu} \quad (6)$$

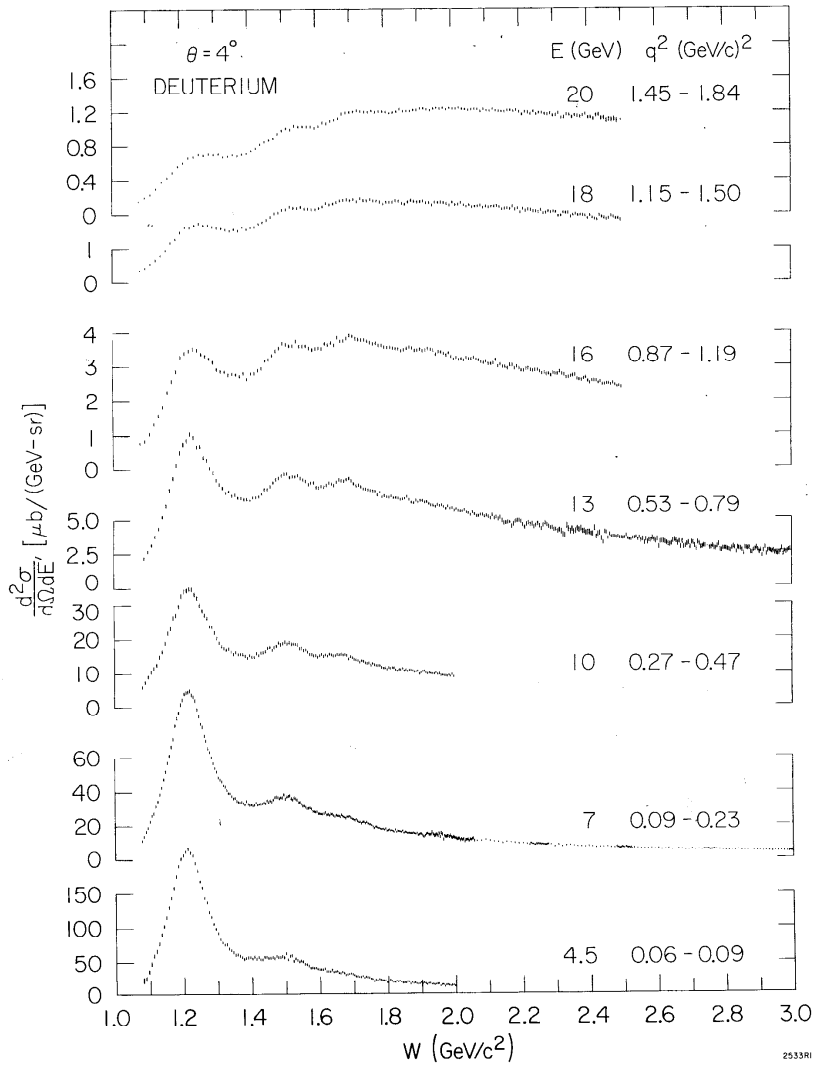


Figure 2: Measured differential cross section as a function of the invariant mass W of electron-proton scattering at SLAC.

Here, $\alpha = e^2/4\pi$ is the fine structure constant. For point-like leptons, the leptonic tensor $L_{\mu\nu}$ can be calculated and solved with Quantum Electro Dynamics (QED) and it contains the information about the emission of the virtual photon by the muon. Taking into account the spin of the leptons, the leptonic tensor can be factorised into a spin independent symmetric part S and a spin dependent asymmetric part A .

$$L_{\mu\nu}(k, s, k') = L_{\mu\nu}^{(S)}(k, k') + iL_{\mu\nu}^{(A)}(k, s, k') \quad (7)$$

The hadronic tensor cannot be easily calculated in quantum chromodynamics due to non-perturbative effects in the strong interaction. But the general form of the hadronic current has to depend on scalar functions (W_i and G_i) to satisfy the Lorentz invariance, the time reversal, the parity and conservation of the electromagnetic current. The *structure functions* W and G hold all the target dependent information in the inclusive scattering process and, similar to the leptonic tensor, the hadronic tensor can be separated into a symmetric part S and an asymmetric part A .

$$W_{\mu\nu}(k, s, k') = W_{\mu\nu}^{(S)}(P, q) + iW_{\mu\nu}^{(A)}(P, S, q) \quad (8)$$

After several simplifications and exclusion of non-contributing parts, the spin independent and spin dependent components of $W_{\mu\nu}$ are

$$W_{\mu\nu}^{(S)} = -W_1 \left(\frac{q_\mu q_\nu}{Q^2} \right) + \frac{1}{M^2} W_2 \left(p_\mu + \frac{p \cdot q}{Q^2} q_\mu \right) \left(p_\nu + \frac{p \cdot q}{Q^2} q_\nu \right) \quad (9)$$

and

$$W_{\mu\nu}^{(A)} = \frac{i}{M^2} \epsilon_{\mu\nu\lambda\sigma} q^\lambda \left[s^\sigma \left(G_1 + \frac{\nu}{M} G_2 \right) - \frac{1}{M} s \cdot q p^\sigma G_2 \right]. \quad (10)$$

For the total inclusive cross section, it means that only symmetric or antisymmetric contractions of the leptonic and hadronic tensor contribute.

$$\frac{d^2\sigma}{dx dQ^2} = \frac{\alpha^2 (\hbar c)^2 E'}{Q^4 E} \cdot \left[L_{\mu\nu}^{(S)}(l, l') W^{\mu\nu(S)}(P, q) - L_{\mu\nu}^{(A)}(k, s, k') W^{\mu\nu(A)}(P, S, q) \right] \quad (11)$$

2.1.3 Structure Functions

The first measurements of the inclusive cross section in the DIS region were performed at the linear accelerator at Stanford (SLAC) with a 20 GeV/c electron beam [3]. For fixed values of x and at $W > 2 \text{ GeV}/c^2$, the cross section showed only a weak dependence on Q^2 . The measured range was between 1 and 10 GeV²/c². Figure 3 left shows the ratio of the measured deep inelastic scattering cross section σ and the Mott cross section σ_{Mott} as a function of Q^2 for different W bins. A comparison to elastic scattering is also shown as a dashed line. The weak dependence on Q^2 in the higher W bin is interpreted by the quark-parton model. The unpolarised structure function W_1 and W_2 and the polarised structure function G_1 and G_2 are changed to dimensionless structure functions F_1 , F_2 , g_1 and g_2 .

$$\left. \begin{aligned} MW_1(\nu, Q^2) &= F_1(x, Q^2) \xrightarrow{\text{exp.}} F_1(x) \\ \nu W_2(\nu, Q^2) &= F_2(x, Q^2) \xrightarrow{\text{exp.}} F_2(x) \end{aligned} \right\} \text{unpolarised structure functions} \quad (12)$$

$$\left. \begin{aligned} \frac{\nu}{M} G_1(\nu, Q^2) &= g_1(x, Q^2) \xrightarrow{\text{exp.}} g_1(x) \\ \frac{\nu^2}{M^2} G_2(\nu, Q^2) &= g_2(x, Q^2) \xrightarrow{\text{exp.}} 0 \end{aligned} \right\} \text{spin structure functions} \quad (12')$$

When averaging over the beam and target polarisation and summing over the final spins, the asymmetric part $W_{\mu\nu}$ vanishes and only the structure functions $F_1(x, Q^2)$ and $F_2(x, Q^2)$ are accessible. In order to measure the spin related properties of the nucleon, such as $g_1(x, Q^2)$, polarised lepton beams and a polarised nucleon target are needed. With Equation (11), (12) and the contraction of the leptonic tensor with the hadronic one, the inclusive cross sections can be written as:

$$\frac{d^2\sigma_{\text{unpol}}}{dx dQ^2} = \frac{4\pi\alpha^2}{Q^4 x} \left[(1-y) F_2(x, Q^2) + xy F_1(x, Q^2) \right] \quad (13)$$

for the unpolarised case and

$$\frac{d^2\sigma_{\text{long.pol}}}{dx dQ^2} = \frac{4\pi\alpha^2}{Q^4 x} \left[(1-y) g_2(x, Q^2) + xy g_1(x, Q^2) \right] \quad (13')$$

for the longitudinal polarised case. The transverse polarisation is not shown here. For a longitudinal polarized target, g_2 is suppressed; the cross-section is mostly sensitive to g_1 .

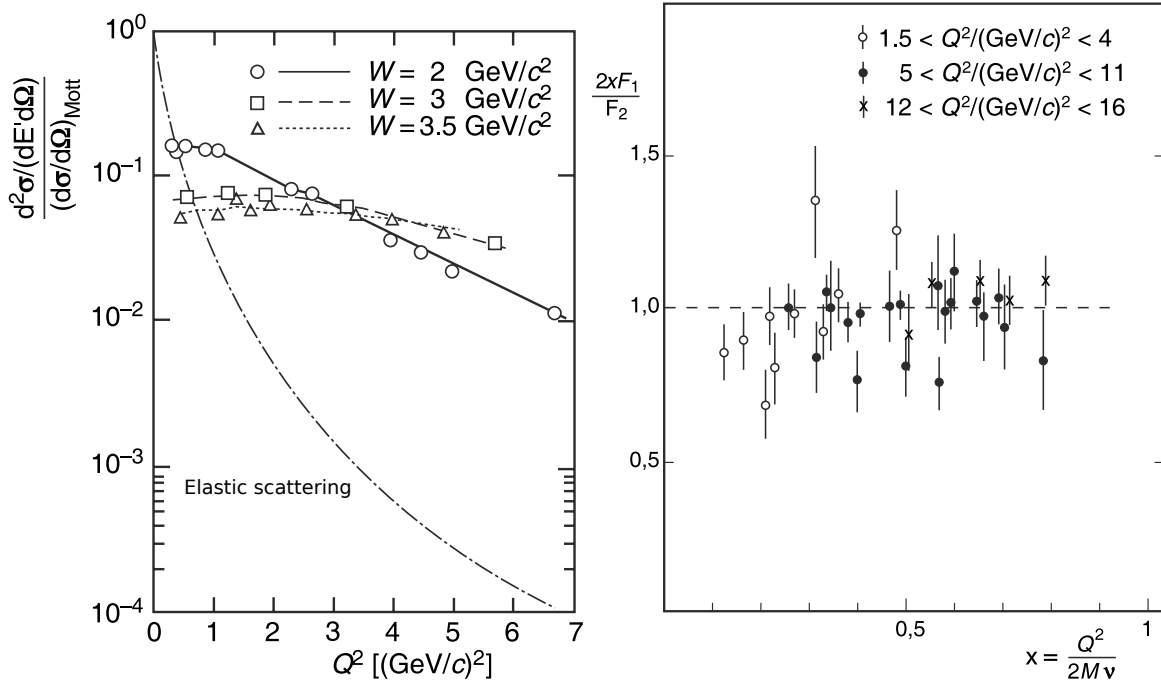


Figure 3: **Left:** $\sigma_{\text{DIS}}/\sigma_{\text{Mott}}$ as a function of Q^2 for different W bins. This ratio is proportional to the structure function F_2 . **Right:** Callan-Cross relation. Both plots are taken from [10].

2.1.3.1 Quark-Parton Model

The weak Q^2 dependence of the structure functions observed with early DIS cross section measurement indicates that the lepton is scattered on a charged point-like object. But former measurements of the proton form factor demonstrated that the proton is an extended object with the size of about 1 fm. The SLAC measurement is therefore interpreted as an evidence for point-like constituents as substructure of the proton. Assuming in addition that these constituents have a spin 1/2, the Callan-Gross relation [11] is obtained between F_1 and F_2 :

$$2xF_1(x) = F_2(x). \quad (14)$$

This relation is verified experimentally in Figure 3 right and shows the ratio of the two structure functions $2xF_1/F_2$ as a function of x for different Q^2 bins. The point-like constituents of the nucleon are fermions. This is the basis of the parton model from Feynman. The nucleon consists of almost massless point-like partons with spin 1/2. Prior to the measurements, models of hadrons were already predicted by Bjorken, Gellmann and Zweig [5]. In these quark models, the nucleon consists of a triplet of quarks (u,d,s) with additional quantum numbers.

The combination of the two models leads to the quark-parton model (QPM) [12] [13]. In this model, the nucleon consists of three valence quarks with the flavour u and d, which hold all the quantum numbers. In addition, the nucleon contains quark anti-quark pairs of all flavours known as *sea quarks*. The valence quarks of a proton are uud and of a neutron udd. The properties of quarks and nucleons are briefly summarised in Table 2.

The QPM is formulated in the infinite momentum frame (*Breit frame*), where the target nucleon moves with a momentum $P_z \rightarrow \infty$. The partons are moving collinearly within the nucleon and the transverse momenta and masses are neglected. Within the time scale of interaction, the virtual photon interacts with one parton and the remaining partons are only

	u	d	c	s	t	b	p (uud)	n (uud)
Charge z	+2/3	-1/3	+2/3	-1/3	+2/3	-1/3	1	0
Spin s	1/2	1/2	1/2	1/2	1/2	1/2	1/2	1/2

Table 2: Summary of quark and nucleon properties.

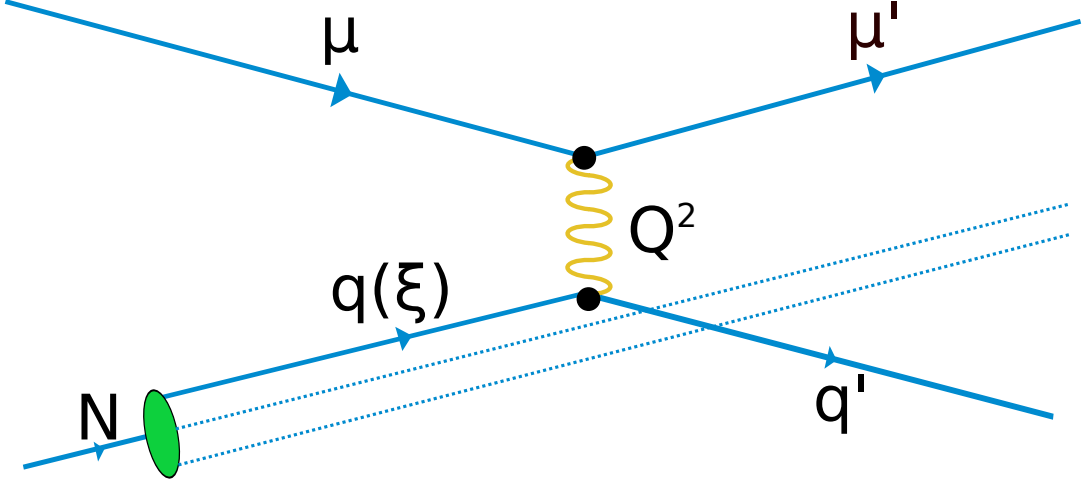


Figure 4: DIS in the QPM: the muon scatters off a single quark, the remaining quarks are only “spectating” the process.

spectators. The lepton-nucleon scattering is viewed as a scattering of virtual photons off free partons (Figure 4). The struck parton carries the momentum fraction ξ of the nucleon. The cross section for lepton-nucleon interaction can be therefore written as the incoherent sum of cross sections for virtual photon-quark scattering. This allows the factorisation of the “hard” lepton-parton scattering, which can explicitly be calculated by QED, and the nucleon, which cannot be calculated in perturbative QCD. The cross section of the DIS process at high momentum transfer² is then

$$\frac{d^2\sigma}{dx dQ^2} \propto \int_0^1 d\xi \sum_i q_i(\xi) \frac{d\sigma_0(x/\xi, Q^2)}{dx dQ^2}. \quad (15)$$

The parton density functions $q_i(\xi)$ are the number density to find a parton of the type i with the momentum fraction ξ in the nucleon. The cross section σ_0 is the cross section of the lepton-quark scattering. The sum runs over all quark and anti-quark flavours. With this new approach and the fact that the momentum fraction ξ is identical to the Bjorken scaling variable x (after the absorption of the virtual photon, the four-momentum of the quark is $(\xi P + q)^2 = 0 \Rightarrow \xi = -q^2/2P \cdot q = x$), the structure functions F_1 and F_2 can be rewritten in terms of parton density functions

$$\begin{aligned} F_1(x) &= \frac{1}{2} \sum_q e_q^2 (q(x) + \bar{q}(x)), \\ F_2(x) &= x \frac{1}{2} \sum_q e_q^2 (q(x) + \bar{q}(x)). \end{aligned} \quad (16)$$

Here, e_q denotes the charge of the quark with the flavour q and $q(x)$ ($\bar{q}(x)$) the corresponding quark (anti-quark) parton distribution. The PDFs $q(x)$ are the number density for finding a

² surprisingly, experiments showed that four-momentum transfers of $Q^2 > 1 \text{ GeV}^2/c^2$ are sufficient for the infinite momentum frame

parton of flavour q with a momentum fraction x inside the nucleon. Only quark distributions contribute to the structure functions (F_1 and F_2) as the gluons are electrically neutral. The PDFs are universal (*i. e.* process-independent) quantities. The quark distributions satisfy the following sum rules for protons, which are interpreted as the net number of the quarks in the simple quark model.

$$\begin{aligned}\int_0^1 [u(x) - \bar{u}(x)] dx &= 2 \\ \int_0^1 [d(x) - \bar{d}(x)] dx &= 1 \\ \int_0^1 [s(x) - \bar{s}(x)] dx &= 0\end{aligned}\tag{17}$$

In the proton there are two up-quarks and one down-quark. The strange quarks and all anti-quarks only appear as *sea*-quarks. By exchanging the light flavours of the proton, the quark content of the neutron is obtained (isospin symmetry). For the quark distribution, it follows:

$$u_v^p = d_v^n \qquad d_v^p = u_v^n\tag{18}$$

The structure functions from DIS can be measured with neutrino beams. As they do not carry any electric charge, the structure function $F_2^{v,N}$ is

$$F_2^{v,N} = x \sum_i (q_i(\cdot) + \bar{q}_i(x)).\tag{19}$$

When integrating over x and comparing with the result of $F_2^{e,N}$, the fraction of the momentum of the nucleon, which are carried by the quarks q , is obtained. The structure function $F_2^{e,N}$ of the nucleon N is the average of the measurements of the proton and the neutron.

$$\int_0^1 F_2^{v,N}(x) dx \approx \frac{18}{5} \int_0^1 F_2^{e,N}(x) dx \approx 0.5\tag{20}$$

The result shows that quarks only carry half of the nucleon momentum. The rest is carried by neutral particles identified as *gluons*, the gauge bosons of the strong force.

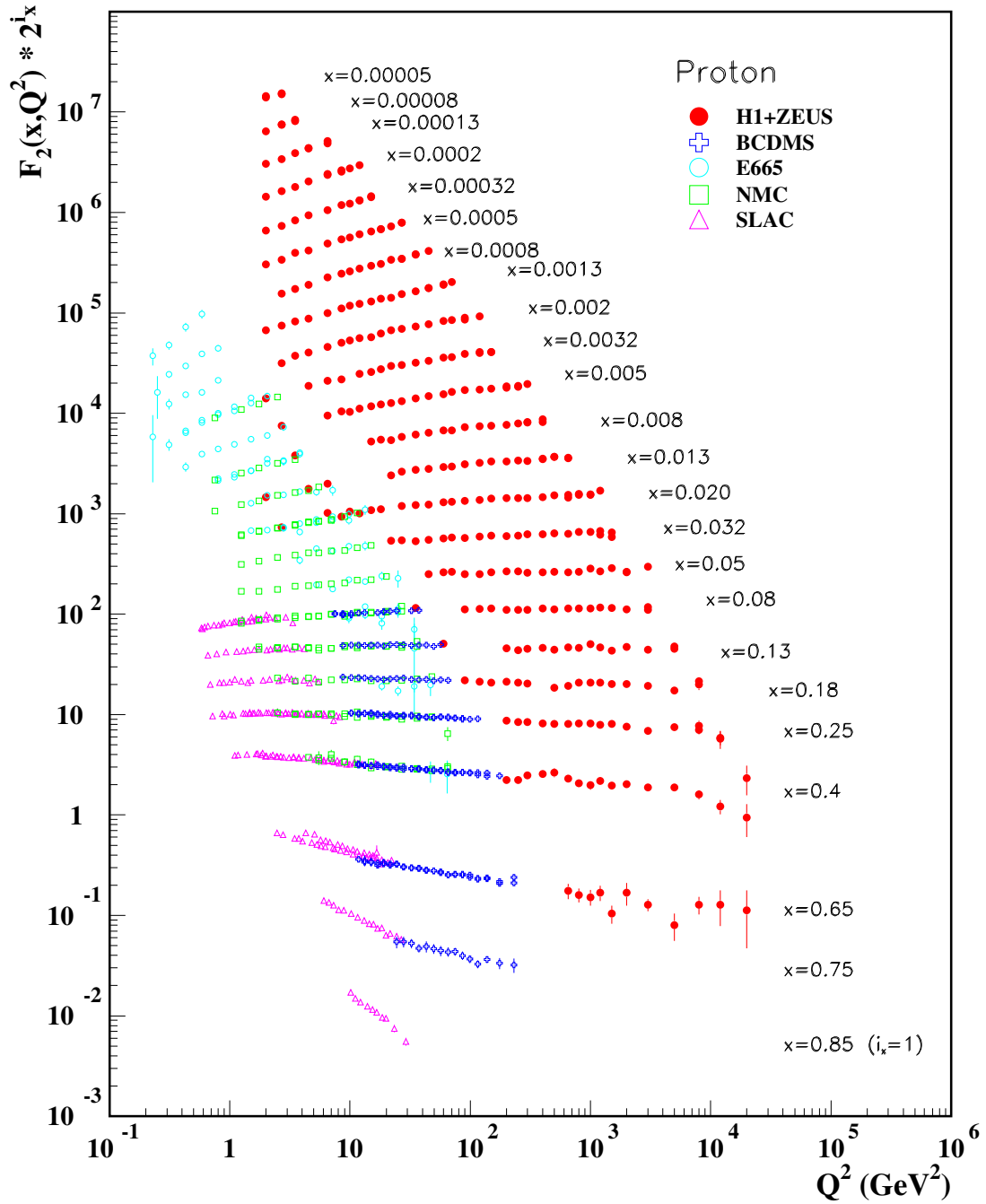


Figure 5: The proton structure function F_2^p measured in electromagnetic scattering of electrons and positrons on protons (collider experiments H1 and ZEUS for $Q^2 \leq 2 \text{ GeV}^2/c^2$), in the kinematic domain of the HERA data, and for electrons (SLAC) and muons (BCDMS, E665, NMC) on a fixed target. Statistical and systematic errors added in quadrature are shown. The data are plotted as a function of Q^2 in bins of fixed x . Some points have been slightly offset in Q^2 for clarity. The H1+ZEUS combined binning in x is used in this plot; all other data are re-binned to the x values of these data. For the purpose of plotting, F_2^p has been multiplied by 2^{i_x} , where i_x is the number of the x bin, ranging from $i_x = 1 (x = 0.85)$ to $i_x = 24 (x = 0.00005)$. Taken from [8].

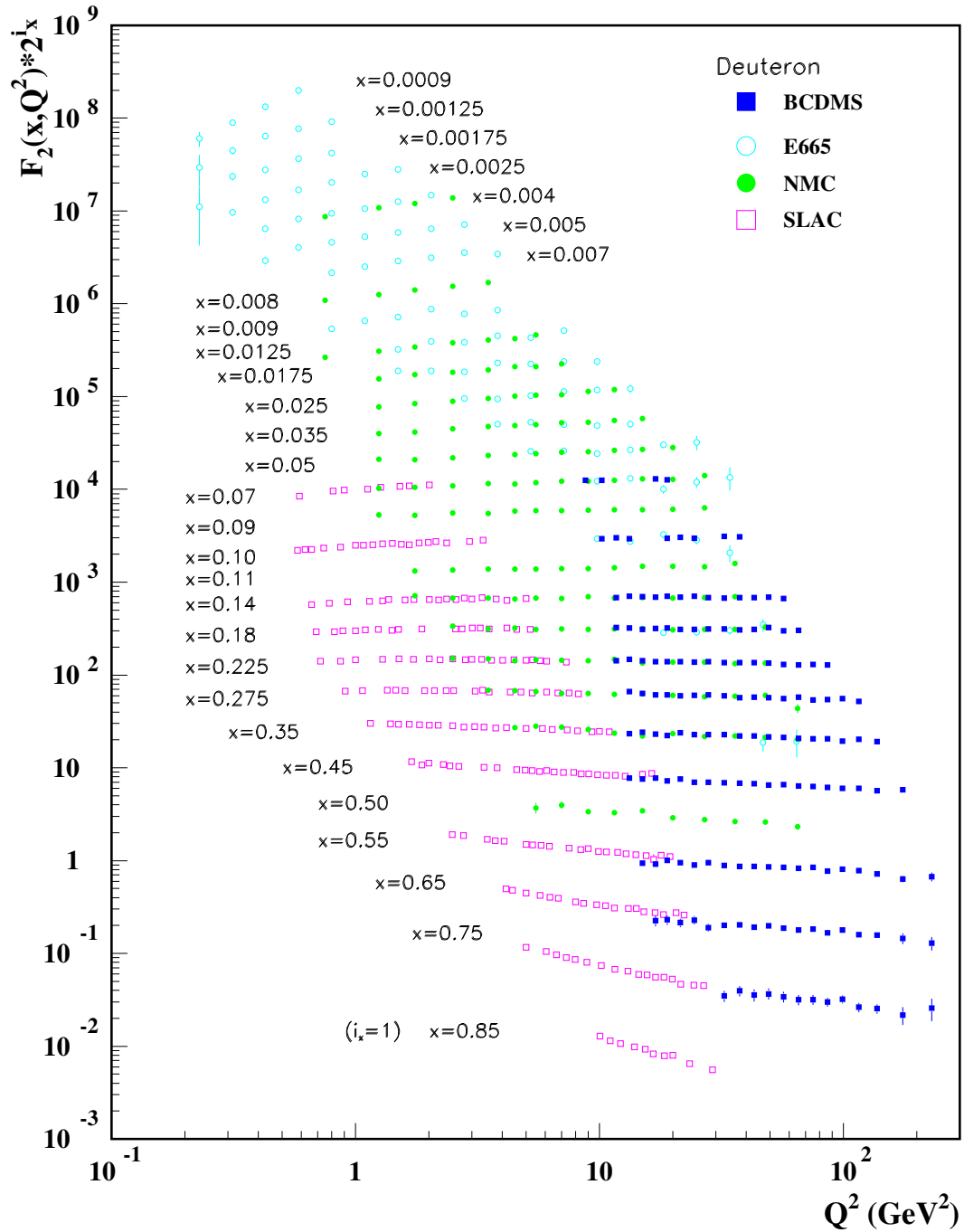


Figure 6: The deuteron structure function F_2^d measured in electromagnetic scattering of electrons (SLAC) and muons (BCDMS, E665, NMC) on a fixed target, shown as a function of Q^2 for bins of fixed x . Statistical and systematic errors added in quadrature are shown. For the purpose of plotting, F_2^d has been multiplied by 2^{i_x} , where i_x is the number of the x bin, ranging from 1 ($x = 0.85$) to 29 ($x = 0.0009$). Taken from [8].

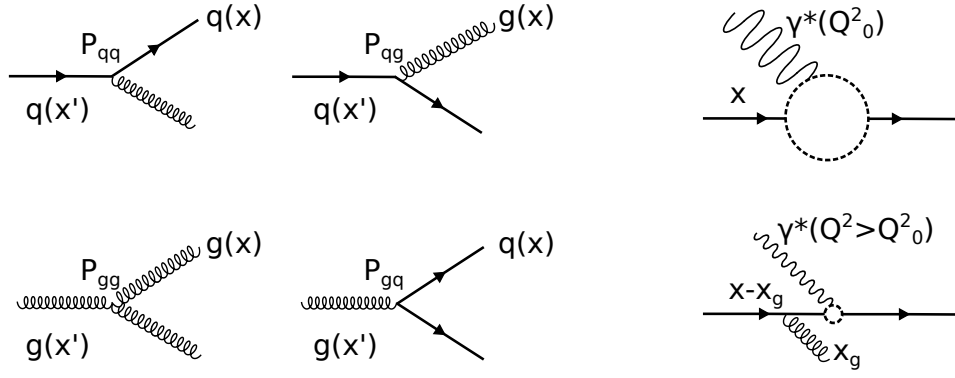


Figure 7: **Left:** The splitting function P_{ab} of a parton a into a parton b . **Right:** Illustration of the Q^2 evolution of the parton density functions. With larger Q^2 , more structures can be resolved. The circle represents the resolution probed by the photon.

2.1.3.2 The QCD-Improved QPM

Meanwhile, the proton structure function $F_2^p(x, Q^2)$ and the deuterium structure function $F_2^d(x, Q^2)$ were measured over a large kinematic range by several experiments. The results are shown in Figures 5 and 6 as a function of x and Q^2 . The measurements include lepton-nucleon scattering on a fixed target as well as lepton-hadron collisions from collider experiments. Only in the $x = 0.2$ region, where SLAC measured, the structure functions F_2^p and F_2^d are independent of Q^2 . Outside this intermediate x range, the structure functions do have a Q^2 dependence. The QPM has to be improved by taking into account gluons and QCD effects.

Quantum chromodynamics is a non-Abelian gauge theory that describes the interaction of quarks by the colour field transmitted by gluons. The charge in the strong interaction is the colour charge. There are three colour charges (r, g, b) and corresponding anti-colour ($\bar{r}, \bar{g}, \bar{b}$). Quarks carry one of the colour charge c , while gluons carry simultaneously one colour and one anti-colour. Gluons do not carry electric charge. Mathematically, the possible colour charge combinations of the gluon are described by a $SU(3)$ symmetry with three colours and three anti-colours ($3 \otimes \bar{3} = 8 \oplus 1$). This results in an anti-symmetric octet and in a symmetric singlet. The singlet is colourless and does not couple with quarks. By carrying colour charge, gluons interact not only with quarks, but also among themselves. The consequence is that the coupling constant α_s strongly depends on the energy scale of the interaction. One can distinguish two regimes:

Asymptotic freedom: at high momentum transfer (in other words, short distance), the strong coupling α_s decreases. Quarks behave as free particles as assumed in the QPM. In this “hard” region, a perturbative expansion can be used for the calculation of *e. g.* cross sections.

Confinement: at low energy (long distance), the phenomena are called “soft” and α_s becomes very large. Particles that carry colour charge cannot be observed as free particles. Coloured particles such as quarks and gluons only appear in hadrons (or other bound states). Processes that involve low energy scales of the interaction cannot be calculated with perturbation theory. The property of confinement is currently the best conjecture.

In the naive QPM, the strong coupling α_s is zero. Quarks inside a nucleon behave as a collinear laminar parton beam. The quark-parton model has to be improved to take into account the interaction between the quarks and the gluons. This can be done at a finite $Q^2 \gg M^2$. At this scale, the strong coupling α_s is non-zero, but still small enough to apply perturbative quantum chromodynamics.

For small values of α_s , as in QED, a factorisation Ansatz is applicable: $\sigma \sim \int q(x)\sigma_0$ in QCD. Introducing a factorisation scale μ_F , the long and short distances of the interaction can be

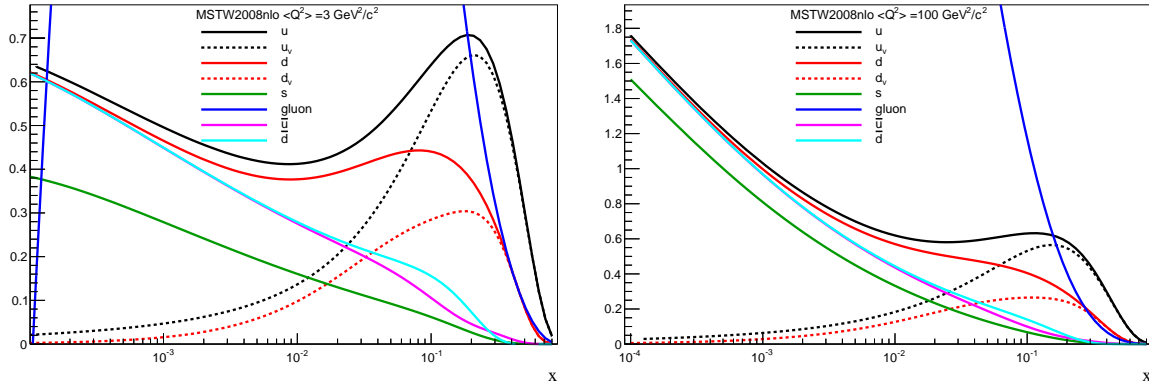
Parton distribution function $xq(x)$ 

Figure 8: Parton distribution function for u , u_v , d , d_v , s , g , \bar{u} and \bar{d} in the reference scale of $Q^2 = 3 \text{ GeV}^2/c^2$ (left) and $Q^2 = 100 \text{ GeV}^2/c^2$ (right).

separated. Experimentally, the four-momentum transfer Q^2 is commonly used for the scale μ_F . The QCD interaction between gluons and quarks and the gluon-gluon coupling are described by the splitting functions $P_{i i'}$ [14]. A quark may emit a gluon in the initial state, a gluon can convert into a quark anti-quark pair and gluons can couple among themselves. The splitting functions are extracted from a power series in α_s from theoretical calculation, considering the various parton interactions. In leading order (LO), only one order of α_s is considered ($\mathcal{O}(\alpha_s)$) and the processes are shown in Figure 7. In next-to-leading order (NLO), the expansion is pursued to $\mathcal{O}(\alpha_s^2)$. Here, additional interaction possibilities are considered, for instance a gluon vertex correction.

Taking into account the qg interaction, the Q^2 dependence of the structure functions is explainable with the right side of Figure 7. A virtual photon probes a quark with the momentum fraction x at a fixed Q_0^2 and a quark distribution $q(x, Q_0^2)$ is measured. With higher resolution ($Q_1^2 > Q_0^2$), radiative effects such as gluon radiation can be resolved and change the measured momentum fraction x . The measured quark momentum would be $x - x_g$, if an emitted gluon with x_g was resolved. With increasing Q^2 , the photon resolves more structures. The interpretation is that each quark is surrounded by a cloud of gluons and further quarks. This Q^2 behaviour is described with

$$\frac{d}{d \ln \mu_F} q_i(x', \mu_F) = \sum_i \int_{x'}^1 \frac{dx}{x} P_{i i'}(x'/x, \alpha_s(\mu_F)) q'_i(x, \mu_F) \quad (21)$$

and is known as the Dokshitzer-Gribov-Lipatov-Altarelli-Parisi equation [15] (short: DGLAP equation). It contains the splitting function $P_{i i'}(x/\xi)$ that gives the probability that a parton of type i (with momentum fraction x') is the parent of the parton i' with the momentum fraction x . The interpretation of the DGLAP evolution is that, with higher resolution of the probing photon, a larger number of quarks can be resolved. The fraction of quarks with high x therefore decreases, while the number with low x increases, as can be seen in Figures 5 and 6.

With the combination of experimental data (ep , en , νp and $\bar{\nu} p$), the parton distribution functions can be computed. Figure 8 shows x times the PDFs of u , u_v , d , d_v , s , g , \bar{u} and \bar{d} for a proton. The u and d distributions contain the valence and the sea quarks: $u = u_v + u_s$ and $d = d_v + d_s$. The NLO parametrisation from MSTW08 [16] is used at $Q^2 = 3 \text{ GeV}^2/c^2$, which represent the mean Q^2 of the COMPASS experiment, and for comparison at a higher Q^2 ($100 \text{ GeV}^2/c^2$). The valence quarks have an expected maximum at $x \sim 0.3$, considering that the proton consists of three valence quarks. With smaller x , the valence quark distribution depletes and the contributions from the sea increases. At very low x , all sea quark distribu-

tions (u, d, \bar{u} and \bar{d}) contribute similarly. The strange quarks, which are not part of the valence quarks, also rise with decreasing x . The gluon distribution is zero at large x but swiftly rises and exceeds all other distributions at low x . At $Q^2 = 100 \text{ GeV}^2/c^2$, the overall structure of the parton distribution functions looks similar to the one at $3 \text{ GeV}^2/c^2$, but the contributions are stronger due to the higher probing resolution. The unpolarised PDFs are determined by a QCD global analysis using a fit of different sets of data covering large kinematic domains and provided by different experiments.

2.1.4 Polarised DIS and polarised PDFs

With the access to longitudinal polarised lepton beams and longitudinal polarised targets, the spin structure of the nucleon can be investigated by measuring the inclusive cross section asymmetries between the two polarisation directions of the target. The scattering muon is used as a virtual photon source and two photon-nucleon cross sections $\sigma_{1/2}$ ($\sigma_{3/2}$) are measured. Here, $\sigma_{1/2}$ ($\sigma_{3/2}$) denotes the cross section of a polarised quark in the target nucleon and the beam polarised in the same (opposite) direction. The spin orientation of the quarks is described by the quark helicity distribution: it denotes the probability to find a quark with a spin parallel (anti-parallel) to the nucleon spin. Within the QPM, leading-order and assuming a one-photon exchange, the photon-nucleon asymmetry is given by

$$A_1 = \frac{\sigma_{1/2}^{\text{DIS}} - \sigma_{3/2}^{\text{DIS}}}{\sigma_{1/2}^{\text{DIS}} + \sigma_{3/2}^{\text{DIS}}} = \frac{g_1(x, Q^2)}{F_1(x, Q^2)} \stackrel{\text{LO}}{=} \frac{\sum_q e_q^2 \Delta q(x, Q^2)}{\sum_q e_q^2 q(x, Q^2)}. \quad (22)$$

Here, the unpolarised PDFs $q(x, Q^2)$ are the sum of both quark helicities, while the difference of the quark helicity is the polarised parton distribution functions $\Delta q(x)$. Instead of measuring the absolute cross section σ^{DIS} , the number of scattered muons on polarised nucleons can be counted, assuming that the muon flux on two opposite polarised target cells cancels out. With the measured asymmetry $A_1(x, Q^2)$ and the structure function $F_1(x, Q^2)$, the spin structure function $g_1(x, Q^2)$ is obtained.

With a perturbative QCD fit using the DGLAP equations for the Q^2 dependence and $g_1(x, Q^2)$ as input, the polarised PDFs are extracted. But in this inclusive measurement, only the sum of each flavour and anti-flavour $\Delta Q = \Delta q + \Delta \bar{q}$ is determined. The total spin contribution of the quarks to the nucleon $\Delta \Sigma$ is the sum of all ΔQ [17] [18]. The nucleons are fermions with a spin 1/2, which can be decomposed into the quark contribution $\Delta \Sigma$, the spin contribution of the gluons ΔG [19] and additional orbital momenta L :

$$\frac{1}{2} = \frac{1}{2} \Delta \Sigma + \Delta G + L. \quad (23)$$

The quark contribution to the total spin of the nucleon was measured by EMC [20] and was found to be about 30% (spin crisis).

The separation of flavour and anti-flavour is only partly possible. In the valence quark region (with x around 0.3), the separation of u and d is possible. In the naive quark-parton model, ignoring any contribution from strange quarks and combining the measurements of g_1 on proton and deuteron, the quark and anti-quark polarizations $\Delta u/u$ and $\Delta d/d$ can be extracted in the valence quark region of large x [21]. But the polarised parton distribution Δs and $\Delta \bar{s}$ cannot be separated. More information is needed, for instance the measurement of an additional hadron in semi-inclusive deep inelastic scattering. By identifying the hadron type, conclusions can be drawn about the flavour of the struck quark. But the transition of the struck quark into the measured final-state hadron is complicated and needs to be understood by investigating the hadronisation process.

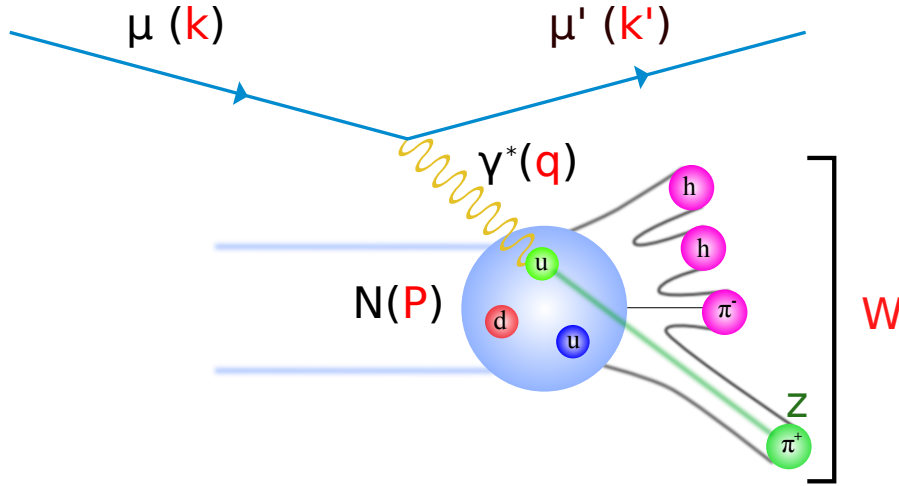


Figure 9: Kinematic of semi-inclusive deep inelastic scattering. Similar to the inclusive case, a lepton scatters off a nucleon. In addition to the scattered lepton, at least one hadron is measured in the final state. A one-photon exchange is assumed.

2.1.5 Semi-Inclusive Deep Inelastic Scattering

In SIDIS, at least one hadron is detected in coincidence with a scattered muon. In Figure 9, the process is shown. When a quark is struck by a high-energy photon, it is propelled out of the bound nucleon compound and eventually a hadron shower is produced.

$$l + N \rightarrow l' + h + X \quad (24)$$

The process and model describing this hadronisation are described in Section 2.2. The hadronisation from the struck parton is called *current fragmentation*, while the hadron shower from the residual nucleon is called *target fragmentation*. The same kinematic variables as in the inclusive case are used, but additional measures are needed. Besides the transverse momentum of the hadron p_T with respect to the direction of the virtual photon and the azimuthal angle of the hadron θ_h , the fractional energy carried by the final-state hadron z is determined

$$z = \frac{P \cdot P_h}{P \cdot p} \stackrel{\text{lab.}}{\equiv} \frac{E_h}{\nu}. \quad (25)$$

Alternatively, the Feynman scaling variable x_F [12]

$$x_F \approx \frac{P_z(h)}{P_z(\text{beam})} \Big|_{\text{CMS}} \quad (26)$$

can be used. Here, $P_z(h)$ ($P_z(\text{beam})$) is the Z component of the hadron (beam) momentum in the center of mass system. Both z and x_F are used to distinguish hadrons coming from the current fragmentation and the target fragmentation

$$\begin{aligned} x_F > 0 &\rightarrow z > 0.1 && \text{current quark hadronisation,} \\ x_F < 0 &\rightarrow z < 0.1 && \text{target hadronisation.} \end{aligned} \quad (27)$$

The hadronisation cannot be calculated by perturbation theory, as the distance scale of this process is too large. In the collinear case, this process is quantified by the parton-to-hadron fragmentation function $D_i^h(x, z, Q^2)$. The fragmentation function (FF) describes the probability of a hadron h to be produced from the struck parton of the type i . The properties of the

FF are further discussed in Section 2.1.5.1. The SIDIS cross section of process is described by the combination of PDFs and FF.

$$\frac{d\sigma^h}{dx dy dz} = \frac{2\pi\alpha^2}{Q^2} \left[\frac{1 + (1-y)^2}{y} 2F_1^h(x, z, Q^2) + \frac{2(1-y)}{y} F_L^h(x, z, Q^2) \right] \quad (28)$$

In leading order, the structure functions F_1^h and F_L^h are given by:

$$\begin{aligned} 2F_1^h(x, z, Q^2) &= \sum_q e_q^2 f_q(x, Q^2) D_q^h(z, Q^2) \\ F_L^h(x, z, Q^2) &= 0 \end{aligned} \quad (29)$$

At NLO, further emission of gluons are taken into account. The structure functions are given by

$$\begin{aligned} 2F_1^h(x, z, Q^2) &= \sum_q e_q^2 \left(f_q(x, Q^2) D_q^h(z, Q^2) \right. \\ &\quad + \frac{\alpha_s(Q^2)}{2\pi} \left[q \otimes C_{qq}^1 \otimes D_q^h \right. \\ &\quad \left. \left. + q \otimes C_{gq}^1 \otimes D_g^h + g \otimes C_{qg}^1 \otimes D_q^h \right] (x, z, Q^2) \right), \\ F_L^h(x, z, Q^2) &= \frac{\alpha_s(Q^2)}{2\pi} \sum_q e_q^2 \left[q \otimes C_{qq}^L \otimes D_q^h \right. \\ &\quad \left. + q \otimes C_{gq}^L \otimes D_g^h + q \otimes C_{qg}^L \otimes D_q^h \right] (x, z, Q^2), \end{aligned} \quad (30)$$

where \otimes is the standard convolution and $C_{ii'}^{1,L}$ are the NLO coefficient functions in the $\overline{\text{MS}}$ scheme.

2.1.5.1 Fragmentation Functions

The fragmentation functions are the final-state analogue of the initial state parton distribution functions. While the PDFs $q(x)$ denote the number density in a given momentum range x to find a quark with the flavour q inside a hadron h , the fragmentation function $D_q^h(z)$ represents the probability that a quark q changes into a hadron h carrying a fraction z of the quark momentum. But with certainty, a quark hadronises into a hadron. The FFs are process-independent, meaning that the origin of a quark or gluon that hadronises is not important for the fragmentation. The FFs from pp collision, e^+e^- annihilation or the ejection of a quark by DIS are the same. The universality of the FFs, predicted by the factorisation theorem, is experimentally tested by comparing the hadron production in e^+e^- collisions and from deep inelastic scattering. The FFs are constrained by conservations law of momentum and charge:

$$\sum_h \int_0^1 dz z D_q^h(z, Q^2) = 1 \quad (31)$$

$$\sum_h \int_0^1 dz e_h D_q^h(z, Q^2) = e_q \quad (32)$$

The momentum in terms of the fractional hadron energy sums up to one if all hadrons are considered. The charge is conserved where $e_h(e_q)$ is the charge of a hadron h (parton q). In

both cases, it is summed over all hadrons h and integrated of the hadron energy z . The sum of the fragmentation function for quarks and anti-quarks has to fulfil

$$\sum_h \int_{z_{min}}^1 [D_q^h(z) + D_{\bar{q}}^h(z)] dz = n_h, \quad (33)$$

where z_{min} is the minimum energy required to produce a hadron and n_h is the multiplicity of hadron h .

In total, there are 12 fragmentation functions when considering the hadronisation to pions. Note that here in this thesis only light quarks (u , d and s) are discussed. In the COMPASS kinematic range, quarks with higher mass do not play a role. To simplify and reduce this number, isospin and charge conjugation invariance are used. Charge conjugation leads to

$$D_q^{h+} = D_{\bar{q}}^{h-}. \quad (34)$$

Applying the isospin symmetry, the probability of an u quark fragmenting into a positive pion is the same as the one of an \bar{u} into a negative pion:

$$D_u^{\pi^+} = D_{\bar{u}}^{\pi^-}. \quad (35)$$

Using both symmetries, the pion fragmentation function can be reduced to a set of two functions, namely a *favoured* D_{fav} and an *unfavoured* fragmentation function D_{unf} . A fragmentation function is "favoured" when the final-state hadron contains the initial quark. It is expected that the favoured fragmentation is larger than the unfavoured one.

Due to the different mass, the strange quarks have their own fragmentation function. In the case of pions, it is often assumed that $D_{str}^{\pi} = D_{unf}^{\pi}$. For the kaons, on the other hand, there are three fragmentation functions, when taking into account isospin symmetry and disregarding the gluon fragmentation functions.

2.1.6 Polarised PDFs from SIDIS

In semi-inclusive deep inelastic scattering, where an additional final-state hadron is measured, the hadron double spin asymmetry A_1^h can be determined. Similar to Section 2.1.4, the number of scattered muons on polarised nucleons is counted and weighted by the number of identified hadrons:

$$A_{1,p}^h = \frac{\sigma_{1/2}^{SIDIS} - \sigma_{3/2}^{SIDIS}}{\sigma_{1/2}^{SIDIS} + \sigma_{3/2}^{SIDIS}} \stackrel{LO}{=} \frac{4(D_u^h \Delta u + D_{\bar{u}}^h \Delta \bar{u}) + (D_d^h \Delta d + D_{\bar{d}}^h \Delta \bar{d}) + 2(D_s^h + D_{\bar{s}}^h) \Delta s}{4(D_u^h u + D_{\bar{u}}^h \bar{u}) + (D_d^h d + D_{\bar{d}}^h \bar{d}) + (D_s^h s + D_{\bar{s}}^h \bar{s})} \quad (36)$$

Equation 36 is the asymmetry for a proton target. With a good knowledge on the fragmentation functions, the polarised parton distribution function can be disentangled using the results of the hadron asymmetry A_1^h for proton and deuteron³. The result of flavour-separated momentum distribution $x\Delta q(x)$ for $q = u, \bar{u}, d, \bar{d}$ and $S = (s+\bar{s})$ is shown in Figure 10 (left) with statistical and systematic uncertainties [22]. The PDF for the u -quark is positive, while the one for the d -quark is negative. The sea-quark distributions are compatible with zero. The uncertainties (statistical and systematics) of strange polarised parton distribution are large and the uncertainty coming from the FFs is not included in the Figure. The difficulty to precisely disentangle the strange PDFs $\Delta s(x)$ is illustrated in Figure 10 (right). It shows the x -integrated PDF $\int \Delta S(x) dx$ with the projections for statistical and systematic uncertainties for different parametrisation of the fragmentation functions [23]. The difference between the

³ for deuteron Equation 36 is very similar, only different coefficients are used resulting from the different quark content.

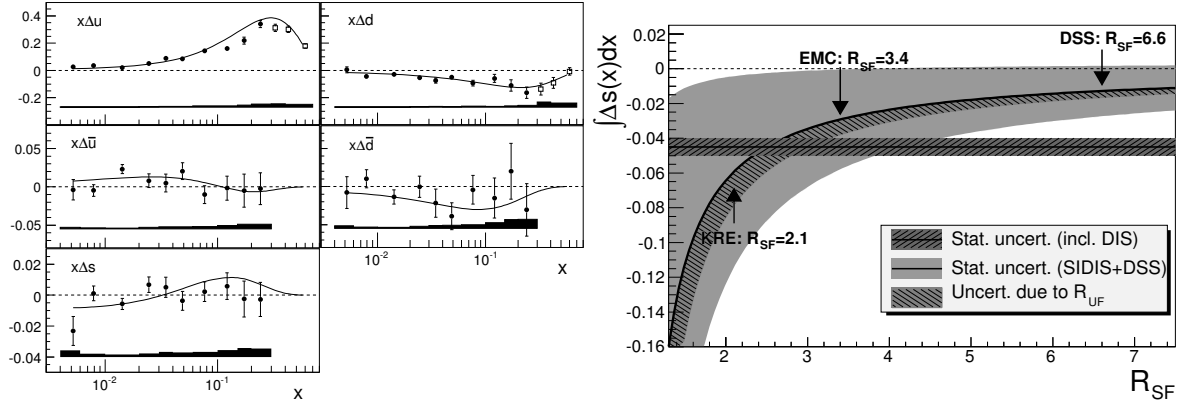


Figure 10: **Left:** Flavour-separated PDF Δq as a function of x for u , \bar{u} , d , \bar{d} and $S=(s+\bar{u})$. **Right:** The integrated strange PDFs $\int \Delta q(x)dx$ as a function of R_{SF} , the ratio of the strange and favoured FF for different parametrisations.

parametrisations (KRETZER [24], EMC [25] and DSS [26]) is given by R_{SF} , the ratio of strange to favoured fragmentation ($\int D_s^{K^+} dx / \int D_u^{K^+} dx$). It also shows the value of $\int \Delta S(x)dx$ coming from the estimate in the inclusive measurement. This emphasises the importance of a precise determination of fragmentation functions, specially the strange one, for flavour-separated polarised PDFs. A sample of fragmentation function parametrisation is discussed in more details in Section 10.3.

2.2 HADRONISATION

The hadronisation process from a parton into a hadron is a fundamental and universal mechanism, which describes the transition from a coloured parton (gluon or quark) into a colourless hadronic object such as a meson or a hadron. The hadronisation process itself cannot be observed and calculated with perturbation theory. The hadronisation is quantified by the parton-to-hadron fragmentation function $D_i^h(z)$.

During the last decades, several different models were created to highlight and simulate the hadronisation process. The *Field-Feynman fragmentation* describes the hadronisation of an initial quark with the creation of quark anti-quark pairs from vacuum fluctuations. The production of the final-state hadrons is classified in ranks and each rank hadronises independently. Two other models, which take into account the colour field between the intermediate quarks, were developed: the *Lund-String-Model* and the *Cluster Model*. All three models are based on experimental results and theoretical approaches. These models are used in Monte Carlo generators. The Field-Feynman model is used in ISAJET [27], the Lund model in JETSET [28] and the Cluster model in the HERWIG [29] event generators. Next, the Field-Feynman model and the Lund-String model are described.

2.2.1 Field-Feynman Hadronisation Model

In the independent hadronisation from Field and Feynman, each parton hadronises independently without influence from other quarks, *e.g.* the struck quark and the target remnant in DIS. It was proposed in [30] by Feynman “to provide a model useful in the design of experiments in which quark jets may be observed, and further to provide a standard to facilitate the comparison of lepton-generated jets with the high- P_L jets found in hadron collisions”. The quark jets are generated on the basis of a recursive principle. An initial quark of the type

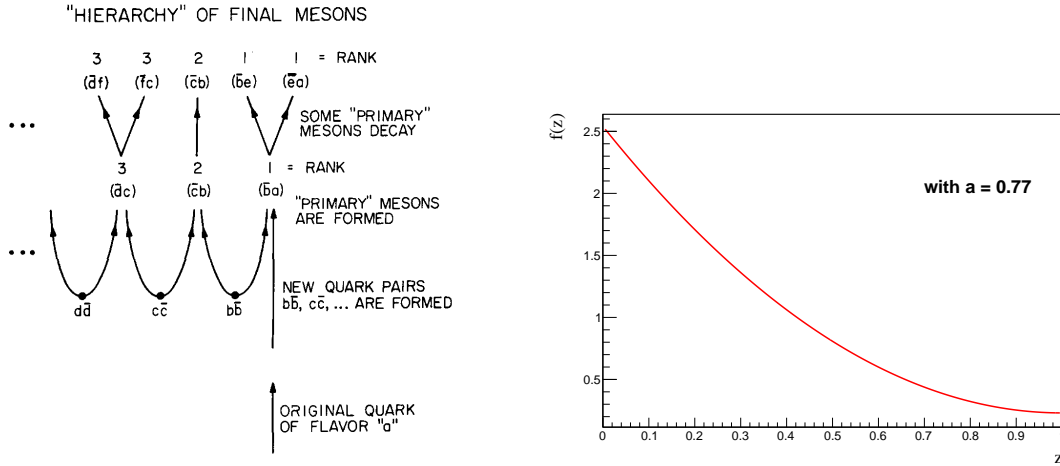


Figure 11: **Left:** Hierarchy of the produced final mesons. **Right:** Fieldman-Feynman fragmentation function from Equation (41). The free parameter a is set to 0.77.

a combines with a quark \bar{b} from a quark anti-quark pair from vacuum fluctuation created by the colour field of the initial quark a . The new meson $a\bar{b}$ has the energy fraction z from the original quark while the quark b is left with the energy $1 - z$. The $a\bar{b}$ meson is named first rank meson and may be observed directly or after its decay. The remaining quark b hadronises in a chain fragmentation similar to the initial quark. Figure 11 shows the hierarchy of the final mesons. In each break-up, the flavour of $q\bar{q}$ pair is chosen randomly along with the ratio whether the produced meson is a vector or a pseudo-scalar meson. The complete structure of the quark jet is determined by an unknown function $f(\eta)$ and three parameters that describe the flavour, the primary meson spin and the transverse momentum. $f(\eta)d\eta$ is the probability that the first hierarchy (rank-1) primary meson leaves a fraction of momentum η to the remaining cascade. The hadronisation cascade stops when the full energy has been split and the remaining energy falls below the production threshold for a new quark pair. For a single particle, the function $F(z)$ is introduced, which is the probability to find any primary meson (independent of the hierarchy) with the fractional energy z . The function $F(z)dz$ is solved by the following recursive form:

$$F(z)dz = f(1-z)dz + \int_z^1 f(\eta)d\eta F(z/\eta)dz/\eta \quad (37)$$

with

- $f(1-z)$, the probability that the primary meson of the first rank has a fractional momentum z in dz ,

- $f(\eta)$, the probability that the primary meson has left a momentum fraction η and

- $F(z/\eta)dz/\eta$, the probability to find a hadron in the remaining cascade z in dz .

Equation 37 is analysed by a Fourier transformation and solved by the simple Equation

$$f(z) = 1 - a + 3a(1-z)^2. \quad (38)$$

The function $f(z)$ fits well to existing data when the parameter a is chosen between 0.77 and 0.88 [30]. Figure 11 right shows the fragmentation function $f(z)$.

Up to now, only longitudinal momenta have been discussed, but in real life the transverse momenta p_t have also to be taken into account. Usually, a Gaussian distribution with a mean

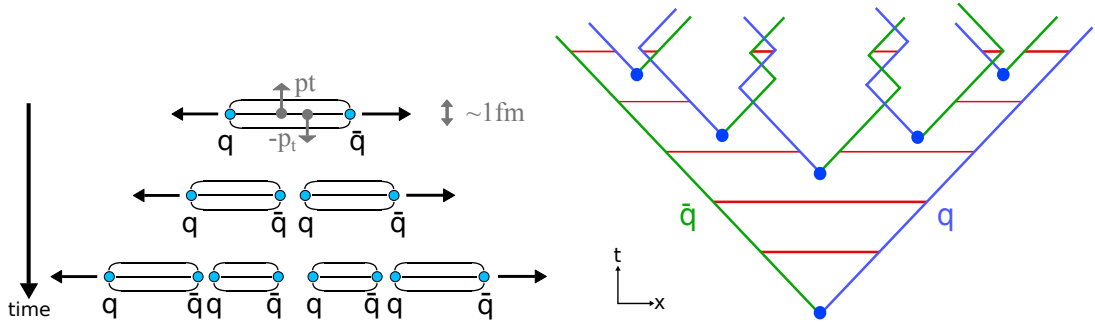


Figure 12: **Left:** Flux tubes created by the strong force field between a $q\bar{q}$ pair. **Right:** Hadronisation in the space-time frame.

value of $350 \text{ MeV}/c^2$ is assumed. The size of the transverse momentum is directly correlated to the final size of the hadron.

2.2.2 String Hadronisation Model

In contrast to the “independent” hadronisation model from Field and Feynman, the *Lund-String Model* [31] [32] considers the colour field between the partons, which is the force behind the hadronisation. The simplest system to study the longitudinal structure of fragmentation is the hadronic final state in electron-positron annihilation ($e^+e^- \rightarrow q\bar{q}$). Based on the production of a $q\bar{q}$ pair back-to-back moving apart, flux tubes are created. The potential energy rises with the distance with $V_{\text{pot}} \sim \chi \cdot r$ with $\chi \sim 1 \text{ GeV}/\text{fm}$. The potential energy is reduced when new $q'\bar{q}'$ pairs are produced and combined with the already existing quarks to $q'\bar{q}$ and $q\bar{q}'$ mesons. The system breaks into smaller and smaller pieces. The breaking continues until the system has not enough energy left to create new quark pairs. The produced particles are aligned with the $q\bar{q}$ and acquire additional transverse momentum up to 400 MeV . Figure 12 shows an example for the potential energy illustrated as the length of the flux tubes as a function of time. The flavour of the primary mesons are strictly ordered in rank but only in the mean of rapidity. In the space-time picture (Figure 12 right), massless quarks move along light-cones. The force field between the quark pairs are indicated with red lines. The $q\bar{q}$ pairs are produced in a single space-time point and are pulled apart by the field. The time ordering depends on the Lorentz frame, slow mesons are produced firstly in a so-called inside-out cascade. In the CM frame, the quark and anti-quark will oscillate back and forth (*Yo-Yo-mode*). The calculations are done in light-cone variables and go beyond the scope of this thesis. To obtain the fragmentation function, the energy and momentum distribution of the various ranks of the hadronisation have to be considered and three models emerge.

The simple Lund model describes the hadronisation as a function of the hadron energy z without taking into account transverse momenta, quark flavour, baryon production and further correction. Assuming that the density of excited $q\bar{q}$ states is constant and that all kinematically allowed states are equally populated in the decay of a $q\bar{q}$ system into mesons and a remainder system, the probability for breaking at a certain point is given by (“simple Lund” model):

$$f(z) = dP/dz = 1 \quad (39)$$

Taking collinear gluons and finite field length into account, the so-called “standard” Lund with a free parameter c is obtained.

$$f(z) = dP/dz = (1+c)(1-z)^c. \quad (40)$$

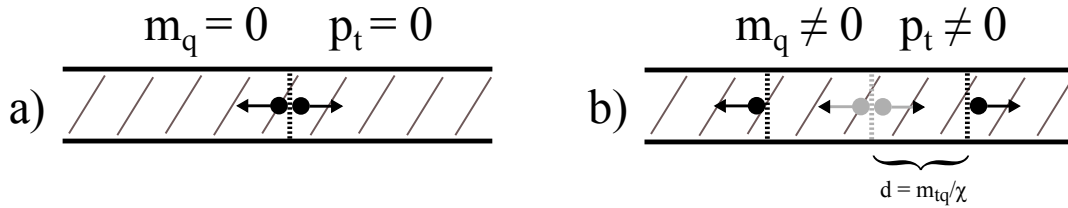


Figure 13: Classically (a), the quark pairs are produced in one point. In quantum mechanics (b), the quark pair is produced at a certain distance due to tunnelling effects. This results in transverse momentum of the produced hadron.

Comparing with, various experimental measurements, the parameter c is between 0.3 and 0.5. The break-up flavour of the $q\bar{q}$ pairs are chosen randomly from the ratio $u\bar{u} : d\bar{d} : s\bar{s} = 1 : 1 : 0.3$. The ratio of the production of vector to pseudo-scalar mesons is $V : PS = 1 : 1$.

In the case that the force field has no excited transverse degrees of freedom, the transverse momentum p_t is locally conserved. Classically, this leads to non-existing transverse contribution to the momentum. The $q\bar{q}$ pair is produced in one point and pulled apart by the field. In quantum mechanics, the pair is produced at a certain distance d from each other and the field energy in between is transformed into transverse momenta p_t . This effect is illustrated in Figure 13. The probability to tunnel out the classical production is given by $P \sim e^{-\frac{1}{\chi}(m^2 + p_t^2)}$ with the quark mass m . The consequences are that heavy quarks are highly suppressed ($u : d : s : c = 1 : 1 : 0.3 : 10^{-11}$) and that the p_t spectrum has a Gaussian distribution with a width of 0.3 - 0.4 GeV/c. The model can be refined further by taking into account the production of baryons. The latter is described by creation of diquark anti-diquark pairs. Furthermore, the fragmentation functions are dependent on the mass of the produced particles: heavier particles have harder fragmentation functions. There are indications of a "left-right" symmetry in the fragmentation of a jet system.

There is a two-parameter solution:

$$f(z) = \frac{dP}{dz} = \frac{(1-z)^\alpha}{z} \cdot e^{-\beta m_t^2/z} \text{ "symmetric Lund"}, \quad (41)$$

where $m_t^2 = m^2 + p_t^2$ and m is the mass of the hadron. Equation 41 introduces a cut-off at low z for heavy particles. The parameters α and β are extracted experimentally from e^+e^- data and it is assumed to be the same for DIS data.

With this model (symmetric Lund), it is possible to study single particles but also correlations and structures of events. The Lund-String hadronisation is used in the JETSET and PYTHIA [33] generator. Figure 14 shows a comparison of the different fragmentation functions as a function of z for the Field-Feynman model, the simple Lund, the standard Lund and the mass-dependent symmetric Lund. For the latter one, α and β are chosen to be 0.5 and a kaon is assumed for the mass. In the middle range of $z \approx 0.5$, all fragmentation functions have a similar value. The largest differences are seen in the low z region.

Experimentally, some JETSET parameters have to be tuned for each experiment. In the case of the MC data at COMPASS, the size of the transverse momentum distribution p_t (PARJ(21) in the JETSET code) was changed to 0.36 GeV/c for a better comparability between real data and Monte Carlo data. To take higher order QCD effects into account, the parton shower approach is used. In the DIS case, the struck quark can emit a gluon, thus leading to an initial or final state parton shower.

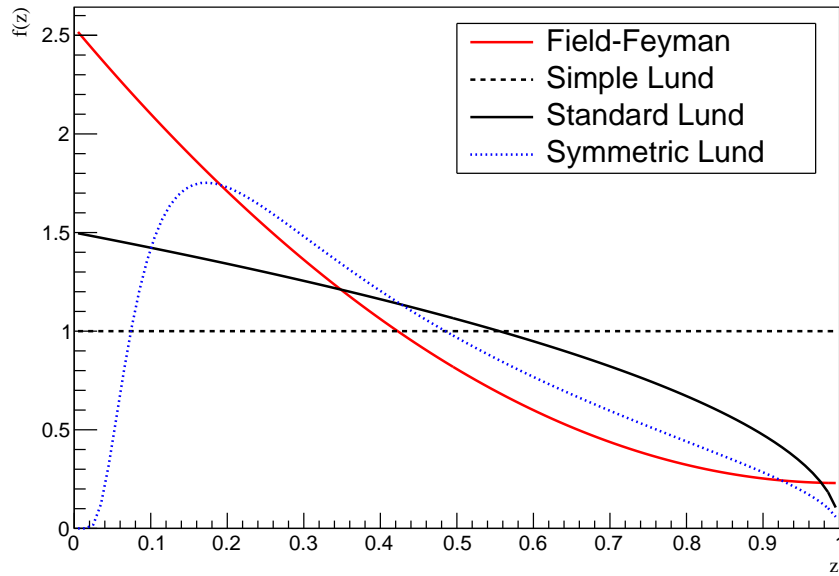


Figure 14: Comparison of the different fragmentation models: the Field-Feynman hadronisation with $c = 0.77$, the simple Lund, the standard Lund and the symmetric mass dependent Lund hadronisation for pions.

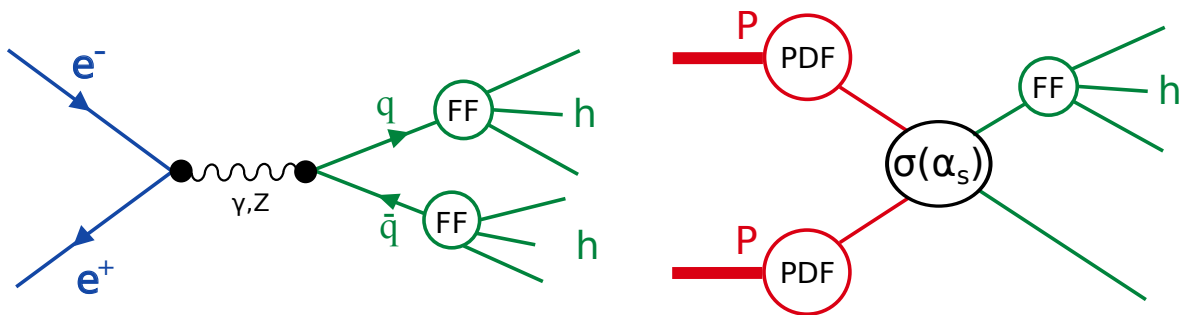


Figure 15: **Left:** e^+e^- collision with hadronisation. **Right:** Hadronisation of pp collisions.

2.3 MEASUREMENT OF FRAGMENTATION FUNCTIONS

Fragmentation functions cannot be accessed directly, but are deduced from processes where hadrons are produced, such as e^+e^- annihilation, pp ($p\bar{p}$) collisions and semi-inclusive deep inelastic scattering. Each process comes with advantages and disadvantages. Figure 15 illustrates the access to the FF for e^+e^- and pp collisions.

The hadron data sample of the e^+e^- collision provides a very clean high statistics approach to fragmentation functions as no initial-state hadron remnant is existent. The electron and the positron annihilate into a photon (Z boson) and decay into a $q\bar{q}$ pair. After the hadronisation, the hadrons are detected. However, as no clear distinction between the quark and the anti-quark is possible, only the sum of fragmentation functions $D_q^h + D_{\bar{q}}^h$ can be measured (e.g. LEP, BELLE, etc...).

In hadron-hadron collisions, such as pp or $p\bar{p}$, many processes contribute to the hadron production (gg , qg , qq ,...). They depend strongly on the strong coupling constant α_s and the parton density functions. The theoretical approach is difficult: processes from initial state QCD radiation, the partonic and spin structure of the hadron target have to be taken into account. Furthermore, the target remnant system disturbs a clean measurement. With all experimental challenges, the hadron-hadron collision is used to constrain the gluon fragmentation D_g^h (e.g. RHIC, Fermi Lab, etc...).

The third process is the determination of fragmentation functions from semi-inclusive deep inelastic scattering.

2.3.1 Multiplicities from SIDIS

In semi-inclusive deep inelastic scattering, a flavour-separated measurement of the fragmentation function is possible, assuming that a quark is struck by the virtual photon coming from the lepton scattering. The quark is ejected and hadronises, as well as the target remnant. By measuring and identifying a final-state hadron h , disregarding the hadronic states of the target and assuming the flavour of the struck quark q with parametrisation of parton distribution functions, the fragmentation D_q^h can be extracted. In the presence of the hard scale, and within the collinear factorisation framework, the semi-inclusive deep-inelastic scattering cross section σ^h can be written as a convolution of three components: σ_0 , the hard scattering cross section of the photon, $q(x)$ the parton distribution functions and the fragmentation function D_q^h .

$$\sigma^h = \sigma_0 \otimes q(x) \otimes D_q^h \quad (42)$$

In leading-order perturbative QCD and assuming a full factorisation, the convolution sign \otimes can be replaced with a simple multiplication⁴. The factorisation is illustrated in Figure 16 by the different colours. An absolute cross section is experimentally very challenging due to the precise knowledge of the luminosity. A convenient observable is obtained with the hadron multiplicity M^h : the ratio of the semi-inclusive cross section σ^h and the inclusive cross section σ_{DIS} . The charged hadron multiplicities depend on five kinematic variables: the Bjorken scaling variable x , the four-momentum transfer Q^2 , the hadron energy fraction z , the transverse hadron momentum p_t and the azimuthal hadron angle θ . In a first step, the multiplicities are determined in x , z and four-momentum transfer Q^2 according to Equation 43. The multiplicities are integrated over p_t and θ . The p_t dependence has been studied for unidentified

⁴ in NLO, the full convolution needs to be taken into account

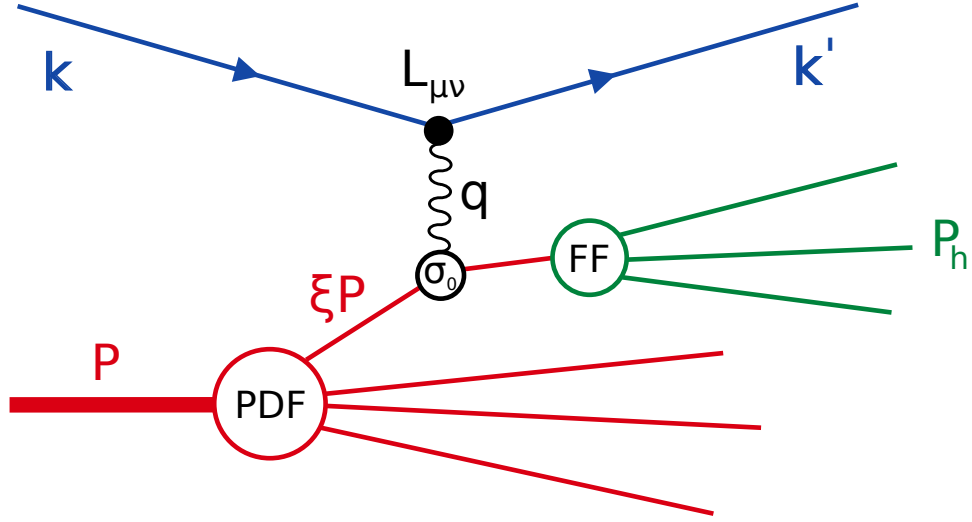


Figure 16: Diagrammatic illustration of factorisation in semi-inclusive deep-inelastic scattering.

hadrons at EMC [34] and at COMPASS [35].

$$\frac{dM^h(x, z, Q^2)}{dz} = \frac{d^3\sigma^h(x, z, Q^2)dx dQ^2}{d^2\sigma^{\text{DIS}}(x, Q^2)dx dQ^2 dz} = \frac{\sum_q e_q^2 q(x, Q^2) D_q^h(z, Q^2)}{\sum_q e_q^2 q(x, Q^2)}. \quad (43)$$

The charged hadron multiplicity $M^h(x, Q^2, z)$ depends on differential DIS cross section in the one-photon-exchange approximation, the parton distribution function $q(x)$ with the corresponding quark charges and the fragmentation function. In simple words, the multiplicity is the number of hadrons produced per deep inelastic scattering event within a chosen bin of x , Q^2 and z . For the interpretation of the FFs, the measured hadrons are supposed to come from the struck quark. The hadrons from the remnant target are disregarded with a cut on the hadron energy fraction z (Equation 27). The charged hadron multiplicities are measured in the frame of this thesis as a function of z in bins of x and y : the Q^2 dependence was exchanged by relative photon energy y .

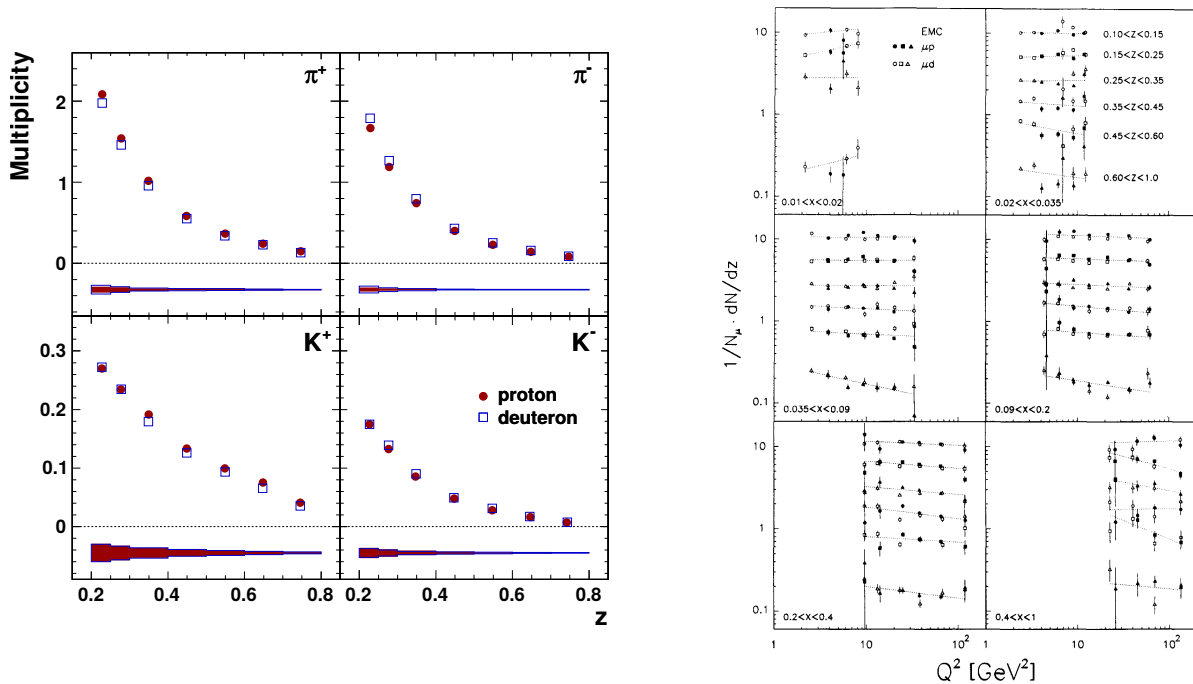


Figure 17: **Left:** HERMES multiplicities as a function of z for protons in red and deuterons in blue. **Right:** Differential charged (unidentified) hadron distribution in bins of x , Q^2 and z , measured on protons and deuterons.

2.3.2 Experimental Results

The charged hadron multiplicities were measured in deep inelastic scattering, *e.g.* at HERMES and EMC. A sample of those results is shown in Figure 17.

The unidentified charged hadron multiplicities were measured at the EMC forward spectrometer [34]. Semi-inclusive deep scattering events were taken on a proton and a deuteron target with different beam energies (120, 200 and 280 GeV). A muon beam was used. The multiplicities for all charged, unidentified hadrons are shown as a function of Q^2 for different x and z bins for both types of targets. The dotted lines represent a linear $\ln Q^2$ QCD fit. The charged hadron multiplicities show little Q^2 and the difference between the two targets is also small. Due to isospin invariance, the pion multiplicities should be equal, but with the addition of protons and kaons in the multiplicities, the small difference is expected. The EMC spectrometer is the predecessor experiment of the COMPASS experiment (Chapter 3). The HERMES experiment [36] was located at DESY and was a forward spectrometer with Cherenkov detector for particle identification. A 27.6 GeV electron beam was used for deep inelastic scattering on a fixed gaseous target, filled either with hydrogen or deuterium. The expected slopes of the charged hadron multiplicities were measured with high precision. In Figure 17 the charged pion and kaon multiplicities [37] as a function of z for both target types (p and d) are shown. The systematic errors are shown as a band. The expected z dependence is seen: the multiplicity decreases with larger z . As the kinematic range of HERMES experiment is in the larger x region, mostly multiplicities from the fragmentation of valence quarks were measured.

The COMPASS experiment has an excellent particle identification and covers larger kinematic range than HERMES, specially in the lower x region. With the scattering on the sea quarks, the aim is to constrain the kaon fragmentation functions with high precision.

I

EXPERIMENTAL PART

THE COMPASS EXPERIMENT

The COMPASS experiment (COMmon Muon and Proton Apparatus for Structure and Spectroscopy) is a two-stage magnetic spectrometer with a fixed target located at the Super Proton Synchrotron at CERN. The main physics program is the investigation of the nucleon structure using a tertiary muon beam. The final state consists of a scattered muon and possibly additional hadrons, which are emitted in the center of mass system (CMS) in 4π , according to momentum conservation. In the laboratory system, all final state particles are emitted in forward direction due to the Lorentz boost. Therefore, it is sufficient to install detectors behind the target to cover most of the acceptance for scattered muons. The opening angle of the production cone depends on the momentum of the incident beam. Figure 18 shows an overview of the experiment with most of the detectors. The spectrometer is divided in two stages for a better momentum resolution. Particles with large angles are detected in the first spectrometer part, called Large Angle Spectrometer (LAS), while in the Small Angle Spectrometer (SAS) particles with small angles and high momenta are detected. The spectrometer is able to track charged and reconstruct neutral particles and, together with a high efficient charged particle identification, the experiment is well-suited to measure semi-inclusive deep inelastic scattering processes. The COMPASS reference system is a right-handed system with the beam in the Z axis, a horizontal X axis and a vertical Y axis. At COMPASS, the positive X is called Saleve side and negative Jura side, as a reference to the surrounding mountains. The direction with (against) the particle beam is called downstream (upstream). The following chapter describes the individual parts of the experiment, including the beam line. The set-up for the muon-physics is described in the COMPASS I paper [38] and the changes towards the COMPASS II phase in [39] and [40].

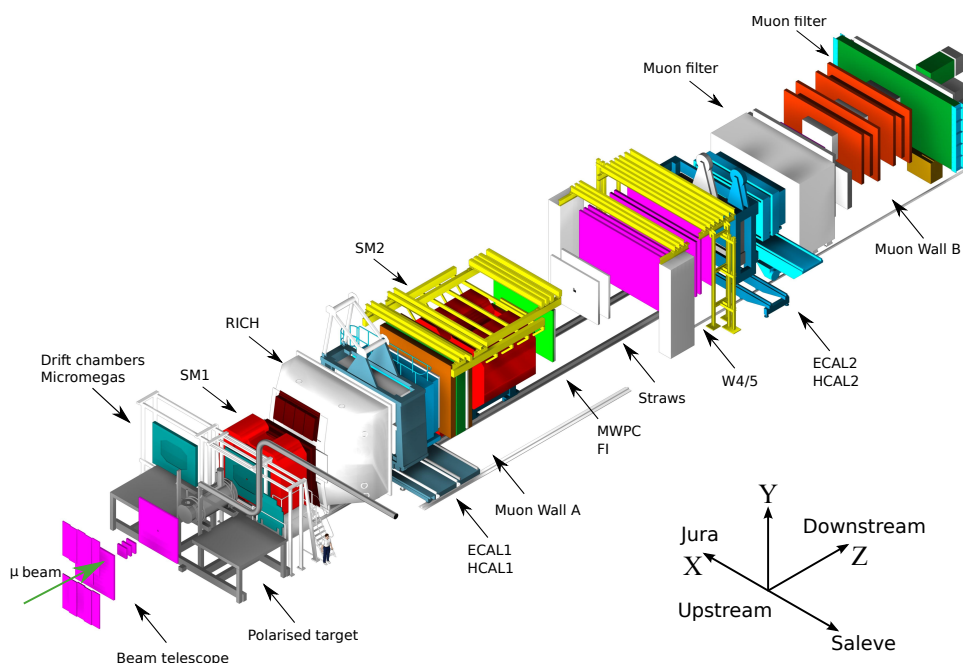


Figure 18: An isometric view of the COMPASS experiment with most of its detectors.

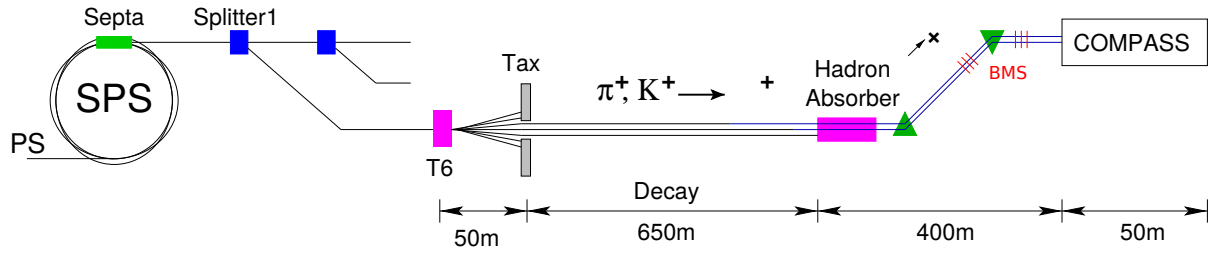


Figure 19: Schematic overview of the beam line from the PS accelerator to the COMPASS experiment. The proton beam from the SPS is extracted and hits the T6 target. The secondary hadrons decay into muons which are transported to the experiment.

W

3.1 BEAM

The muon beam used in the experimental hall originates from a bottle of hydrogen. The hydrogen molecules are ionised with a strong electric field. The protons are then accelerated to 50 MeV in a linear accelerator (LINAC2) and injected into the Proton Synchrotron Booster (PSB), where the beam is again accelerated to 1.4 GeV. Subsequently, it reaches the Proton Synchrotron (PS), a circular accelerator with a diameter of 628 meters. It drives the beam up to 25 GeV and feeds the Super Proton Synchrotron (SPS). The SPS accelerates the proton beam up to 400 GeV and provides beams for several experiments, *e.g.* NA61/SHINE, NA62, CNGS and the COMPASS experiment.

3.1.1 The M2 Beam Line

The M2 beam line [40] [41] is 1.13 km long and connects the COMPASS experiment to the SPS accelerator. Figure 19 shows a schematic overview of the beam line from the Proton Synchrotron to the COMPASS experiment. The 400 GeV/c protons are extracted from the SPS with an extraction magnet (Septum) [42] and then shared between the three main experimental halls: EHN1(test-beam), EHN2 (NA58) and EHN3 (NA48) by the means of splitter magnets. The portions for the COMPASS experiment (NA58) are directed to the T6 primary target, where secondary hadrons (π^\pm , p , \bar{p} and K^\pm) are produced. The T6 production target consists of beryllium blocks with variable sizes adjusting the particle flux to the experiment. The proton flux on T6 is around $1.3 \cdot 10^{13}$ protons per extraction cycle (spill). Behind T6, the momentum range of the pions, kaons and protons are selected by collimators and absorbers. In the 650 m long decay section, the pions decay into muons and the corresponding neutrinos. The mean length for this decay is 9.5 km at energies of 10^2 GeV, therefore large absorbers (9 m long beryllium rods) have to be inserted at the end of the pion decay section to filter out the remaining hadronic states. With a dipole, the momentum range of the muon beam is selected and transported through a FODO section. FODO is a regular array of alternately focusing and defocusing quadrupole magnets which have a large momentum acceptance. The momentum of the incident particles is then measured with the beam momentum stations BMS (Section 3.2.1), which are placed around a dipole magnet. Before entering the COMPASS experiment, two dipole magnets and a quadrupole magnet steer the beam to the desired position in the target. In the appendix Figure 117, a full view of the beam line elements is shown.

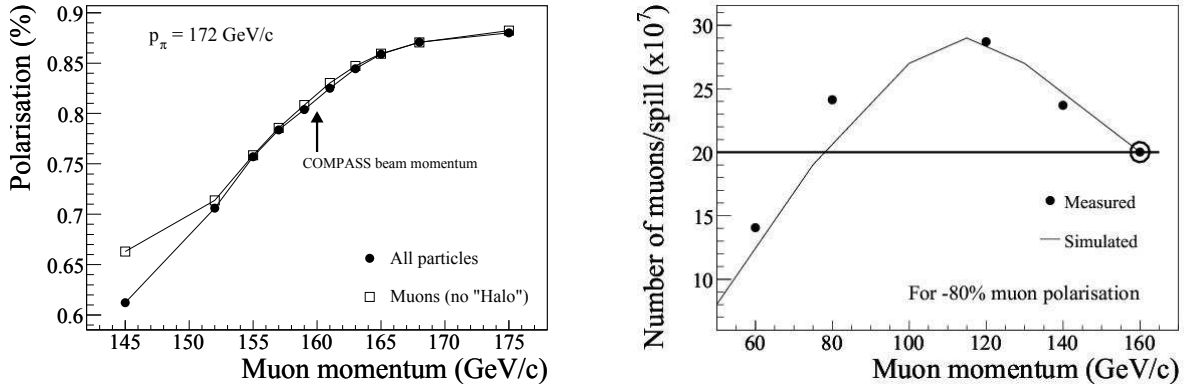


Figure 20: **Left** : Muon beam polarisation as a function of the muon momentum. **Right** : Maximal beam intensity as a function of the muon momentum, assuming p_μ/p_π corresponding to 80% muon polarisation.

3.1.2 Polarised Tertiary Muon Beam

The muon beam is produced by the weak decay of the secondary pions and kaons, whose dominant decay modes are [8]

$$\pi^+ \rightarrow \mu^+ + \nu_\mu \text{ Branching ratio: } (99.98770 \pm 0.00004)\% \quad (44)$$

$$K^+ \rightarrow \mu^+ + \nu_\mu \text{ Branching ratio: } (63.55 \pm 0.11)\%. \quad (45)$$

The muon beam is naturally polarised due to the weak decay of pions and kaons. The phase space of the pion decay would allow -and even prefer- a decay into electrons but due to the parity violation, the mode of the decay into muons is favoured. Depending on the parent particle energy (a pion with the momentum p_π), a high polarisation grade of up to 80% is achieved. The muon beam momentum p_μ can be chosen between 60 and 200 GeV/c. The experiments were performed at 160 GeV/c, at which high beam flux and high Q^2 are reached. Only in 2011 a beam momentum of 200 GeV/c was used, to reach lower x_{bj} with and even higher Q^2 for the price of 50% of the beam flux. To obtain high flux, a larger momentum range of 5% is selected. Figure 20 shows the polarisation grade of the incident muons as a function of the muon momentum originating from a pion with a momentum of 172 GeV/c. The Figure also shows the maximum obtainable muon flux as a function of the muon momentum. The maximum intensity lies at a muon momentum of 120 GeV/c, but with a lower polarisation. Negative muon beams can also be produced, but with a lower intensity as the primary particles are positively charged protons. The beam flux at 160 GeV/c per spill is around $2.5 \cdot 10^7 \text{s}^{-1}$. The maximum flux is limited by radio protection regulation at CERN, the halo of the beam, the proton rate on T6, the septum and the splitter.

3.1.3 Spill Structure

The beam is delivered in bunches, also called spills. The length of the spill depends on the share of the beam assigned to COMPASS by CERN and the stability of the extraction magnets. An electronic signal coming from the SPS indicates the begin of the spill (BOS) and end of the spill (EOS). A spill is typically between 5 and 10 seconds long, repeated after a break of 15 to 60 seconds. During the break the SPS is refilled and other experiments are supplied with the SPS proton beam. The first seconds of the spill are not recorded, as a BOS veto is applied.

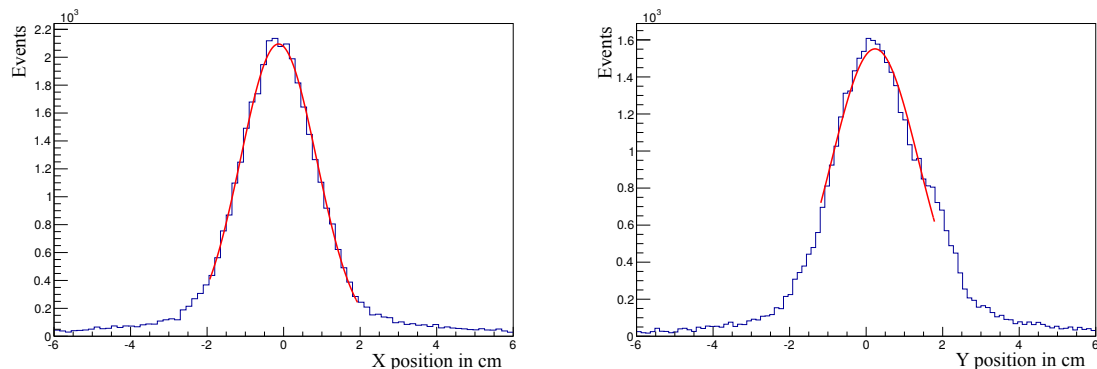


Figure 21: The beam profile in X and Y from reconstructed muons in front of the target measured by the scintillating fibre stations.

This veto is used to remove the first particles from the accelerator, where the extraction is not stable. Within the spill, the beam intensity raises and then stays constant until the spill is over (flat top). For the 2009 DVCS run, the total length of the spill was 10.4 s with a flat top of 8 s and a break of 45 s. In 2006, the spill length was 4.8 s with a cycle time of 16.8 s.

3.1.4 Beam Profile and Beam Halo

Figure 21 shows the profile in X and Y for the year 2006 measured by a scintillating fibre detector in front of the COMPASS target. The size depends strongly on setting, focusing and steering of the muon beam with the beam line. The muon beam should be focused inside the target material and centrally hit the target material. The beam spot is determined with a Gaussian fit and has a size (X, Y) of $9 \times 11 \text{ mm}^2$. The X profile follows nicely a Gaussian profile, while the Y profile seems to be more smeared out. This is an effect of the dipoles used to select the energy range of the beam. The divergence of the beam is $0.4 \times 0.8 \text{ mrad}^2$ and is measured with the beam telescope. The beam is accompanied by halo muons. Those are muons with wrong energies and angles which could not be absorbed or deflected in the beam line. The halo is separated into two contributions: the near halo and the far halo. The near halo are incoming muons outside of the target up to a distance to 30 cm from the target center. The far halo are all incoming particles 30 cm away from the target.

3.2 BEAM TELESCOPE

The beam telescope is located in front of the target and measures the properties of the incoming beam such as timing, position, momentum and divergence. For the μ physics program, the telescope consists of the beam momentum station (BMS), the scintillating fibre detectors (FI) and the silicon micro-strip detectors (SI).

3.2.1 Beam Momentum Stations (BMS)

The beam transported through the beam line has a momentum spread of about 5%. The Beam Momentum Station measures the momentum of the incoming muons with high precision. This is necessary for the determination of accurate kinematic quantities *e.g.* the four-momentum transfer Q^2 . The beam momentum station is an array of four scintillator hodoscope detectors arranged around the dipole magnet B6 and the quadrupole elements Q29-

Q32 in the beam line in front of the COMPASS experiment. B6 is the last dipole magnet before the beam enters the experiment and is used to steer the beam. BMS 1 and BMS 2 are located in front of the dipole, while BMS 3 and BMS 4 are situated behind B6. The momentum is measured by the deflection of the muons in the magnetic field. Each BMS consists of 64 horizontal elements of 5 mm width and 20 mm thickness for a large signal output. The detectors are read out with photomultiplier tubes. The BMS has been upgraded by two stations in order to deal with higher beam rates. The new detectors BMS 5 and 6 are located between the old ones. The BMS measures the momentum of incoming particles with a precision of 1 % and more than 93 % efficiency [43].

3.2.2 Scintillating Fibre Station (FI)

Two scintillating-fibre stations (FI01 and FI02) are located in front of the target. These two detectors have the highest time resolution in the experiment (with 300 ps) and therefore are used to determine the timing of each incident muon. The time information of FI01 and FI02 is used to link tracks reconstructed in the BMS to tracks reconstructed before the target, in order to assign the correct momentum. With the spacial resolution of $130 \mu\text{m}$, the FI stations provide information about the angles and positions of incident particles crossing the active area of the detector. Both stations have an identical layout. Each has an X and Y plane, which consists of 14 overlapping layers of scintillator fibres. The active area is $(3.9 \text{ cm})^2$, and the diameter of each fibre is 0.5 mm with a pitch of 0.41 mm. This results in 96 individual channels which are read out by 16-channel multi-anode PMTs (MAPMT) from HAMAMATSU, six for each plane. The dynode signal on the last stage of the MAPMT is also read out by TDCs and scalers. The two FI stations are also used as a beam trigger.

3.2.3 Silicon Micro-Strip Detectors (SI)

The timing of the incident muons is well determined by the FI stations, but their spacial resolutions are limited. To provide a precise measurement of the location of the incident muon, silicon micro-strip detectors are used. These were developed at HERA [44] and were adapted to the high flux requirements of COMPASS [45]. With excellent spacial resolution, from 4 to $11 \mu\text{m}$, they provide precise track informations of the incoming beam. The time resolution is 2.5 ns. The silicon micro-strip detectors consist of $300 \mu\text{m}$ thick n-type wafer with an active area of $5 \times 7 \text{ cm}^2$. To have redundancy and to eliminate ambiguities, each detector consists of two sub-stations: one is covering the X and Y projections and the second is rotated around this axis by 5° for additional U and V projections. Further improvements have been done to increase the performance of the SI detectors: the wafers are cooled with liquid nitrogen to 80 K to increase the spacial and time resolution, as with lower temperatures the noise of the detector is reduced.

3.3 TARGET REGION

In this thesis, two different years with two different targets are discussed. In 2006, a polarised solid state target was used, while in 2009 a liquid hydrogen target was used.

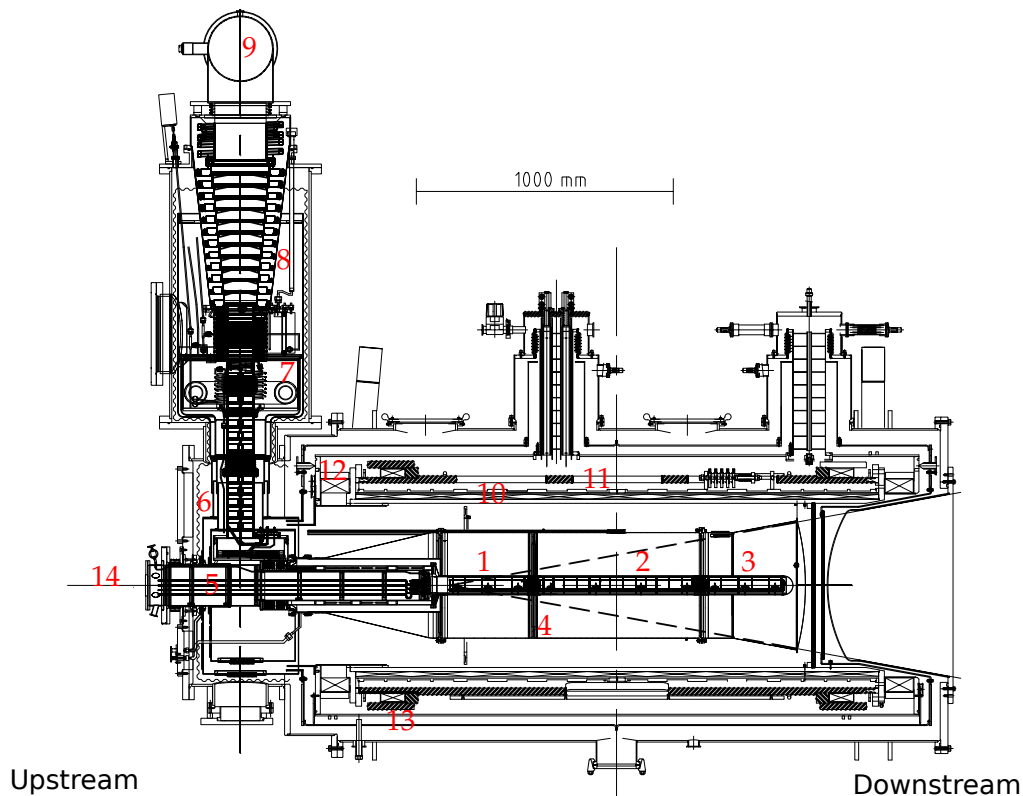


Figure 22: Technical drawing of the COMPASS polarised target. 1-3: the three target cells (U, C, D), 4: microwave cavity, 5: target holder, 6-9: ^3He - ^4He refrigerator, 10: solenoid coil, 11 and 12: array compensation coils, 13: dipole coil, 14: muon beam entrance.

3.3.1 Polarised Target

For the measurements of the spin structure of the nucleon, a high polarised target is needed in addition to the polarised beam. Also, to obtain a high luminosity, a large solid state target is needed. For the 2006 data taking, the new COMPASS polarised target with a large aperture was designed with three cylindrical cells (upstream U, center C and downstream D). Figure 22 shows a technical drawing of the target with the important parts. The diameter of each cell is 3 cm. The U and D cells are 30 cm long and separated by the 60 cm long central C cell. In addition, each cell is separated by a 5 cm wide gap. The target cell can either be filled with NH_3 for a polarised proton measurement or with ^6LiD for the measurement on isoscalar deuterium. The polarisation is achieved with high magnetic fields and low temperature: a ^3He - ^4He refrigerator is used to cool down the target material to 70 mK and a superconducting solenoid provides a \vec{B} field of 2.5 T along the beam axis. In this condition, almost all electrons of the target molecules are polarised. With Dynamic Nuclear Polarization (DNP) [46], the spin of the electrons is transferred to the nucleons of the molecules. This requires target materials with paramagnetic centers, which are created by irradiation [47]. The persistence of the magnetic field and the low temperature conserve the polarisation of the target material. The target material in 2006 consists of 4 mm small ^6LiD pellets, which are filled into the target cells. The packing fraction is between 0.49 and 0.54 and the gaps between the pellets are filled with a mixture of ^3He , ^4He and ^6Li . A polarisation of 50% is reached for this material mixture. The fraction of polarisable material (dilution factor) is 38%. The U and D target cells are polarised in the same direction, while the central cell is polarised in the opposite direction. With this polarisation configuration, systematic uncertainties coming from acceptance, beam flux and further time dependences are cancelled out, if the polarisation of

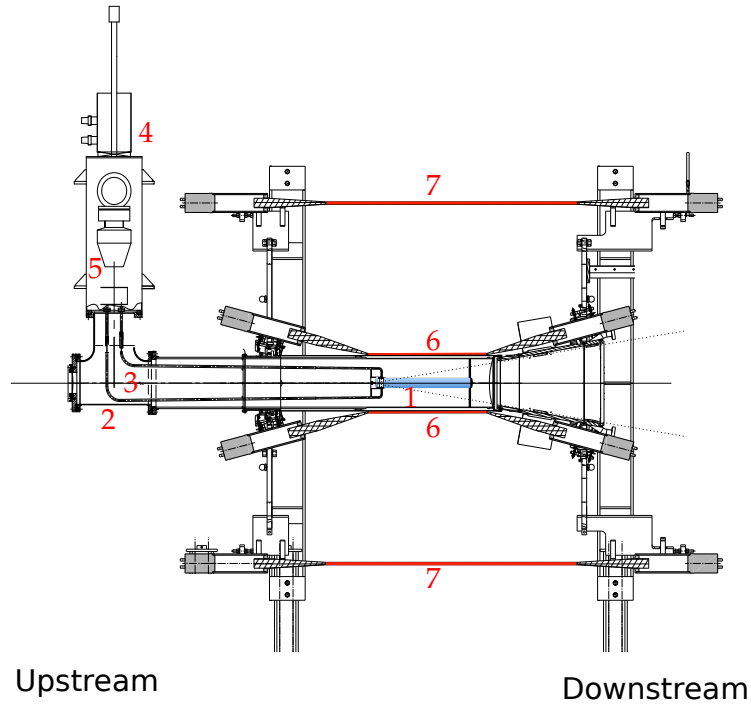


Figure 23: Technical drawing of the COMPASS liquid hydrogen target with the recoil proton detector.
 1: target cell, 2: cryostat, 3: liquid hydrogen in/outlet, 4: ℓH_2 refrigerator, 5: vacuum system,
 6: RPD ring A scintillator, 7: RPD ring B scintillator.

all cells is reversed on a regular basis. For the measurement of unpolarised semi-inclusive deep inelastic scattering, the full target length is analysed: an average over the polarisation is used.

3.3.2 Liquid Hydrogen with Recoil Proton Detector

For the meson spectroscopy measurement and the muon beam measurement during 2009, an unpolarised 40 cm long liquid hydrogen target, surrounded by a recoil proton detector (RPD), was used. The target material itself is contained in a mylar tube with a diameter of 3.5 cm. The total volume of the target cell and the liquid hydrogen system is situated in a cryostat made of aluminium. Figure 23 shows the set-up of the liquid hydrogen target with all components: the ℓH_2 , the liquid hydrogen pipe system (H_2 in/outlet), the refrigerator and the recoil proton detector (RPD). The operation temperature of hydrogen is 18 K (4 K below the boiling point of 22.15 K) with a pressure of 1020 mbar. The target is attached to the frame of the RPD [48] [49].

The recoil proton detector consists of two concentric layers of scintillator (Ring A and Ring B), which are read out via long light guides by photomultiplier tubes. The scintillator of the inner (outer) ring have a thickness of 0.5 cm (1 cm). Charged particles coming from the target are measured at polar angles of 50° to 90° . This detector is used to identify slow recoiling protons up to 1 GeV/c by measuring the energy loss in the scintillator and the time-of-flight between the two layers.

3.4 SPECTROMETER

A variety of redundant tracking detectors are distributed within the spectrometer to measure the tracks of charged particles. In Table 3, the characteristics of most detectors (time resolution and spacial resolution) are summarised. The spectrometer is divided into two parts:

- The large angle spectrometer (LAS) has tracking detectors and the first spectrometer magnet, a RICH for particle identification. Each part has a central hole which matches to the second stage. The achieved momentum resolution is about 0.3 % for tracks identified with SM1.
- The stage behind the second and larger spectrometer magnet is called small angle spectrometer (SAS) and detects particles at small angles (± 30 mrad) and large momenta of 5 GeV/c and higher. Besides various tracking detectors, most of the trigger elements are located in this stage. The achieved momentum resolution is about 0.1 % in the SAS.

3.4.1 Spectrometer Magnets

The momentum of the final-state particles are determined by spectrometer magnets. Reconstructed tracks in front and behind the magnets are compared to obtain the momentum of each particle within the acceptance of the spectrometer. At COMPASS, two spectrometer magnets are used, one in each stage of the spectrometer. Spectrometer Magnet 1 (SM1) is a dipole magnet located downstream of the target. The main field component is in the vertical direction. It is 110 cm long, has a horizontal gap of 229 cm and a vertical gap of 152 cm. The SM1 vertical size matches the required angular acceptance of ± 180 mrad. Its field integral was measured to be 1.0 Tm. Due to the bending power of SM1, the LAS detectors located downstream of SM1 have an angular acceptance of ± 250 mrad in the horizontal plane. Spectrometer Magnet 2 (SM2) is the larger spectrometer magnet and is located in the SAS. The SM2 is a rectangular dipole magnet with a gap of 2×1 m² and a total field integral of 4.4 Tm for its nominal current of 4000 A or 5000 A, depending on the beam energy.

3.4.2 Tracking Detectors

The spectrometer is equipped with micro pattern gas detectors such as gaseous electron multipliers (GEM) [50] and gaseous micro-strip (MicroMega) detectors [51], drift chambers (DC), multi-wire proportional chambers (MWPC) and straw tube detectors (Straws). In addition, more scintillating fibre stations (FI), larger than the one used in the beam telescope. Also, the trigger hodoscopes are included in the track reconstruction.

3.4.2.1 Micromegas (MM)

The micromegas are the first detectors behind the target and are therefore crucial for the measurement of the vertex position. Each of the three MM stations consists of four planes and covers an active area of 40×40 cm² with a dead zone of 5 cm diameter, to avoid damage from the beam. The detector volume is filled with a Ne/C₂H₆/CF₆ gas mixture and divided by a thin metallic mesh into a conversion gap and an amplification gap. Charged particles traversing the conversion gap ionise the gas into positive ions and electrons, which drift towards the mesh. The ions are absorbed, while the electrons create a shower in the amplification gap. The electrons are then read out by parallel micro-strips with a pitch of 360 μ m. Figure 24 left shows the detection principles for the micromega detector. The detectors have a spatial resolution of 90 μ m, a time resolution of 9 ns and an efficiency of 97 %.

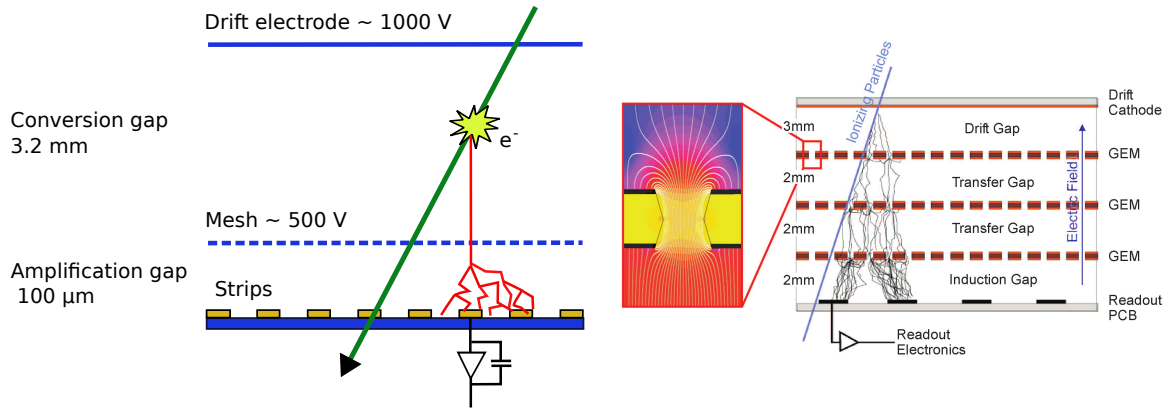


Figure 24: Principle of the micro pattern gas detectors at COMPASS. In both cases, electrons are amplified and read-out. The difference between the GEM and the Micromegas is the amount of amplification gaps and the structure of the micro pattern. **Left:** Principle of the Micromegas detector. **Right:** Principle of the GEM detector, showing the layout and the field configuration for typical GEM voltages.

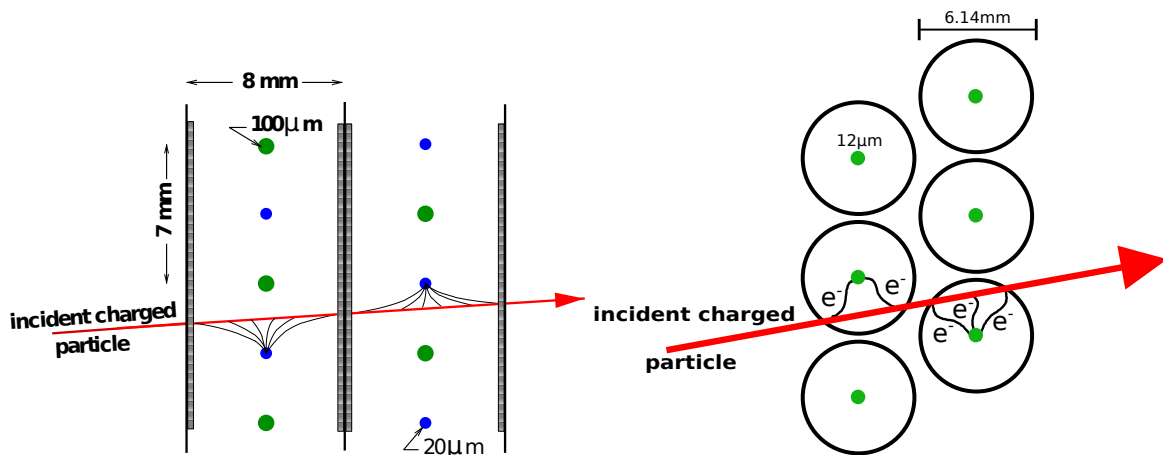


Figure 25: **Left:** Principle and geometric layout of the drift chamber. **Right:** Layout of a straw tube detector.

3.4.2.2 Gas Electron Multiplier (GEM)

Similar to the micromegas, the GEM detectors rely on the measurement of electrons created in an avalanche shower inside the fiducial volume of the detector. The COMPASS GEM detector volume is divided into several sub volumes (Drift, $2 \times$ transfer and an induction gap) by a thin foil with a large number of micro-holes. This thin polyimide foil ($50 \mu\text{m}$ thick) is coated with copper and a few hundred volts are applied. Electrons drifting through the hole are multiplied in an avalanche and the electric signal is then read out by $80 \mu\text{m}$ wide strips. Figure 24 shows the detection principles for the GEM detector and the typical electric field lines in the holes of the foil. The gas mixture of the GEM detectors is Ar/Co₂ in a 7:3 ratio. The active area of those detectors is $41 \times 41 \text{ cm}^2$. Ten GEM stations are distributed along the experiment. Their small size and high resolution makes them ideal for small angle tracking. The spatial resolution of the GEM system is $70 \mu\text{m}$ with a time resolution of 12 ns, which is slightly higher than the one of the micromegas one. The efficiency for the GEM detectors is 97%.

3.4.2.3 Drift Chambers (DC and W4/5)

The drift chambers are large area trackers for charged particles at COMPASS. There are two drift chambers systems set up in the experiment: the DC in the LAS and the W4/5 in SAS. Figure 25 shows the detection principle. The detectors consist of a drift cell filled with gas, cathode planes, anode wires and potential wires. The potential wires are used to shape the form of the electric field inside the detector volume. A homogenous field is desired, as much as possible. Fast charged particles, traversing the detector volume, ionise the gas mixture inside the drift cell. The electrons are accelerated and multiplied in avalanche through the acceleration in the electric field. This electron cloud is then read out by the anode wire. The hit position is reconstructed by the fired wire and the drift time of the electrons. The drift velocity of electrons depends on the gas mixture and the applied high voltage, and is typically a few centimeters per nanosecond.

The DC in LAS of the spectrometer consists of 256 active wires made of gold-plated tungsten and 257 alternating potential wires made of beryllium, with diameters of $20\ \mu\text{m}$ and $100\ \mu\text{m}$. The active wires are 8 mm apart. All three DCs have an active area of $180 \times 27\ \text{cm}^2$, fully covering the acceptance of the SMC target magnet upstream as well as downstream of SM1. At nominal muon beam intensity, a mean value for the resolution of a single DC wire layer of $270\ \mu\text{m}$ was measured. The detectors are filled with a gas mixture of Ar, C_2H_6 and CF_4 at a volume ratio 9:9:2. The drift chambers consist of several layers in X and Y (and in the slightly rotated U and V planes).

The W4/5 detectors have an active area of $5 \times 2.5\ \text{m}^2$, and consist of 4 anode wire layers with a wire pitch of 4 cm. The anode wires are separated by layers of cathode wires with a pitch of 2 mm. The diameter of the anode wire is $20\ \mu\text{m}$ and of the potential wires, $200\ \mu\text{m}$. A CF_4 -based gas mixture, Ar/ CF_4 / CO_2 (85/10/5), is used.

3.4.2.4 MWPC

The tracking of particles at large medium distances to the beam in the SAS is mainly based on a system of multi wire proportional chambers (MWPC). The 34 wire layers are distributed over 9 detectors, resulting in about 25000 detector channels in the experiment. There are three types of MWPC, which differ by the number of layers, the size of the dead zone for the beam and the combination of the measured projections (X, Y, U and V). All layers are characterised by a wire length of about 1 m, a wire diameter of $20\ \mu\text{m}$, a wire pitch of 2 mm and an anode/cathode gap of 8 mm. The MWPCs are operated with a gas mixture of Ar/ CO_2 / CF_4 in proportions 74/6/20 with an addition of CF_4 .

3.4.2.5 Straw

The straw tube detectors are very large angle trackers in the LAS. Similar to the drift chambers, the straw tube detector measures the position of the incident charged track with the wire hit and the known drift velocity of electrons in gas. The anode wires are made of gold-coated tungsten and have a thickness of $12\ \mu\text{m}$. The name originates from the design: each wire is surrounded by a two-layer plastic tube (outside carbon loaded capton and inside aluminised capton) with an outer diameter of 9.65 mm. In total 12440 straw tubes are assembled into 15 detector planes. The overall dimensions of the Straw tube detector are $3570 \times 4117\ \text{cm}^2$ for the X plane and $4567 \times 3160\ \text{cm}^2$ for the Y plane. The average resolution is $190\ \mu\text{m}$.

Detector type	Active area	Spacial resolution	Time resolution
Scintillating Fibre	$(3.9)^2 - (12.3)^2 \text{ cm}^2$	130 - 210 μm	400 ps
Silicon Micro-strip	$5 \times 7 \text{ cm}^2$	8 - 11 μm	2.5 ns
GEM	$31 \times 31 \text{ cm}^2$	70 μm	12 ns
Micromega	$40 \times 40 \text{ cm}^2$	90 μm	9 ns
MWPC	$178x \times (90 - 120) \text{ cm}^2$	1.6 μm	N/A
DC	$180 \times 127 \text{ cm}^2$	190 - 500 μm	N/A
Straws	$280 \times 323 \text{ cm}^2$	190 μm	N/A

Table 3: Table with the characteristics of a selection of tracking detectors.

3.4.3 Particle Identification

The trajectories of the outgoing final-state particles are measured with tracking detectors. In addition, the particle type has to be determined.

3.4.3.1 Muon Identification with Muon Walls and Muon Filters

An efficient way to identify muons is to use an absorber surrounded by two tracking detectors. With a radiation length large enough to absorb all hadrons, particles detected behind the absorber are considered muons. At COMPASS, this is done in the LAS with the Muon Wall 1 (MW1) and the Muon Filter 1 (MF1). In the SAS, the Muon Wall 2 (MW2) in combination with the Muon Filter 2 (MF2) identify the muons. At the very end of the spectrometer, the Muon Filter 3 (MF3) is located in front of the hodoscope HI5, the last detector in the spectrometer and a part of the trigger system. The three muon filters are made of steel or concrete. Figure 18 indicates the position of the muon filters, the muon walls and the hodoscope HI5. The MW1 system is located in the LAS of COMPASS and consists of Mini Drift Tubes (similar to the Straws), which work in the proportional mode. The tubes are made of 0.6 mm thick aluminum tubes surrounding a 50 μm thick tungsten wire. The muon filter surrounded by the MW1 system is made of 60 cm of steel. The active areas are $4845 \times 4050 \text{ mm}^2$ (hole: $1445 \times 880 \text{ mm}^2$) and $4730 \times 4165 \text{ mm}^2$ (hole: $1475 \times 765 \text{ mm}^2$) for the X and Y planes. The gas mixture of MW1 is Ar/CO₂ (70/30).

The MW2 system in the SAS has two identical stations of layers of drift tubes. Each of the two stations consists of 6 layers with an active area of $4470 \times 2020 \text{ mm}^2$. A gas mixture of Ar/CH₄ (75/25) is used. The stainless steel drift tubes have an inner diameter of 29 mm and a wall thickness of 0.5 mm and the wires are 50 μm thick.

3.4.3.2 Ring Imaging Cherenkov Detector (RICH)

The identification of the final-state charged particles is performed by the Ring Imaging Cherenkov detector (RICH), which is located in SAS of the experiment. The RICH measures the velocity of traversing charged particles. In combination with the measured momentum, the particle mass can be determined. The detector consists of three parts: a radiator volume, a mirror array and a photon detection system. The largest part of the detector is the radiator volume, which is filled with C₄F₁₀, a gas with a refractive index n of 1.0015. Charged particles traversing the detector emit Cherenkov light with an angle θ of

$$\cos \theta = \frac{1}{n\beta} \quad (46)$$

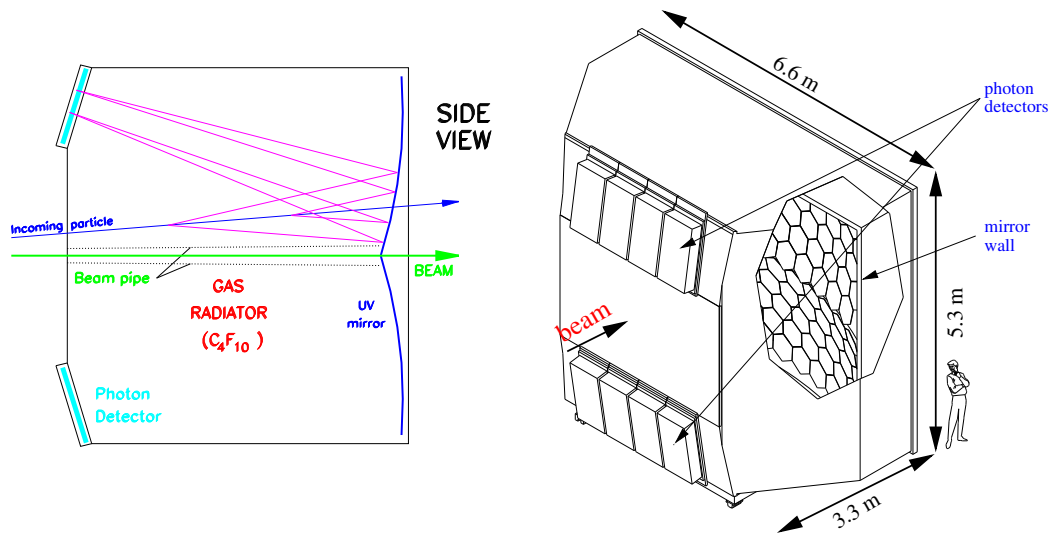


Figure 26: **Left:** Side view of the RICH, showing the path of the light. **Right:** Isometric view of the detector with dimensions.

where β denotes the fraction of the light speed c . Two large arrays of concave mirrors reflect the light towards the front of the detector, where the photon detection system is placed. The focal point of the mirrors was chosen to be 3.3 m, such that the reflected light creates light rings at the place of the photon detectors. The radius of the ring is proportional to the velocity of the particle. To avoid a high background and therefore a high dead time, the inner part of the detector, where the non-interacted beam passes, is inactive. This is done with the installation of a stainless steel pipe. The principle and the detector design are illustrated in Figure 26. Until 2006, the photon detection system only consisted of multi wire proportional chambers, where the wires are coated with CsI. To cope with the high event rate and the high level of uncorrelated background, the read-out was upgraded in 2006: the central part of the photon detection area was replaced with multi anode photomultipliers (MAPMT). The outer regions remained unchanged but were equipped with a new front-end and read-out. The identification method with the RICH and the determination of the Likelihoods are described in Section 7.1.1.

3.4.4 Calorimetry

Charged tracks are measured by the trackers and identified by the RICH detector. In addition, electrons and hadrons can be separated with the help of calorimetry, which, in each spectrometer stage, consists of an electromagnetic calorimeter (ECAL) followed by a hadronic calorimeter (HCAL). The ECALs detect mainly particles that interact electromagnetically (electrons, positrons and photons). The HCALs are used to determine the energy of hadrons.

3.4.4.1 Electromagnetic Calorimeter

ECAL1 in the LAS and ECAL2 in the SAS are homogeneous lead glass calorimeters. Impinging photons, electrons or positrons in the fiducial volume lose their energy through bremsstrahlung and the Cherenkov effect. The emitted light is detected by photomultiplier tubes. The thickness of the calorimeter corresponds up to 23 radiation lengths, which is large enough to contain the full electromagnetic shower. Each cell of the ECALs is calibrated every year with an electron beam.

3.4.4.2 Hadronic Calorimeter

The hadronic calorimeters are designed to stop hadrons with a dense matter (lead or iron) and measure the energy of the produced particle shower with a scintillator. This is achieved with a sandwich construction with alternating layers of scintillator material and iron plates. The iron slows down incoming hadronic particles. The light produced in the scintillator is read out by photomultiplier tubes. The HCAL1 is located behind the ECAL1 in the LAS, while HCAL2 is behind ECAL2 in the SAS.

3.5 DATA ACQUISITION AND ONLINE-MONITORING

An important component for the data taking is the data acquisition (DAQ), which handles the data transfer of the 250000 electronic channels used in the experiment. The COMPASS DAQ is designed to run with trigger rates up to 100 kHz. An overview of the data flow is shown in Figure 27. A trigger signal provided by the trigger control system [52] starts the read-out of the buffers of the CATCH modules (COMPASS Accumulate, Transfer and Control Hardware [53]), where the data of a detector, coming from the front-end electronics, is accumulated. The trigger principles are described in Section 4. The raw data is temporarily stored in the read-out buffer, where the data of all detectors is merged. Then, the event is assembled in the event builder. Typically, an event is characterised by a 12.5 ns time window around the timing of an accepted trigger. An event comprises the event, spill and run number, and a map of detector hits and timings, that are later used to reconstruct tracks. The raw data is then stored with the CERN Advanced STORAge manager (CASTOR).

3.5.1 Trigger Control System (TCS)

The trigger control system (TCS) is an electronic device that connect all read-out CATCH modules and starts the read-out, whenever a trigger signal is generated. It consists of a TCS controller, a laser system and several TCS receivers. The TCS receiver is installed in each VME crate, where the CATCH modules are located. The signal is transmitted by an optical fibre network to over 100 locations spread over the 50 m long experiment. The main function is to distribute the trigger signal (see Section 4) and to transmit the common clock. The TCS also introduces the DAQ dead time, which is necessary to guarantee a stable operation of the DAQ. It reduces the number of triggers in a certain time window. The TCS permits to add and remove detectors from the DAQ. The TCS works synchronously with the SPS duty cycle, therefore data is taken during the spill only.

3.5.2 Detector Read-Out

The detectors are connected to the read-out through the front-end. The detectors deliver analogue signals, that have to be digitised by the read-out electronics. The read-out is done, for most detectors, by the CATCH modules, a development of the University of Freiburg, Germany. The raw output of detectors read-out by CATCH modules is constantly saved on a ring buffer. The ring buffer allows a temporary storage of a few microseconds, enough time for the trigger logic to decide on the relevance of an event. The event header contains specific information about the event, such as the event time, the spill numbers and which trigger started the read-out. The modules are controlled by Linux VME computers via the VME bus. The CATCH modules either contain a TDC, for timing measurement, or a scaler, for counting

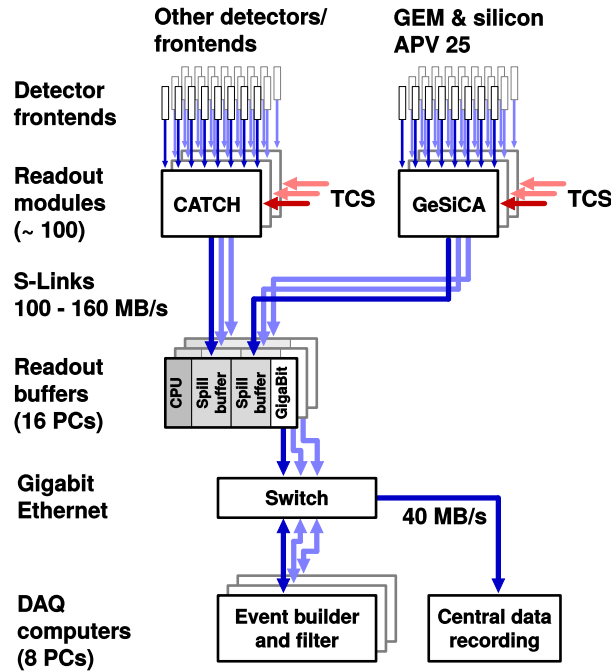


Figure 27: Overview of the data acquisition of COMPASS. With a trigger signal, the buffer of the front-end is read out and temporarily stored in read-out buffers (LDC). The trigger-wise events are then created in the Event builder. The raw data is stored on CASTOR at CERN.

rates. The data is multiplexed and merged with the event header delivered by the TCS.

- **TDC:** The time information of each detector is measured by the F1-TDC chip (time-to-digital converter) developed by the University of Freiburg, Germany [54]. TDC chips provide a digitisation width of either 128 ps or 108 ns. The time resolution can be improved by a factor of two in the “double resolution” mode, in exchange for half of the usable channels per chip. Before reaching the input of the F1 chip, the signals are digitised by discriminators.
- **Scalers:** Some of the discriminated signals, which are digitized with TDCs, are also counted by scaler modules. The counts are stored for each event. This is useful to monitor rates of various systems such as trigger counts or veto rates. As shown later in Section 6.3.3, the scalers are used to determine the incident particle flux.
- **ADC:** For some detectors, the analogue signal shape is of interest, *e. g.* the calorimeters. The analogue-to-digital converter digitises signals with a rate of 38.88 MHz. In this case, GeSiCA read-out module is used. This module is based on a APV25 chip [55].

3.5.3 Readout Buffer and Event Builders

The read-out buffers or spill buffers collect and sort all the data coming from the different CATCH or GeSiCA modules and temporarily store data before being processed by the event builders. The read-out buffers are PCI cards with an internal memory of 512 MB. This eases the load of the event builder and the rest of the DAQ. The central part of the DAQ are the event builders, whose function is to collect all data and sort them into the corresponding event. The disk space of the event builders is large enough to store the recorded data for one day.

3.5.4 DAQ Dead Time

The DAQ dead time is the time while the DAQ processes an event and is unable to treat more events. This dead time varies with the size and complexity of the event: an elastic scattering comprises less data than an inelastic scattering with multiple hadrons in the final state. To ensure a well working DAQ with a constant load and event mixtures, an artificial, larger DAQ dead time is superimposed by the TCS. It limits the multiplicity of trigger (1, 3 and 10 triggers) for chosen time windows. The DAQ dead time is measured by the ratio of accepted (and therefore recorded) triggers and trigger attempts sent via the TCS; both numbers are counted by scalers and the information is stored in the database. For the data taking in 2006, the setting (5, 75, 250) μs was used, resulting in a DAQ dead time of 9.2%. In 2009, the settings were (5, 30, 250) μs with a DAQ dead time of 11%. The final DAQ dead time is calculated on a spill-by-spill basis by dividing the number of triggers generated and submitted to the DAQ, and the numbers of triggers actually processed by the data acquisition.

3.5.5 Data Online Monitoring

The read-out chain and the front-end electronics of the detectors are monitored by a software tool named MurphyTV. It helps to identify faulty front-end electronics and ensures a fast reaction of the shift crew, who is responsible for the data taking. In addition, the online quality is checked with a software package named COOL (COMPASS Online toOL). It has been designed to decode the raw data and allows a real time look at various detector quantities in form of ROOT histograms, which can be browsed interactively during the data taking. Timing and hit patterns of each detector can be reviewed and compared to previous reference. The COOL package is also extensively used for detector commissioning.

3.5.6 Detector Control System (DCS)

An essential part of the monitoring is the detector control system. The DCS provides a user-friendly interface for setting and reading all the relevant parameters of the experiment for various detectors and DAQ elements, including high voltages, low voltages, VME crate status, gas pressures and mixtures, temperatures and magnetic fields. The information is obtained by either reading out directly the hardware components (HV crates, sensors, etc...) or by reading the database. In addition to experiment specific information, the SPS database is utilised to obtain information about the beam intensity, quality and the status equipments provided by CERN, *e.g.* magnets of the beam line.

A reference for each parameter is generated. The data taking within certain alarm limits ensures stable data quality.

THE COMPASS MUON TRIGGER

The characteristic signature of deep inelastic events is the presence of a scattered muon with a certain scattering angle and energy loss. In addition, final-state hadrons can be detected in the experiment. Therefore, a system triggering on scattered muons is a logical choice, which is realised using a set of trigger hodoscopes. All muon trigger systems consist of pairs of scintillator hodoscopes channels, read out by photomultiplier tubes. Well-chosen coincidences of the hodoscopes and the absence of a veto signal are used to trigger on DIS events and start the data acquisition. The high penetration ability of muons makes it easy to clearly identify them by installing the trigger detectors behind large hadron absorbers. Most of the trigger elements are located behind these muon filters (MF1, MF2 or MF3) to make sure that only muons reach the trigger detectors. In addition, calorimeter conditions can be used to trigger on an energy deposition in the hadronic calorimeter in coincidence with a scattered muon to obtain a semi-inclusive trigger. The maintenance and set-up of the muon trigger system, as well as the hadron triggers, are the responsibility of the COMPASS Bonn and Mainz group. The COMPASS trigger system is summarised in [56]. In [57], the set-up of the detectors is presented. In this chapter, first the trigger principles and then the veto system is explained. Furthermore, the realisation of the triggers in the COMPASS experiment is shown, including a description of the trigger electronics.

4.1 TRIGGER PRINCIPLES

At COMPASS, different kinds of triggers are utilised, which also can be used in combination: target pointing triggers, energy loss triggers, calorimeter triggers, random triggers and the veto system. The muon trigger mostly consists of pairs of horizontal or vertical scintillator slabs, which are put into a special coincidence to obtain a desired topology of an event. To obtain a clean data sample, a veto system is used in anti-coincidence with the muon triggers, preventing the firing of a trigger by undesired particles such as halo muons.

4.1.1 Target Pointing Triggers

With the muon target pointing triggers, DIS events are selected by measuring the vertical projection of the scattering angle in the non-bending plane and checking the compatibility with a track originating from an interaction in the target. This is done by pairs of hodoscopes consisting of horizontally arranged scintillator slabs. The read-out is done with photomultiplier tubes on both sides of the strips. This trigger system is used to measure inclusive deep inelastic scattering events. Figure 28 shows the principle of target pointing with an example of two muon candidates: a scattered muon coming from the target (a) and a halo muon (b). The coincidence matrix is configurated in such a way that only (a) is creating a trigger signal (the shape of the matrix is a diagonal). In the center, the distinction between scattered muons and near halo muons is not possible. With the coincidence, most of the muons are rejected which do not stem from the target region. But due to the divergence of the beam and the halo, beam muons that fulfill the coincidence pattern have to be rejected using a veto system in

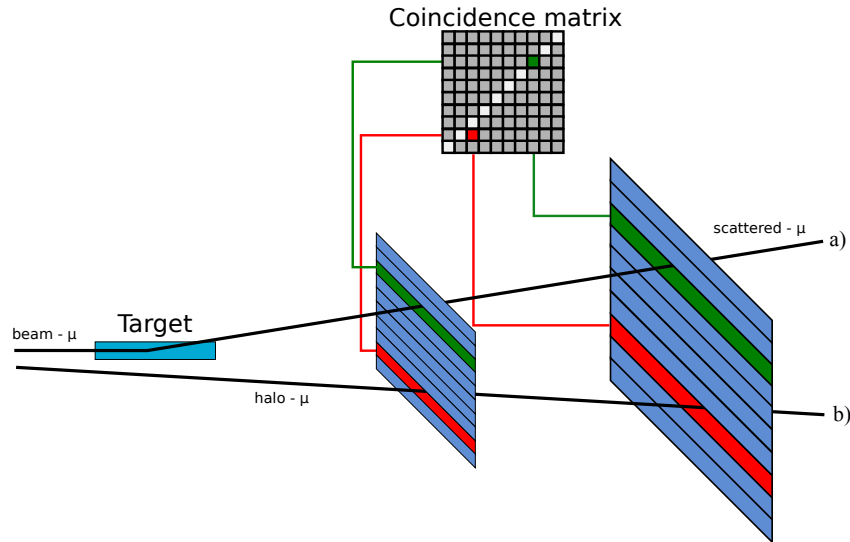


Figure 28: Principle of the target pointing trigger in the non-bending plane. The coincidence matrix distinguishes between halo muons and scattered muons coming from the target.

front of the target. The size of the trigger hodoscope pairs depends on the distance to the target and the distance between the hodoscopes. The width of the hodoscope slabs is chosen to be minimal, considering the multiple Coulomb scattering [58]. The hindmost detector needs to be the larger one with wider slabs to account for the interception of the scattered particles. The acceptance of this trigger systems ranges up to a $Q^2 > 100 (\text{GeV}/c)^2$ and $0.1 < y < 0.9$.

4.1.2 Energy Loss Trigger

Muons scattered under small angle θ cannot be selected using target pointing triggers. But, in case the scattered muons sustained a large energy loss in the target, they can be selected by looking at the large deflection of the tracks in the spectrometer magnets. The energy loss trigger consists of a system of two hodoscope planes with vertical scintillator slabs. It uses the direction of the scattered muons behind the spectrometer magnets. Additional to the scattering angle, the muons are deflected by the magnet. Similar to the target pointing trigger, the hodoscope slabs are read out by photomultiplier tubes and brought to coincidence using a coincidence matrix. The shape of the matrix is triangular, as indicated in Figure 29, where the principle of the energy loss trigger is shown. This trigger aims to cut on a minimal energy loss of the muon in the target; halo muons, which do not deposit any energy in the target and therefore are not deflected strong enough in the spectrometer magnet, do not fire the trigger.

4.1.3 Calorimeter Trigger and Semi-Inclusive Triggers

The calorimeters are used to trigger on events with hadrons in the final state. This requires a cluster of energy in one of the calorimeters with an energy deposition that is larger than the one expected for a scattered muon. The characteristic energy deposition and cluster size of a hadron are transverse to the calorimeter, while a muon deposits its energy in a small shower along the track. To obtain a high efficiency for hadrons, the energy deposition is summed up over several summation layers of 2×2 calorimeter cells, which is close to the lateral shower size. To separate those two energy deposition types, two different thresholds are used. A higher threshold of 6 GeV, which is more than three times of the most probable energy deposition of a muon (MIP), is chosen to reject more than 90% of the clusters created by

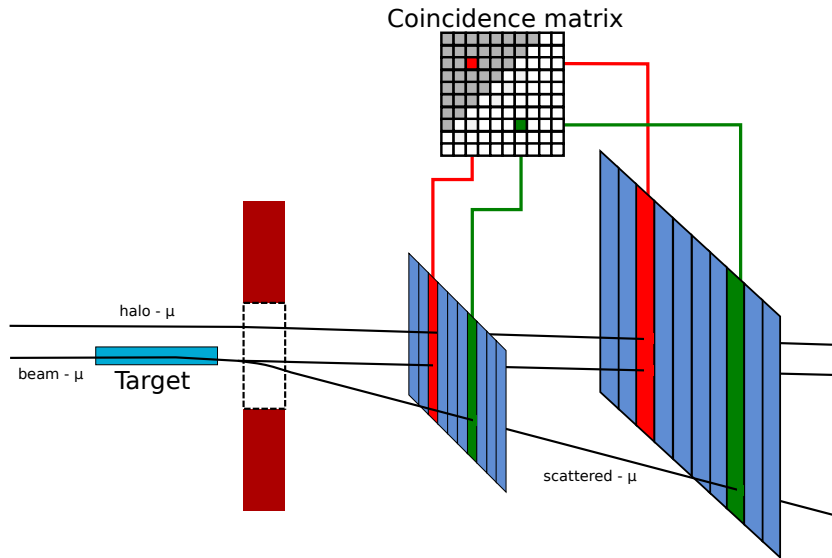


Figure 29: Principle of the energy loss trigger in the bending plane. Scattered muons lose energy in the target and are deflected by the spectrometer magnets. Only muons with sufficient energy loss are used to fire the trigger.

the scattered muons. The calorimeter condition with the threshold of 6 GeV is used with the divergence of a veto signal to form the calorimeter trigger (CT).

In addition, a lower threshold is used, which corresponds to 2 MIPs. Muon triggers in coincidence with the low threshold condition of the calorimeter are used to trigger on semi-inclusive deep inelastic events.

4.1.4 Random Trigger

The random trigger is an unbiased, non-physics trigger, which delivers an adjustable trigger rate with no time correlation to the beam. This trigger is used to check detector performances and is also used for the flux determination. The trigger signal generator consists of a radioactive ^{22}Na source, two photomultiplier tubes and the corresponding electronics. The electronics of this trigger are set-up several hundred meters away from the experiment, reducing influences of the beam and electronic noise from the experiment. The set-up is illustrated in Figure 30. The positrons emitted by the source recombine with electrons and annihilate to two back-to-back photons, which are detected in coincidence. The half-life of this sodium isotope is $t_{1/2} = 2.6027\text{ a}$ [59]. Due to the long lifetime, the trigger rate is constant over the data taking of a few months. The logical signal is transmitted to the Trigger Control System and is treated as a physics trigger. The rate of this trigger is adjustable with the high voltage of the PMT and the discriminator threshold. The trigger signal should not be prescaled in the DAQ, as it loses the random character and turns to a "clock".

4.1.5 Veto System

Due to the halo and the divergence of the muon beam, target pointing and energy loss triggers have a high rate of events with no physics interest. In addition, halo muons may interact with the material of detector support frames, leading to scattered halo muons which may satisfy the matrix coincidence. The sole coincidence between two hodoscopes would lead to a trigger rate of the order of 10^6 , especially for low Q^2 triggers, which is too high for the DAQ. To prevent this kind of events, a veto system is installed in front of the target,

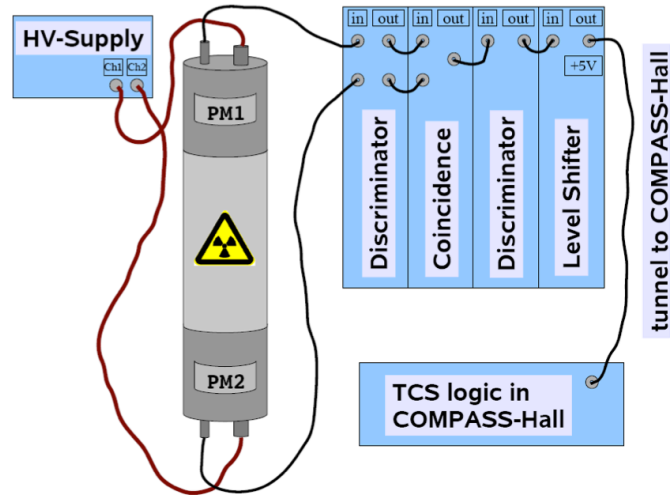


Figure 30: Set-up of the true random trigger with the two PMTs, the electronics and the radioactive source

consisting of scintillator slabs. If one of the veto subsystems is hit by an incident particle, a veto signal is created, which inhibits the trigger. The veto system is divided into two parts: one for the near and one the far halo.

The near halo is the tail of the beam distribution in the X-Y projection, which is outside the diameter of the target. This halo component is rejected by small scintillator veto detectors around the beam. Three veto subsystems are used: Veto beam line (V_{bl}), Veto inner 1 (V_{i1}) and Veto inner 2 (V_{i2}), which are placed on different positions along the beam in front of the target. The far halo is the remaining component of the halo, further away from the beam. This component is rejected by large area scintillator detectors. Two large veto subsystems: Veto outer (V_{outer1}) and Veto up/down (V_{ud}) are used. In Figure 34, all veto elements are shown. The final veto signal is a combination (logical OR) of all veto subsystems, which is called V_{tot} . The veto signal is used in most physics triggers.

The advantage of using the veto system is clearly the reduction of the number of events, which has to be treated by the DAQ. This leads to a decrease of the DAQ dead time. Using the veto also increases the purity of the triggers. But a new dead is introduced: the veto dead time, which is given by the rate of the veto system R_{Veto} and the duration of the veto time gate T_{Veto} , which prohibits a trigger signal. The duration of the veto time gate is adjustable by the coincidence module. A compromise between the minimal time gate, given by the time jitter of the veto and the trigger elements, and a large time gate, resulting in a large veto dead time, is chosen. The time gate T_{Veto} varies from 8 ns for the Inner Vetos and 20 ns for the Outer Veto.

4.2 HODOSCOPES AND VETO DETECTORS

The trigger hodoscopes and veto detectors at COMPASS are made of scintillator counters generally composed of three main elements: the scintillator, the optical coupling (in form of a light guide) and the photomultiplier tube, where the emitted light is converted into an electronic signal. At COMPASS, all scintillators are organic solid-state scintillators.

4.2.1 Scintillator

In particle physics, solid-state scintillators are mainly used to provide fast time information, especially for trigger purposes. Due to the fast response, plastic scintillators are selected. Plastic scintillators consist of a transparent plastic medium such as polyvinyltoluene, polyphenylbenzene or polystyrene. Fluorescent material (naphthalene, anthracene, p-terphenyl, etc...) is added in a concentration of about 10 g/l. An additional wavelength shifter (POPOP, MSB) is included to shift the wavelength of the light. As radiation passes through the scintillator material, the atoms and the molecules are excited and emit light. This light comes from free valence electrons. A characteristic energy diagram is shown in Figure 33 with the spin singlet state S and the spin triple state T [60]. The ground states are denoted with the index 0 and the excited ones with *. Each level also has a fine structure in form of vibrational states (e.g. $S^{0'}$). The vibrational states have typically energies of a few tenths eV.

Through the energy deposition of the traversing charged particle, the valence electrons are elevated to the S^{**} . Their vibrational states immediately (<10 ps) decay via internal degradation without emission of light to the ground states of S^* . Subsequently, S^* decays to an excited vibrational state of S^0 under emission of a photon. The photon energy is $E(S^*) - E(S^{0'})$. Because S^* decays into an excited state $S^{0'}$, the emitted photon cannot be used for the transition $S^0 \rightarrow S^*$: this explains the transparency of scintillator for their own light. The process happens on the scale of a few nanoseconds and is therefore called "prompt" light component of the scintillation light.

Through internal degradation, the excited triple state decays to the lowest ground state T_0 . The transition from the triple ground state to the singlet ground state is forbidden by the multipole selection rules. But the interaction of two T_0 molecules leave one of the molecules in the S^* state,



The light is then produced as described for the single state. This light component is slower than the one produced in the single state.

The light produced within the scintillator is transported through total reflection of the flat surfaces. A careful handling of the scintillator is mandatory to ensure the quality of the surface. Scratches and irregularities lead to light loss. In COMPASS, the scintillator type BC408¹ is commonly used.

4.2.2 Photomultiplier Tubes

The photomultiplier tube (PMT) is an evacuated volume with an entrance photocathode, a multistage dynode system and an end anode for the read-out of the weak electron signal. The high voltage supply of the various electrodes is done with a voltage divider.

The photocathode consists of a sensitive material with a low work function, which converts photons into electrons by the photoeffect [61]. Typically, alkali compounds are used. The quantum efficiency varies between 10 and 40 %, depending on the material used. The right illustration of Figure 31 shows the quantum efficiency as a function of the input light for a bialkali (Sb-K-Cs) photo cathode, which is commonly used at COMPASS². The maximum quantum efficiency of 30 % is reached with blue to violet light with a wavelength between 300 and 500 nm. The slow photoelectrons are then accelerated through a focusing electrode towards the first dynode, where upon hitting, more low energy electrons are emitted, which

1 <http://www.crystals.saint-gobain.com/uploadedFiles/SG-Crystals/Documents/SGC%20BC400-404-408-412-416%20Data%20Sheet.pdf>

2 <http://my.et-enterprises.com/pdf/9814B.pdf>

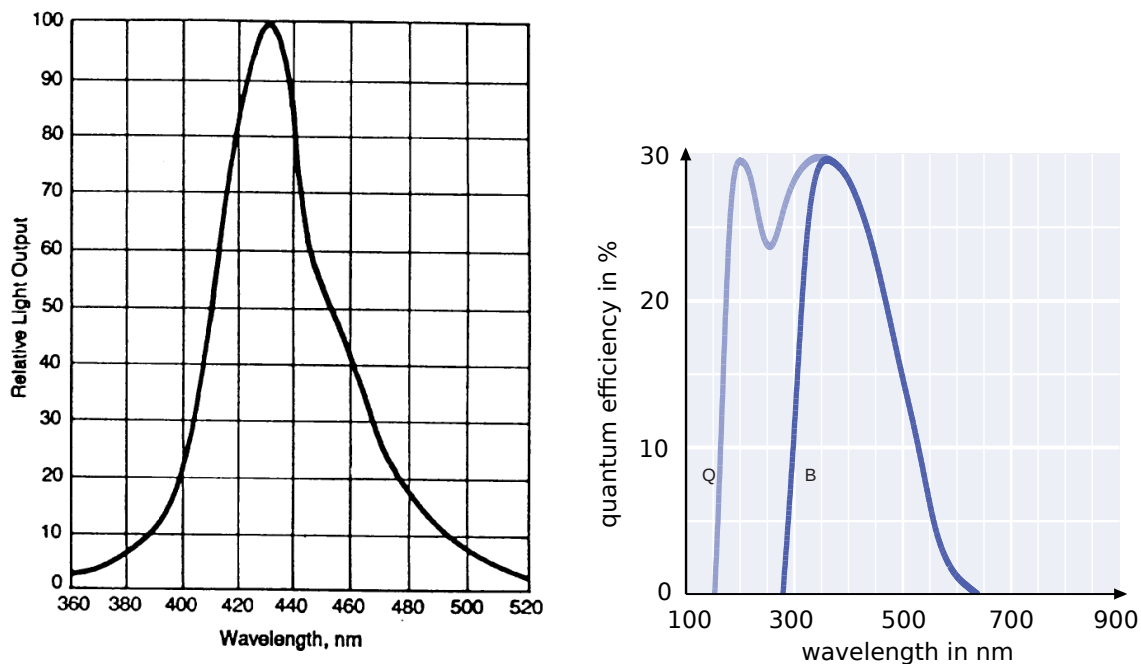


Figure 31: **Left:** Relative light output for the scintillator material BC408. **Right:** Quantum efficiency for the PMT 9814KB from Electron Tubes, the “B” version is used in the experiment for the new hodoscope H2.

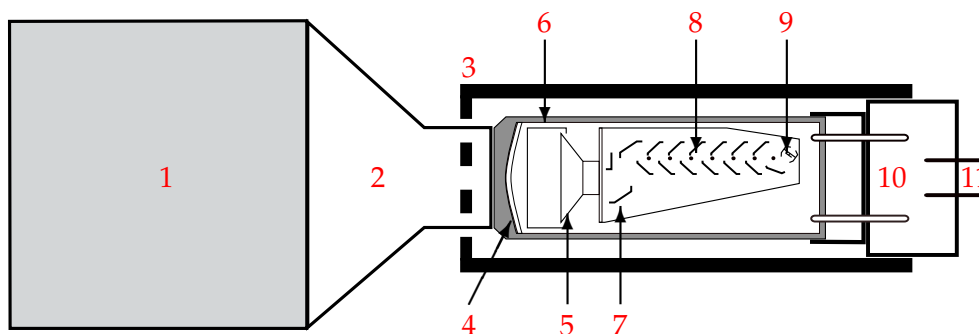


Figure 32: Example for a scintillator count with 1: scintillator, 2: light guide, 3: magnetic shielding, 4: photocathode, 5: focusing electrode, 6: vacuum bulb, 7: first dynode, 8: multiplier dynodes, 9: anode, 10: voltage divider and 11: high voltage input and signal output.

are focused on the next dynode. On each dynode, around 3 to 10 secondary electrons are released. Because the array of dynodes operates with increasing voltage difference, the characteristic gain of a typical PMT is 10^6 to 10^8 , depending on the amount of used dynode stages. On the final anode, the electric signal is measured.

4.2.3 Final Composed Scintillator Slab

It is important to match the components of the scintillator counter to obtain an efficient scintillator counter. Figure 31 shows the relative light output of a BC408 scintillator and the quantum efficiency of a 9814K PMT, whose maxima match. Those two components are examples for PMTs and scintillators used at COMPASS. A complete scintillator slab (Figure 32) consists of an active area made of scintillator material, light guides, photomultiplier tubes and high voltage dividers. Optionally, the scintillator can be read out on both side to improve the precision of the time measurement.

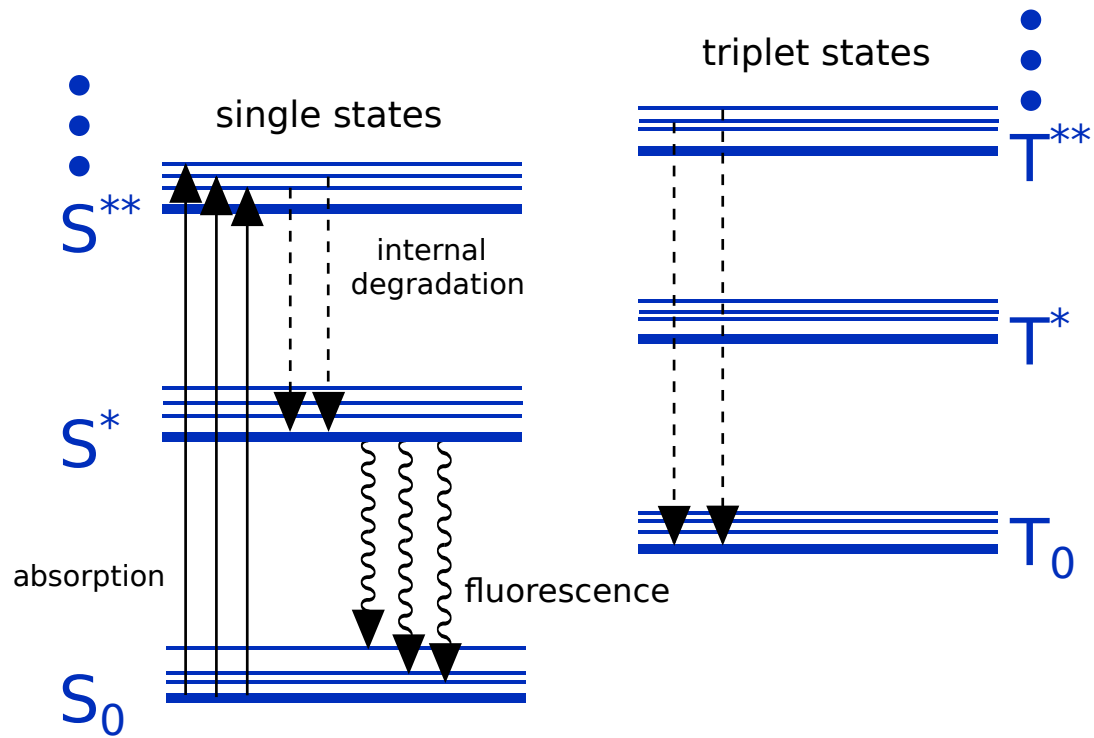


Figure 33: Overview of the singlet and triplet energy levels in a scintillator. The valence electrons are excited via absorption. Photons are emitted when relaxing to the ground state (fluorescence).

The scintillator is wrapped in a crumpled reflective foil. Under some photon angle, the light can escape the total reflection of the scintillator. The crumpling changes the angle of the escaped photons that are then reinjected in the scintillator. This reduces the loss of photons. In addition, a light tight plastic foil encloses the scintillator, preventing the read-out of environmental light. Light guides made of plexiglas (PMMA) are used to connect the scintillator to the entrance window of the PMT. The light guide has two functions. The active material has rectangular faces, while the photomultiplier tubes mostly have round faces. The light guide conducts the photons from the front boundary of the scintillator to the sensitive shape of the photomultiplier tube with few losses. As PMMA is easy to handle, longer light guides in different shapes can be used to bring the read-out away from the acceptance of other detectors. An example is shown in Figure 23: the PMTs of the RPD are brought out of the acceptance with long light guides. Mostly, fish-tail light guides are glued directly onto the scintillator material. The fish tail is also wrapped in the crumpled and the light tight foil. With a mechanical construction, the entrance window of the photomultiplier is pressed onto the round face of the light guide. Optionally, optical grease or transparent silicon discs can be used to improve the light transport from the light guide to the photomultiplier.

Photomultiplier tubes are sensitive to magnetic fields. The magnetic field of the spectrometer magnet or even the magnetic field of the earth are large enough to deviate the electrons from their optimal path through the photomultiplier and thus reduce the efficiency drastically. A magnetic shield made of a thin μ -metal layer is enough to protect the photomultiplier from weak magnetic fields. For stronger fields, additional soft iron shieldings have to be used. The size of the shielding depends on magnetic field strength, the number of dynodes and electron acceleration gap between the dynodes. Thus, larger photomultiplier tubes require thicker shielding for optimal operation .

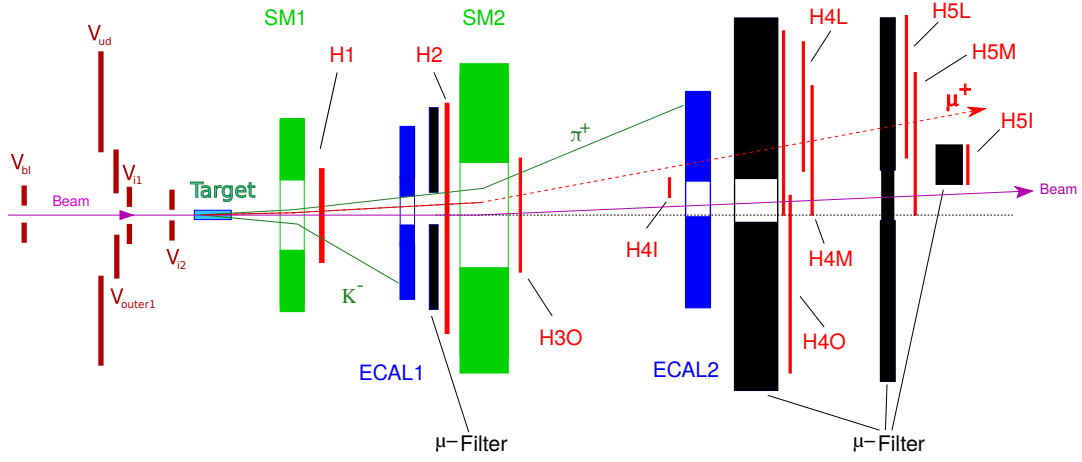


Figure 34: Schematic overview of all physics trigger elements (not to scale), showing the veto elements, the trigger hodoscope, the muon filter and the calorimeters. The spectrometer magnets are shown in green.

4.2.4 Trigger Subsystems

Figure 34 shows the position of all trigger hodoscope elements and the veto elements in the COMPASS spectrometer and the characteristics are summarised in Table 8 in the Appendix. Hereinafter, starting with the triggers from low Q^2 to higher Q^2 , the various triggers are explained. Most hodoscopes have a rectangular shape, adapted to the acceptance of the spectrometer and the kinematic region. To reduce rates, the undeflected beam is not detected by the hodoscopes. This is done either by a rectangular hole in the center or by replacing the central scintillator part by an inactive material. The larger hodoscopes are separated into two halves to increase the stability with shorter scintillator slabs. The individual trigger elements are shown in Figure 35. The Inner hodoscopes are not shown in this Figure, due to their small dimensions and the more complicated geometry with diagonal slabs. Figure 36 shows the kinematic coverage by the different trigger systems in the Q^2 and y plane with black lines indicating constant Bjorken x . It is coming from a calculation with 160 GeV/c muon beam, the Z position of the hodoscope pairs and their sizes.

1. **Inner Trigger (IT)** is an energy loss trigger and consists of the hodoscopes HI4 and HI5 with vertical strips. HI4 is installed in front of the ECAL2, while HI5 is installed behind the last muon filter (MF3) at the very end of the spectrometer. The Inner Trigger hodoscopes are only read out on one side. It is used for the smallest energy loss measurements of the scattered muon. HI5 is a special hodoscope: with its small scintillator strips and thus higher resolution, it is also used as a tracking detector. The IT is used to collect data of low four-momentum transfer $0.001 (\text{GeV}/c)^2 < Q^2 < 1 (\text{GeV}/c)^2$ and $y > 0.2$. The IT is the only physics trigger that does not include the anti-coincidence with the veto. With the proximity of the scintillator elements to the beam, the veto would be constantly interfering and considerably decreasing the purity. To reduce the rate, this trigger can only be used as a semi-inclusive trigger, thus the calorimeter condition with the low threshold is applied.
2. **Ladder Trigger (LT)** is an energy loss trigger, which consists of two vertical hodoscopes (HL4 and HL5) with varying slab sizes: fine slabs close to the beam and larger ones outside. Starting in 2010, this trigger was used as an inclusive trigger. Before 2010, LT was used as a semi-inclusive trigger, thus the calorimeter condition was applied.

3. **Middle Trigger (MT)** is a target pointing trigger covering angles from 0.5 mrad to 5 mrad. To reduce the rate at these small angles, the horizontal planes are supplemented by vertical ones providing an energy loss trigger. It consists of two vertical hodoscopes (HM4X and HM5X), which are read out by one side. In addition, the MT has four horizontal hodoscope planes: HM4Y (up), HM4Y (dn), HM5Y (up) and HM5Y (dn), read out on both sides. This trigger is simultaneously used inclusively and semi-inclusively.
4. **Outer Trigger (OT)** is a large target pointing trigger. It consists of two horizontal hodoscopes (HO3 and HO4). Due to the size, HO4 is divided into two halves. The OT covers angles θ larger than 5 mrad, up to the end of the acceptance of the small angle spectrometer. The OT is mainly used to select muons in the momentum-transfer range of $10 (\text{GeV}/c)^2 < Q^2 < 20 (\text{GeV}/c)^2$.
5. **Large Angle Spectrometer Trigger (LAST)** is a target pointing trigger and is the only trigger system that is completely set up in the large angle spectrometer of COMPASS. It consists of two horizontal hodoscopes: H1 and H2, with H2 further divided into two hodoscope halves. This trigger covers the range of large momentum-transfers ($Q^2 > 10 (\text{GeV}/c)^2$) and large x . This trigger was newly implemented in the COMPASS setup in 2010; more technical details are given in Chapter 5.
6. **Calorimeter Trigger (CT)** covers a large kinematic range. Both HCALs are used to make the trigger. A cluster in one of the calorimeters with a minimal energy deposition fires the trigger when no veto signal is applied. The CT has also a large kinematic overlap with all the other physics triggers. The CT is mainly used for high Q^2 analysis and as an unbiased trigger sample to determine the trigger efficiencies.

Figure 37 shows the kinematic variables y and Q^2 for the different triggers. The kinematic distributions are taken from 2006 data with minimal cuts on the data: a beam muon and a scattered muon with an interaction point within the target material were required. One nicely sees the contribution of the various triggers to the different kinematic regions. The peak at $Q^2 = 0.1$, which is seen by all triggers, is originating from the elastic scattering of the muons on the hull electrons of the target.

4.2.5 List of Auxiliary Triggers

In addition to the physics trigger, a set of technical triggers is used, mainly during the data taking for spectrometer alignment.

1. **Beam Trigger (BT)** triggers on the incoming beam, using the scintillating fibre detectors FI01 and FI02 as explained in Section 3.2.2. This trigger has a simple set-up and is used in the start of run to time in all other triggers. This trigger is also used for the spectrometer alignment.
2. **Veto Inner Trigger (VI)** is a coincidence of the two inner veto detectors (V_{i1} and V_{i2}). It is used in the alignment to illuminate small angle detectors. The VI trigger rates help to investigate the quality of the beam; a higher rate might indicate a beam focusing problem.
3. **Halo Trigger (Halo)** triggers on halo muons further away from the beam axis. This is achieved by a coincidence of the V_{outer} and the hodoscope HO4. Again, this auxiliary trigger is used for the alignment runs and to estimate the halo beam rates.

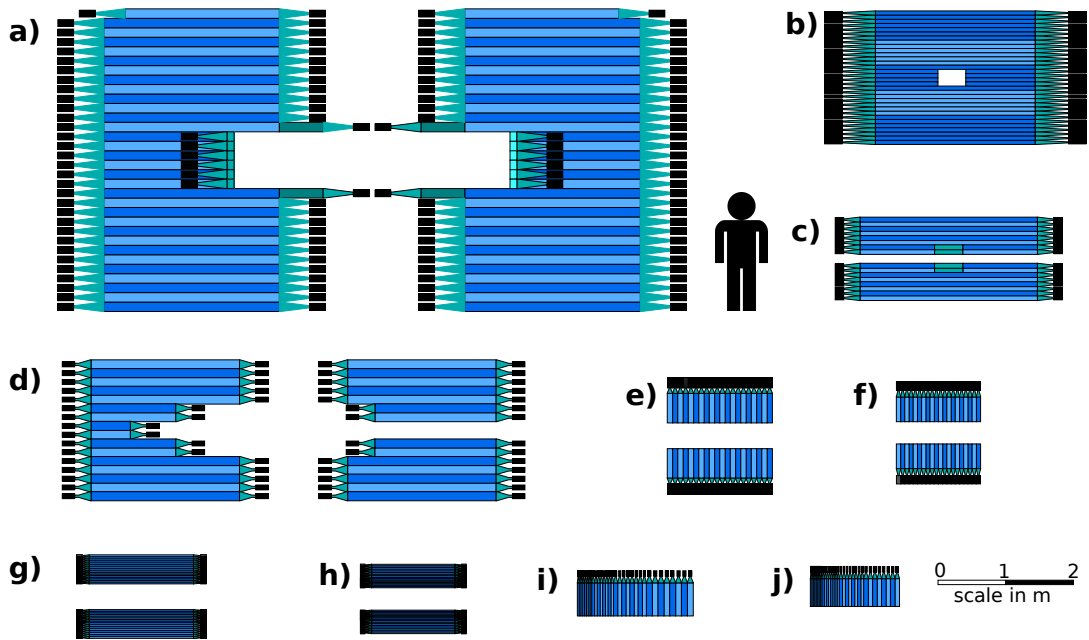


Figure 35: Overview of all hodoscope of the COMPASS experiment from a) to j): H2, H1, HO3, HO4, HM4X, HM5X, HM4Y, HM5Y, HL4 and HL5. The hodoscopes are shown in scale with a reference scale. The Inner Trigger elements are not shown here.

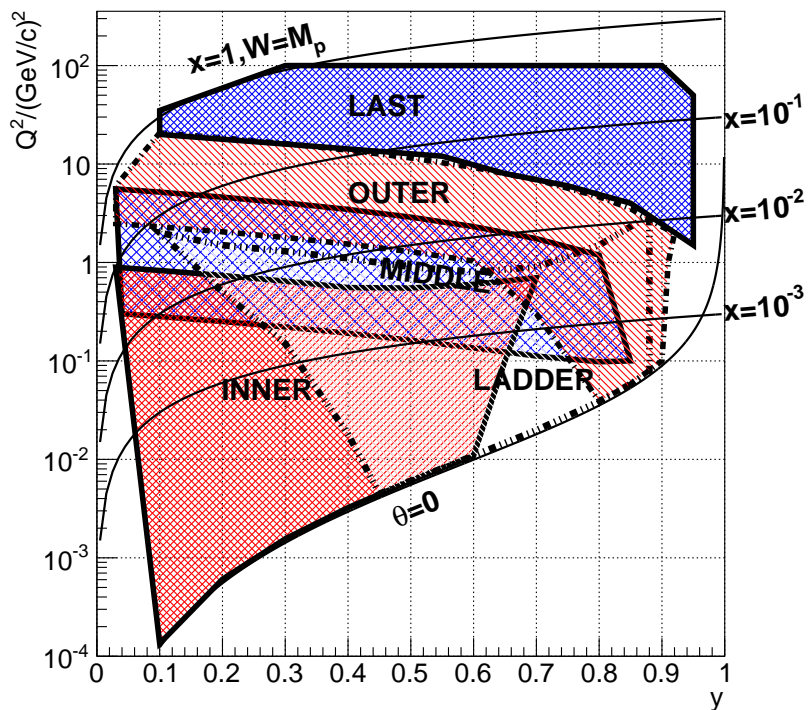


Figure 36: Overview of the kinematic range for the different COMPASS triggers. The two lines $x = 1$, $W = M_p$ and $\theta = 0$ show the kinematic limits of elastic scattering and forward scattering.

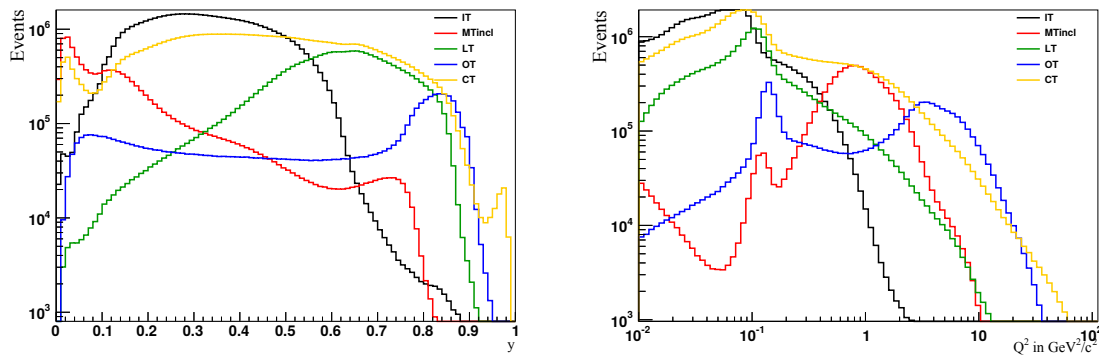


Figure 37: Inclusive kinematic variables for the 2006 run separated by the most important physics triggers.

4. **Random Trigger (RT)**, as described above generates a randomly distributed trigger signal that is used for flux measurements (Section 6.3) and unbiased detector tests.

4.2.6 Trigger Pattern and the Event

Each trigger has an individual identification number, which is used in the analysis to relate the events to the fired triggers. In total, there are 12 physics triggers with some auxiliary triggers numbered from 0 to 11. As the triggers have a kinematic overlap, it is possible to have an event with several triggers activated. The trigger arriving first is the time leading trigger. Any physics trigger arriving within a time window of 25 ns with respect to the time leading trigger is accepted. For a clear distinction, an alternative numbering is used offline: the *Trigger Mask* is made by the decoding library in the data reconstruction algorithm. It uses the information from the Prescaler module, where all trigger signals arrive. The trigger bit is translated into the mask by:

$$\text{mask} = 2^{\text{Bit}}$$

For several triggers in one event, the masks can be added, leading to a distinct trigger number. For example, in one event trigger bit 0 and 4, fired. Translated to the trigger mask, it is 1 and 16, thus the event has the trigger mask 17.

4.3 TRIGGER ELECTRONICS

The analogue signals coming from the PMTs are discriminated and split into two signals. The first one is read out by TDCs for the time information and monitoring of the hodoscope slabs. The second signal stream is used as input for the coincidence matrices. The setting of the matrices depends on the trigger type. For the MT, the outputs of the matrices (energy loss and target pointing) are combined. Then, the veto is applied yielding the final trigger signal which is split again: to be counted by a scaler and to be used as input for the Trigger Control System. Figure 38 shows the electronics chain from the PMT analogue signals to the final trigger signal for the Middle Trigger.

4.3.1 Discriminator

Constant fraction discriminators (CFD) developed by IPN Orsay are used to convert the analogue signals from the PMT into digital ones. For the both-sided hodoscope slabs, the

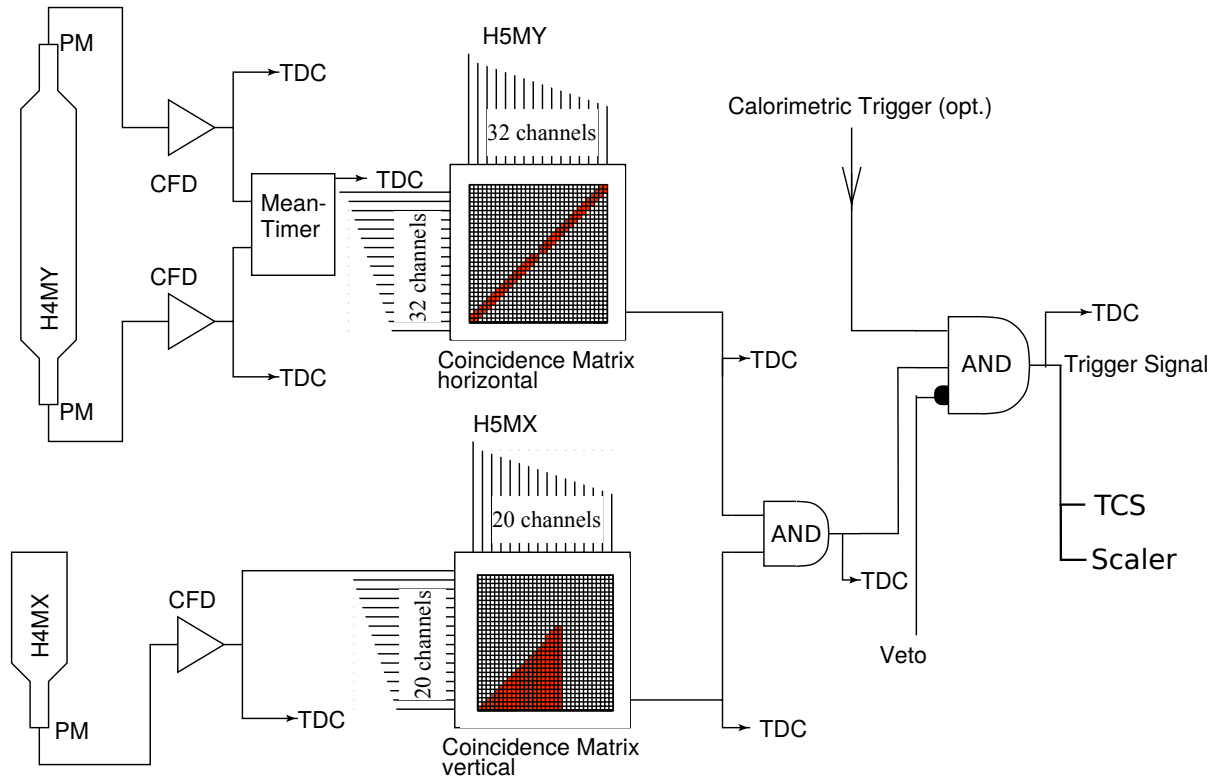


Figure 38: The electronic chain from the analogue PMT signal to the final trigger signal with the discriminator, the mean timer, the coincidence matrices and the final coincidence, where the veto signal and the calorimeter conditions are applied. Each step is monitored by TDCs.

average time (meantime) of the two PMTs is used. The meantime is used so that the hit time of the hodoscope is independent of the hit location along the scintillator slab. Using the meantime also assures a better time correlation to the other detectors in the experiment. The meantime is determined directly on the discriminator boards. The CFDs employ one comparator for threshold discrimination, and another one which compares the differentiated with the integrated signal for a pulse height independent timing. The meantimer works with one current source per input to ramp a voltage across a capacitor up to a threshold level [62]. This allows to choose the delay and the range of the mean timing stage as needed. With the 64 available inputs, each coincidence board allows to read out and process either 64 single-sided counters or 32 double-sided counters. The output of the discriminator board is provided as LVDS (Low-voltage differential signaling) and directly split into two signal streams. The first one is sent to TDC modules for monitoring and measurement of the timing. The second one is sent to the coincidence matrix.

4.3.2 Matrix Coincidence

A coincidence matrix is used for a pair of hodoscopes planes. The input are the digital signals provided by the discriminator. They are checked for the presence of allowed combinations. All muon triggers use a coincidence matrix. The shape of the allowed coincidences of the matrix is shown in Figure 38 for the MT. The shape depends on the type of the used trigger. The coincidence matrix for all target pointing triggers are shaped as a diagonal matrix with a hole in the center to reject near halo, which has not been vetoed and appears to come from the target. For energy loss triggers, the coincidence matrix is set to a triangular shape as the trigger condition in the bending plane of the spectrometer magnet is smeared out, what means a threshold energy loss is required.

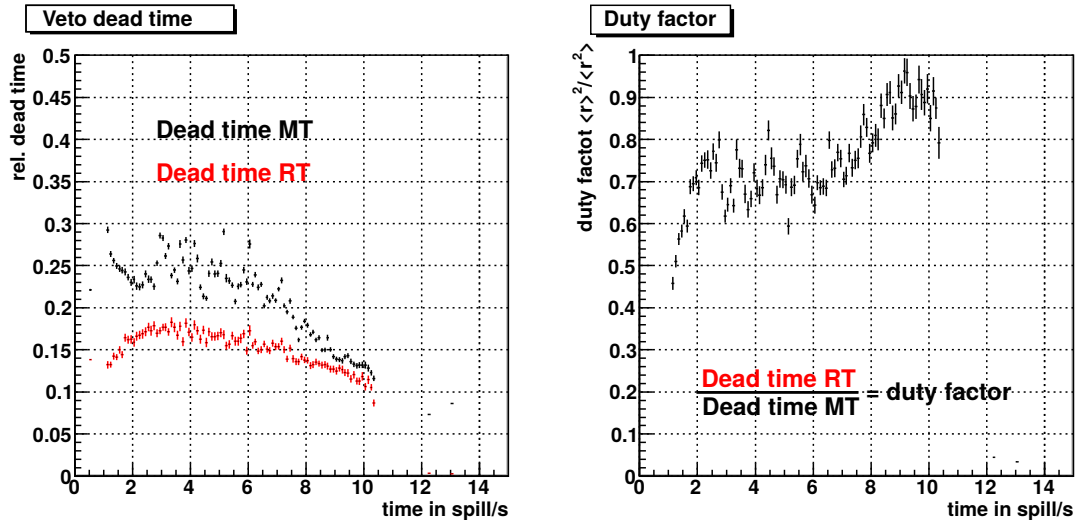


Figure 39: **Left:** Veto dead time as a function of the time in spill for two triggers: the Middle Trigger and the Random Trigger. **Right:** The ratio of the two dead times leads to the duty factor, which shows the quality of the delivered beam.

The coincidence matrix boards, with programmable delay for each input and pulse shaper, are built for 6U VME crates and have 64 inputs, which allow the treatment of 32×32 channels.

4.3.3 Final Trigger Logic

In the case of the MT, the two outputs of the coincidence matrix (one for target pointing and one for energy loss) are put into coincidence to combine the two trigger types. The veto and/or the calorimeter condition are applied with a coincidence to finalise the trigger. Most of the triggers only fire with the absence of a veto signal, with the exception of the Inner trigger. The calorimeter condition is used to obtain semi-inclusive triggers. The final trigger is then sent to the prescaler module. Here, the number of triggers can be reduced by a division factor to reduce the load on the DAQ. The auxiliary triggers do not yield interesting events and are prescaled by a large number. The prescaler is connected to the trigger control system, which enables the read out of the front-end of the detectors.

The signals from the PMTs to the final trigger are monitored in each step of the electronic chain using TDCs. The final triggers are counted by a scaler to obtain the numbers of trigger attempts. The actual number of triggers processed by the DAQ is called accepted triggers.

4.3.4 Veto Dead Time

When a veto signal is created by halo muons, the ability to trigger on a new event is inhibited for a certain time. The veto dead time is characterised as the fraction of data taking time during which no triggers can be accepted because veto signals are present. This time is dictated by the trigger electronics, the veto electronics and the width of the time window of the veto signal. Also random coincidences between the hodoscopes and the veto system cause this dead time of the trigger system. In addition, the stability and quality of the beam delivered by the SPS influence the veto dead time. The halo muon rate increases with the beam intensity and a defocused beam mainly hits the veto detectors. In absolute measurements of cross section, the veto dead time needs to be corrected for. An overview and a nice description for

the veto dead time measurement can be found in [63] and [64]. Two methods are used to measure the veto dead time (VDT).

4.3.4.1 Middle Trigger Veto Dead Time

The veto dead time is measured with two modified versions of the Middle trigger, a MT without veto and a MT with a delayed veto. This veto delay has to be chosen large enough (32 ns) to create random veto coincidence. The veto dead time is then measured by the ratio

$$R_{\text{MT}} = \frac{\text{MT}(\text{delayed Veto})}{\text{MT}(\text{no Veto})}. \quad (47)$$

This is the fraction of time, in which a veto signal randomly suppresses the trigger signal. In the ideal case, the veto dead time should not depend on the chosen trigger. This method takes into account all effects coming from the beam line, such as the intensity and beam time structure.

4.3.4.2 Random Trigger Veto Dead Time

Similar to the first method, in which the Middle trigger is utilised, the dead time can be measured with the random trigger, with and without the veto. Due to the random character of the random trigger, the veto signal does not need a delay.

$$R^{\text{RT}} = \frac{\text{RT}(\text{Veto})}{\text{RT}} \quad (48)$$

Figure 39 shows the veto dead time measured for the Random Trigger (red) and for the Middle Trigger (black) as a function of the time in spill for one spill of the year 2010. All relevant numbers to calculate the dead times are stored in the database. For MT, the dead time starts with a high value coming from a large number of halo muons at the start of the extraction. At the end of the spill, the veto dead time decreases as the beam intensity drops. For the RT, the veto dead time rises slowly until it drops due to the beam depletion. The MT dead time is always higher than the RT dead time as more effects are taken into account. The division of those two dead times

$$\frac{R^{\text{RT}}}{R^{\text{MT}}} = D \quad (49)$$

leads to the duty factor D , which describes the quality of the delivered beam from SPS.

THE LARGE ANGLE SPECTROMETER TRIGGER (LAST)

The COMPASS II phase started in 2012 and focuses on measurements of Deep Virtual Compton Scattering ($\mu + p \rightarrow \mu' + p' + \gamma$) and the Drell-Yan process ($\pi + p \rightarrow 2\mu + X$). For DVCS, a new trigger system was requested to enlarge the acceptance towards larger Q^2 . The Calorimeter Trigger cannot be used as it triggers only on final-state hadrons, which are not available in this process. In DY, the focus lays on the measurement of muon pairs with large angles. The hadronic state X is absorbed using large hadron absorbers right behind the target, in the best case, only two muon with opposite charged remain in the final state. To meet the requirements (large Q^2 and large scattering angle) of both physics programs, a trigger system was designed and set-up in the LAS part of the COMPASS spectrometer. The system consists of two trigger hodoscopes with horizontal slabs for target pointing and a suitable trigger electronics, which allows to trigger on events with one or two outgoing muons. The new hodoscopes are called H1 and H2, in accordance with the nomenclature of the existing hodoscopes. The trigger system was conceptualised in 2009 and put in place during the 2010 run with a transverse polarised target. The detectors were commissioned, so that in the same year, the collaboration could already benefit from the increased kinematic range in Q^2 and x for inclusive triggers [65].

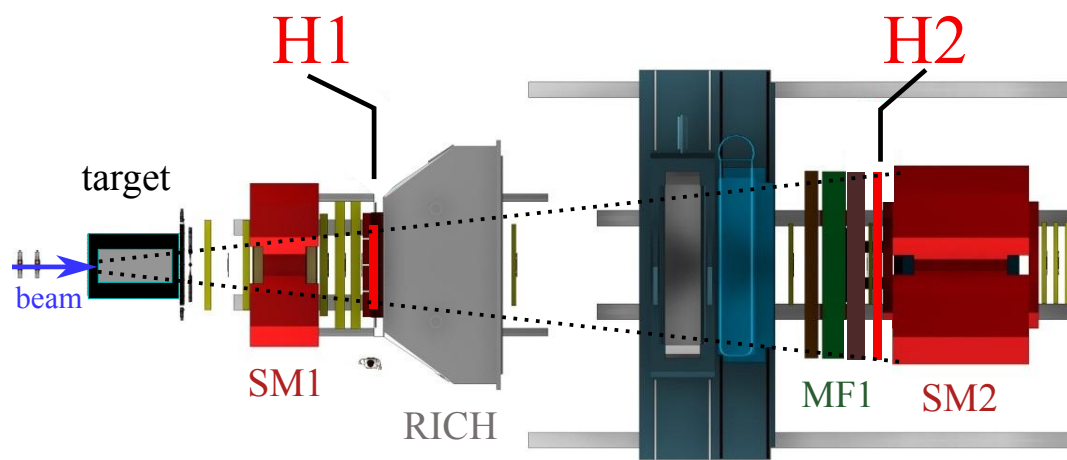


Figure 40: The first stage of the COMPASS spectrometer with the position of the hodoscopes H1 and H2. The dashed black lines indicate the maximal acceptance.

5.1 CONCEPT

To reach larger angles, a muon trigger on the basis of target pointing is appropriate with two scintillator hodoscope in the LAS of the COMPASS spectrometer. One of the hodoscopes has to be placed behind an absorber to allow for muon identification. The only absorber in the LAS is the MF1, leading to position behind MF1 before SM2. The size of the larger hodoscope H2 has to match the size of the large area tracker (DC, MW1) to assure the reconstruction

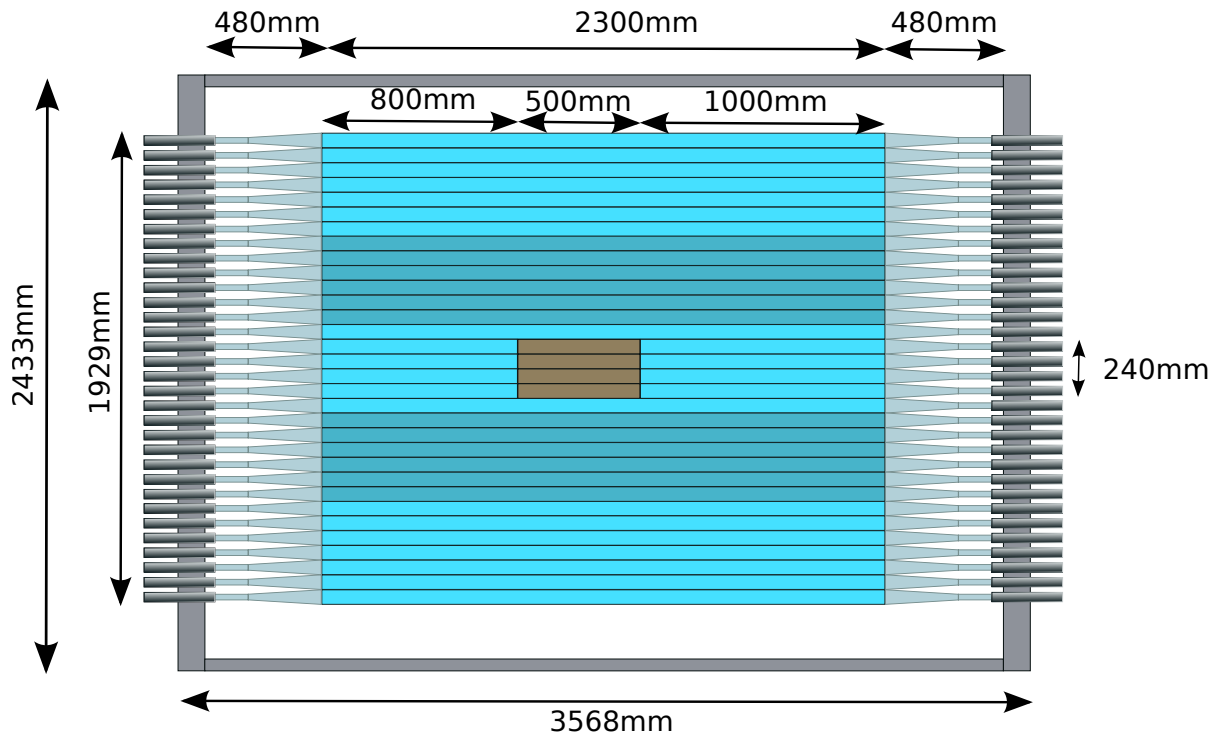


Figure 41: Technical drawing of the 2010 H1. The groupings (outer, inner and hole) are shown in different colours. The air light guide is shown in brown. The soft iron shieldings are attached to the grey aluminium frame. The ROHACELL structure is not shown here.

of muon tracks. The hodoscope H2 has a central hole, matching the aperture of SM2, to free the acceptance for the second spectrometer part (SAS). The size of the horizontal scintillator slabs are optimised for the Drell-Yan data taking. This granularity is chosen such that it is possible to suppress events coming from the hadron absorber and taking into account the multiple Coulomb scattering. The hodoscope H2 is divided into two halves for mechanical stability. The smaller counterpart H1 is installed as far as possible from H2 and as close as possible to SM1. The only free space in the spectrometer was directly in front of the RICH. The resulting distance between the two hodoscopes is 10.2 m. Because of the proximity to the hadron PID detector, H1 had to be as thin as possible. In Figure 40, the position of both hodoscopes (H1 and H2) is shown. Like most hodoscopes, H1 and H2 are read out by PMTs on both sides. Due to the proximity of the hodoscope to the spectrometer magnets, a suitable magnetic shielding is used.

5.2 HODOSCOPE H1

The hodoscope H1 is located in the first spectrometer part, directly in front of the RICH, the detector responsible for the ID of hadrons. The hodoscope has thin scintillator slabs to minimise the material. In addition, the soft iron shieldings are brought out of the acceptance of the RICH with long plexiglas light guides. Muons or other particles hitting the massive soft iron shieldings are likely to produce additional hadrons, messing up the RICH detector response and the identification of hadrons. The hodoscope H1 has a central hole, matching the acceptance for the second spectrometer. The inactive area is realised with a air light guide. In Figure 41, a technical drawing of H1 is shown.

5.2.1 Dimensions and Position

The hodoscope H1 has a size of 2300 mm \times 1920 mm and consists of 32 horizontal scintillator strips. It has a central hole of 500 mm \times 240 mm, so the total active area is 4.3 m². The hodoscope H1 is located at the Z-position 582 cm in the COMPASS reference system. The available space for H1 was approx. 30 cm along the beam direction. The detector is held in place by a frame made of BOSH aluminium rods, to which each soft iron shield is attached. Deformation studies of this profile have been done by the COMPASS Trieste group. The studies were performed assuming that 350 kg are attached to the center of the bar. The result is illustrated in the Appendix (Figure 124). The maximum deformation is 3.6 mm.

5.2.2 Substructure and Hole

To minimise the material in front of the RICH, the individual scintillator strips are not staggered like in most of the other scintillator hodoscopes. H1 is divided into five subsections: 2 groups of 7 slabs for the outer region of the hodoscope (top and bottom), 2 groups of 6 slabs for the inner region and one group of 6 slabs for the central hole region. The grouping assures the mechanical stability of H1. To measure the meantime, the slab has to be read out on both sides. The central hole cannot be equipped with PMT with soft iron shieldings. For DVCS, the shielding would absorb the final-state photons. Connecting the two sides of the central hole with plexiglas would lead to too much material. Therefore, a construction with a high reflective foil was used to make air light guides. In 2010 and 2011 for the nominal position of the polarised target position, the central hole group consisted of 4 air light guide slabs and two normal long slabs. The air light guides are made of high reflective ESR foil¹ (Enhanced Specular Reflector) produced by 3M. The foil is folded into a rectangular casing and slipped over the end of the central scintillator slabs. The principles of the air light guides were developed in Mainz and are described in [66] and [67].

The position and the size of the hole was changed in 2012 to a symmetric geometry [68] for the more upstream position of the target of the DVCS and the DY data taking. The number of air light guides was increased to six.

5.2.3 Scintillator Slabs and Light Guides

The scintillator material is BC408 from St. Gobain². The normal slabs are 230 cm long, 6 cm wide and 1 cm thick. The slabs in the hole region are 80 cm long in the bending direction of SM1 for positive muons and 100 cm in the opposite direction. Since 2012, the central slabs with air light guides are 90 cm long, on both sides. The single scintillator slabs are wrapped in a 0.2 mm thick aluminised mylar foil. The grouping is wrapped in 0.5 mm thick black foil for light tightness. To collect the light, polished light guides made of PMMA are glued to both ends of the scintillator slabs. The geometry is a cylinder with an attached truncated cone (frustum) which has been cut to match a more rectangular shape for the scintillator slab, leading to a "fish-tail" like shape. The construction plans are shown in the Appendix in Figure 118. The light guides are 48 cm long. The wide part of the light guides matches the cross section of the slab, while the round side matches the entrance window of the PMT.

1 <http://multimedia.3m.com/mws/media/3808020/vikuititm-esr-msds.pdf?fn=ESR.pdf>

2 <http://www.crystals.saint-gobain.com/uploadedFiles/SG-Crystals/Documents/SGC%20BC400-404-408-412-416%20Data%20Sheet.pdf>



Figure 42: The soft iron shielding, the voltage divider, the PMT, the μ metal shielding and the capton insulation of H1. The aluminium part serve as a fixation.

5.2.4 Read-out, PMT and Shielding

Each scintillator strip is read out on both sides by PMTs of the type XP2982 or XP2900 (in the outer region). XP2982 is a fast, 11-stage, $1\frac{1}{8}$ inch photomultiplier tube with a bi-alkali cathode³. The voltage divider was designed at the University of Warsaw, Poland and the circuit diagram is shown in Figure 121. Due to interferences of the target solenoid field and SM1, the PMTs are shielded with a double layer of μ metal with a thickness of 0.2 mm and by a 4 mm thick cylindrical soft iron tube. The dimensions of the soft iron shielding are $\varnothing = 46$ mm and a length of 290 mm. In between these magnetic shieldings, a 0.2 mm thick capton foil for insulation is placed. An aluminium ring fitting on the cylindrical part of the light guide is used to attach the soft iron shielding. The PMTs and their voltage dividers are mounted on the end cap of the shielding with a spring as place holder. The PMT is inserted into the soft iron shielding and hold in place with the end cap. Inside the magnetic shieldings, the spring pushes the detection window of the PMT onto the light guide. In Figure 42, all parts of the H1 read out are shown. The shielding was tested in the magnetic field of SM1. Different kinds of magnetic shielding were test and the analogue signal of the PMT observed. The current shielding set-up is fit and no visible change of the analogue signal is observed in the magnetic field. To keep the attenuation low, thick cables (COAX C-50-6-1 50 OHM) are used for the signals. As the H1 and H2 signals are put to a coincidence, the cable length of H1 to the electronic has to compensate for the time of flight of the muons between H1 and H2. It also has to compensate for the different transit times of the different PMT types.

The nominal voltage for the XP2982 PMT is around 1600 V. Each channel has been tuned individually during spill by observing the muon band with oscilloscope. The high voltage is provided by a SY1527 crate from CAEN with three 24-channel modules with the corre-

³ www.photonis.com/upload/industryscience/pdf/pmt/XP2982.PDF

sponding distribution boxes (A1932 Radial to SHV Cable adapter). The analogue signals are converted to digital signals by CFD from CAEN⁴.

5.2.5 Mechanical Stability

The low material budget and the lack of place made the mechanical stability of the detector challenging. The groups of scintillator slabs are attached to the aluminium frame at the soft iron shieldings with clamps. Due to the length and the thickness of only 1 cm of the scintillators, each group had to be reinforced with a casing with a very low material budget composed of ROHACELL (1 cm and 2 cm thickness) and fibre glass strips. Each group of H1 has 2 cm of ROHACELL IG 31 (0.032 g/cm³ density) on one side and 1 cm of Rohacell IG 51 (0.052 g/cm³ density)⁵ on the other side. These parts are glued with ARALDITE rapid⁶ to a rectangular envelope around the scintillator groups to avoid sagging and vibrations of the groups. ROHACELL is a structural foam with low density and high mechanical stability. The ROHACELL fibre glass casing is also mandatory for the stability of the air light guide group. Figure 122 (Appendix) shows an overview of H1 with the ROHACELL casing, the light guides, the shieldings and the BOSH aluminium frame. The different groups are mounted on top of each other. The weight is distributed on the clamped soft iron shielding and the supported ROHACELL/fibre glass casings.

5.3 HODOSCOPE H2

H2 is the larger hodoscope of the LAS trigger and also one of the largest detectors in the experiment.

5.3.1 Dimension and Position

The hodoscope H2 has a size of 4995 mm × 4197 mm and a central hole of 1495 mm × 781 mm, and thus a total active area of 19.8 m². A technical drawing of this detector is shown in Figure 43. H2 is installed directly in front of the second spectrometer magnet (SM2), behind the MF1 and the second half of MW1. This corresponds to 1600 cm from the target center in the COMPASS reference system. H2 is attached to a cross beam bar resting on a support frame of SM2, the position along the beam may change by moving SM2. The total mass of the hodoscope is 2.5 tons. Due to lack of space, the width of H2 had to stay below 30 cm.

5.3.2 Substructure and Hole

For mechanical stability, the large hodoscope H2 is divided into two symmetric halves (Y1 and Y2). A central hole, made by shorter scintillator slabs, matches the acceptance of the second spectrometer part. The hodoscope halves Y1 and Y2 have an overlap of 50 mm. Each half consists of 32 scintillator slabs. The slabs are staggered with an overlap of 2 mm to avoid acceptance holes. The gap between Y1 and Y2 in Z is 50 mm. H2 has 128 readout channels.

4 <http://www.caen.it/csite/CaenProd.jsp?parent=11&idmod=46#>

5 http://www.roehmschweiz.ch/fileadmin/Roehm/PDF_Rohacell/ROHACELL_IG_IG-F_Product_Information.pdf

6 <http://www.go-araldite.com/products/epoxy-adhesives/araldite-rapid-2-x-15ml-tube>

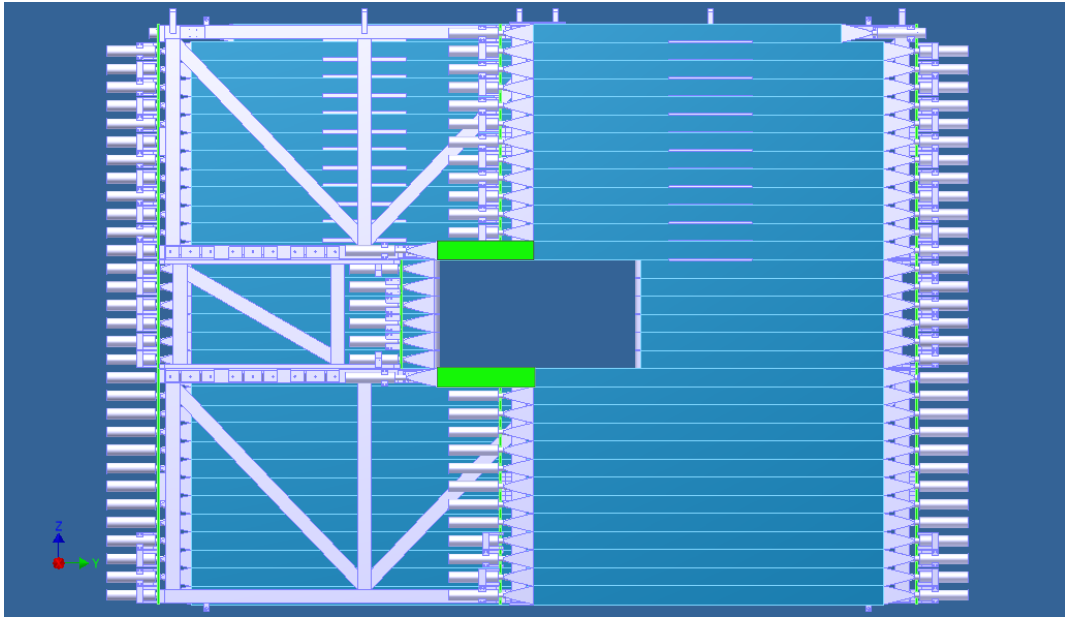


Figure 43: Technical drawing of H2 with the normal slabs, the long ones above the central hole, the top-most short ones and the slabs at the central hole with the bent light guide. The plexiglas elongation of the long slab is shown in green.

5.3.3 Scintillator Slabs and Light Guides

For the scintillator slabs of H2, BC408 is used. The standard slabs are 252.5 cm long, 13.6 cm wide and 2 cm thick. For different regions in H2, the slabs are cut to the appropriate size. After cutting, the surface had to be machined with a diamond tool turning machine to obtain a transparent surface without scratches. Each slab of H2 is wrapped in a layer of crumpled aluminised mylar foil for light reflection and a layer of black foil for light tightness. The following slabs are used in H2 and are summarised in Table 4:

- Short: the top-most slab is shortened by approx. 30 cm because of the structure of SM2, where H2 is installed, interferes with the insertion of PMT and the voltage divider.
- Normal: the standard slabs are used for the largest part of H2.
- Bent: in the central hole standard slabs are used. To obtain a both-sided read-out without perturbation of the detectors in the SAS, special light guides are used.
- Long: the slabs directly above and below the hole are extended with 630 mm PMMA slabs to have the PMT shielding out of the SM2 acceptance.

For the light collection, three different light guides made of PMMA were developed and produced. Figure 119 (Appendix) shows the fishtail light guide used in most of the (normal) hodoscope slabs of H2. For the slabs prolonged by PMMA, a modified version of the fishtail light guide is used for mechanical reasons. A both-sided read-out is needed, even in the central hole region. With only conventional light guides in the center, the soft iron shielding with high atomic Z would perturb tracks heading towards the second spectrometer. A combination of a normal fishtail light guide and a bent light guide is used. The bent light guides (Appendix, Figure 120) are hollow PMMA cylinders with a radius of 4.5 cm, cut in half and glued on the straight light guides. They bend the light around 180 degrees, thus bringing the PMTs with their shielding out of the acceptance of the Small Angle Spectrometer. Naturally, those bent light guides are not as efficient as straight ones. On a test bench, the performance

element name	quantity	length in mm	function
Short	2	2217	top
Normal	46	2525	normal
Long	4	2525 + 630 PMMA	slabs around hole
Bent	12	1775	bent light guide on hole

Table 4: Summary of the H2 elements.

of a bent light guide was tested: around 50 % of the scintillator light is lost in addition to the lost of the attenuation. To maintain the staggering in the central region with the bent light guides, the straight light guides are narrower than the scintillator slab (130 mm compared to 136 mm).

5.3.4 Readout, PMT and Shielding

The H2 scintillator slabs are read out on both sides with 9814KB PMTs with the matching voltage dividers⁷. H2 is situated directly in front of SM2, so the hodoscope was designed with soft iron shielding to ensure PMT performance. As in H1, metal rings are attached to the cylindrical part of the light guide to hold the soft iron shielding in place. The PMTs with the voltage divider casing (with springs to prevent PMT entrance window damage) is screwed to the shielding. A μ -metal shielding around the PMTs and a standard CERN soft iron shielding are used. The two shieldings are separated by an insulator (capton or teflon is used). It has a diameter of 80 mm, a length of 36 cm and a thickness of 5 mm. Figure 10 shows a dismantled readout for H2. Figure 44 shows the read-out parts for H2. As described in the H1 section, thick COAX cables are used for signals. The signal cable length for each channel in H2 (H1) is 51 m (63 m). Patch panels for the flexible cables are put on top of SM2.

The high voltage is provided by a SY1527 crate from CAEN. Six distribution boxes of the type A1535N from CAEN (three on each side of the hodoscope) with 24 channels supply the 128 PMTs. Each channel was individually tuned during the spill with an oscilloscope for optimal HV settings. The HV varies between 1300 and 1600 V.

5.3.5 Mechanical Stability

The main requirement was to make the support as thin as possible due to the lack of space. The support structure consists of six separate pieces and a suspension bar. The material used is aluminium to allow the installation close to SM2, in the region with the presence of the magnetic field of around 0.01 Tesla. Only the photomultiplier tube holders are made from stainless steel. To check the stability in the magnetic field of SM2 and the load of the weight, the support structure was simulated and optimised using CAD tools by the COMPASS group of INFN Torino. The result of this study is shown in Figure 125 (Appendix). With the simulated weight of 2.5 t, the maximum deformation is only 4.3 mm.

⁷ <http://www.electrontubes.com/pdf/9814B.pdf>. The 9814KB is a 51 mm (2 inch) diameter, end window photo-multiplier with blue-green sensitive bialkali photo-cathode and 12 BeCu dynodes of linear focused design



Figure 44: The PMT, the μ metal shielding, the soft iron shielding, the Teflon insulation, the metal connector and the voltage divider used in H2.

5.4 TRIGGER ELECTRONICS

Instead of using the same design for the matrix electronic and the discriminator as the other muon triggers, it was decided to take advantage of a new technology. The meantimer and the matrix electronic are simulated on a FPGA (Field-Programmable Gate Array), an integrated circuit, whose purpose can be configured by a software. The signal chain from the hodoscopes to a trigger signal is shown in Figure 45. First, the analogue signals of H1, H2Y1 and H2Y2 (64 from H1 and 128 from H2) are brought to a Constant Fraction Discriminator (CFD) with low loss cables, where each channel is discriminated. The discriminator has a LEMO input and two ECL outputs, which are converted to LVDS. One output is sent to a TDC read-out for the time measurement of the hodoscope hits and for monitoring. The second output is brought to a GANDALF board, where both, the meantimers and the matrix circuit, are programmed on the FPGA. Two GANDALF boards are used, one for each half of H2. The digital signals of H1 are split into two, using an active LVDS splitter, to provide the signals for each H2 half. In [69] and [70], the GANDALF board is described in details. The development of the trigger electronics is reported in [71] and [72] by the Bonn part of the COMPASS trigger group.

5.4.1 Constant Fraction Discriminator

The CAEN V812 board⁸ is a 1-unit wide VME module housing a 16 channel CFD. The module accepts negative inputs and generates ECL pulses when the input signals exceeds a given threshold. The constant fraction technique allows to precisely determine the timing of the signal, as it does not depend on the signal height as in a leading edge discriminator (LED). First, the input signal is duplicated: one of the signals is delayed by a fixed time, the other one is damped and inverted. The sum of both signals gives a zero-crossing which is used as the discriminator threshold, independent of the input signal height. After the high voltage

⁸ <http://www.caen.it/csite/CaenProd.jsp?parent=11&idmod=46>

tuning of each hodoscope, the discriminator threshold is set. The discriminator threshold has to lie between the muon band and the background. For H2, the threshold of the discriminator is set to 32 mV, which is around $\frac{1}{3}$ of the average analogue muon signal band during the spill. Due to the smaller PMTs in H1 and the resulting smaller analogue signals, the threshold in H1 is 16 mV.

The CAEN V812 board has an adjustable dead time from 150 ns to 2 μ s per channel, the lowest possible dead time is used. The output gate width can be adjusted from around 15 ns to 250 ns. A 15 ns (25 ns) gate is chosen for H1 (H2).

5.4.2 GANDALF

The GANDALF is a multi-purpose FPGA board, developed by the Freiburg group to analyse the signals of the new Recoil Proton Detector of COMPASS (CAMERA) using GHz-sampling. The board can be equipped with up to two mezzanine (IEEE P1386.1) cards providing 64 LVDS inputs, 64 LVDS outputs or 8 analogue inputs. The actual signals are processed by an FPGA (Virtex 5 by Xilinx⁹), allowing the implementation of different logic functions. Constructed as 6U-VME64x/VXS modules, the GANDALF boards can be controlled via VME bus to load a configuration into FPGA, read and/or write to the FPGA memory.

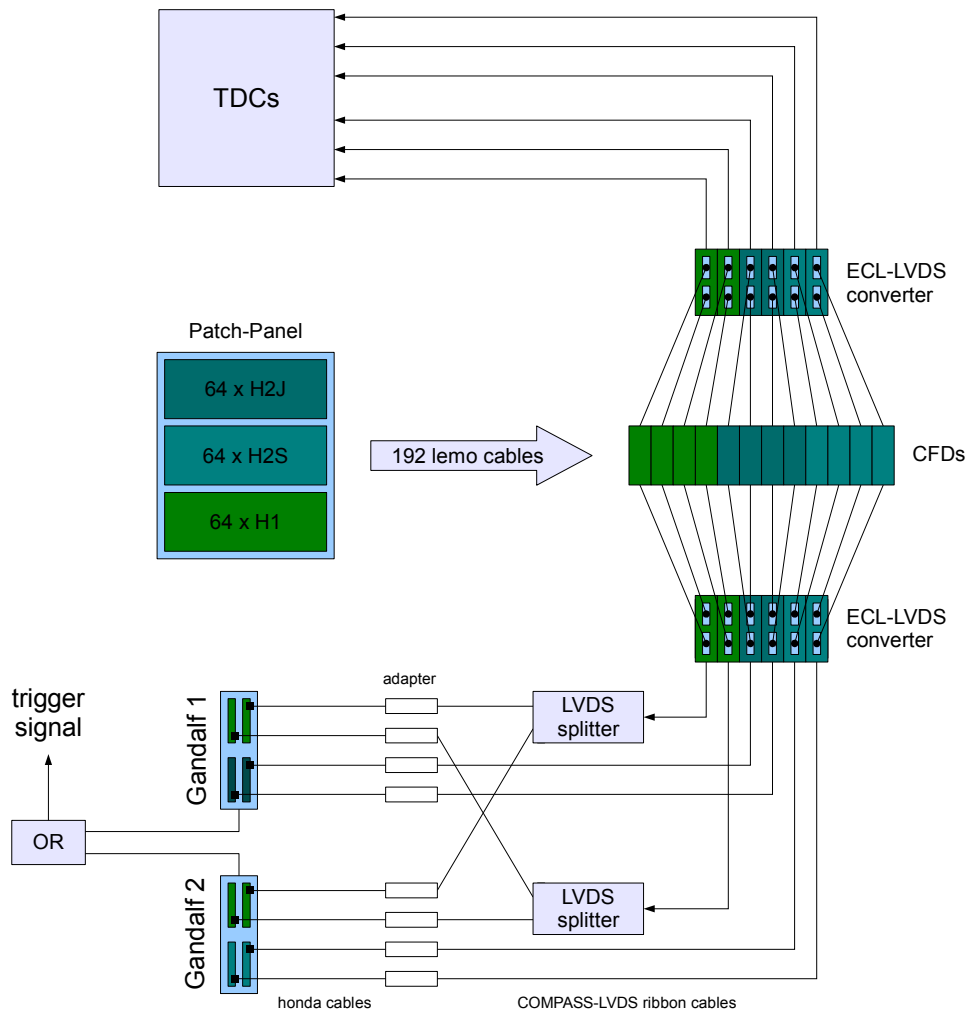


Figure 45: Interconnection of the different devices of the LAS-Trigger.

⁹ http://www.xilinx.com/support/documentation/data_sheets/ds202.pdf

5.4.3 FPGA-Based Meantimer and Coincidence Matrix

The meantimer and the coincidence matrix are programmed on a FPGA. The meantime is calculated with the discriminator outputs. It has a dynamic range of 23 ns, which defines the maximum offset between the two discriminated PMT signals of one slab. This range is sufficient to cover the full slab length of H1 and H2 (around 2.5 m). A veto input is implemented for each meantimer to suppress any output, if the offset of the input signals exceeds the dynamic range to prevent false outputs. For the 32 slabs of each hodoscope, one needs 64 parallel meantimers per GANDALF board. All these meantimers work independently.

To obtain the target pointing trigger condition, the meantimers of each slab and hodoscope are connected to the coincidence matrix. This is done with an adjustable delay for each channel. Inside the coincidence matrix, each of the 32 H1 slabs is compared to the 32 slabs of each hodoscope half of H2. To minimize the complexity, the 1024 parallel coincidence checks are partially serialized. Each GANDALF module has a single hit output and a double hit output. The veto signal V_{tot} is applied directly on the FPGA. The coincidence matrix pattern looks similar to the ones of the target pointing triggers in the SAS. A diagonal is used to reject parallel halo tracks.

5.4.4 Single Muon and Dimuon Trigger

The LAST is used to trigger on scattered muons in DIS with large Q^2 . This is achieved with the combination of the single hit outputs of the GANDALF modules (H1/H2Y1 and H1/H2Y2) and the absence of a veto signal.

The Drell-Yan process has two muons with opposite charges in the final state. Each muon of the pair can either hit one H2 half or both hit the same H2 half. For this di-muon trigger, the double hit output and the single hit output of the GANDALF are combined. In addition, the one muon trigger can be combined with the already existing hodoscope triggers. The performance of these di-muon trigger are under current investigation using data from the DY data taking of 2014/2015.

5.5 PERFORMANCE

Analogue Signal and Hit Distribution: The left side of Figure 46 shows an analogue output of two H2 PMTs of the same slab on a sampling oscilloscope (PMT1 in blue and PMT2 in yellow). The measurement was taken with a muon beam and shows one muon hitting the slab. It also shows the typical analogue signal of a scintillator read out by PMT. The rapid falling flank of the signal originates from direct light produced in the scintillator, reaching directly the photocathode of the PMT. The long tail is due to the indirect light, which reaches the PMT photocathode later due to the reflection on the surface of the scintillator. The signal height depends on the hit position of the muon along the scintillator (distance to the PMT). The muon hit the scintillator slab closer to PMT1, the signal of PMT2 arrives later and the signal height is smaller due to the attenuation of the light inside the scintillator [60].

With the monitoring tool COOL, the hit distribution of the hodoscopes can be checked by TDC entries. On the right side of Figure 46, the typical distribution for one half of H2 is shown. As expected, the intensity is roughly symmetrical around the central slab and also the different slab geometries and length can be deduced from the hit distribution.

Timing: Time resolution is the characteristic property of a trigger hodoscope. The resolution is measured with a special COMPASS trigger monitoring software using the time information of the hodoscope from a TDC read-out. The timing of each PMT (t_1 and t_2) is measured with

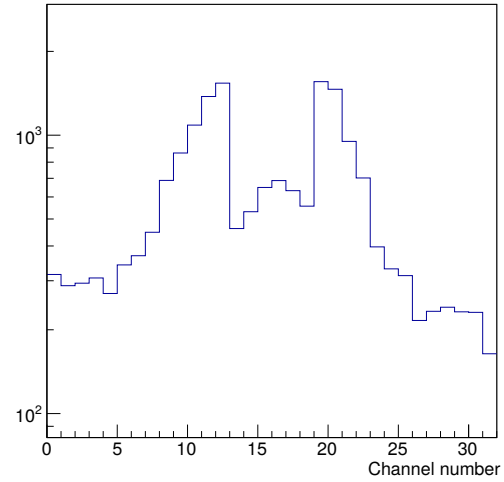
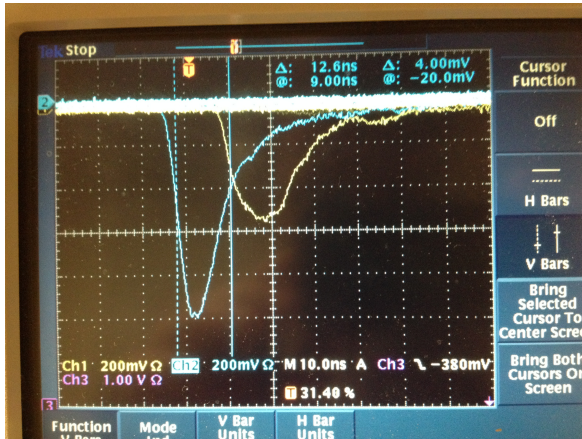


Figure 46: **Left:** Analogue signal of two PMTs of one H2 slab. **Right:** Hit distribution of one half of hodoscope H2.

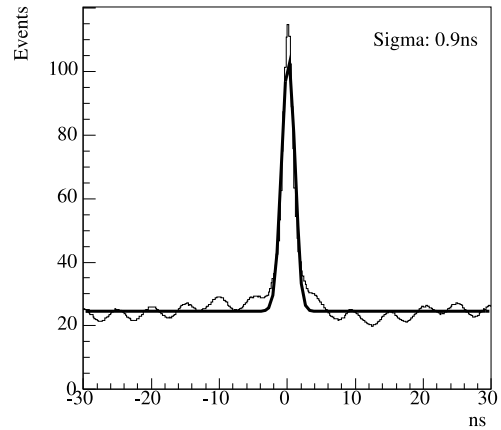
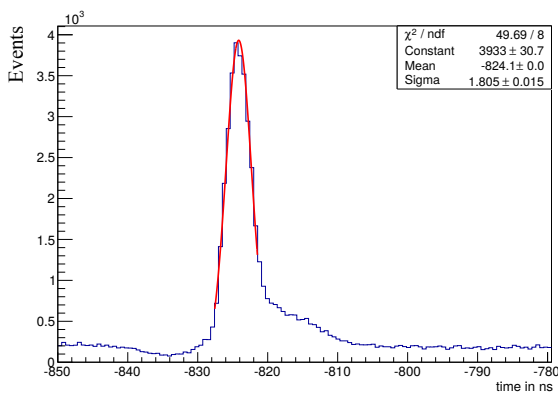


Figure 47: **Left:** Timing of one H2 slab (Channel 12). **Right:** Timing of the LAST, measured with the BMS.

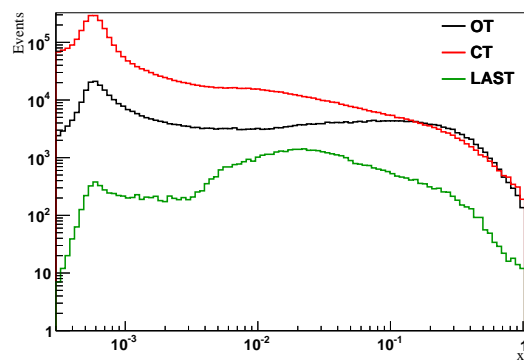
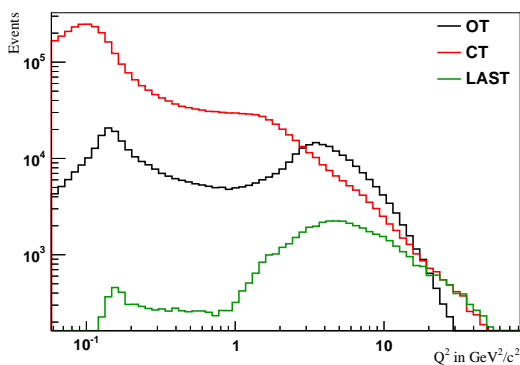


Figure 48: Kinematic distribution of the LAST in comparison to the Outer Trigger and the Calo Trigger. **Left:** Q^2 . **Right:** x . Similar to Figure 37 in the Trigger Section, only a well-defined beam muon and a reconstructed scattered muon are required with an interaction inside the target material.

respect to the timing of the BMS. Figure 47 shows the timing for an exemplary PMT of H2 and the overall timing of the LAST. To determine the timing, the meantime is calculated with

$$t_{\text{mean}} = \frac{t_1 - t_2}{2}. \quad (50)$$

The average time resolution per slab is around 250 ps. Combining all slabs and adding the time uncertainties from the trigger electronic, the overall timing of the LAST is 0.9 ns. The wavy time structure left and right of the main timing peak is coming from time structures in the beam line and the accelerator system. The timing is determined by the standard deviation σ of a Gaussian fit on the timing. The timing peak is shifted to zero like every trigger at COMPASS: the trigger time gives the event time.

Trigger Performance: In Figure 48 shows the kinematic distribution for Q^2 and the Bjorken scaling variable x for the Outer Trigger, the CT and the LAST. The data shown in the kinematic plots are taken from the COMPASS run in the year 2010, the year of the installation. As expected, the LAST is able to trigger on events with large Q^2 , exceeding the Outer acceptance. The kinematic overlap in the high Q^2 region (>20 GeV) is very similar between LAST and CT. And in the largest Q^2 bins, there are events, which are exclusively triggered by the LAST. The new LAST is able to trigger on scattered muons only, rather than hadrons as in the CT case. The events are mostly expected at low W^2 , corresponding to high x , where the produced hadrons do not enter in the COMPASS acceptance due to their low momentum. The peak at $x \sim 4 \cdot 10^{-4}$ and $Q^2 \sim$ is due to elastic muon scattering on the electrons of the target molecules.

In Figure 49, an extract of the scaler display during the 2010 runs is shown. It is used to monitor the stability of the trigger rates, veto rates, dead times and beam specific quantities, such as position and a estimation of the beam flux. As expected the LAST trigger rates are as stable as the rates of the already existing triggers and follows nicely the trend of the beam intensity.

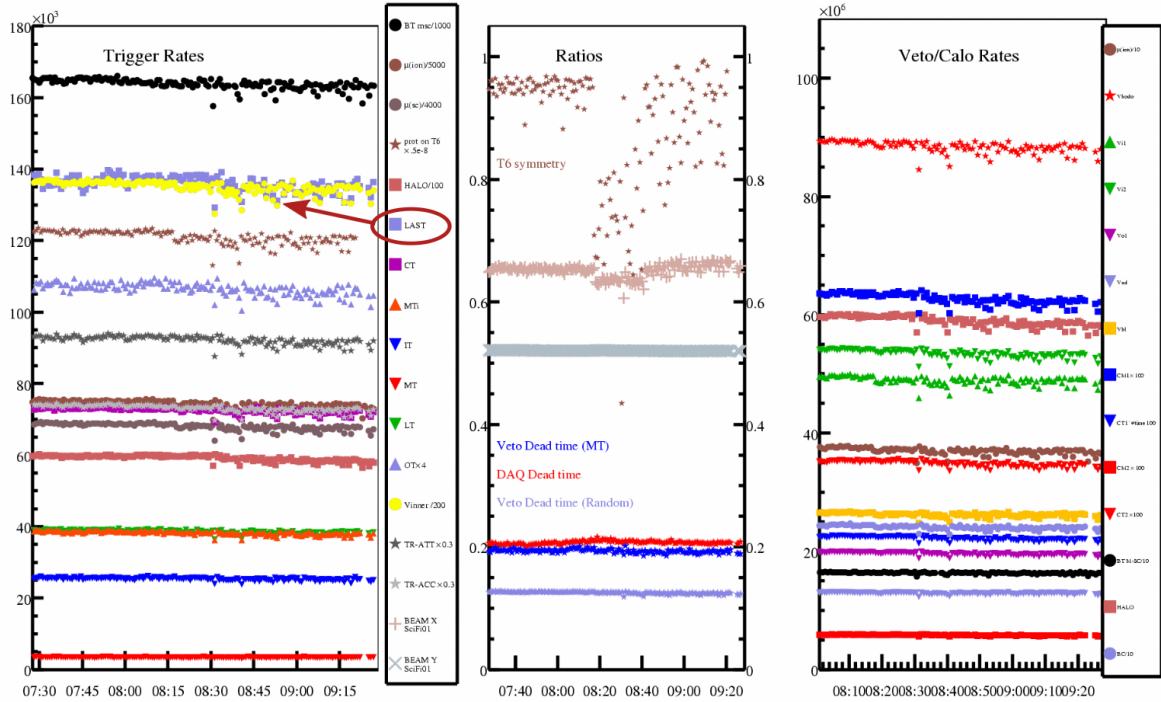


Figure 49: The scaler display of the trigger rate in 2010. The LAST trigger is shown as purple squares.

TRIGGER EFFICIENCY AND LUMINOSITY FROM DATA

In this Chapter, the treatment of the COMPASS data and the event structure are described. In addition, two data analyses using special triggers are presented. First, the hodoscope efficiencies are determined using the calorimeter trigger. In the second part, the true random trigger is used to determine the useful particle flux in the COMPASS experiment. Together with the target density, the luminosity is extracted.

6.1 DATA FLOW AND COMPASS ANALYSIS

The unprocessed data coming from the detectors is saved on an event-by-event basis. The events contain TDC, ADC data and the channel numbers of hits for each detector. For a physics analysis, the raw data has to be decoded, and calibration and correction procedures for the detectors to be applied. The reconstruction program CORAL¹ is used to reconstruct trajectories in the spectrometer, determine interaction vertices and extract detector specific information, *e.g.* RICH information and calorimeter clusters. An option file for CORAL is used to specify the reconstruction parameters for each year and physics program. For physics analysis, the ROOT²-based software tool PHAST³ is used, allowing an easy access to all kinematic and geometric parameters of the reconstructed tracks on an event-by-event basis. The data flow is illustrated in Figure 50.

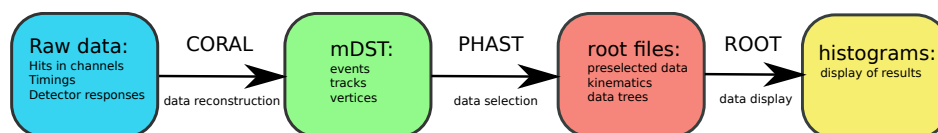


Figure 50: Flow chart of the COMPASS data. The raw detector information is stored event-wise. The reconstruction algorithm CORAL is used to decode the data. With PHAST and ROOT, the data is analysed and display in a comprehensive way with histograms.

6.1.1 The DIS Event Structure

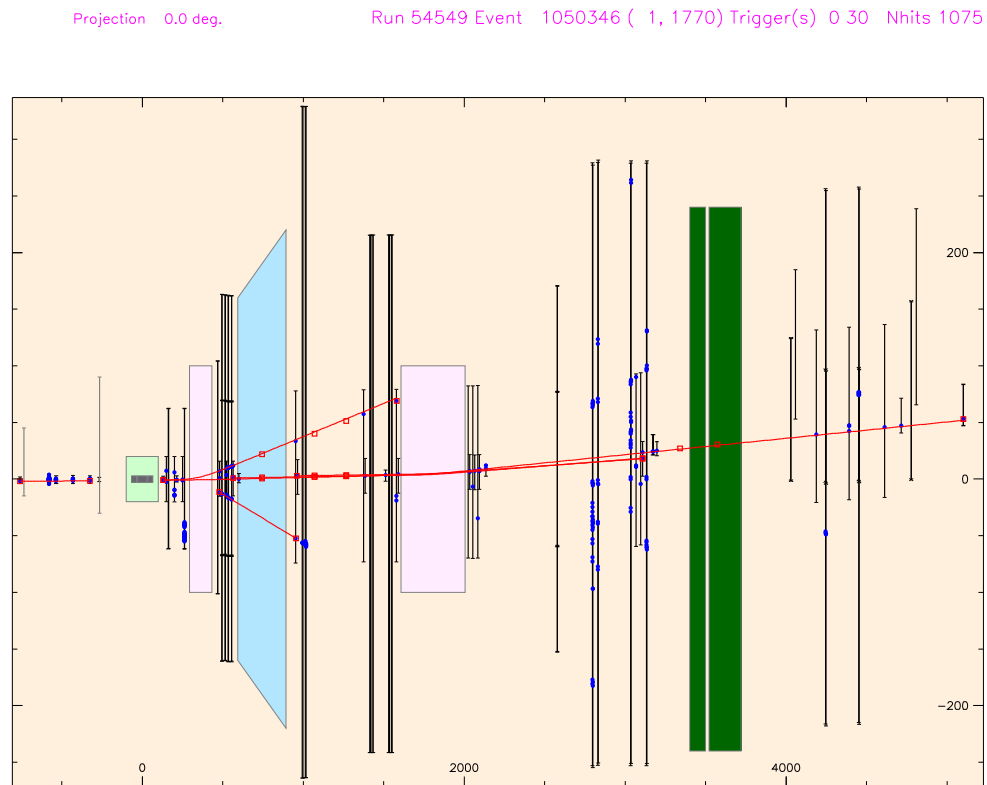
A DIS event must contain an incoming muon, an interaction in the target material, a scattered muon and eventually additional outgoing hadrons. The identification of muons is crucial for the physics analysis of deep inelastic scattering. From the reconstructed incoming and scattered muon, all inclusive kinematics are calculated. For investigation of the structure of the nucleon, the interaction vertex has to lie inside the ⁶LiD volume. Figure 51 shows a typical reconstructed event by CORAL from a top view. The experiment is schematically drawn with all detector positions and dimensions. The beam enters from the left and is detected in the

¹ Compass Reconstruction ALgorithm <http://coral.cern.ch>

² <http://root.cern.ch>

³ PHysics Analysis Software Tools, <http://ges.home.cern.ch/ges/phast/>

beam telescope. The red lines indicate reconstructed tracks, while the blue circles imply hits on detectors. The red squares are hits associated to a track. Of note, not every hit is linked to a reconstructed track, as it can also be caused by *e.g.* cosmics or detector noises. Behind the target, there are at least four visible tracks with different properties. The two short tracks are deflected in different directions by the first spectrometer magnet, thus are likely to be hadrons with opposite charge and lower momenta. The long track passes the muon filters and is reconstructed in the muon section by the MW2, hence this is the candidate for the scattered muon. The fourth track is not bend strongly by the spectrometer magnets but the reconstructed tracks end before the muon filter. This points to a charged hadron candidate with high momentum, which was stopped by either the calorimeters or the muon filters.



TRAFFIC (version 1.71) event display

(1

Figure 51: A reconstructed DIS event by CORAL. It shows a schematic experiment (top view). The beam enters from the left. Blue markers indicate hits in detectors and red lines show the reconstructed track.

6.1.2 Incoming Muon

All tracks reconstructed in front of the target by the beam telescope are interpreted as the incoming muons. Track parameters are measured by the scintillating fibres and the silicon detectors. The momentum of the track is determined in the BMS. When the momentum cannot be measured, it is set to $160 \text{ GeV}/c$ in the reconstruction algorithm. The incoming beam from the M2 beam line consists mostly of muons due to the set-up of the beam line; any kind of secondary particles are absorbed by the hadron absorbers in the beam line. The pion contamination is smaller than 10^{-5} . Muons in the tails of the spacial distribution are called

halo muons and are removed from the data recording by the veto system.

6.1.3 Scattered Muon Track

As the final state may also contain hadrons, the scattered muon has to be identified. With the help of the muon filters (MF1, MF2 and MF3) and the Muon Wall detectors, the scattered muon can be identified. Due to the large absorption length of the filters, all tracks behind there are assumed to be muons. The properties of a scattered muon track are: (1) it is a reconstructed outgoing track that crosses at least 15 radiation length of material and (2) comes from the target region. The charge corresponds to that of the incoming muon charge and this track has to be compatible with the hits in the trigger hodoscopes. If several tracks pass the requirements, the candidate with the largest momentum is chosen as the scattered muon.

6.1.4 Vertex Selection

Interaction vertices are constructed out of intersections of tracks with a fit. So called primary vertices have one incoming track, one scattered muon track and potentially further outgoing hadron candidates. If several primary vertices are present, the best primary vertex is chosen, which is the one with the smallest χ^2 of the track combination fit. The vertex X and Y positions are determined using the incoming track, which is most precisely measured due to the use of silicon strip detectors in the beam telescope. The Z position of the vertex is the average Z of all tracks attached to that vertex.

Secondary vertices are intersections of reconstructed tracks that are not associated with the incoming or the scattered muon. Generally, secondary vertices have exactly two outgoing tracks. One example is the decay of a K_S^0 into a $\pi^+\pi^-$ pair. The π^0 does not have a secondary vertex because photons do not have tracks, only energy deposition in the electromagnetic calorimeters.

6.2 HODOSCOPE AND TRIGGER EFFICIENCIES

One of the main tasks of the COMPASS trigger group is to maintain and monitor the trigger system. During data taking, the performance of the detectors is checked by using online monitoring tools (COOL and DCS). With this method, detector issues, *e.g.* switched off scintillator slabs and timing problems, can be seen and swiftly be resolved.

To determine the hodoscope and the trigger efficiencies, reconstructed data is needed. With the hodoscope efficiency, hodoscope slabs with problems, either on the electronic or on the detector side, can be identified. With the trigger efficiency, the treatment and the correct transmission of the trigger signal to the DAQ is checked. The offline efficiencies are needed for the acceptance calculations and for quality checks of the collected data. Hodoscope slabs with low efficiency are excluded from the data, as well as in the Monte Carlo simulations.

The hodoscope efficiencies are determined from reconstructed data on PHAST-level for each hodoscope plane. An unbiased data sample is needed, where hodoscope hits are not required to trigger the events. As described in Chapter 4.1.3, the Calo Trigger selects events, in which hadrons leave a large enough energy cluster in the calorimeters. Thus, scattered muons from Calo Trigger events can be used to check the performance of the hodoscopes. The efficiency ϵ

is calculated by comparing the number of muons with and without hits in the corresponding hodoscope.

6.2.1 Efficiency Event Selection

The hodoscope and trigger efficiencies are determined for each hodoscope and for each year, for each muon trigger (OT, LT, MT and IT), except for LAST. The data selection, which is adapted for each year of data taking, is the following: only Calo Trigger events with an incoming and a scattered muon with a primary vertex inside the fiducial target volume are considered. The momentum of the scattered muon has to be larger than 40 GeV to reject muons coming from the pion decay. Six hits along the track behind MF2 are required to identify the muon and the muon track has been measured accurately.

The scattered muon tracks are then extrapolated to the Z position of each hodoscope and the X and Y position of the track is saved in a position map. Only tracks within the active area of the hodoscope are considered. The same is done but with the requirement that a detector response associated to that hit was found. This leads to two X-Y distribution for each hodoscope. The geometrical acceptance of the hodoscope is checked in the analysis software. Tracks outside the active detector area are rejected to remove edge effects and other mismatches, which locally reduce the efficiency. The track parameters from the data are only stored on a few positions (close to target and at last detector hit). In between these positions, the parameters are calculated and multiple scattering is taken into account with a statistical method. The position of the extrapolated track can be pushed away from the actual position, which in a histogram leads to bin migrations. In addition, the position of the detectors used in the data reconstruction algorithm CORAL and the actual position of the detector in the experiment slightly differ. The hodoscope efficiency ϵ_{hod} is given by

$$\epsilon_{hod} = \frac{\text{expected tracks with hit}}{\text{expected tracks}}. \quad (51)$$

The same procedure applies for the trigger efficiency with the additional trigger bit:

$$\epsilon_{trig} = \frac{\text{expected tracks with hit and trigger bit set}}{\text{expected tracks with hit}}. \quad (52)$$

As an example, the hodoscope and the trigger efficiency are shown using the 2006 data for one half of the HO04 hodoscope, the counter part hodoscope HO03 and for HM05X, a part of the Middle Trigger.

6.2.2 Requirement of the Efficiency Determination

The determination of the trigger efficiency with the Calo Trigger has limitations. The main reason is that the CT is also used as a physics trigger, but with a different veto signal gate length than the muon physics trigger. In addition, the CT is delayed by six nanoseconds compared to the other physics triggers. The calorimeter trigger should not be time-leading, when in coincidence with a muon trigger, as the main focus of physics data taking lies on the events coming from the muon hodoscope trigger. The time shift is then compensated in the reconstruction software. For this reason, no absolute trigger efficiency can be calculated, only a lower limit.

All hodoscopes are also used as tracking detector. With their good time resolution, the timing of the muon tracks is improved by the TDC information of the hodoscope. For scattered muons with small angle and entering the acceptance of the hodoscope of the Inner Trigger,

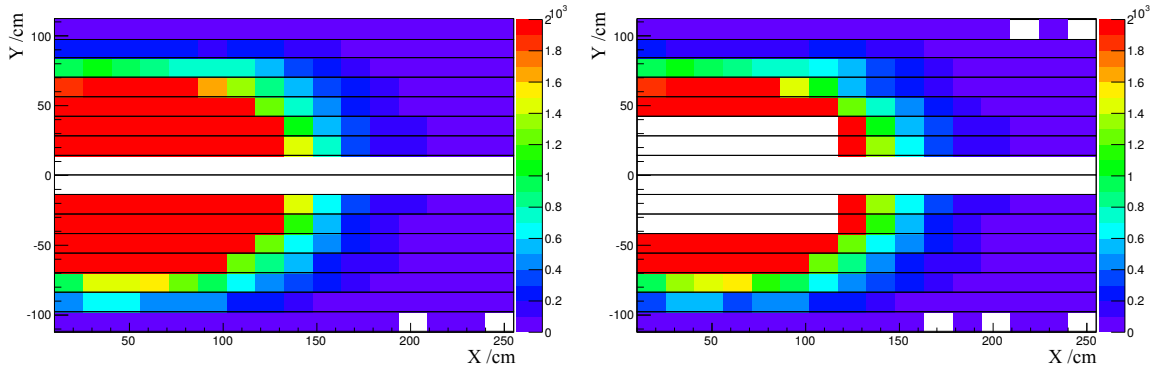


Figure 52: **Left:** X-Y positions of the extrapolated tracks at the hodoscope HO04_Y1. **Right:** X-Y positions of the extrapolated muon tracks at the hodoscope H004_Y1 with a recorded hit.

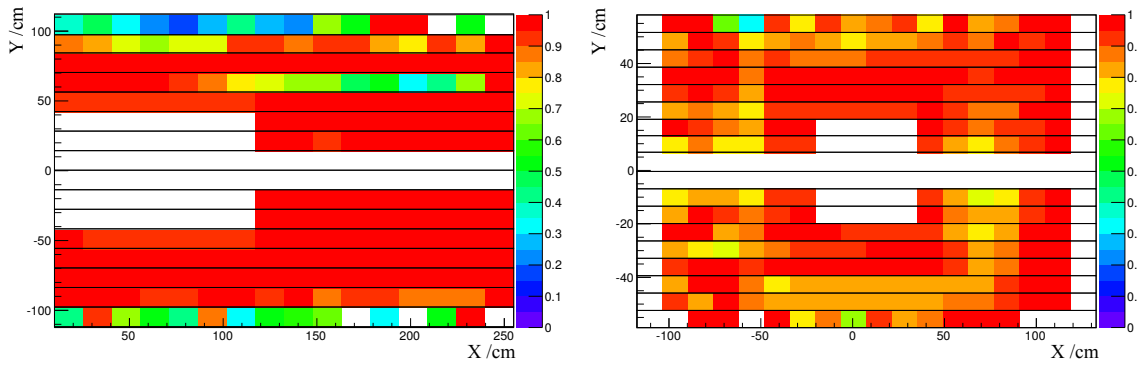


Figure 53: **Left:** Hodoscope efficiency scatter plot for H004_Y1. **Right:** The hodoscope efficiency of H003, the counter hodoscope for the Outer Trigger.

the muons are identified by requiring a hit in the hodoscope HI05. Thus, the efficiency cannot be calculated for that specific detector. But, by studying the hit pattern on HI5, an assessment of the performance can be done.

For the newest trigger hodoscope system LAST, it is still a challenge to obtain the correct hodoscope and trigger efficiencies. In the year of the installation (2010), the focus was on transverse spin asymmetries. In that year, the stability of all trigger hodoscope was most important, which was monitored online. The information of the used hits is not yet available in this data. So no efficiency for 2010 were calculated. In 2011, the LAST was used as a semi-inclusive trigger with the calorimeter condition. The LAST efficiency determination is not meaningful. In 2012, only a short muon run was taken and the LAST was heavily prescaled, leaving to too few events for a efficiency determination. With the data collected in 2014 and 2015, the LAST trigger efficiency will be calculated. For that, a change in the reconstruction algorithm is mandatory.

This efficiency determination method requires a large amount of Calo Trigger events. During the physics data taking, the main attention lies on data recorded with the hodoscope triggers. To reduce the load on the DAQ, the number of CT events is reduced by a scaling factor. The data of a full year of data taking has to be analysed to obtain the efficiency. Anyway, in the region of large angles, the statistics remains an issue.

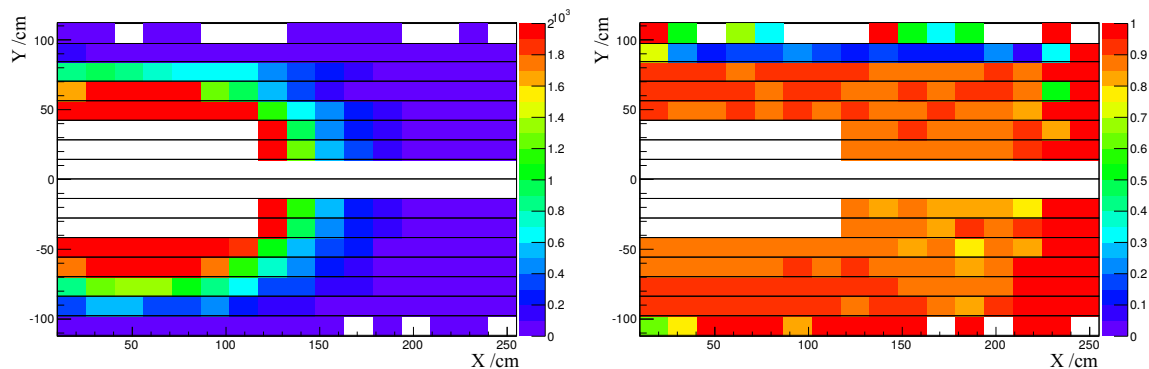


Figure 54: **Left:** X-Y distribution of muon tracks with hits in H004_Y1 and trigger bit. **Right:** Trigger efficiency of HM05X_d.

6.2.3 Hodoscope Efficiency

As an example, the hodoscope efficiency is shown for HO04_Y1, a part of the OT. The geometry of this detector is shown in Figure 35 (left hodoscope of d; please note that in this figure the hodoscope is mirrored). The hodoscope consists of 14 horizontal scintillator slabs, separated in the center by a two-slab wide gap. In addition, the four inner slabs are shorter to form the central hole. Figure 52 (left) shows the X-Y distribution of the extrapolated muon position on the Z position of HO04_Y1. The individual scintillator slabs are indicated by the black lines. The central track positions in the missing slabs are removed for a better orientation. As expected, the region with a higher number of muons is in the center, due to the high rate of scattered muons with small angles. The number decreases when moving towards the edges of the hodoscope.

The right picture shows the same X-Y distribution of extrapolated tracks at HO04 with a hit in the detector itself. Here, the geometry of the detector is now visible due to the hit requirement.

By dividing the two position distributions, the hodoscope efficiency map is obtained. The left side of Figure 53 shows the hodoscope efficiency of the hodoscope half HO04_Y1. The efficiency over most of the hodoscope is between 95 % and 100%. Only, the most upper and lower slabs seem to be not as efficient, but this is coming from the limited statistics in the region of scattered muons with large angles. The scintillator slab at $Y = 58$ cm shows a region with lower efficiency of around 60%. The fact that the hodoscope slab only partially shows an inefficiency, points to timing problem in the meantimer stage of this particular slab. Of course, this flaw has been resolved for the next data taking period. The right side of Figure 53 shows the hodoscope efficiency for HO03. It is the counter part of the HO04 hodoscope system for the Outer Trigger. The efficiency of this hodoscope looks good and ranges between 0.9 and 1. But a rectangular region around the central hole of HO03 with lower efficiency of 80% is visible. A scintillator should have the same efficiency along the slab. A partially efficient slab, either points toward a meantimer problem or to a reconstruction problem. In this case, the rectangular shape is coming from a frame of a MWPC.

6.2.4 Trigger Efficiency

For the trigger efficiency, the position of the extrapolated muon track with a hit in the corresponding hodoscope and an additional physics trigger fired are needed. Figure 54 shows this hit distribution, again for HO04_Y1. This distribution with hit and trigger shows the

same features as the distribution with only the hit required. Only in the most upper and lower slabs the statistics are further reduced. The right plot shows the trigger efficiency of the hodoscope HO04_Y1 and, as mentioned above, it is only a relative trigger efficiency due to the Calorimeter Trigger. The efficiency is almost homogenous and ranges between 80 % and 95 %. The most upper slab shows again an apparent inefficiency due to the lack of statistics. The second most upper slab is inefficient with 15 %. The problem was a mistuning of the coincidence matrix pixel between this hodoscope and the hodoscope HO03. This issue was resolved for the following data taking period.

6.2.5 The Middle Trigger 2006

The Middle Trigger consists of four hodoscope planes with horizontal and vertical slabs. A Middle Trigger requires a hit in all four planes, rendering this trigger logic more complicated. The hodoscope efficiency of HM05X_d, a part of the Middle Trigger with vertical scintillator slabs (Figure 35 f) is shown in Figure 55 (left). Except for some structures in the top part, the efficiency is 99 % over a large parte of the hodoscope. In the trigger efficiency, on the other hand, two inefficient regions can be observed. The left part of the hodoscope has an efficiency of less than 10 %, a clear indication towards a hardware problem. In the center of this hodoscope, an additional slab with a lower efficiency (50 %) is observed. Unfortunately, the inefficient part of the Middle Trigger was not seen with online methods present at that time. All the rates, the wire maps with hit pattern and timing, which are accessible via the online monitoring program COOL, did not show any perturbation during the data taking of 2006. The tools for online monitoring has been improved for later data taking. A very carefull offline analysis of the trigger efficiency is mandatory. For the multiplicity analysis 2006 and the corresponding Monte Carlo simulation, the non-working parts of the trigger are removed with the following piece of code:

```
int idet = PaSetup::Ref().iDetector("HM05X1_d");
  const PaDetect& HM05 = PaSetup::Ref().Detector(idet);
  HM05z = HM05.Z();
int Npars = scatmuon.NTPar(); // track is the PaTrack of the mu1
PaTPar partr = scatmuon.vTPar(Npars-1);
PaTPar parHM;
partr.Extrapolate(HM05z, parHM, false);
HM05x = parHM(1);
HM05y = parHM(2);
static const double xminHM05X1_u = 14.55 -0.15; // values taken from detectors.52959.plus.dat
static const double xminHM05X1_d = 22.02864 -0.12864;
if((trigMask&256) && HM05x < (HM05y>0. ? xminHM05X1_u:xminHM05X1_d) )
{ // eliminate iMT bit
  trigMask -= 256;
}
```

Muon tracks are extrapolated to the Z position of the Middle Trigger hodoscope HM05X1_d. The Middle Trigger bit is removed, if the trigger was fired from a scattered muon hitting the inefficient part of the hodoscope.

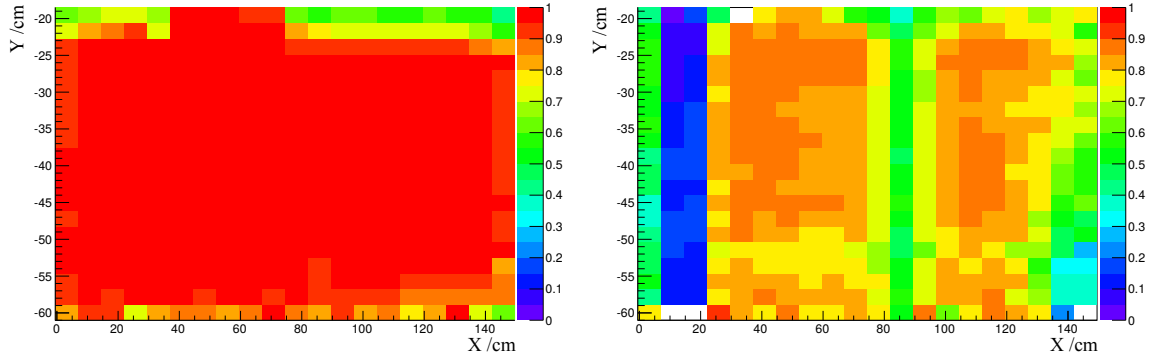


Figure 55: **Left:** X-Y hodoscope efficiency distribution of HM05X_d. **Right:** Trigger efficiency of HM05X_d.

6.3 LUMINOSITY DETERMINATION

For cross section determination, the measurement of the integrated luminosity $\int L dt$, the acceptance Acc and corrections C , such as veto and DAQ dead times, are mandatory. A cross section is given by:

$$\sigma = \frac{N}{\int L dt \cdot C \cdot Acc'} \quad (53)$$

where N denotes the number of events with the desired final state. In a fixed target experiment, the integrated luminosity $\int L dt$ is given by the integrated beam flux ϕ hitting the target material and the target density ρ_{target} , which is the number of scattering centers per area. For DIS, the target area density is usually calculated per nucleons:

$$\frac{L}{\text{s/cm}^2} = \int \frac{\phi}{\text{s}} dt \cdot \frac{\rho_{\text{target}}}{\text{cm}^2}. \quad (54)$$

Two different methods to determine the incoming reconstructed muon flux through the target are presented. The first method uses the scalers of the scintillating fibre station 2 dynodes (2006 and 2009). The second method uses the True Random Trigger to select beam tracks (only for 2009). The selection of the beam tracks as well as the two methods are described and compared. The integrated luminosity for 2006 is calculated with the Scaler Method while for 2009 the more precise Random Trigger Method is used and compared to the scaler method.

6.3.1 2009 Data Set

During the DVCS run in September 2009, three weeks of data were recorded with a 160 GeV muon beam impinging on an unpolarised liquid hydrogen target:

- W38 (run 79576-79685), μ^+ with 4049 non-empty spills,
- W39 (run 79779-79791), μ^- with 885 non-empty spills,
- W40 (run 79797-79964), μ^+ with 8862 non-empty spills.

The number of spills is given after data quality checks and rejection of bad spills.

	A	U	C	D	Σ
H/mol	1	0.052±0.006	0.100±0.010	0.053±0.006	0.205
D/mol	2	10.261±0.214	19.940±0.329	10.558±0.227	40.759
³ He/mol	3	0.292±0.040	0.599±0.077	0.284±0.040	1.175
⁴ He/mol	4	3.633±0.357	7.455±0.667	3.536±0.352	14.624
⁶ Li/mol	6	9.859±0.212	19.159±0.329	10.144±0.224	39.162
⁷ Li/mol	7	0.454±0.020	0.882±0.035	0.467±0.021	1.803

Table 5: Contents of the 2006 LiD target for each target cell

6.3.2 Target Density

The target area density in cm^{-2} is given by:

$$\rho_{\text{target}} = l \cdot \rho_{\text{nucleon}} \cdot N_A \quad (55)$$

with the target length l , the molar density of nucleons in target ρ_{nucleon} and the Avogadro constant N_A . The density is calculated for the years 2006 where a solid state ⁶LiD target is used, and for 2009, where a liquid hydrogen target is used.

6.3.2.1 The 2006 Lithium-Deuterid Target

In 2006, an isoscalar solid-state ⁶LiD target was used. The main part of the target material are LiD beads swimming inside a liquid helium bath contained in a mylar cylinder. After the beam time, the target was emptied and the material was weighted and analysed. The target material contains hydrogen, deuterium, helium-3, helium-4, lithium-6 and lithium-7, the portions in mol are given in Table 5. It is assumed that the different materials are homogeneously distributed within the target cells. The mylar target material holder has a total volume of 848.23 cm^3 . The weighted molar mass for nucleons is 391.337 mol, here the molar mass of each element is multiplied by its atomic weight. This number corresponds to $2.36 \cdot 10^{26}$ nucleons. To obtain the correct target density, the target cuts from the physics analysis and from the luminosity determination have to match. For the 2006 luminosity determination, the same target cuts and incident particle requirements are used as in the 2006 charge hadron multiplicity analysis (Section 7.1.3). The longitudinal Z cut is $-56 \text{ cm} < Z < -35 \text{ cm}$, $-20 \text{ cm} < Z < 31 \text{ cm}$ and $43 \text{ cm} < Z < 66 \text{ cm}$ to cut out each of the three target cells with an additional radial cut of 1.4 cm. These target cuts ensure that the fiducial volume is selected. The impact of this vertex cut on the data is shown in Figure 56 for the longitudinal primary vertex distribution in Z . Also the transverse primary vertex distribution in X and Y is shown. The weighted sum of the target material adapted to the analysis cuts is $\rho_{\text{target}} = 2.64 \cdot 10^{25} \text{ cm}^{-2}$. Unfortunately, the target cells were not completely filled so that the homogeneous material distribution is not correct. With the target cuts, parts with lower density are excluded, leading to an additional systematic uncertainty.

6.3.2.2 The 2009 Liquid Hydrogen Target

In 2009, the target material used during the DVCS run was liquid hydrogen (H_2), contained in a 40 cm long mylar cell with a diameter of 35 mm. The H_2 was provided by CERN, and has according to the specifications a chemical purity of 99.9%. Contaminations of *e.g.* hydrogen deuterid (HD) are negligible. The target cut is determined from the primary vertex distribution. Figure 57 shows all vertices without cuts. A radial cut of 1.6 cm is chosen. With a larger

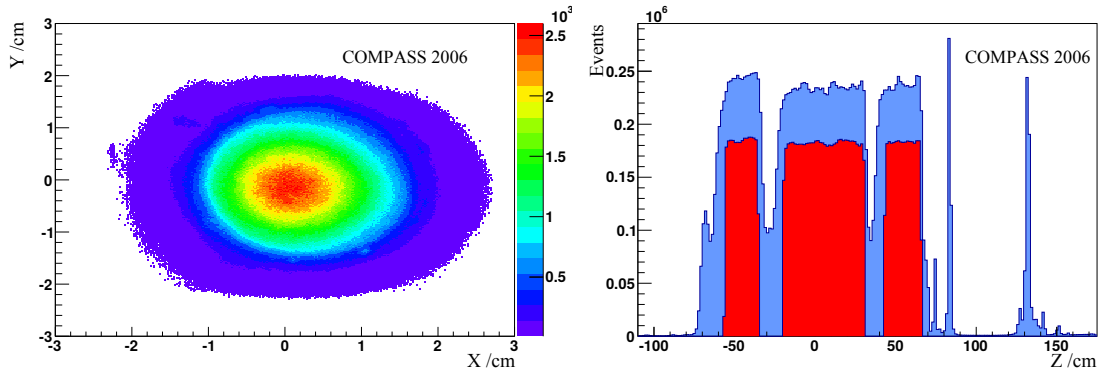


Figure 56: Primary vertex distribution of the ${}^6\text{LiD}$ target used in 2006 in the COMPASS reference frame. **Left:** Primary vertex distribution perpendicular to the beam, in the X,Y plane. **Right:** Z projection. In red: vertex distribution with all target and kinematic cuts applied. In blue: only kinematic cuts applied. The peaks between 75 cm and 150 cm are vertices in tracking detector (SI04).

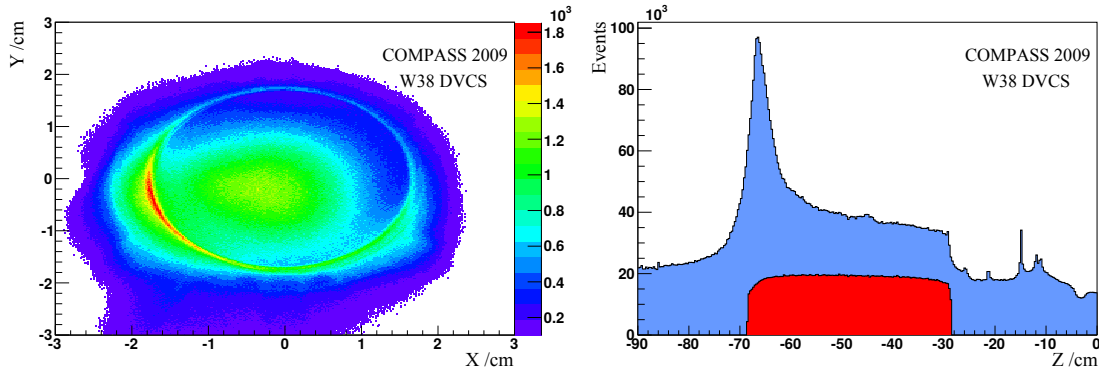


Figure 57: Primary vertex distribution of the lH_2 target used in 2009. **Left:** Primary vertex distribution in the X,Y plane, perpendicular to the beam. The elliptical shape is the stainless steel target holder ring. **Right:** Z projection. In red: vertex distribution along the beam with all target and kinematic cuts applied. The peak at -68 cm is coming from the target holder ring.

radial cut, muons would hit the stainless steel ring of the target holder. The longitudinal target cut corresponds to the target cell length and position, $Z \geq -68.4$ cm and $Z \leq -28.4$ cm. The typical target temperature in 2009 was 18 K at 1020 mbar. The molar density of lH_2 for this temperature and pressure is $0.0363 \frac{\text{mol}}{\text{cm}^3}$ [73]; for the atomic hydrogen, the number has to be multiplied by 2. The final target area density of the 2009 liquid hydrogen target for the selected target cuts is $1.75 \cdot 10^{24} \frac{\text{nucleons}}{\text{cm}^2}$.

A possible source of error is the production of hydrogen bubbles generated by energy deposition of the beam inside the target cell. The COMPASS target group monitored the pressure during in- and off-spill periods and no evidence for a significant pressure fluctuation could be found. The size of the systematic uncertainty is discussed in Section 6.3.5.1.

6.3.3 Scaler Method in 2006 and 2009

The first method of flux determination is using a fast and efficient detector in the beam telescope. The particle rate is counted by a scaler system. The number of measured incident particles has to be corrected in case the detection area is larger than the target. For physics

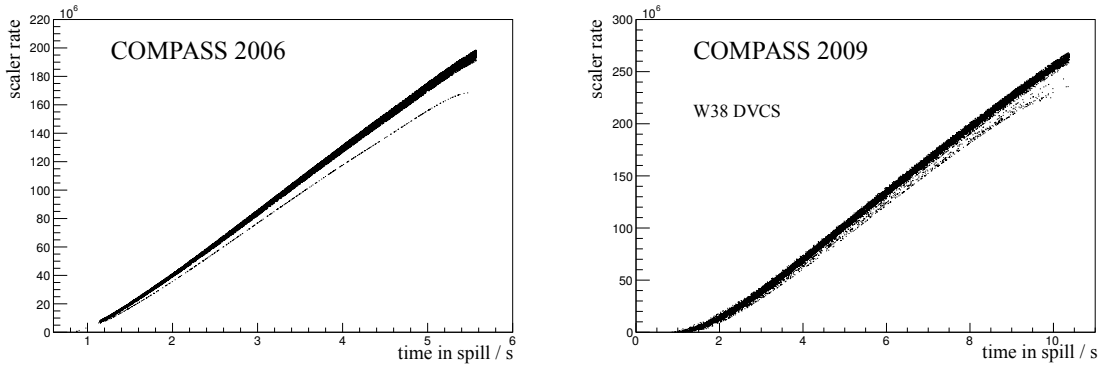


Figure 58: **Left:** Scaler rate vs. time in spill of the run 52959 (2006). **Right:** Same plots for the 2009 data (run 79652).

data, the DAQ and the veto dead time have to be taken into account. For this method, a scintillating fibre detector named FI02 station is used.

6.3.3.1 Scintillating Fibre and Scaler

The detector FI02 is introduced in Section 3.2.2. For this study, only the X projection of the detector is used. It has 96 channels and is read out by six multi-anode PMT. The anodes of the six 16-channel MAPMT are read out by a scaler system, which is gated by the DAQ. The scaler saves the number of hits per MAPMT on an event-by-event basis, so for each trigger the scaler entries can be extracted. A detailed description of the scaler system is given in [74]. Figure 58 shows an example of the scaler rate over time-in-spill for a run of 2006 (left) and 2009 (right). As expected, the scaler rate rises over time-in-spill. In this scatter plot, lines can be made, which correspond to one spill of the given example run. From this Figure, the length of the spill can be seen: 4.8 s in 2006 and around 10 s in 2009.

By summing up the 6 scaler entries of the last event in the spill, the total number of detector hits in the FI station is extracted. The integrated scaler rate for each spill of the chosen example run (2006 and 2009) is shown in Figure 59. The example run from 2006 (run number 52959) has 100 spills with around $1.9 \cdot 10^8$ muons per spill. The example run of 2009 (run number 79652) has around 200 spills with some empty spills and spills with lower intensity. The average scaler rate per spill is around $2.6 \cdot 10^8$ muons per spill. For the luminosity determination, the integrated flux is needed. For that, the integrated scaler rate of each spill is summed up.

6.3.3.2 Correction Factors

As the FI02 detector is larger than the target, the rate has to be corrected to match the size of the target. The active area of the FI station is rectangular with a size of $4 \times 4 \text{ cm}^2$, while the target area is round. Depending on the year, a different radial target cut is used. To obtain this correction factor, the data of the corresponding year is examined by looking at the muon tracks in front of the target. The incident muon tracks with a hit in the FI02 detector are counted (T_{FI}). Then, the number $T_{\text{FI,target}}$ of muon tracks with at least one hit in FI02 and an extrapolated track through the full target length are counted. The ratio of these two numbers leads to the geometric correction factor G :

$$G = \frac{T_{\text{FI,target}}}{T_{\text{FI}}}. \quad (56)$$

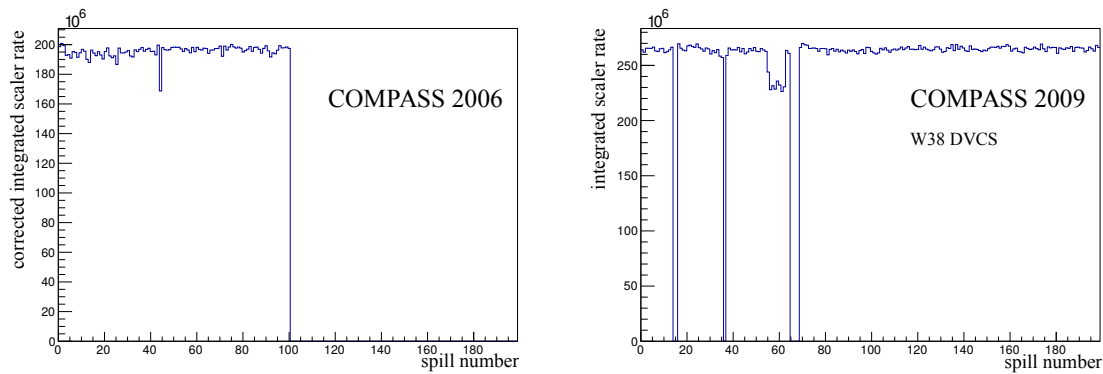


Figure 59: **Left:** The integrated scaler rate of each spill vs. the spill number in the run 52959 (2006). **Right:** Same plots for the 2009 data (run 79652).

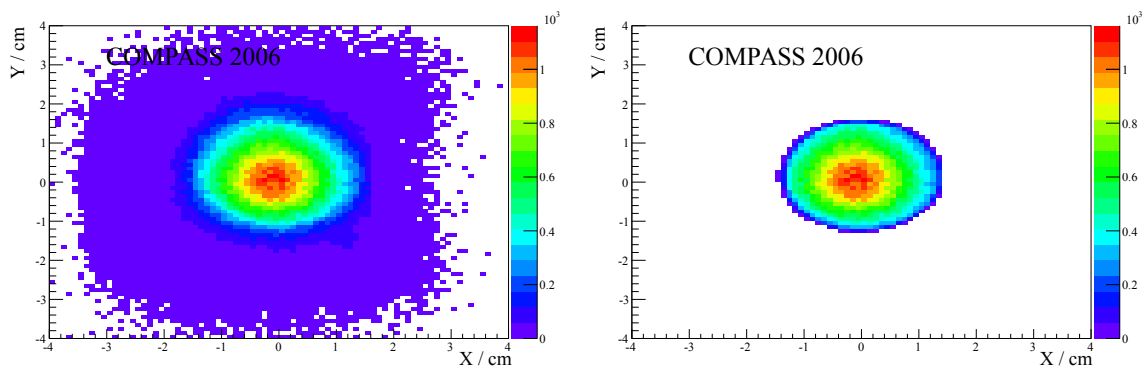


Figure 60: Illustration of the geometric correction factor G for 2006. **Left:** XY position of the incident muons with a hit in the fibre station FI02. **Right:** XY position of incident muons with hit in FI02 and the track passes the all target cells.

In Figure 60, the determination of the correction factor G is illustrated. The left side shows the hit distribution of the incident muons on FI02, and the rectangular shape of the detector is visible. On the right side, only muon tracks passing through the full target (with the target radial cut used in the analysis) are accepted. The integrated scaler rate has to be multiplied by G , which is done on a spill-by-spill basis. In 2009, this geometric correction G is obtained using the Random Trigger to select the incident muons.

In 2006, too few Random Trigger events were recorded, so that the unbiased method with the Random Trigger could not be applied. Instead, all physics triggers were used to obtain the geometric correction G . In addition, for both cases, a reconstructed momentum is required. This corrects for the inefficiency of the BMS. The two plots in Figure 61 show the geometric correction factor G for an example run for the 2006 and the 2009 data. In 2006, the correction is constant and about 0.79. In 2009, the correction factor G is also constant and is about 0.83. The difference of the correction between the years is due to the different radial target cuts (1.4 cm in 2006 and 1.6 cm in 2009), the different target length and due to slightly different settings of the beam line. To obtain the final flux, the veto and the DAQ dead time have to be taken into account. Figure 62 shows the corrected scaler rate for an example run for the two years 2006 and 2009. Note that the 2009 data is also corrected for time-in-spill due to the data quality requirements in the analysis. The time-in-spill cut is introduced in the next Section and ranges from 2 s to 10 s.

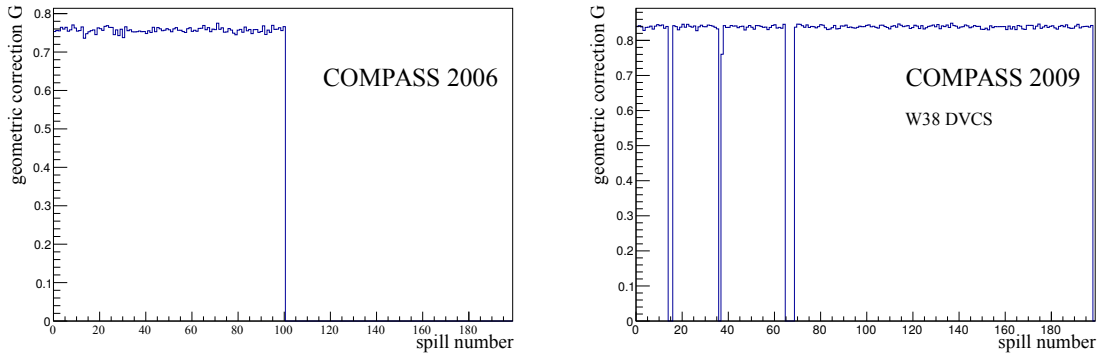


Figure 61: **Left:** Geometric correction factor G for the year 2006 (52959). **Right:** Geometric correction factor G for the year 2009 (79652).

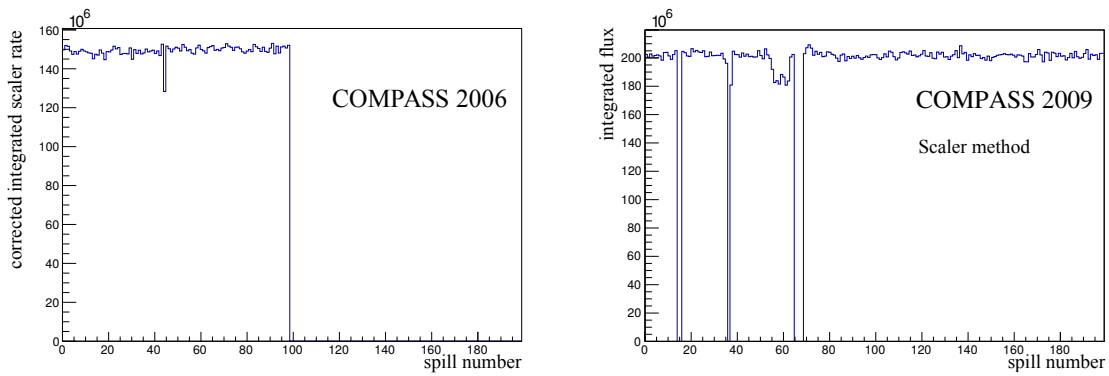


Figure 62: **Left:** The corrected integrated scaler for run 52959 of the 2006 data taking. **Right:** The corrected integrated scaler for the run 79652 (2009).

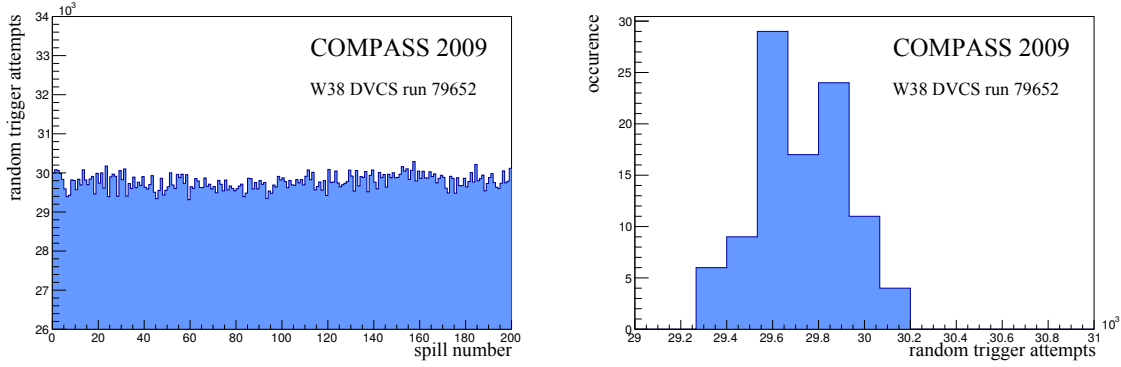


Figure 63: **Left:** True Random Trigger attempts for Run 79652 of 2009. **Right:** Projection of the trigger attempts.

6.3.3.3 Result

The integrated flux for the 2006 run with the scaler method is $1.7083 \cdot 10^{13}$ with an average flux of $1.6 \cdot 10^8$ muons per spill. With a target density (LiD) of $2.64 \cdot 10^{25} \text{ cm}^{-2}$, this yields a total integrated luminosity of 0.54 fb^{-1} .

The shorter 2009 run with the liquid hydrogen target has an integrated luminosity of 3.8 fb^{-1} . The average integrated flux per spill is around $1.6 \cdot 10^8$. The shorter and lighter liquid hydrogen target had an area density of $1.75 \cdot 10^{24} \frac{\text{nucleons}}{\text{cm}^2}$.

As the scaler method solely depends on one detector, it is dependent on the stability of FI02 and the scaler system. The systematic uncertainties for the scaler method is 10 % [75] and [76].

6.3.4 The True Random Trigger Method 2009

For the physics programs where absolute cross sections are measured, a precise luminosity with a systematic uncertainty of a few percent only is needed. The alternative method of flux determination with the scaler system uses a randomly distributed trigger signal [77]. The particle rate R -or the flux- is calculated by counting the number of beam tracks N_μ , the number of Random Trigger attempts N_{RT} and the time window Δt in which tracks from the Random Trigger are reconstructable by the software:

$$R = \frac{N_\mu}{N_{RT} \cdot \Delta t}. \quad (57)$$

It is important to note the difference between trigger attempts (number of triggers delivered to the DAQ) and accepted triggers (number of processed triggers). One advantage of this method is that the obtained flux only needs to be corrected for the veto dead time. The DAQ dead is included in this method, as the Random Trigger is subjected to the same DAQ dead time as all the physics triggers.

The setup of the Random Trigger is shown in Section 4.1.4. In 2009, the rate of random trigger attempts was set to $\approx 3 \text{ kHz}$. This rate is high enough to calculate the incident flux with a statistical error of 2.1 % per spill. The trigger attempts are counted by a scaler system and are saved in the COMPASS database. In some cases, the trigger information was missing in the database, the average number of trigger attempts for the data taking period is then used. The rate of random trigger attempts is stable over a data taking period. The stability of this trigger is shown for a representative run (79652) of the 2009 data taking in Figure 63.

6.3.4.1 Track Time Window Δt and Beam Track Selection

The time gate width Δt for track reconstruction of the Random Trigger is given by the reconstruction software CORAL, which is in the CORAL option file of the production. The software-wise introduced cut is set to 10 ns. To investigate the distribution of Δt , the time of each reconstructed beam track is determined with the detectors of the beam telescope (two scintillating fibre and six silicon stations) and is the weighted mean of the measured times. The weight is given by the time resolution of the beam telescope detectors. The track time is measured with respect to the trigger time⁴. For a physics trigger, a peak centered around 0 ns is expected. The incident muon time is measured and subsequently the scattered muon fires the triggers, if the beam track belongs to the event. For the Random Trigger, a flat distribution is expected; the tracks are randomly distributed in the time window Δt of ± 5 ns.

The time window during which the DAQ accepts trigger signals to define one event is 25 s. If a physics trigger overlaps with a random trigger, the track time is given by the physics one. The time information of the random trigger is lost. Only events in which the random trigger is the time defining trigger (Master Trigger) are selected⁵ for the flux determination. In any case, the coincidence rate between the Random Trigger and physics trigger is very low (<1 %). Figure 64 shows the track time for the different cuts of the beam track selection. The blue coloured histogram shows the beam track time distribution after all beam track selection cuts. One clearly sees the flat and consequently random track time distribution. The beam track time Δt is approximately ± 5 ns, as set in the reconstruction. On the edges of the histogram, at -5 ns and +5 ns, the threshold effect from the reconstruction is visible. To reduce this edge effects, a track time cut of ± 2 ns is applied. This introduced cut and uncertainty is discussed in Section 6.3.5.2.

Figure 64 right shows the time-in-spill distribution of beam tracks selected with the random trigger distribution for W38. The beam rate rises at 0.4 s and saturates around 2 s. The period with an almost constant rate is called flat-top. In the last half second of the spill, the rate drops until the DAQ stops recording events at 10.4 s. A time-in-spill cut from 2 s to 10 s is chosen, where the beam flux in the experiment is constant. This assures that all detectors have the same load and that various correction factors are constant over the spill. The veto dead time, for instance, was only measured as average over the spill. This time-in-spill cut also has to be applied to the number of random trigger attempts. Random Trigger attempts from the radioactive source are counted when the DAQ is active, which is between 0.2 and 10.4 s, so just before beam tracks are recorded. To calculate the flux according to Equation (57), the number of attempted random triggers has to be scaled to the time-in-spill cut. This reduces the attempts by 21.6 %.

The beam tracks from the Random Trigger are selected with the same requirements than beam tracks in the physics analysis: a beam track in front of the target with a reconstructed momentum. The extrapolated beam track has to cross the full target length and the two time cuts (time-in-spill and track time) are applied:

- True Random Trigger Bit set (as Master Trigger),
- Hits in FI01 and FI02,
- Track has a reconstructed momentum,
- Extrapolated track crossing the target,
- Track time Δt cut ± 2 ns,

⁴ with the PHAST function PaTrack::Meantime()

⁵ with the PHAST function PaEvent::MasterTrigMask()

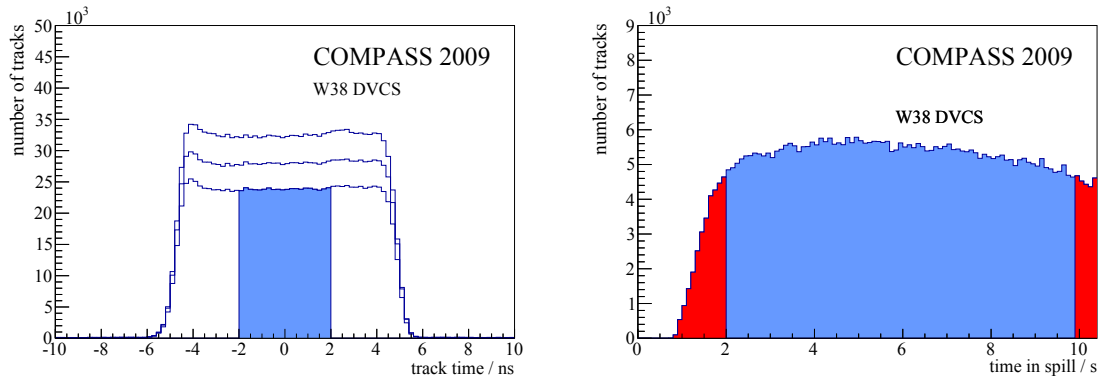


Figure 64: **Left:** Shows the track time Δt for the different cuts of the beam track selection. The tracks within the blue area are used for the flux determination. **Right:** Time-in-spill distribution of beam track selected with the Random Trigger, the red area is rejected due to the time-in-spill cut.

- Time-in-spill > 2.0 s and < 10.0 s.

The statistics reduction is summarized in Figure 65 with the corresponding table. Applying all the cuts, in average 2400 beam tracks per spill for a positive muon beam are obtained. In addition, beam momentum is required to be between 140 GeV/c and 180 GeV/c. This cut rejects only a few tracks in some spills.

The incident muon rate for each spill is calculated using the number Random Trigger attempts (30000), the size of the track time window (± 2 ns) and the number of beam tracks (around 2400). To obtain the integrated muon flux per spill, the muon flux rate is multiplied by the time-in-spill (8 s). The final result and the comparison to the scaler method are shown after data quality and the systematic studies.

6.3.4.2 Data Quality Checks

A clean data sample is mandatory for precise measurements: half empty spills, spills with detector errors and other possible instabilities have to be excluded. Those faulty spills are registered in a "badspill list" and excluded from the analysis. A special PHAST userevent is used to check the stability of different quality variables (various kinematics and detector specific quantities) for time stability. For the 2009 DVCS data, three different groups of quality control were:

- Flux, Event per flux, primary vertices per flux and reconstructed beam momentum,
- Stable response of the ECALs,
- Stable trigger conditions.

The data quality checks are done for each data taking period (W38, W39 and W40) of the 2009 data taking. The average of the quality variables is determined within a range of neighbouring spills and then compared to each individual spills. If the deviation of one of the quality criteria of a spill is outside a set deviation, the spill is marked as bad. The fine tuning is done by changing the two input parameters: the number of neighbours and the deviation criteria can be set independently for the three quality control groups. Figure 66 shows, as an example, one of the quality criteria for the data taking period W38. The number of primary vertices per incoming muon is shown for each spill. The red points are spills excluded from the analysis. One clearly sees in this figure a problem with the data: the number of primary vertices per incident muon is much larger than in the rest of the data taking period.

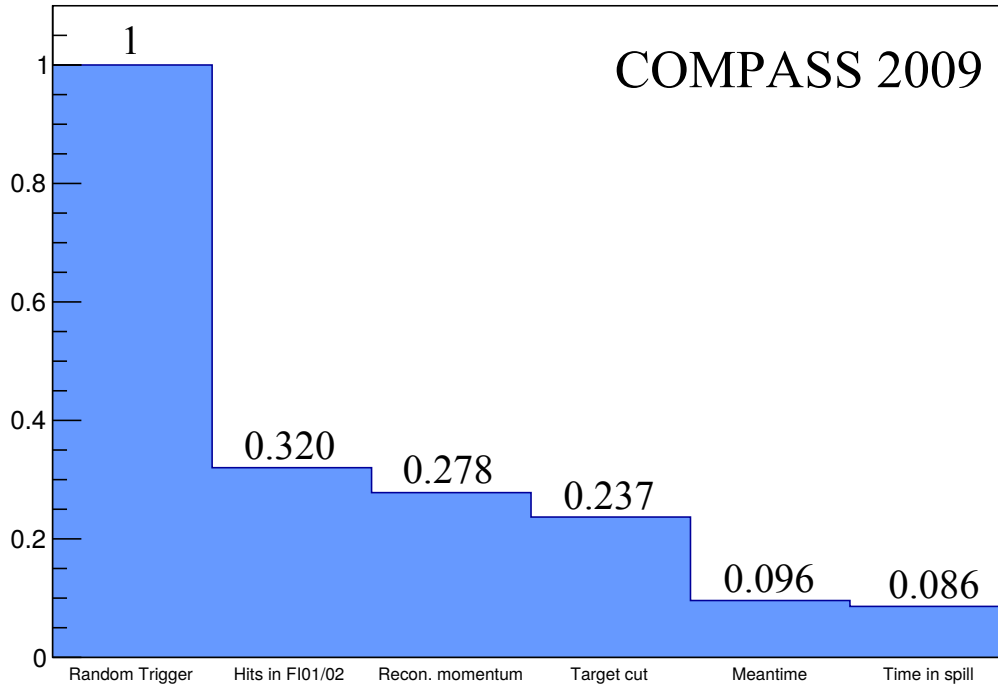


Figure 65: Statistics reduction for random beam track selection. The numbers denote the percentage of the tracks after each cut.

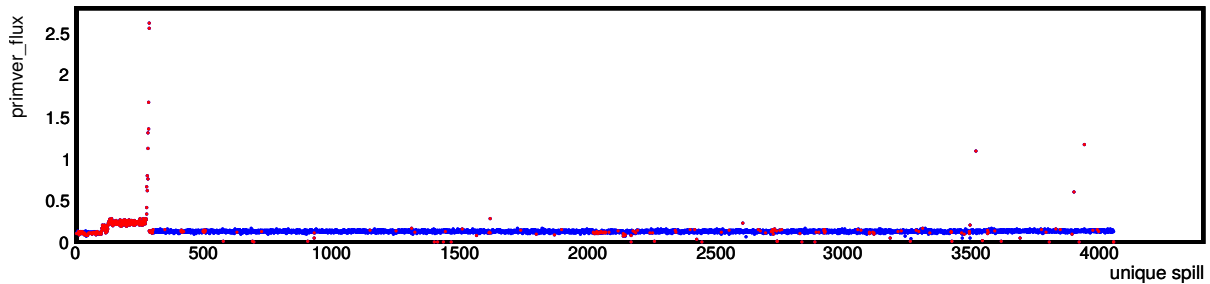


Figure 66: The number of primary vertex per incoming flux for each spill of W38. The points in red are included into the bad spill list.

Figure 67 shows the number of neighbouring spills for a fixed deviation parameter of 3σ . It was decided to use the 3σ cut within 200 neighbouring spills for determination of the bad spills of the 2009 data. In addition, a table with the fraction of rejected spills for each data taking period is displayed. The rejection fraction is 8 % for W38 and 7 % for W40. The larger rejection factor of W39 is due to a detector issue in the beam telescope.

6.3.4.3 K_0 Mass Stability

With the clean decay of a K_S^0 into two pions with opposite charges, the spectrometer can be checked for stabilities. The neutral kaon candidates are selected for each run and period with the following data cuts. A primary vertex is required inside the target with an associated incident muon and a scattered muon. A secondary vertex, separated by at least 2σ of the precision of the primary vertex measurement, with two outgoing particles of opposite charge, is also required. The pion mass is assumed for the two final-state particles. The invariant mass

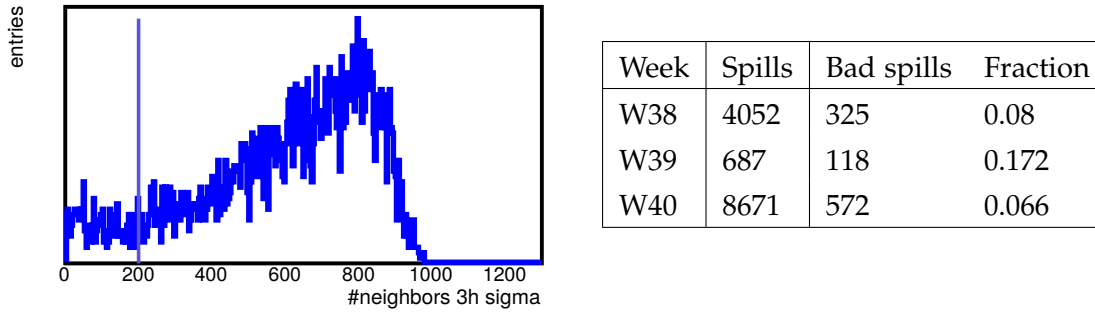


Figure 67: **Left:** Number of neighbouring spills within a deviation of 3σ of the average. The blue line indicates the cut on number of spill neighbours used in the analysis. **Right:** Summary of the fraction of the rejected spills of the 2009 data taking.

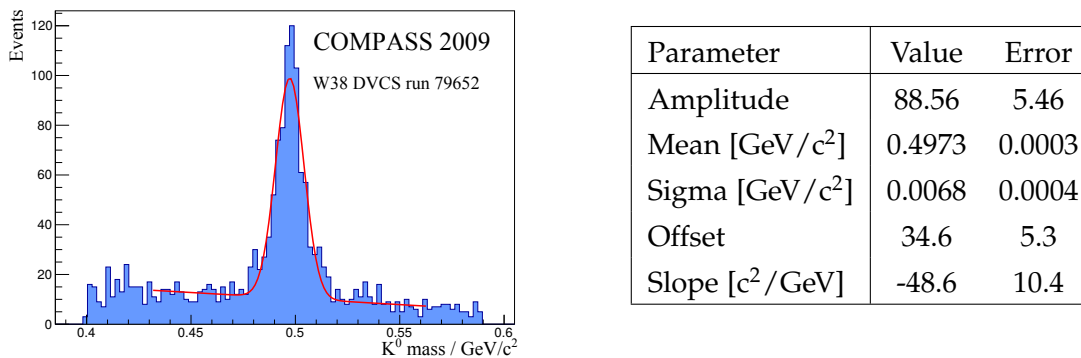


Figure 68: Invariant 2π mass for run 79652 of W38. The red line indicates the fit: a gaussian with a linear background is used. The corresponding results are shown in the table.

of the two pions is obtained with the two four-vectors. To further localise the K^0 , an invariant mass range between 0.4 and 0.59 GeV/c^2 is chosen. Figure 68 shows the invariant 2π mass distribution for one run (79652) of W38. The expected peak on the K^0 mass is seen, over a background contribution. A separated fit to determine the K^0 mass is performed for the data of each run. For the fit, a gaussian signal with a linear background is used.

In Figures 69 and 70, the fitted K^0 mass for each run is shown. For a data taking period, the fitted invariant mass is stable. Only a few runs have a large deviation from the expected value (497.614 ± 0.022 [8]) or have large statistical errors. Runs with larger deviation point towards a problem in the spectrometer. In both cases, these runs are excluded from the analysis. The criteria is that the fit result of the invariant mass is between 0.495 GeV/c^2 and 0.5 GeV/c^2 and that the width of the mass fit is smaller than 0.0025 GeV/c^2 . The result for W39 is not shown here, as this data taking period only contains very few runs.

6.3.5 Statistical Uncertainties and Systematic Studies

The number of reconstructed beam muons is large due to the number of random triggers per spill. With 30000 random triggers and roughly 2400 muons, the statistical uncertainty is 2% per spill. For each full data taking period, the statistical errors are thus negligible and the uncertainties are dominated by systematics. For example: after the quality checks, there are 7676303 (17717827) beam muons selected with the Random Trigger in W38 (W40) of 2009, yielding 0.036% (0.023%) statistical uncertainty. In W39, only 6 runs were taken, with 758318

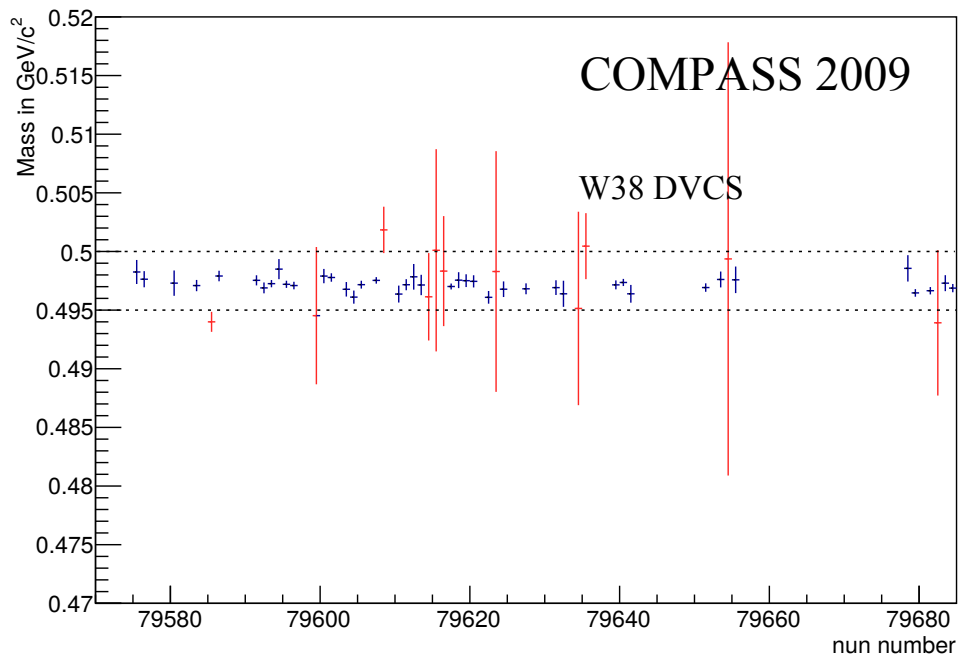


Figure 69: Results of the K^0 mass fit for each run in W38. The red points are excluded due to too large errors or too large deviation from the expected K^0 mass.

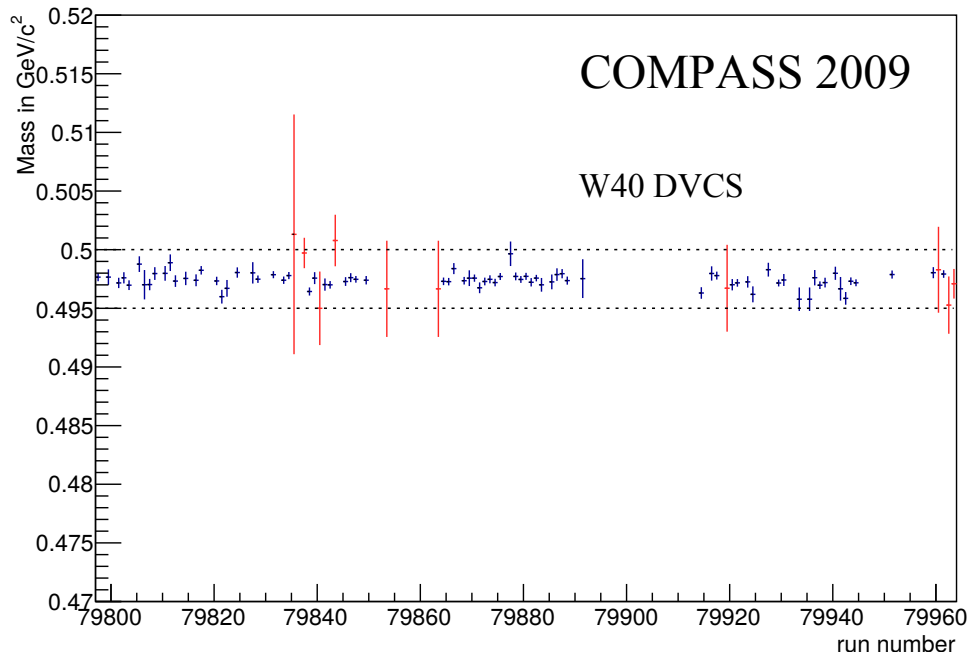


Figure 70: Results of the K^0 mass fit for each run in W40. The red points are excluded due to too large errors or too large deviation from the expected K^0 mass.

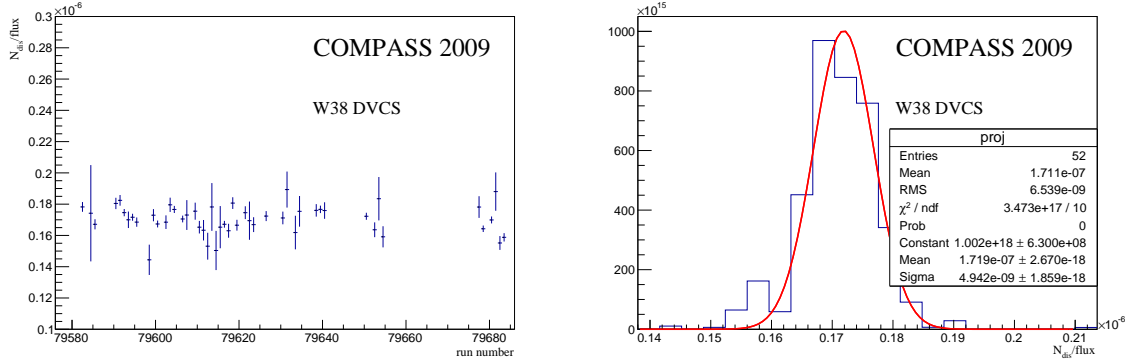


Figure 71: **Left:** Number of DIS events divided by the flux and corrected for the veto dead time, for each run of W38. This number is proportional to the target density. The badspill list is applied. **Right:** Projection of target density with a Gaussian fit.

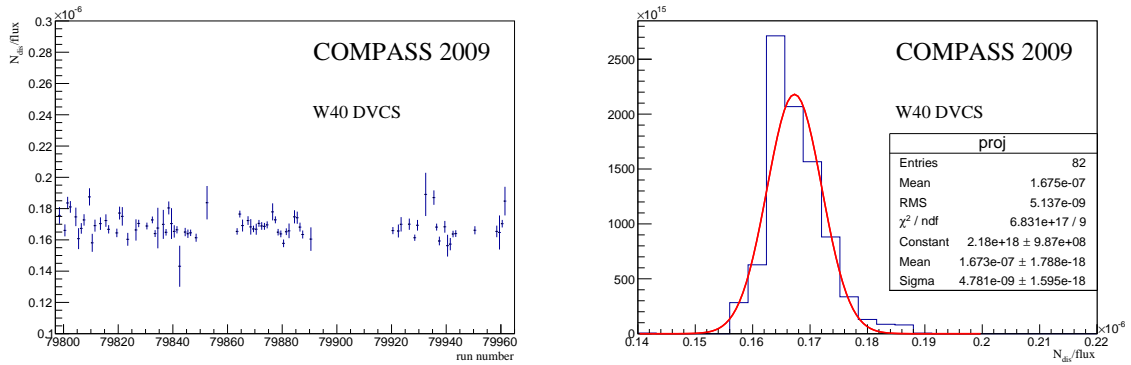


Figure 72: **Left:** Number of DIS events divided by the flux and corrected for the veto dead time, for each run of W40. This number is proportional to the target density. The badspill list is applied. **Right:** Projection of target density with a Gaussian fit.

beam muons detected, one obtains a statistical uncertainty of 0.145 %. In the next Section, the major sources of systematic uncertainties are discussed.

6.3.5.1 Cross Section Stability and Target Density

During the 2009 data taking, the monitoring of the liquid hydrogen target was limited to the measurement of temperature and pressure. The precision of this measurement was not suitable to check for the time stability. The DIS cross section can be used to test the target density ρ_{target} .

$$\sigma = \frac{N_{DIS}}{\phi \cdot \rho_{\text{target}} \cdot A \cdot L_{\text{Veto}}} \rightarrow \kappa = \frac{N_{DIS}}{\phi \cdot L_{\text{Veto}}} \propto \rho_{\text{target}} \quad (58)$$

According to Equation 58, the number of scattered muons N_{DIS} , the target density ρ_{target} , the integrated flux ϕ , the veto life time L_{Veto} and the acceptance correction are needed to calculate the cross section σ . By rearranging the Equation, the variable κ is obtained, which is proportional to the target density ρ_{target} . The number of DIS events N_{DIS} is determined with the following cuts: an incoming muon with reconstructed momentum is required, as well as a scattered muon. The interaction vertex has to be inside the target material. The kinematic requirements are $Q^2 > 0.001$ and $0.2 < y < 0.85$ and only Middle Trigger events are used. The integrated flux ϕ is determined with the Random Trigger Method for each run. From the remaining factors, only the veto life time L_{Veto} is used: the acceptance A , the

cross section σ and smaller corrections are regarded as constant over the data taking period and therefore disregarded (set to 1) for this exercise. The DAQ life time is not needed to calculate the cross section, as it is included in the flux ϕ and N_{DIS} . The veto dead life time (1 - veto dead time) is extracted from the database and is measured with the Middle Trigger (see Section 4.3.4). The variable κ is shown for each run with statistical errors in Figures 71 and 72 and is supposed to constant. By checking the stability of κ , the systematic uncertainty coming from the target density and the luminosity determination method is checked. The projection is shown, weighted with statistical errors ($1/\sigma^2$) and a Gaussian fit is performed. The ratio of the mean and the RMS is used to estimate the uncertainty. The systematic uncertainty obtained with this method is 3.7% for W38 and 3.06% for W40. The larger number is used for the final luminosity uncertainty.

6.3.5.2 Track Time Symmetry

The track time window used for the random beam track selection is tested for its symmetry and flatness. This demonstrates the randomness of the random trigger and an unbiased time distribution of the track. This test is done for W38 and W40. The numbers of beam tracks selected with the random trigger are plotted versus different track time window Δt cuts (in steps of 0.5 ns) and divided by the width of the corresponding time window. A flat distribution is expected. Figures 73 and 74 show that the ratio is flat (with only a small slope) up to 3 ns. The slope then increases stronger till 4.5 ns. The maximum range of 3% is shown in the figures. The maximum difference between the bin with a width of ± 0.5 ns to the bin with a width of ± 4.5 ns has a spread of 1.4%. A systematic uncertainty of 0.7% for the meantime window selection can be assumed from half of the maximum spread. For the analysis, a track time window of ± 2 ns is used.

6.3.5.3 Beam Momentum Reconstruction Efficiency

The incoming muon momentum is required in the physics analysis to calculate the kinematic variables. For the flux determination, the same requirements on the incoming muons are applied. It is tested if the beam momentum reconstruction efficiency is constant for beam tracks reconstructed with the Random Trigger over the track time window Δt . By comparing random beam tracks with and without reconstructed beam momentum, this reconstruction efficiency is obtained. Figures 75 and 76 show the beam momentum reconstruction efficiency as a function of the track time for W38 and W40 (the error bars are not displayed). The momentum reconstruction efficiency is around 0.9 (0.89) at a track time of 0 ns for W38 (W39). The efficiency drops to minimum at ± 3 ns in both weeks. When moving further out towards ± 5 ns, the efficiency seemingly rises. But this rise is not significant, as at the edges of this time distribution the statistics drops to zero (compare with Figure 64). The difference of the maximal reconstruction efficiency at 0 ns to 2 ns (the cut used in the analysis) is used to estimate the systematic uncertainty for the beam momentum reconstruction efficiency. The uncertainty is assumed to be 0.5%.

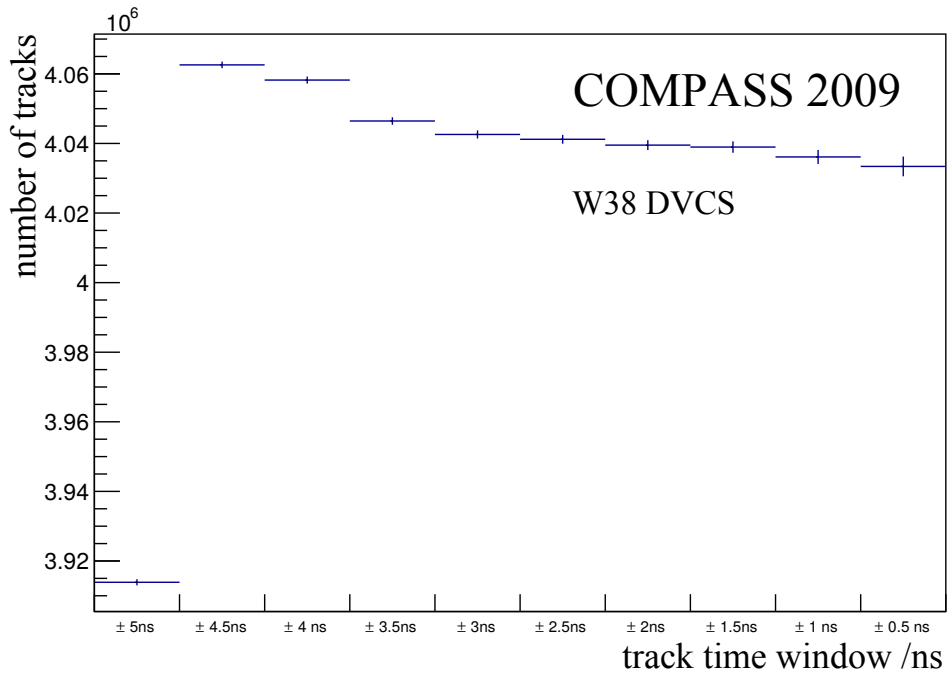


Figure 73: Sum of all beam tracks for W38 for different track time cuts divided by the track time window.

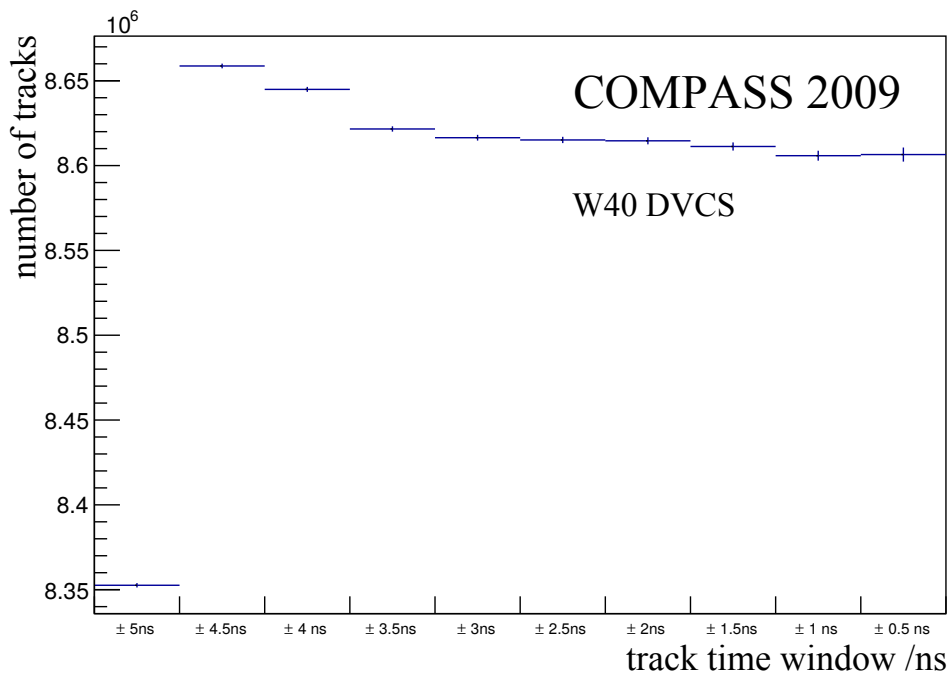


Figure 74: Sum of all beam tracks for W40 for different track time cuts divided by the track time window.

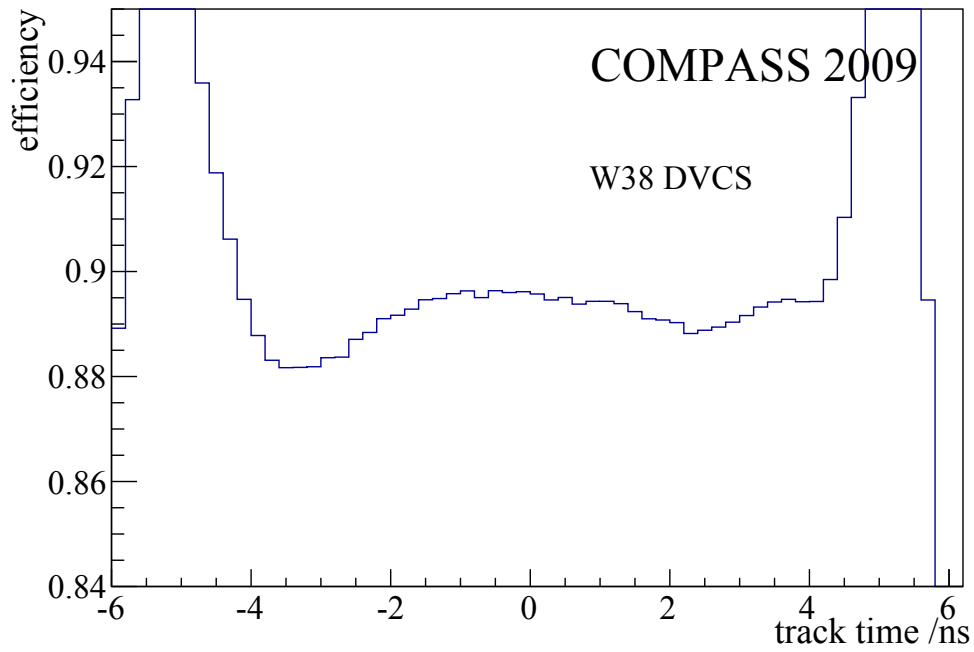


Figure 75: Momentum reconstruction efficiency of random beam tracks as a function of the mean time for W38.

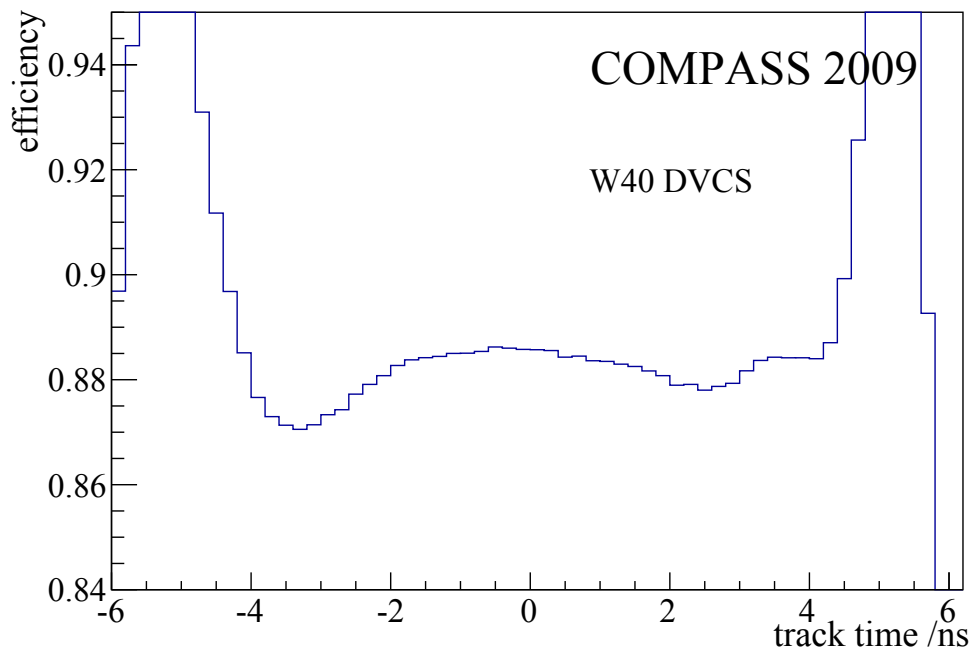


Figure 76: Momentum reconstruction efficiency of random beam tracks as a function of the mean time for W40.

	Integrated flux	Luminosity (pb^{-1})
W38	$6.70 \cdot 10^{11}$	1.17
W39	$6.53 \cdot 10^{10}$	0.11
W40	$1.47 \cdot 10^{12}$	2.58
Sum	$2.21 \cdot 10^{12}$	3.86

Table 6: Luminosity result for the 2009 run separated for each week of data taking.

6.3.5.4 Result

Figure 77 shows the integrated flux of the example run 79652 taken during the DVCS 2009 data taking for both methods: the scaler method (left) and the Random Trigger method (right). The integrated flux is around $2.0 \cdot 10^8$ beam particles per spill. It shows features such as empty spills and spills with lesser intensity. At a first look, the Random Trigger flux looks more jittery than the one determined with the scaler method. But with the Random Trigger, the reconstructible flux is measured; it underlies the whole reconstruction chain of CORAL as beam muon of physics trigger do. Therefore, the Random Trigger flux matches better the physics events.

The 2009 data set consists of 3 periods W38, W39 and W40. The result of the integrated luminosity is given in Table 6 and add to a total of 3.86 pb^{-1} with the target density of $1.75 \cdot 10^{24} \frac{1}{\text{cm}^2}$. This luminosity is only valid for the cuts applied in the determination: the requirement on the incoming muons and the same data set has to be used by excluding bad spills and runs. Some changes, *e.g.* a longitudinal target, can easily be corrected. The total systematic error is the quadratic sum of the uncertainties due to the target density, the track time window and the beam momentum reconstruction efficiency, and amounts to 5%. Using this luminosity for a cross section measurement requires the application of the veto dead. In 2009, the veto dead was measured to be on average of 31% with a systematic uncertainty of 2%.

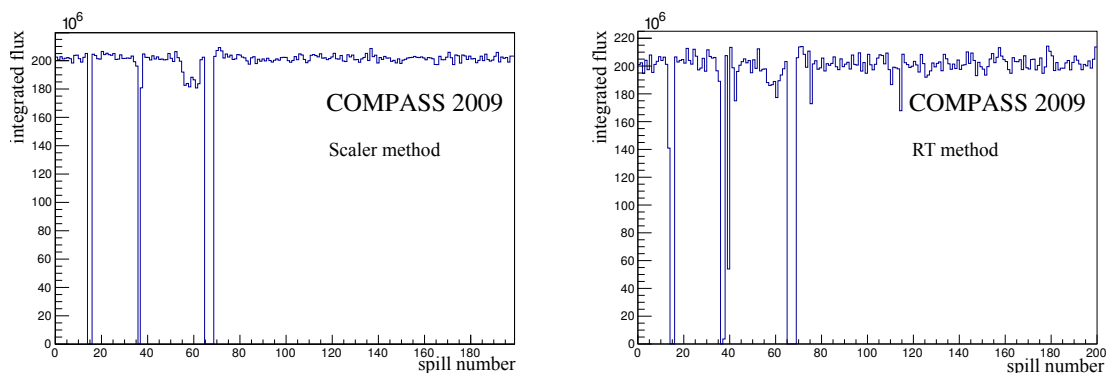


Figure 77: **Left:** Integrated flux per spill of the run 79652 taken during the DVCS test run 2009. **Right:** Integrated flux of the same run with the Scaler Method.

II

THE 2006 MULTIPLICITY ANALYSIS

DETERMINATION OF THE 2006 RAW MULTIPLICITIES

The charged hadron multiplicities are determined from data collected in 2006 with a 160 GeV muon beam and an isoscalar lithium-deuterid target. The first steps of the analysis, the raw multiplicities are determined. The multiplicities are calculated by the number of hadrons N^h normalised by the numbers of DIS events N^{DIS} as a function of z and bins of x and y . The Q^2 dependence from Equation 43 is replaced by photon energy fraction y ; the change of the variables allows for a better treatment of the data and a better description in the Monte Carlo. The word *raw* means that only corrections on an event-by-event basis are applied. These include radiative corrections and the correction for the hadron identification efficiency.

7.1 PARTICLE IDENTIFICATION WITH THE RICH

For the determination of the charged pion and kaon hadron multiplicities, the final-state hadrons have to be identified. This identification process is done offline, using the information provided by the RICH detector for each reconstructed track. For that, the tracks are extrapolated to the position of the RICH and correlated to the photon distribution. In Figure 78, the Cherenkov angle is shown as a function of the hadron momentum. This figure is not used in the analysis, but serves as an illustration. Four characteristic bands stand out for electron, pions, kaons and protons. A closer look also reveals a muon band which is smeared into the pion band because of the similar masses.

- The detection threshold for pions T_π is $\sim 3 \text{ GeV}/c$,
- The kaon threshold T_K is $\sim 8 \text{ GeV}/c$,
- The proton threshold T_p is $\sim 18 \text{ GeV}/c$,
- Pions and kaons can be distinguished up to $40 \text{ GeV}/c$,
- Background contribution outside the characteristic bands,
- Electrons at low momenta.

A mathematical method is necessary to distinguish the different particle types taking into account the background signal.

7.1.1 Likelihood

The particle identity by determining the ring radius is hindered by several problems. Only a few photons of the Cherenkov light are detected, the rings are not fully visible and the radius might not be obvious. Overlapping rings from other particles make it difficult, specially the constant presence of photon rings from the scattered muons. Additional photons coming from particles without reconstructed tracks, *e.g.* halo muons or cosmics, create background that has to be taken into account. As an example, the two-dimensional photon distribution

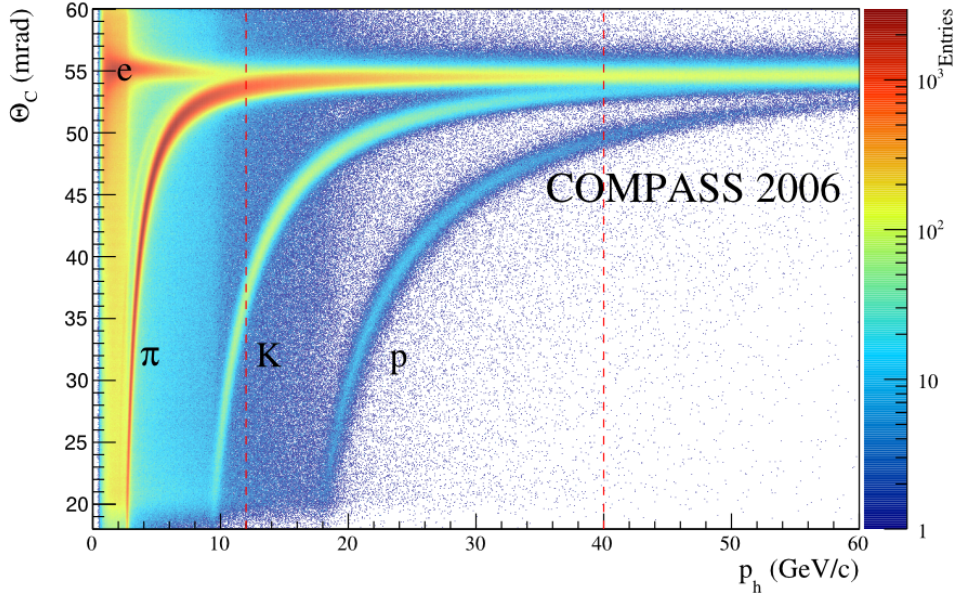


Figure 78: Cherenkov angle as a function of the hadron momentum. The four characteristic bands correspond to e , π , K and p . The red lines indicate the hadron momentum cut ($12 \text{ GeV}/c < p_h < 40 \text{ GeV}/c$) done in the multiplicity analysis.

and the radial photon distribution for one hadron candidate (proton) is shown in Figure 79. The red lines indicate the expected circles for pions, kaons and protons for this particle. The small yellow squares indicate the position of measured photons. The left figure shows the radial photon distribution for the same proton candidate. Black lines at 40 cm, 50 cm and 55 cm indicate the expected radii for protons, kaons and pions.

Instead of fitting rings, likelihoods [78] for each relevant particle are determined from the radial photon distribution. The center of the circle is calculated from the reconstructed track parameters. The charged particle track is extrapolated to the RICH detector to determine the point of impact and the entrance angle θ . The angle distribution of all Cherenkov photons with respect to the track position is measured. The likelihood L_N with the total numbers of photons N is described by

$$L_N = \prod_{k=1}^{N^{\text{photon}}} \left[(1 - \epsilon) G(\theta_{\text{rec},k}^{\text{photon}}, \phi_{\text{rec},k}^{\text{photon}}) + \epsilon B(\theta_{\text{rec},k}^{\text{photon}}) \right]. \quad (59)$$

This likelihood is described in [79] and consists of a Gaussian signal distribution $G(\theta_{\text{rec},k}^{\text{photon}}, \phi_{\text{rec},k}^{\text{photon}})$ and a linear background contribution $B(\theta_{\text{rec},k}^{\text{photon}})$. The background fraction ϵ is determined from a Monte Carlo simulation. The Gaussian distribution $G(\theta_{\text{rec},k}^{\text{photon}}, \phi_{\text{rec},k}^{\text{photon}})$ in the $(\theta^{\text{photon}}, \phi^{\text{photon}})$ plane is given for a fixed ϕ^{photon} angle. The Cherenkov photon angle Θ_{mass} is used and is calculated for each mass hypothesis with the refractive index of the RICH gas [80]. The standard deviation is given by $\sigma_{\text{rec},k}^{\text{photon}}$.

$$G(\theta_{\text{rec},k}^{\text{photon}}, \phi_{\text{rec},k}^{\text{photon}}) = \frac{1}{\sigma_{\theta,k}^{\text{photon}} \sqrt{2\pi}} \exp\left(-\frac{1}{2} \frac{(\theta_{\text{rec},k}^{\text{photon}} - \Theta_{\text{mass}})^2}{(\sigma_{\theta,k}^{\text{photon}})^2}\right) \frac{\theta_{\text{rec},k}^{\text{photon}}}{\Theta_{\text{mass}}} \quad (60)$$

For the background coming from electronic noise of the RICH photon detector, a linear contribution

$$B(\theta_{\text{rec},k}^{\text{photon}}) = \frac{2}{(\Theta_M)^2} \theta_{\text{rec},k}^{\text{photon}} \quad (61)$$

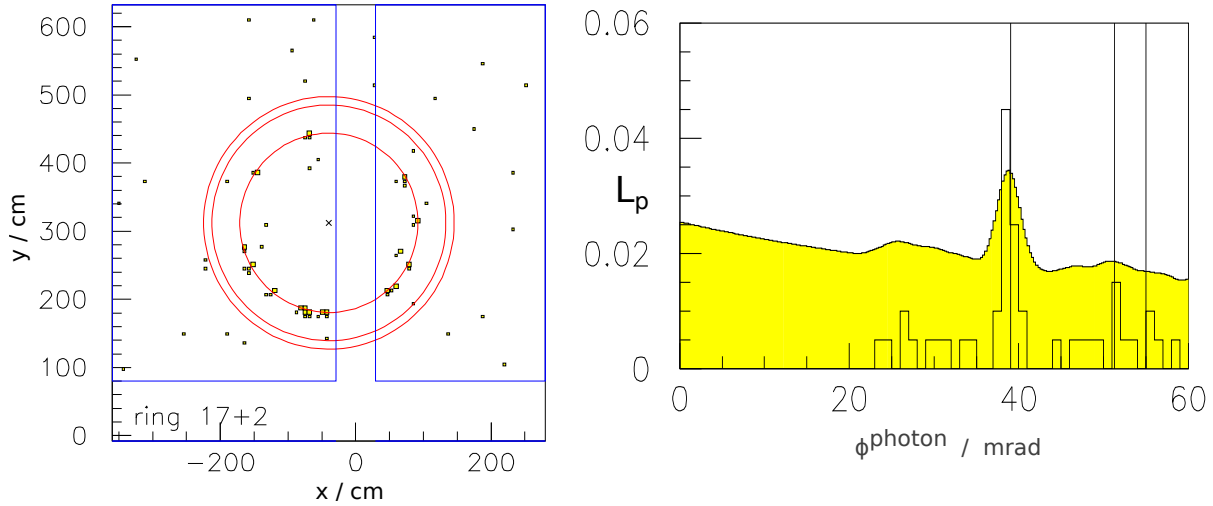


Figure 79: **Left:** Distribution of Cherenkov photons relative to the track impact point from an identified proton. Measured photons are shown as yellow squares. **Right:** Likelihood distribution for the proton hypothesis L_p according to Equation 59 with the angular distribution of photons superimposed. The π , K and p hypothesis are shown as circles (left) and lines (right).

is assumed. It depends on the photon angle $\theta_{\text{rec},k}^{\text{photon}}$ and Θ_M , the upper limit of the range of the photon rings (70 mrad). The likelihood is normalised to the number of photons. To compare the likelihoods of different particles, the likelihood is normalised to the numbers of photons: $L = \sqrt[N]{L_N}$. A set of likelihoods for each mass hypothesis (LH_π , LH_K , LH_p , LH_{bg} and LH_e) is calculated and is available for data analysis. The identification of muons is done already in the track reconstruction, as discussed in Section 3.4.3.1.

7.1.2 RICH Efficiency

The detector itself and the identification methods have inefficiencies. With only a few photons, the likelihood for a certain hadron might not be significant. A kaon can be misidentified as a pion, if the two circles cannot be distinguished. As seen in Figure 79, the pion and kaon hypothesis rings are close together. Due to this misidentification, the number of measured hadron type needs to be corrected to obtain the true numbers of this hadron types. The RICH efficiency is determined from real data and typically done for each year. For this, particle decays into two final-state particles are used: $K_S^0 \rightarrow \pi^+\pi^-$ for pion, $\Lambda^0 \rightarrow p\pi^-$, $\bar{\Lambda}^0 \rightarrow \bar{p}\pi^+$ for proton and anti-proton and $\phi \rightarrow K^+K^- + X$ for kaon efficiencies. The efficiency is determined in real data by selecting an event topology matching those decays with a hadron pair in the relevant mass range. The type of one decay particle is determined, which fixes the type of the second particle. The detector response is checked for the second particle. The identification or misidentification efficiency ϵ is given by:

$$\epsilon(t \rightarrow i) = \frac{N^{t \rightarrow i}}{N^t} \quad (t, i = \pi, K, p) \quad (62)$$

where $N^{t \rightarrow i}$ denotes the number of particles t identified as particle i and N^t is the total number of measured particles. The number of particles is extracted by an extended likelihood fit [81] on the invariant mass distribution. To obtain the correct numbers, the background needs to be understood and taken into account, either by fitting of a background parametrisation or by subtraction with the side-bin method. For the K_S^0 decay, a double Gaussian fit with a polynomial background function is used. The two Gaussians correspond to the two reconstruction resolutions of the two spectrometer parts of the COMPASS experiment. For the ϕ

decay, a convolution of a Gaussian and a Breit-Wigner function is used to parametrise the signal. A background function describing the threshold effect is used (an exponential and a power function). The signal of the two lambda decays ($\bar{\Lambda}$ and Λ) is fitted with two Gaussian functions and the same background function of the ϕ decay. The uncertainty is obtained from the covariance matrix of the fit, taking into account the correlation matrix of the fit parameters.

With pions, kaons and protons, this leads to a 3x3 efficiency matrix as seen in Equation 63. With a perfect working detector and reconstruction, the diagonal elements are close to 1.

$$M = \begin{pmatrix} \epsilon(\pi \rightarrow \pi) & \epsilon(K \rightarrow \pi) & \epsilon(p \rightarrow \pi) \\ \epsilon(\pi \rightarrow K) & \epsilon(K \rightarrow K) & \epsilon(p \rightarrow K) \\ \epsilon(\pi \rightarrow p) & \epsilon(K \rightarrow p) & \epsilon(p \rightarrow p) \end{pmatrix} \quad (63)$$

To obtain the true number of hadrons \vec{T}_h corrected for the RICH efficiency, the RICH matrix M has to be inverted and multiplied to the vector \vec{I}_h of identified hadrons

$$\vec{N}^t = M^{-1} \vec{N}^i \text{ with } \vec{N}^i = \begin{pmatrix} \pi \\ K \\ p \end{pmatrix}. \quad (64)$$

For each element $\epsilon(h \rightarrow h')$, an error is calculated in the fitting process. The uncertainties determined for the RICH matrices have to be propagated correctly through the matrix inversion. The error is

$$\sigma_h^2 = \text{cov}(M_{hr}^{-1}, M_{hr}^{-1}) + (M_{hr}^{-1})^2, \quad (65)$$

where M_{hr} is the element of the RICH efficiency matrix with the corresponding inverse (M_{hr}^{-1}) for the hadron h and the identified hadron r , reconstructed by the RICH. The covariance is taken into account with

$$\text{cov}(M_{hr}^{-1}, M_{ab}^{-1}) = M_{hi}^{-1} M_{jr}^{-1} M_{hk}^{-1} M_{lr}^{-1} \text{cov}(M_{ij}, M_{kl}). \quad (66)$$

A full derivation of error propagation for matrix inversion is shown in [82]. With the high identification efficiency of the RICH, the efficiency matrix is close to a diagonal unity matrix. The contribution from the covariance to the error are very small.

7.1.3 Event Selection 2006

For the determination of the RICH matrices, the full year 2006 is used. The matrices are calculated in bins of the hadron momentum P_h and the hadron entrance angle θ . After rejection of bad spills, the best primary interaction vertex is selected. For the ϕ decay, additional outgoing particles with opposite charges are selected. For the weak decaying particles (K^0 , Λ and $\bar{\Lambda}$), a secondary vertex with two outgoing particles with opposite charges is required. The outgoing particle energy is limited to the range 2 GeV/c to 70 GeV/c. Tracks passing the detector in the central part are cut out with a radial cut of 5 cm to suppress signals coming from the incident muons. Two additional kinematical cuts are applied: the distance between the primary and secondary vertex has to be larger than 2σ of the vertex precision and a collinearity cut is applied ($\cos\theta > 0.9996$ for the K^0 and $\cos\theta > 0.9999$ for the lambda baryons). The transverse momentum of the Λ has to be larger than 0.25 GeV/c to suppress the electron background contribution.

7.1.4 RICH Particle Identification with Likelihoods

In the easiest case, the largest likelihood leads to the identification. But in cases where only a few Cherenkov photons are detected, the likelihoods of the different hypotheses become similar. The hadron momentum cut used in the analysis is $12 \text{ GeV}/c < p_h < 40 \text{ GeV}/c$: the minimal momentum lays above the kaon detection threshold. The electron contribution starts at very low momenta and smears into the μ/π band. It can only be distinguished up to a few GeV/c , thus at low momenta L_e is also calculated. Fluctuations of the refractive index (temperature and pressure of the gas volume) and thus the Cherenkov angle are monitored by the COMPASS RICH group and used in the calculation of the likelihoods. To identify particles with the RICH, the likelihoods for each particle are compared. The cuts on the likelihoods are discussed and motivated in [83]. The determination of the final likelihood cuts is an iterative process, compromising between efficiency and purity. The same likelihood cuts below have to be used for identification of hadron candidates in the charged multiplicity analysis and in the determination of the RICH efficiencies. There are 5 likelihoods LH_i : e for electron, π for pion, K for kaons, p for proton and bg for background. The second largest likelihood is denoted by $i = 2\text{cd}$.

1. If $LH_e > 1.8 LH_i$ all five hypotheses LH_e, LH_π, LH_K, LH_p and LH_{bg} are used.
If $LH_e < 1.8 LH_i$ only LH_π, LH_K, LH_p and LH_{bg} are used.
This cut is applied to reduce electron contribution; if the electron likelihood is not clearly the largest, the likelihood LH_e is disregarded.

2. Pion selection

- LH_π must be the largest
- $\frac{LH_\pi}{LH_{2\text{cd}}} > 1.02$
- $\frac{LH_\pi}{LH_{bg}} > 2.02$

3. Kaon selection

- LH_K must be the largest
- $\frac{LH_K}{LH_{2\text{cd}}} > 1.08$
- $\frac{LH_K}{LH_{bg}} > 2.08$

4. Proton selection: the identification of protons in the momentum range between 12 and 40 GeV is special because the detection threshold is in the middle of the momentum range. This is taken into account using the following procedure:

- a) for momenta below proton threshold: kaon threshold $< p_h <$ proton threshold - 5 GeV/c

p	\bar{p}
Not identified as π or K	
$\frac{\pi}{bg} < 2.2$	$\frac{\pi}{bg} < 2.1$
$\frac{K}{bg} < 2.9$	$\frac{K}{bg} < 2.8$
Or all $LH_i = 0$	

- b) Above proton threshold: $p_h > T_p + 5 \text{ GeV}/c$

- LH_p must be the largest
- $\frac{LH_p}{LH_{2\text{cd}}} > 1$

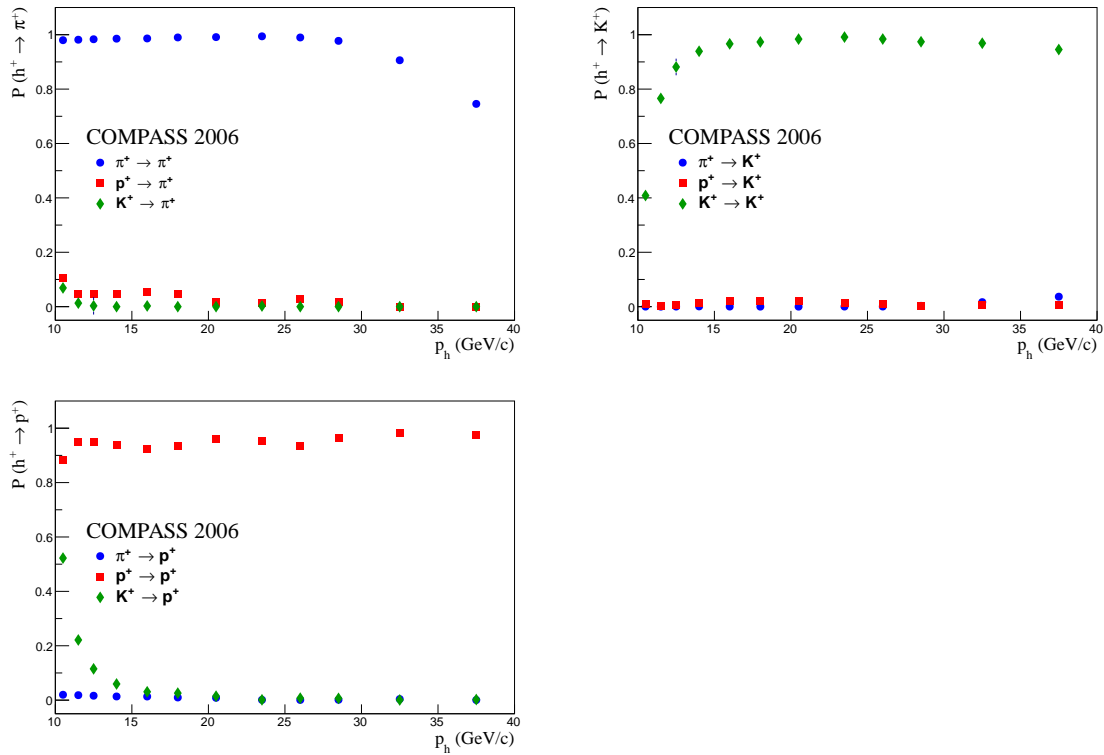


Figure 80: Result of the RICH efficiency determination for positive hadrons in the first θ bin 0.01 - 0.04.

- c) Around P threshold: $T_p - 5 \text{ GeV}/c < p_h < T_p + 5 \text{ GeV}/c$
 – Both a) and b) are applied

For the proton identification, one distinguishes between protons and anti-protons and a different likelihood cut is used due to the different signal height. The number of produced \bar{p} is smaller. The condition that all likelihoods are zero for a particle track is interpreted as a proton entering the RICH below the detection threshold T_p and no Cherenkov photons are emitted. The proton threshold T_p is calculated by the refraction index and is in average $17.95 \text{ GeV}/c$. For the calculation of the likelihoods in CORAL, the current refraction index (depending on temperature and pressure) is used.

7.1.5 RICH Matrix 2006

The efficiency was calculated for different bins of the hadron momentum p_h and the RICH entrance window angle θ . The dependence of the momentum is stronger than θ , therefore the RICH matrices are calculated for 10 hadron momentum bins p_h and 2 θ bins:

- p_h bins in GeV/c : 12, 13, 15, 17, 19, 22, 25, 27, 30, 35, 40
- θ bins in rad : 0.01, 0.04, 0.12.

The results for positive hadrons (π , K and p) are shown in Figure 80 for one θ bin. The RICH matrices for positive and negative hadrons are very similar. The identification efficiency is overall very high (>98%). The misidentification is in most bins below 5%, except for kaon to proton misidentification at low momenta between $12 \text{ GeV}/c$ and the detection threshold of protons at $18 \text{ GeV}/c$. The systematic uncertainties are checked with different likelihood cuts and range between 1% and 15%, depending on the momentum and the type of hadrons.

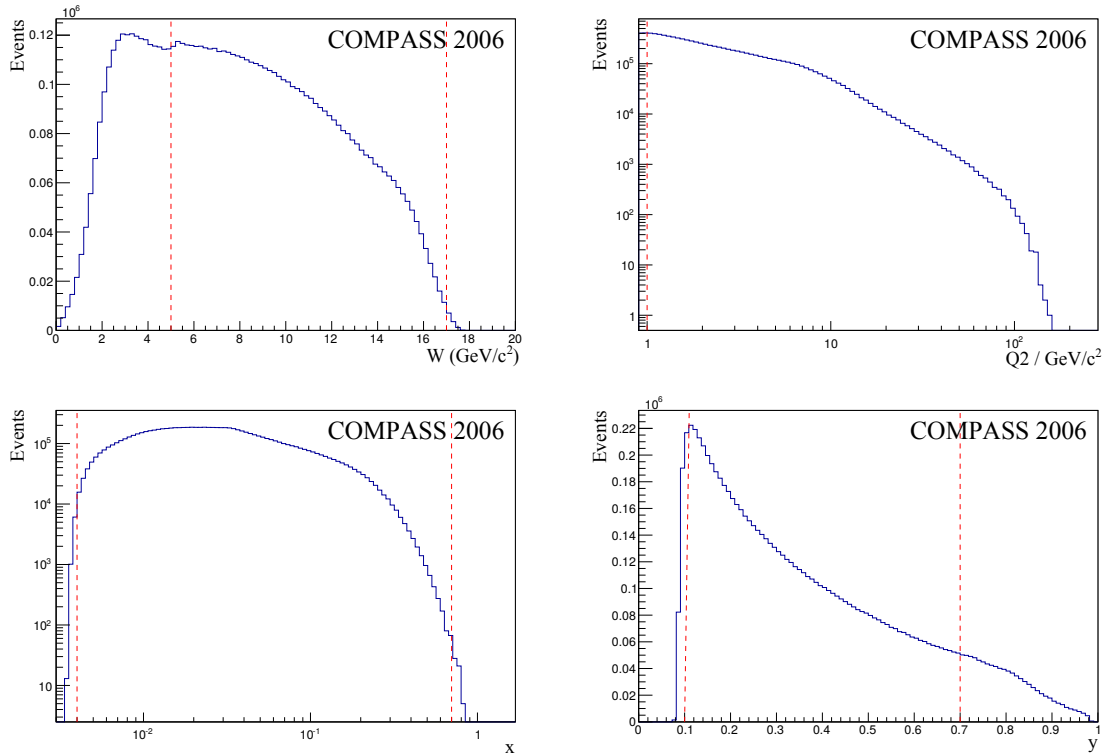


Figure 81: Inclusive kinematic variables: the invariant mass W , the four-momentum transfer Q^2 , the Bjorken scaling x and relative photon energy y for the 2006 data taking. The red dotted lines indicate the cuts used in the analysis.

7.2 DATA SET

The 2006 data were taken with a 160 GeV/c positive muon beam using a polarised lithium-deuterid target (${}^6\text{LiD}$). From this data, six weeks are used for the multiplicity analysis, which are reconstructed with the same CORAL version.

- W40 (run 52921-52931)
- W41 (run 53217-53231)
- W42 (run 53459-53468)
- W43 (run 53756-53760)
- W45 (run 54341-54356)
- W46 (run 54627-54663)

After quality checks and rejection of bad spills, 68101 non-empty spills are used for the following analysis. Figure 81 shows the inclusive kinematics of the 2006 data, namely the four-momentum transfer Q^2 , the Bjorken scaling variable x , the relative photon energy y and the invariant mass W . In each figure, the cut applied in the multiplicity analysis is shown with a red dashed line.

Figure 82 shows the hadron kinematics: the hadron momentum p_h , the hadron energy fraction z , the azimuthal hadron angle θ and the transverse hadron momentum p_t . All kinematic plots are displayed with the kinematic cuts of the analysis, except the cut on the shown quantity. The red lines indicate the cuts used in the DIS event selection and the hadron selection.

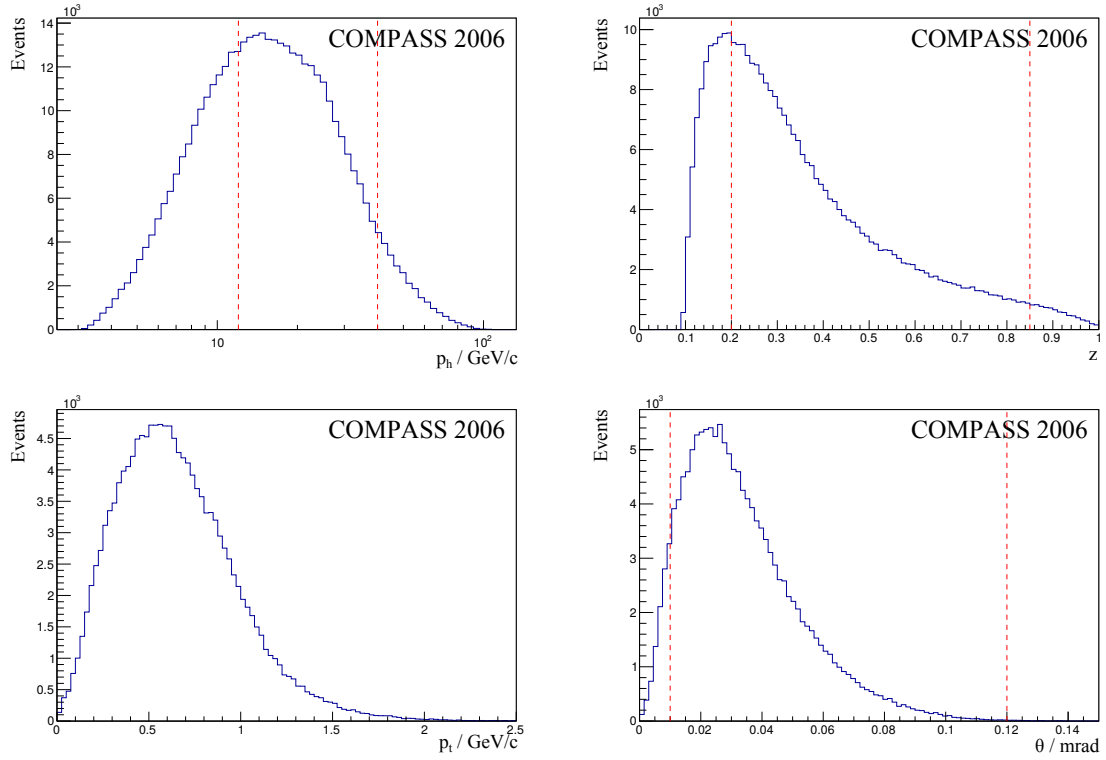


Figure 82: Semi-inclusive kinematic variables for the 2006 data taking: the hadron momentum p_h , the hadron energy fraction z , the transverse hadron momentum p_t and the azimuthal hadron angle θ_h . The red dotted lines indicate the cuts used in the analysis.

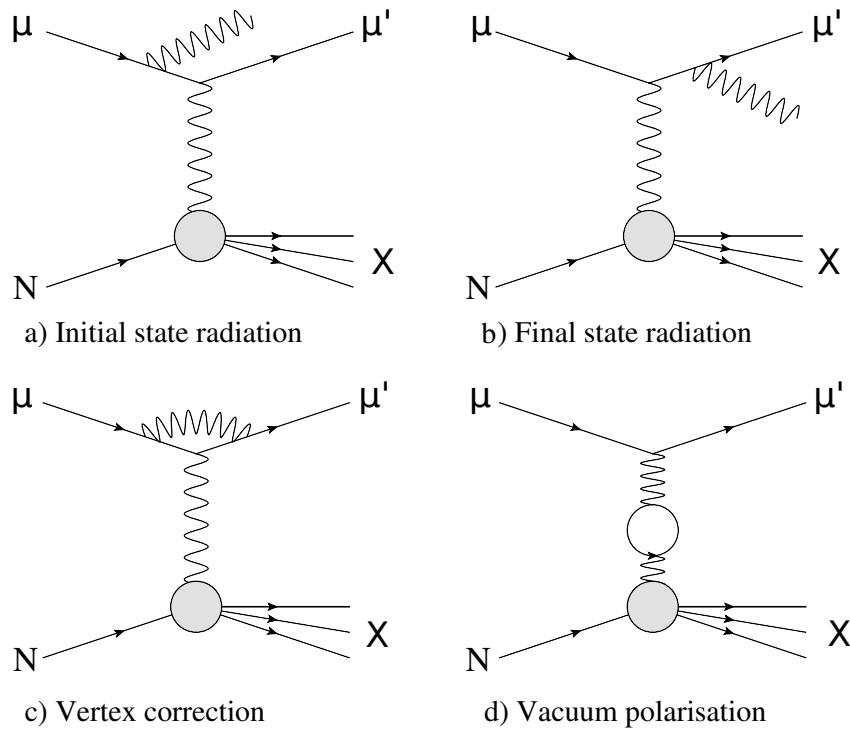


Figure 83: Possible QED radiative effects in inclusive deep inelastic scattering.

7.2.1 Radiative correction

For the extraction of PDFs and FFs one-photon cross section $\sigma_{1\gamma}$ are needed. In first order ($\mathcal{O}(\alpha)$), the DIS process is well described by the exchange of one virtual photon. The illustration of the DIS process in Figure 1 in Chapter 2 shows the scattering of a muon by the exchange of one virtual photon. But when measuring the real processes, not only the one-photon exchange is observed and processes involving more photons have to be taken into account. Figure 83 shows the most prominent effects of higher order, *e.g.* the radiation of a photon in the initial a) or the final state b) [84]. Furthermore, a photon can be emitted by the incident particle and be reabsorbed by the scattered one c). Another possibility is the vacuum polarisation, where the virtual photon creates an intermediate charged fermion anti-fermion pair d). Experimentally, only the incident muon and the scattered muon are measured, most of the other photon remain undetected. The measured kinematics of the muon do not reflect the true ones when an additional photon carries energy away. Higher orders of radiative events involve more photons and the number of possible processes is larger, but their contribution decreases. The radiative corrections depend on the type of lepton, on the target material and on the kinematic range.

To compare results between experiments, the cross sections are published in terms of the one-photon exchange. Therefore, the measured cross sections or DIS events are corrected for these higher order processes by radiative corrections by the correction factor

$$\eta(x, y) = \frac{\sigma_{1\gamma}}{\sigma_{\text{measured}}}. \quad (67)$$

In Figure 1, sample of higher order processes are shown for the inelastic case. But also in the elastic and the quasi-elastic case, Bremstrahlung can be emitted in the initial or final state. The elastic contribution are include in the radiative correction. In semi-inclusive deep inelastic scattering, besides the scattered muon, an additional hadron is measured. With the additional observation of the hadron, the process cannot be elastic. In this case, the radiative correction are modified as the elastic and quasi-elastic part do not contribute. One distinguishes between inclusive radiative corrections and semi-inclusive radiative corrections.

For this analysis, the radiative corrections (both inclusive and semi-inclusive) are calculated with the program TERAD [85], [86] and [87] and were adapted to the kinematic range of COMPASS [88]. The corrections are available in the analysis program PHAST (for a given x , y and specification of the used target material) and are calculated to the order α^4 . In Figure 84, the inclusive and semi-inclusive radiative corrections are shown as a function of y for three different x bins for the COMPASS kinematic range and an isoscalar LID target. The red dashed lines indicate the y cut used in the 2006 multiplicity analysis. In both cases, the radiative corrections decrease with increasing y and x . In the range $0.2 < y < 0.7$, the variation of the radiative corrections are about 10%.

For the determination of charged hadron multiplicities, radiative corrections are applied. Each DIS events is corrected by the inclusive radiative corrections η_{incl} , while each hadron is corrected by the semi-inclusive radiative corrections η_{semi} .

7.3 RAW MULTIPLICITIES

The raw multiplicities are the pure experimental results and calculated by the ratio of the number of hadrons and DIS events. The only corrections applied are the inclusive radiative correction for the DIS events, the semi-inclusive one for the hadron candidates and the cor-

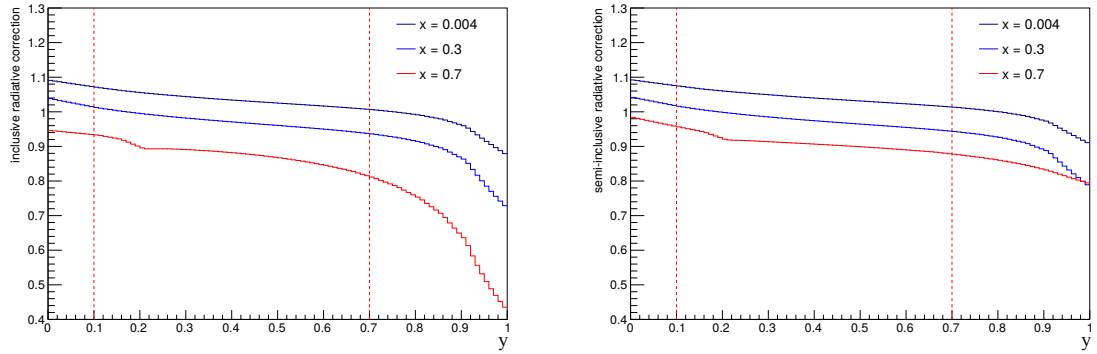


Figure 84: **Left:** Inclusive radiative correction as a function of y for three different x bins. The red-dashed lines indicate the y cut used in the multiplicity analysis. **Right:** Semi-inclusive radiative correction with the same binning as for the inclusive one.

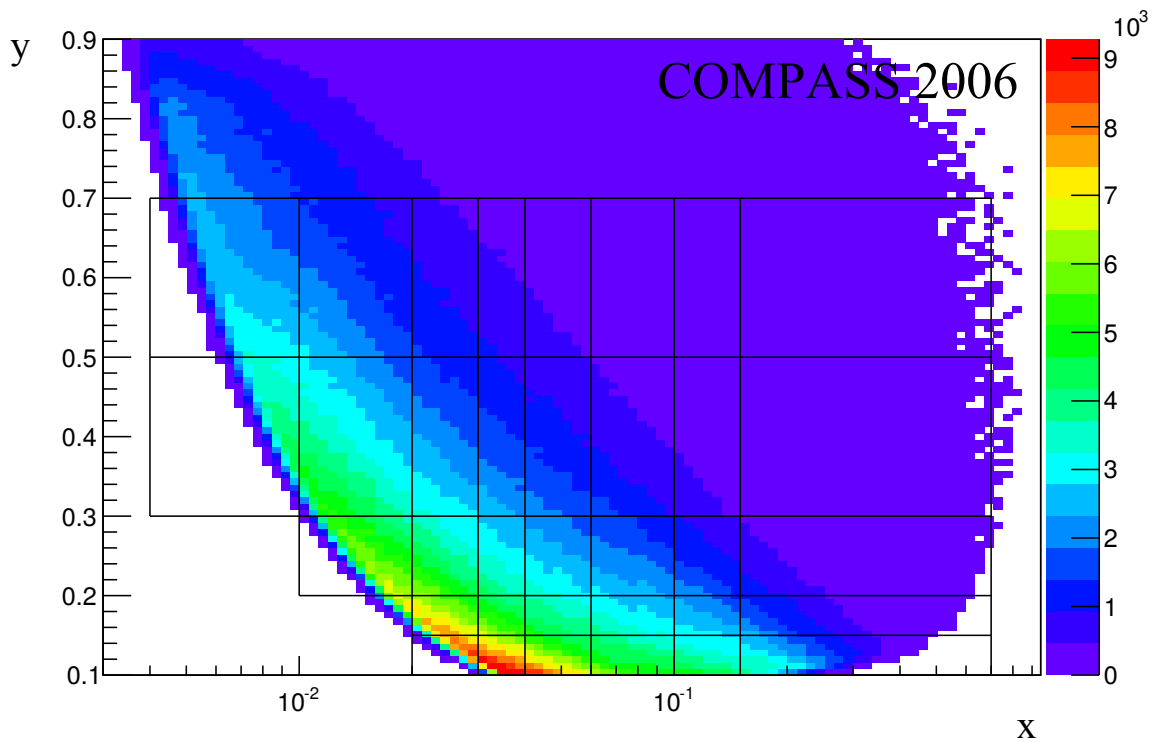


Figure 85: The inclusive kinematic plane of x and y with the inclusive binning.

rection for the RICH efficiencies. The selection of the DIS events and the hadron candidates are shown. The raw experimental multiplicities are calculated with:

$$M_{\text{raw}}^h(x, y, z) = \frac{N_{h,i}(x, y, z)}{N_{\text{DIS}}(x, y) \cdot \Delta z} \quad (68)$$

where $N_{h,i}$ is the number of charged hadron of type i (unidentified, π or kaon) in x , y and z bins and $N_{\text{DIS}}(x, y)$ the number of DIS events in the corresponding inclusive bin in x and y with Δz the width of the z bin.

The multiplicities are calculated in a 3-dimensional binning of 8 x bins, 5 y bins and 12 z bins:

- x : {0.004, 0.01, 0.02, 0.03, 0.04, 0.06, 0.1, 0.15, 0.7}
- y : {0.1, 0.15, 0.2, 0.3, 0.5, 0.7}
- z : {0.2, 0.25, 0.3, 0.35, 0.4, 0.45, 0.5, 0.55, 0.6, 0.65, 0.7, 0.75, 0.85}

The binning is shown in Figure 85 in the kinematic plane of x and y and covers most of the phase space. The first iteration of the analysis included the additional y bin from $0.7 > y > 0.9$. Due to the size of the radiative corrections, this bin was finally excluded from the analysis.

7.3.1 DIS Event Selection for the 2006 Multiplicities

The following cuts are applied to select DIS events.

1. Outer and (corrected) inclusive Middle trigger bit set
2. Measured momentum for the incoming muon by BMS
3. Selection of the best primary vertex (PHAST)
4. Reconstructed scattered muon attached to the vertex
5. Target cuts:
 - Vertex within the target material
 - Extrapolated beam trajectory crosses all three target cells
 - Radial target cut of 1.4 cm
 - Vertex position Z cut: $-56 \text{ cm} < Z < -35 \text{ cm}$ or $-20 \text{ cm} < Z < 31 \text{ cm}$ or $43 \text{ cm} < Z < 66 \text{ cm}$
6. $Q^2 > 1 (\text{GeV}/c)^2$
7. $140 \text{ GeV} > E_\mu > 180 \text{ GeV}$
8. $0.1 > y > 0.7$
9. $5 \text{ GeV} > W > 17 \text{ GeV}$
10. $x > 0.7$

The y and the Q^2 cut lead to a lower limit of $x > 0.004$. The lower cut on y is used to reject elastic scattering events. To avoid any bias due to the use of hadron information, only inclusive triggers (MT, OT) are used. The typical trigger rates in 2006 were 30000 (MT) and 13000 (OT) per spill. As shown in Section 6.2.5, the inclusive Middle trigger had an inefficient

part during the 2006 data taking. Scattered muons traversing this part of the detector are excluded from the analysis. The target cuts are applied to assure a reaction in the ${}^6\text{LiD}$ target; the Z target cut is narrower as the target itself, to reduce systematics from edge effects of the target filling. With the cut on the invariant mass W , the region outside the nucleon resonances is selected. The Bjorken scaling variable x is determined by the acceptance of the detector. The cut on the relative photon energy is chosen such that radiative corrections are not too large. The remaining criteria such as vertex and track conditions ensure a correct DIS event topology. The inclusive radiative corrections are applied.

7.3.2 Hadron Selection for the 2006 Multiplicities

Hadrons are selected from the outgoing particles for each vertex passing the DIS cuts described above. The following criteria are applied:

1. The outgoing particle is not the scattered muon,
2. A reconstructed track segment before and behind SM1,
3. Track has passed less than 15 radiation length,
4. Cut on the hadron energy fraction z : $0.2 > z > 0.85$,
5. Cut on the azimuthal angle at the RICH entrance: $0.01 > \theta > 0.12$,
6. Rejection of tracks passing through the RICH pipe (5 cm radial cut),
7. Hadron momentum cut for improving the RICH identification: $12 \text{ GeV}/c > p_h > 40 \text{ GeV}/c$.

To calculate the Lorentz four-vectors a mass hypothesis is done. For the unidentified hadrons the pion mass is assumed, as well as for the identified pions. For the kaon count, the kaon mass is considered. The track conditions around SM1 ensure that the hadron momentum was measured. The cut on a maximal traversed radiation length is performed to reject muons. The lower cut on the hadron energy fraction $z > 0.2$ rejects hadrons coming from the target fragmentation. The high cut on $z < 0.85$ reduces the contribution from exclusively produced hadrons, such as diffractive ρ in the case of pion multiplicities. The cuts on the RICH geometry are done for the RICH acceptance. The hadron momentum p_h limitation is done to adapt the hadron kinematics to the detection threshold of the RICH. All charged particles passing the requirements are used for the unidentified hadron multiplicities. For the charged identified multiplicities, the RICH detector is used for the identification, as explained in Section 7.1.4, and corrected for its efficiency according to Section 7.1.2. The semi-inclusive radiative corrections are applied. As an example, the number of corrected pions is given by

$$N_{\pi}^{\text{correct}} = N_{\pi}^{\text{measured}} \cdot \epsilon(\pi \rightarrow \pi) + N_K^{\text{measured}} \cdot \epsilon(K \rightarrow \pi) + N_p^{\text{measured}} \cdot \epsilon(p \rightarrow \pi).$$

The statistical uncertainties of the DIS events and the number of hadrons are each given by \sqrt{N} . For the identified hadrons, the uncertainties of the RICH efficiency matrix are taken into account. The statistical uncertainties on the multiplicities are calculated with the correct propagation of uncertainty. Figures 86, 87 and 88 show the raw charged multiplicities for unidentified hadrons, pions and kaons. The z dependence of the multiplicities in bins of x and y is presented. The rows correspond to increasing x and the columns for decreasing y . Positive hadrons are always shown in red, and negative in blue. The multiplicities of unidentified hadrons and charged pions are similar, as around 70 % of the produced hadrons are in

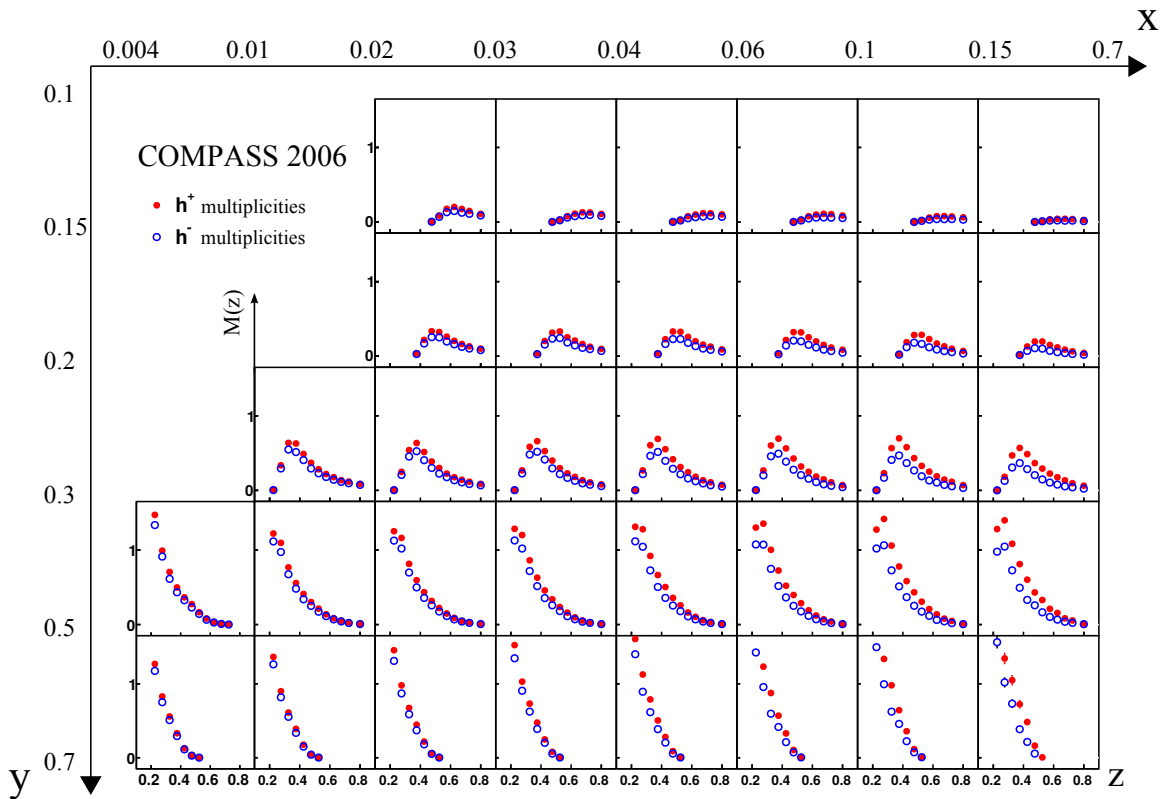


Figure 86: The raw unidentified hadron multiplicities in the three-dimensional binning of x , y and z . The z range is from 0 to 1.5.

fact pions. Statistical errors are hardly visible due to the high-statistics data set. The first observation is the strong, expected z dependence. With increasing z the multiplicities decrease. The dip at low z is coming from the cut on the hadron momentum. In a later step, a correction will be applied for the non-measured momentum region. The x dependence, which is coming from the PDFs, is weak as expected. With increasing x , an asymmetry between the positive and negative hadron multiplicities is striking, specially in the case of charged kaons. This effect is discussed in Chapter 9.

Corrections necessary to calculate the final result from the raw multiplicities are discussed in the next Chapter.

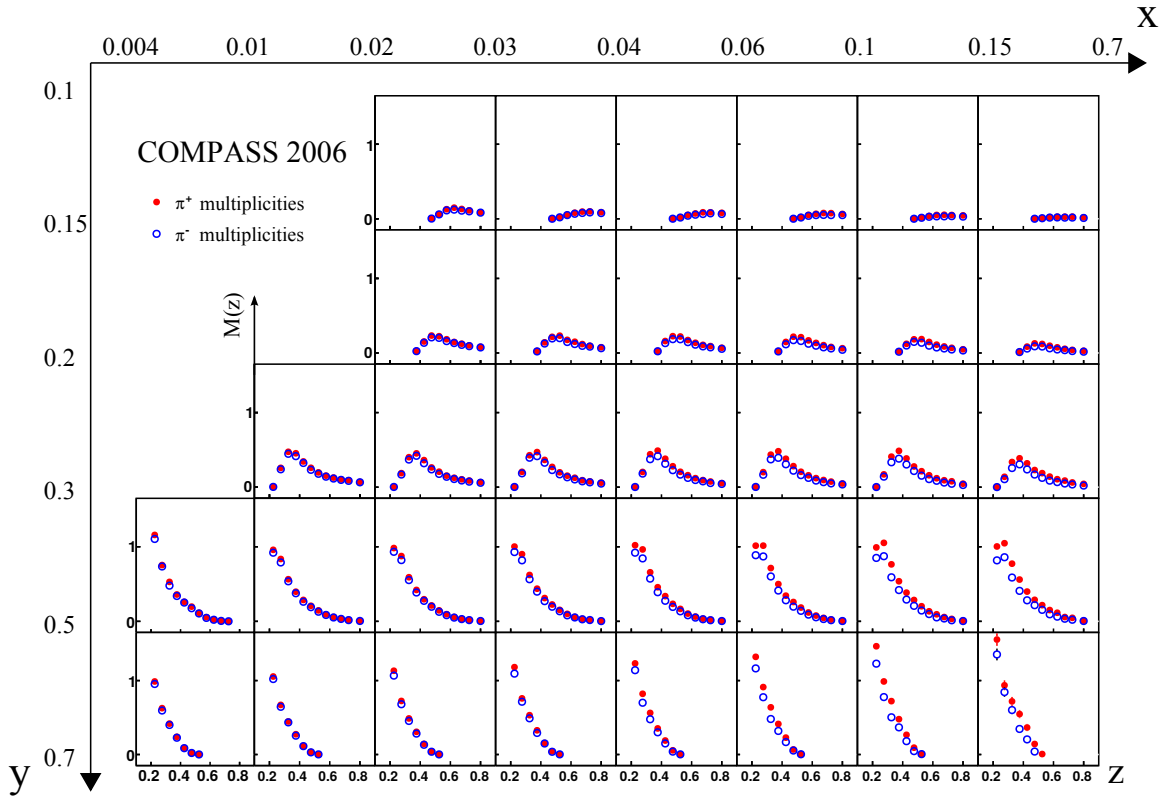


Figure 87: The raw charged pion multiplicities in the three-dimensional binning of x , y and z . The z range is from 0 to 1.5.

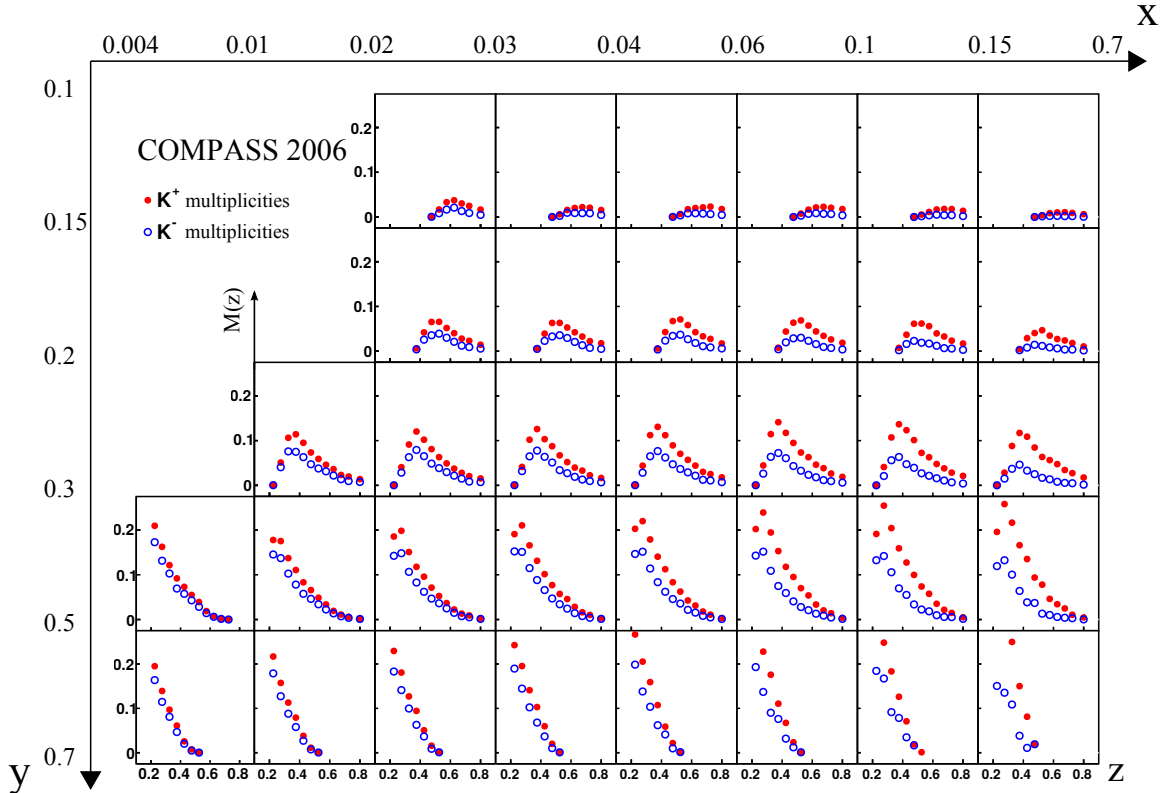


Figure 88: The raw charged kaon hadron multiplicities in the three-dimensional binning of x , y and z . The z range is from 0 to 0.3.

CORRECTION FACTORS FOR MULTIPLICITIES

The charged hadron multiplicities have been corrected up to now for radiative effects and for the particle identification efficiency only. Here, additional correction factors are discussed, which are mainly determined using Monte Carlo simulation. The corrections include the acceptance correction and correction for particle contamination such as vector mesons and electrons. A method is described to extrapolate the measured results towards the non-measured momentum range using multiplicities coming from the Monte Carlo model.

8.1 MONTE CARLO SIMULATION

Monte Carlo data is a computer generated data sample based on parametrisation of physics models. In this case, deep inelastic scattering is simulated. The main aim of the MC is to obtain the apparatus acceptance. The acceptance includes, besides the geometric acceptance, detector efficiencies, detector resolution, the track reconstruction efficiency and the kinematic smearing. The produced particles are subject to energy loss in the material, which is described by the Bethe-Bloch formula [89]. This alternates the kinematic properties and the direction of the particles tracks. The COMPASS MC data is produced in three steps: the event generation (LEPTO and JETSET), the detector simulation (COMGEANT) and the reconstruction (CORAL). For the reconstruction of the MC data, the same reconstruction program CORAL (and the same version) as for real data is used. The Monte Carlo data chain is illustrated in Figure 89.

8.1.1 Event Generator

The LEPTO generator is a standard event generator that simulates deep inelastic lepton nucleon scattering. The basic lepton-quark scattering cross section within the standard model and the parton density function are included.

The basic kinematics of the DIS event are created, starting by choosing the lepton and nucleon momenta. The muon beam momentum is randomly chosen from a simulated beam momentum distribution, adapted to the SPS muon beam delivered to the COMPASS experiment. The momentum of the struck nucleon is zero, as expected for a fixed-target experiment. The type of the target nucleon (n,p) hit by the beam is chosen randomly. With the isoscalar ${}^6\text{LiD}$ target the ratio is 1:1. The kinematics are chosen randomly according to the input differ-

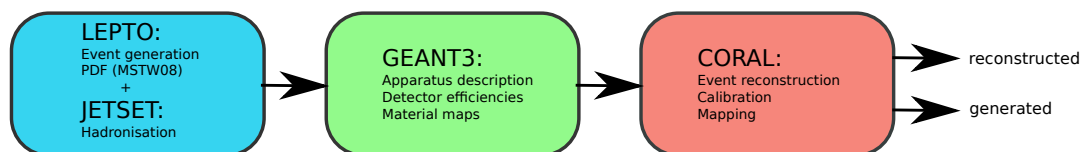


Figure 89: Three step chain for the production of Monte Carlo data at COMPASS: generation, simulation and reconstruction.

ential cross section and the available phase space. The interaction between the beam muon and the struck quark is simulated according to the electro-weak cross section, assuming a 1γ exchange. The remaining non-interacting quarks are treated as spectator quarks.

Using the recent parton distribution functions MSTW08 [16], the flavour of the struck quark is selected. These PDFs describe well the structure function F_2 , measured by NMC [90], in the COMPASS kinematic domain.

The hadronisation of the coloured quarks q to the hadronic final state, according to the LUND model, is simulated by JETSET with the according parameters for the transverse momenta, the flavour distribution and the ratio of vector and pseudo-scalar meson. Furthermore, the Monte Carlo data was tuned to match the COMPASS data [91]. Originally, this tuning was used to match the COMPASS data in the high p_T region, but it has been found that it matches well to the whole kinematic range of COMPASS. In addition, the program FLUKA [92] [93] is used to better reproduce secondary interactions in the target. The systematic uncertainties of the event generation from LEPTO and JETSET are discussed in Section 9.1.

8.1.2 Simulation of the Experiment

The output of the event generator are four-vectors of the particles participating in the reaction. The GEANT3¹ framework is used to simulate the COMPASS spectrometer, including the material maps, the magnetic field, detector responses, detector efficiencies, the triggers and multiple scattering of charged particles. This requires a proper description of the spectrometer detectors. The adaptation of GEANT3 to the COMPASS experiment is called COMGEANT. Although the RICH detector is simulated in COMGEANT, the MC data set is not used to correct for the RICH performance. This correction has already been done and is discussed in Section 7.1.4. The generated four-vectors are propagated through this simulation. The COMGEANT output contains wire signals, timings and other responses of detectors, similar to the detector responses recorded with the spectrometer. The simulation of the experiment is checked by comparing reconstructed MC data with real data from the experiment.

8.1.3 Reconstruction of MC Events with CORAL

After the simulation of the experiment, the COMGEANT output is treated very similarly to the physics data recorded by the spectrometer: the reconstruction algorithm CORAL is used to decode the detector responses and reconstruct particle tracks. For significant comparison between reconstructed real data and the MC data, it is mandatory to use the same CORAL version for both. After reconstruction, the MC data contains events with two different data streams: the *generated* MC data contains all produced particles (from the event generator) with the “true” kinematics. The *reconstructed* MC contains the reconstructed tracks with the kinematic, smeared by the reconstruction and various other effects in the spectrometer. The reconstructed data sample is a sub-sample of the generated one. For (almost) each reconstructed track, the generated properties are accessible, *e.g.* the particle type and the correct kinematics. “Almost” means that, due to reconstruction errors, ghost tracks, with no corresponding physics tracks, can be created in the reconstructed MC data.

¹ GEometry ANd Tracking

8.2 ACCEPTANCE CORRECTION

The acceptance is determined by comparing the reconstructed and the generated Monte Carlo data. This reveals the loss of events due to the limited geometric acceptance and the limited detection/reconstruction efficiency. For this analysis, only the hadron acceptance is needed. Due to the choice of the observable (hadron multiplicity), the muon acceptance cancels out. The acceptance correction is calculated in the same three-dimensional binning (x , y and z) as the real data. In the following, the variables x , y and z refer to the reconstructed values, while x' , y' and z' refer to the true kinematic values, taken from the generated MC. The hadron acceptance is evaluated with two different methods, the *single ratio method* and the *double ratio method*. Both methods are compared in Section 8.2.6.

8.2.1 Generated Monte Carlo

The generated MC data contains the true properties of each particle. This includes all kinematics and the correct particle type. Only kinematic cuts are applied to select the DIS events and the hadrons. The only geometric cut on the generated MC data is the selection of the vertices inside the relevant target volume. The same cut as for the real data is applied. The scattered muons and other muons of the outgoing system are excluded. In summary, the kinematic cuts are:

- $Q^2 > 1 \text{ (GeV/c)}^2$
- $0.1 < y < 0.7$
- $5 \text{ GeV/c}^2 > W > 17 \text{ GeV/c}^2$
- $0.004 < x < 0.7$
- $0.2 < z < 0.85$
- $12 \text{ GeV/c} < p_h < 40 \text{ GeV/c}$

This leads to the number of generated DIS events $N_{\text{gen}}^{\text{DIS}}$ and the number of hadrons $N_{\text{gen}}^{\text{h}}$. The hadron type h is accessible in the generated MC data.

8.2.2 Reconstructed Monte Carlo

For the reconstructed MC, the same cuts are done as for the real data analysis. This includes the cuts on the kinematics and the geometric cuts, *e. g.* the cut on the RICH pipe. These cuts are summarised in Section 7.3.1 and 7.3.2. The only difference is the determination of the hadron type: in the real data, the RICH detector, in combination with the unfolding of the RICH efficiency matrices, is used to determine the type of hadrons. In the reconstructed MC, the hadron type is taken from the generated MC. The number of DIS event $N_{\text{rec}}^{\text{DIS}}$ and the number of hadrons of the type h $N_{\text{rec}}^{\text{h}}$ are obtained.

Bin migration due to the reconstruction smearing occurs in about 10% of the events; this smearing effect in the acceptance correction has to be taken into account in the different methods of acceptance determination.

8.2.3 The COMPASS Monte Carlo Data Set

The comparison of the real data and the reconstructed MC data is shown here and it demonstrates that the simulation of the detector responses are correctly done in COMGEANT. This

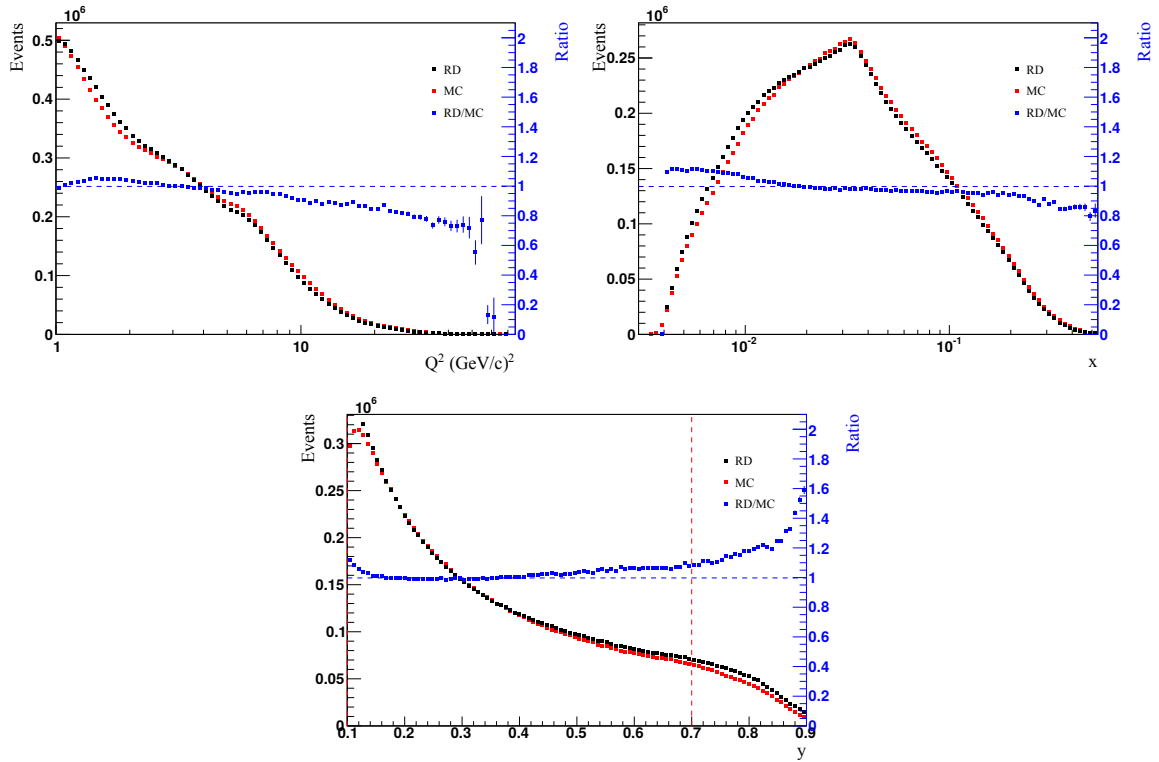


Figure 90: Comparison of real data (black) and MC data (red) for the inclusive kinematic variables Q^2 , x and y . The ratio is shown in blue.

requires that the physics model used in the MC generator is correct. The same cuts are applied to both data sets. Figure 90 shows the inclusive kinematic distributions with the according ratios and Figure 91, the semi-inclusive ones. On all Figures, all analysis cuts are applied, except the one of the shown variable. The red dashed lines indicate the cuts done in the analysis of both data sets. Within the cuts, the data and the MC are comparable. The real data MC comparison for the inclusive variables agree to a maximum of 15% for x and y . The Q^2 comparison is worse in the higher momentum transfer region. The semi-inclusive laboratory variables p_h and θ_h also show a good match. The comparison for the two remaining variables p_t and z is not as good as the other ones. The data/MC ratio of z has a wavy structure and, for p_t , a systematic decrease towards higher momenta is visible. For the multiplicity analysis, the data is binned in z and integrated over p_t , so this does not pose an issue.

8.2.4 Single Ratio Acceptance

The first method of acceptance determination is given by the ratio of the number of reconstructed hadrons $N_{\text{rec}}^h(x, y, z)$ and the number of generated hadrons $N_{\text{gen}}^h(x, y, z')|_{\text{rec.DIS}}$, coming from a reconstructed DIS event (Equation 69). The method was motivated by [35], which lead to the publication [94]. In this method, it is assumed that the total acceptance factorises into the muon acceptance and the hadron acceptance. The number of generated hadrons is taken from the sample, in which a reconstructed DIS event was seen. The reconstructed DIS event is obtained as mentioned in Section 8.2.2 and then the outgoing particles are extracted

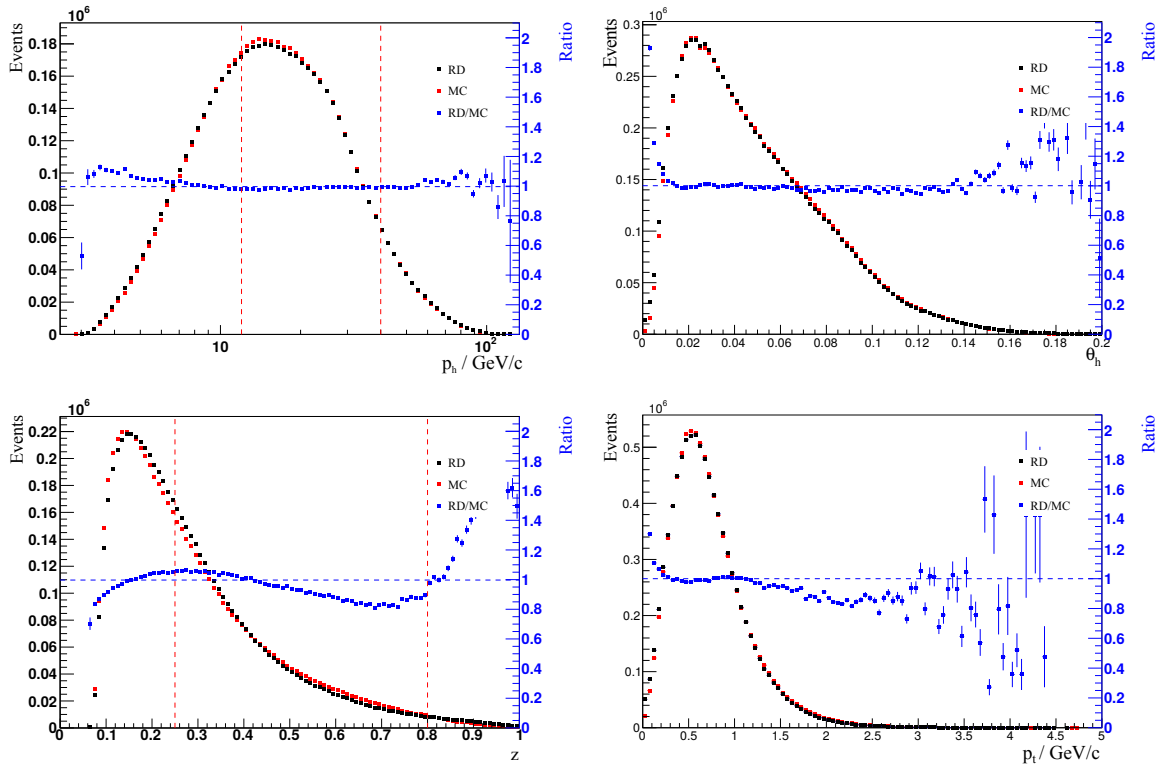


Figure 91: Comparison of real data (black) and MC data (red) for the semi-inclusive kinematic variables p_h , θ_h , z and p_t . The ratio is shown in blue.

from the generated MC. The inclusive variables x and y are coming from the reconstructed MC data set, while the hadron energy fraction z' is coming from the generated MC.

$$A^h(x, y, z) = \frac{N_{\text{rec}}^h(x, y, z)}{N_{\text{gen}}^h(x, y, z')|_{\text{rec.DIS}}} \quad (69)$$

For simplification, $N_{\text{gen}}^h(x, y, z')|_{\text{rec.DIS}}$ is now shortened as N_{gen}^h in this Sub-Section. According to [95], the error of an acceptance $A = \frac{N_{\text{rec}}^h}{N_{\text{gen}}^h}$ can be derived from a binomial distribution. After a partial integration of the distribution, the standard deviation leads to the error

$$(\Delta A)^2 = \frac{(N_{\text{rec}}^h + 1)(N_{\text{gen}}^h - N_{\text{rec}}^h + 1)}{(N_{\text{gen}}^h + 2)^2(N_{\text{gen}}^h + 3)}. \quad (70)$$

By using different hadron kinematics z and z' , bin migration effect (in the order 10%) and contamination of electrons have to be taken into account. The number of reconstructed hadrons N_{rec}^h is decomposed into two samples: the number of reconstructed hadrons without z bin migration $N_{\text{rec}^0}^h$ and $N_{\text{rec}'^0}^h$, the number of reconstructed hadrons with z bin smearing and a contribution of electrons. The sample $N_{\text{rec}^0}^h$ is a sub-sample of N_{gen}^h , while $N_{\text{rec}'^0}^h$ is not. With this four samples, an alternated error estimation for the single ratio method is given by:

$$(\Delta A)^2 = \frac{(N_{\text{rec}^0}^h + 1)(N_{\text{gen}}^h - N_{\text{rec}^0}^h + 1)}{(N_{\text{gen}}^h + 2)^2(N_{\text{gen}}^h + 3)} + \frac{N_{\text{rec}'^0}^h}{N_{\text{gen}}^h} + \frac{N_{\text{rec}'^0}^h{}^2}{N_{\text{gen}}^h{}^3} \quad (71)$$

Equation 71 was worked out from Equation 70, assuming the smeared hadrons are independent from the other hadrons. The acceptance is calculated in the multiplicity binning of x , y and z , using the error determination with the z bin smearing. The results for unidentified hadrons, pions and kaons are shown in Figures 92, 93 and 94 and discussed in Section 8.2.6.

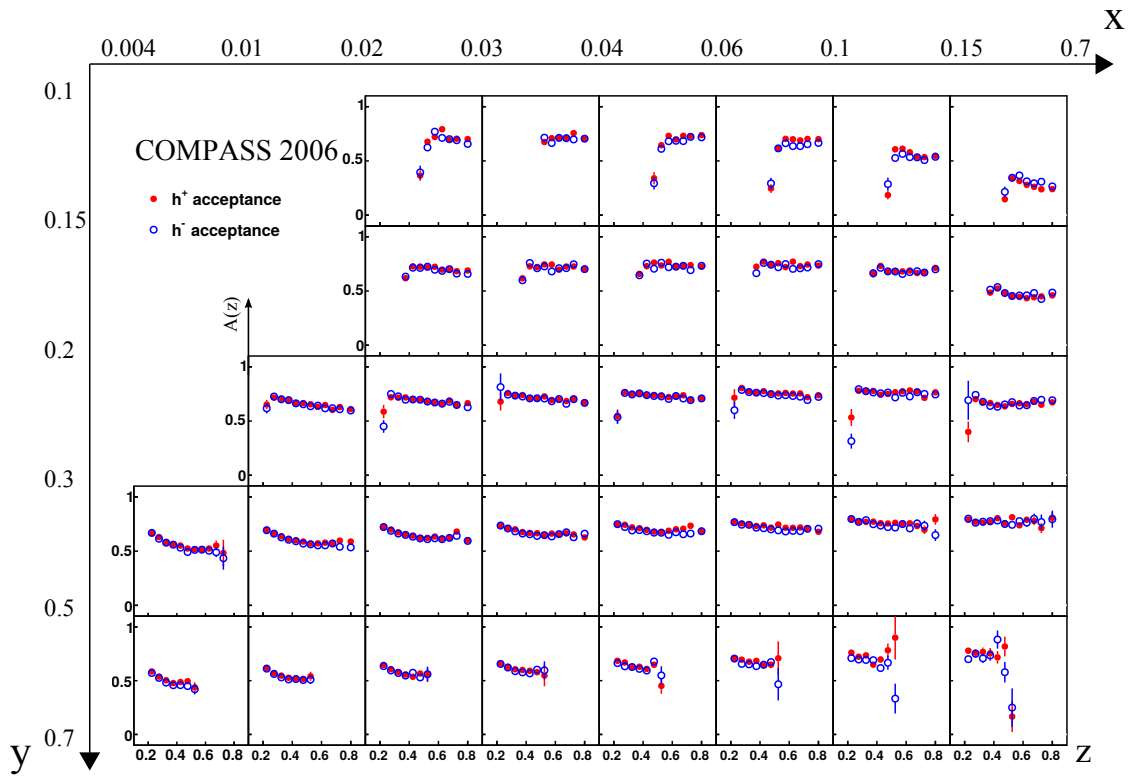


Figure 92: Single ratio acceptance of the unidentified hadrons. Positive in red and negative in blue.

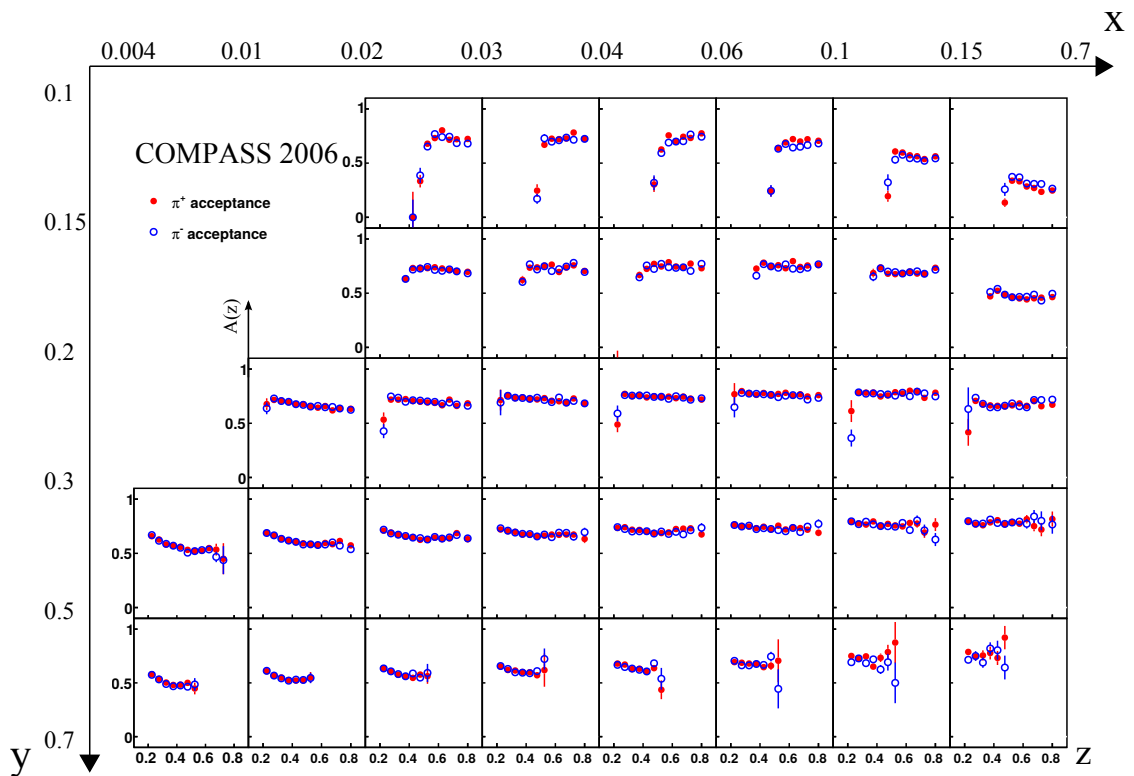


Figure 93: Single ratio acceptance of the charged pions. Positive in red and negative in blue.

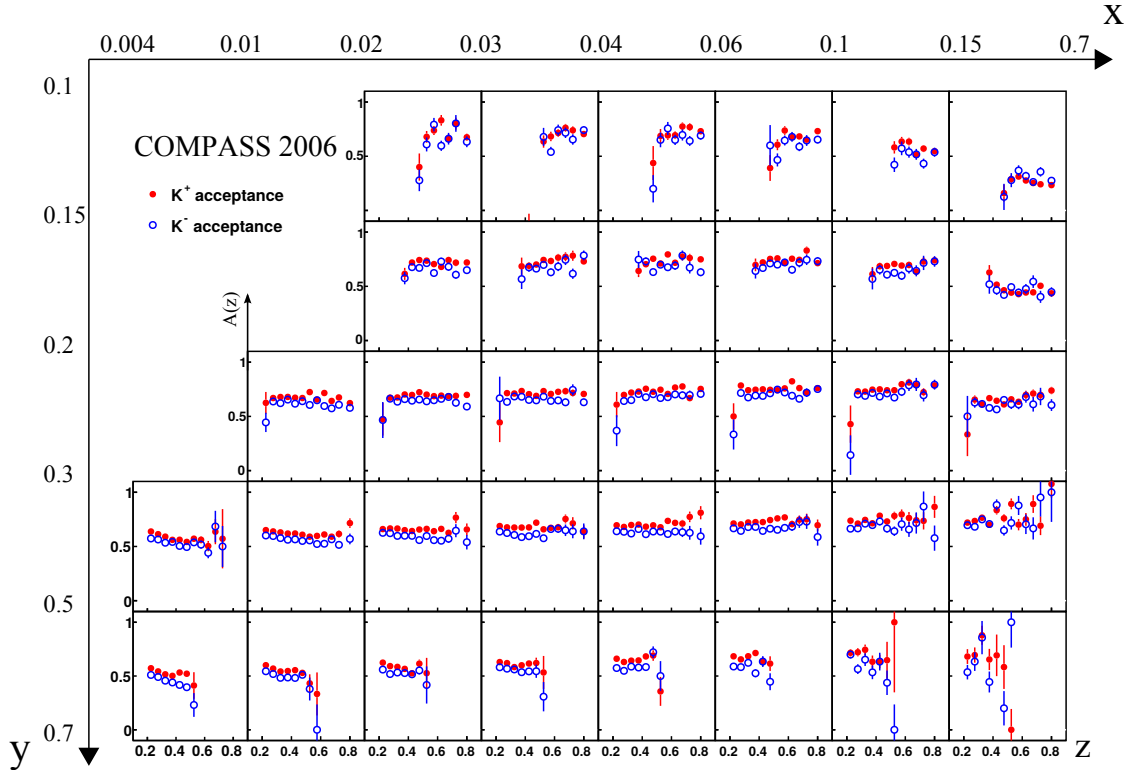


Figure 94: Single ratio acceptance of the charged kaons. Positive in red and negative in blue.

8.2.5 Double Ratio Acceptance

In the second method, the acceptance is determined according to Equation 72 by the ratio of reconstructed multiplicities M_{rec}^h and generated multiplicities M_{gen}^h . In this method, the assumption that the hadron and muon acceptance factorise is not done. The number of reconstructed (generated) DIS events $N_{\text{rec}(\text{gen})}^{\text{DIS}}$ and the number of reconstructed (generated) hadrons $N_{\text{rec}(\text{gen})}^h$ are used, as mentioned above.

$$A^h(x, y, z) = \frac{M_{\text{rec}}^h}{M_{\text{gen}}^h} = \frac{\frac{N_{\text{rec}}^h(x, y, z)}{N_{\text{rec}}^{\text{DIS}}(x, y, z)}}{\frac{N_{\text{gen}}^h(x', y', z')}{N_{\text{gen}}^{\text{DIS}}(x', y', z')}} \quad (72)$$

With this method, the acceptance is well described. But the error estimation is difficult, as the number of evaluated hadrons and DIS events, in both cases reconstructed and generated, are not independent. For an uncomplicated error estimation, the two data sets are considered as independent. With the two ratios

$$R_h = \frac{N_{\text{rec}}^h}{N_{\text{gen}}^h} \text{ and } R_{\text{DIS}} = \frac{N_{\text{rec}}^{\text{DIS}}}{N_{\text{gen}}^{\text{DIS}}}, \quad (73)$$

the corresponding error $\Delta R_{h(\text{DIS})}$ and the standard error propagation, the uncertainty on the hadron acceptance is given by:

$$A^h = \frac{R_h}{R_{\text{DIS}}} \cdot \sqrt{\left(\frac{\Delta R_h}{R_h}\right)^2 + \left(\frac{\Delta R_{\text{DIS}}}{R_{\text{DIS}}}\right)^2}. \quad (74)$$

The results of the double ratio method for unidentified hadrons, pions and kaons are shown in Figures 95, 96 and 97.

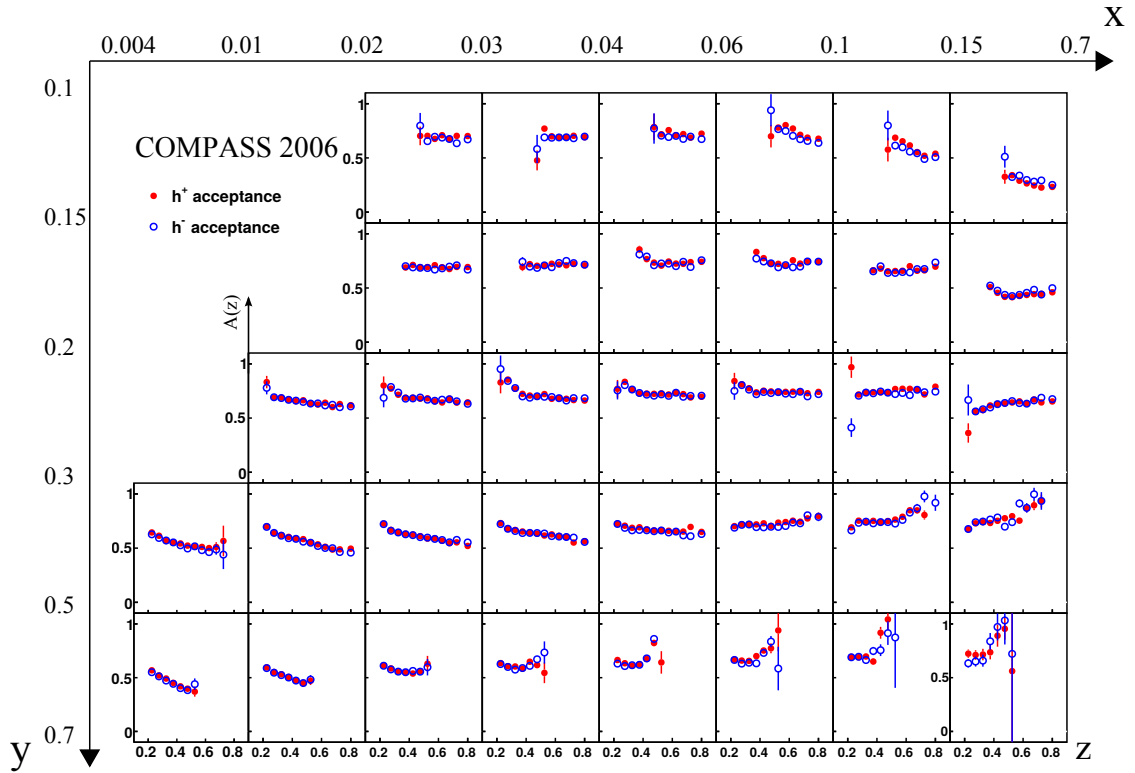


Figure 95: Double ratio acceptance of the unidentified hadrons. Positive in red and negative in blue.

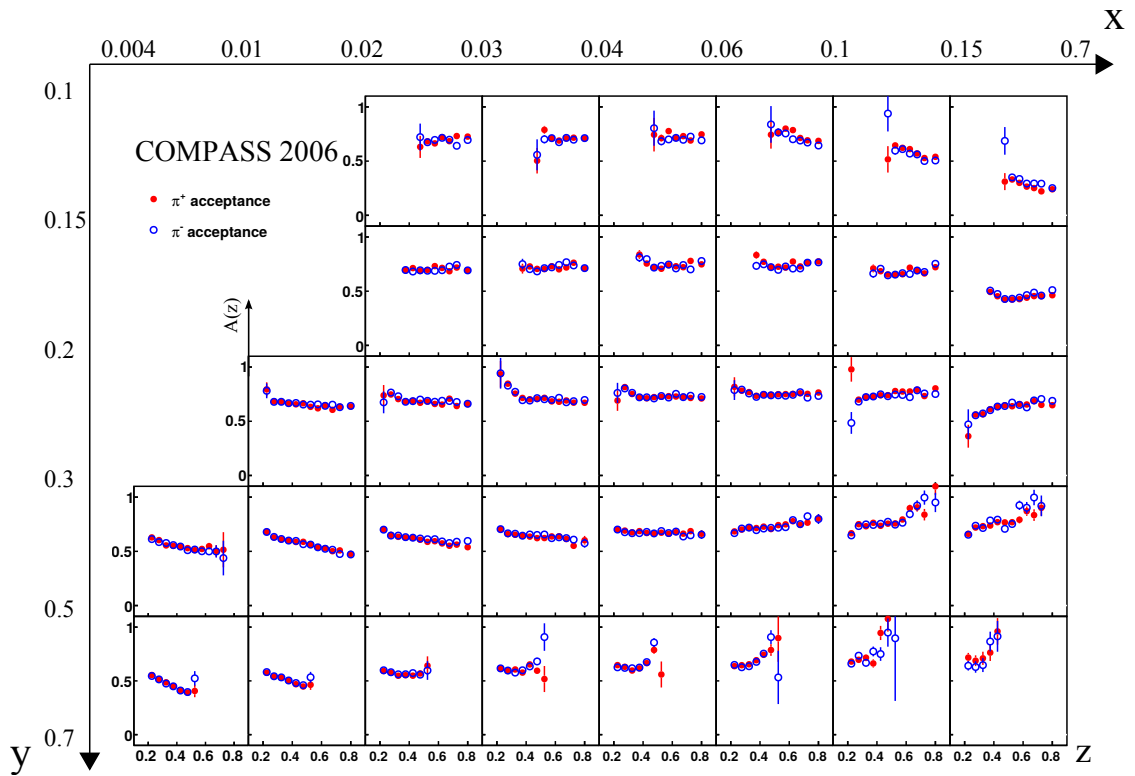


Figure 96: Double ratio acceptance of the charged pions. Positive in red and negative in blue.

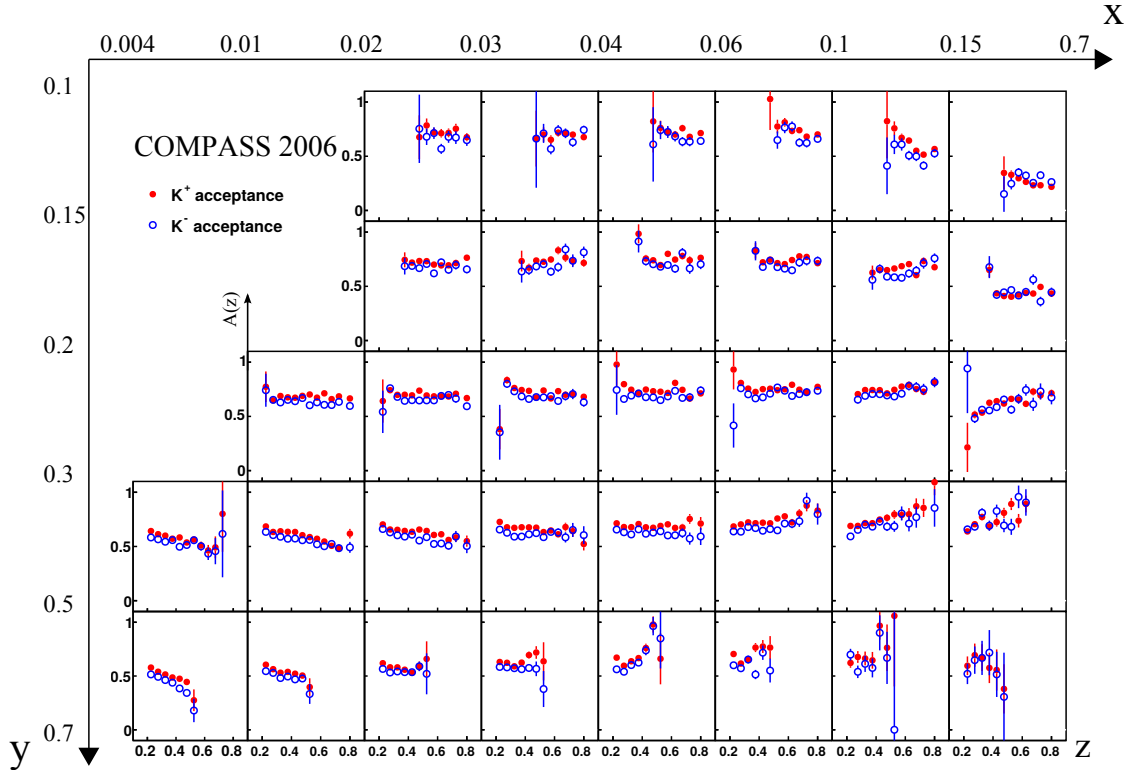


Figure 97: Double ratio acceptance of the charged kaons. Positive in red and negative in blue.

8.2.6 Result and Method Comparison

The results for the hadron acceptance, determined by the two methods, are displayed in Figures 92-97 in the typical three-dimensional binning of the multiplicity analysis. The positive (negative) hadrons are shown in red (blue). Some of the z bins, in which the acceptance is zero or the error is not calculable, are omitted. At first glance, the acceptance looks similar for all particles (h , π , K) and for each charge.

In general, the hadron acceptance is almost constant over the hadron energy fraction z , specially in the intermediate x and y region, with variation up to 20%. The acceptance ranges from 75% at low y to around 50% with increasing y . Also, an x dependence can be seen: in the low y region, the acceptance decreases from 70% to 40% with increasing x . In the case of unidentified hadrons and pions, the error bars are smaller than the size of the symbols in most bins, except on the edge of the z distribution. As only 20-25% of the final-state hadrons are kaons, the statistics for kaons is more limited, implying larger error bars and larger statistical fluctuations. The kaon acceptance shows a small asymmetry between the two charges. The acceptance of the positive kaons is systematically larger (5-10%). The kaon quark content is $K^+ = u\bar{s}$ and $K^- = s\bar{u}$. The \bar{u} quark of the negative kaon can annihilate with the valence u quarks of the target (isoscalar LiD target). For the positive kaon quark, this annihilation can only occur with the sea quarks, resulting in a smaller cross section for secondary interactions in the target material.

In Figure 98, the double and single ratio acceptance for positive pions are compared. The single ratio is shown in red and the double ratio in blue. Both methods of acceptance determination lead to a very similar result and the kinematic dependences in x , y and z are similar. In an example bin ($0.01 < x < 0.02$ and $0.3 < y < 0.5$), the two acceptances are almost identical up to $z = 0.5$, then they start to deviate. The single ratio acceptance remains more constant (around 58%), while the double ratio acceptance drops to 47%. Correlations between the hadron and muon kinematics can be the reason for this deviation. But over a large

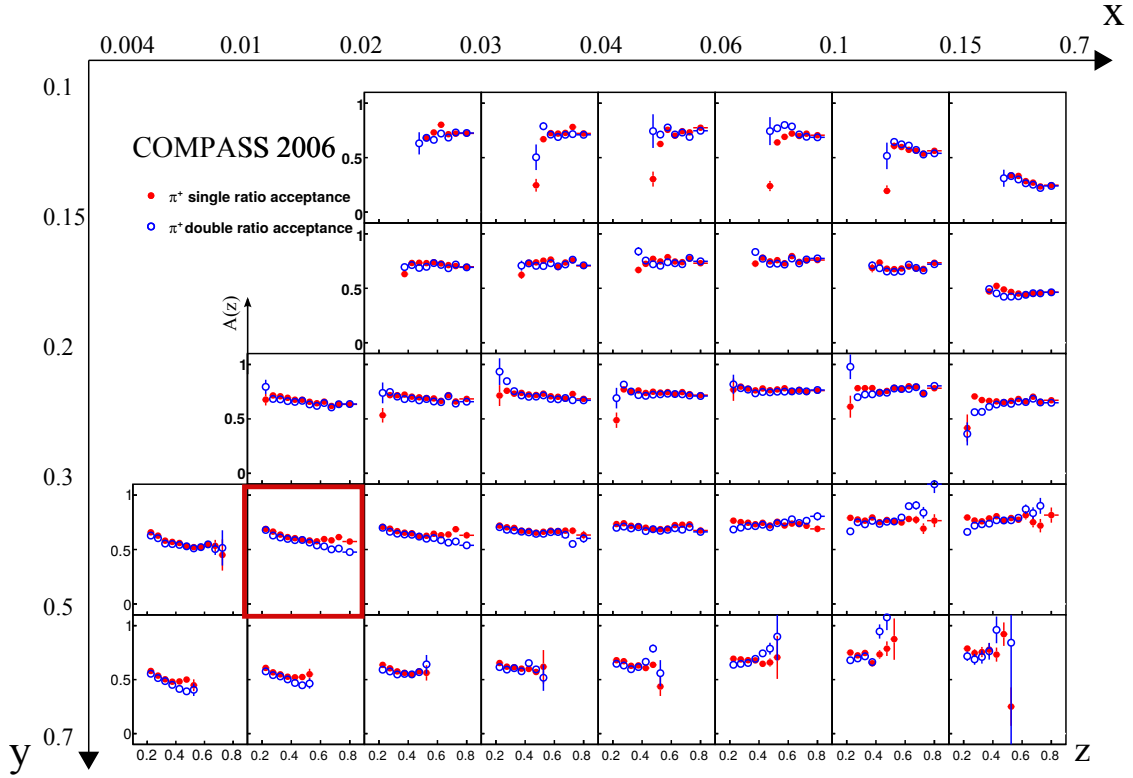


Figure 98: Comparison of the pion acceptance, determined with the single ratio method (red) and the double ratio method (blue). The two acceptances are similar, except at the edge z bins.

z range, the comparison of the two methods shows the factorisation of the hadron and muon acceptance. In the single ratio, it was assumed, while in the double ratio it was correctly calculated. The assumption of factorisation is solid as the events are triggered by the inclusive muon trigger hodoscope. The triggering is supposed to be independent from hadrons.

The single ratio acceptance method was used as long as the MC sample had low statistics. Also, the error calculation is more straight-forward and the point-to-point fluctuation is smaller in comparison to the double ratio method due to the cancellation of the muon acceptance. With the new production of the MC data, the statistics was increased by a factor of 8 in comparison to the first MC data set. With higher statistics, the double ratio method can be applied as it gives a more correct result for the acceptance. Thus, all charged hadron multiplicities are determined using the double ratio acceptance.

8.3 ELECTRON CONTAMINATION

Figure 78 shows the Cherenkov angle of outgoing particles from the vertex. In the used momentum range, starting at 12 GeV/c, the electron and the pion bands overlap, so that an electron can be mistaken as a pion. The RICH detector has problems to distinguish between those two particles in the hadron momentum range used for the multiplicity analysis. This correction is evaluated using the MC simulation. The electron contamination is studied in two momentum regions:

- Momentum region 3-8 GeV/c: in this region the RICH detector can distinguish between electrons and pions, so that a comparison between real data and Monte Carlo data is possible.

	e^-	π^-	fraction
MC	67419	716227	0.086
RD (loose)	29326	297252	0.099
RD (strict)	28680	292911	0.09
	e^+	π^+	fraction
MC	68317	862110	0.073
RD (loose)	30368	366644	0.083
RD (strict)	29245	360258	0.081

Table 7: Comparison of the number of electrons and pions from the MC simulation and the real data in the lower momentum region between 3 GeV/c and 8 GeV/c.

- Momentum region 12-40 GeV/c: The RICH detector can no longer discriminate electrons from pions, kaons or protons. The electron contamination is calculated using the Monte Carlo simulation.

In both cases, the DIS and hadron candidate cuts are used. For the momentum region 3-8 GeV/c, two sets of RICH likelihood cuts are used to distinguish electrons and the π -mesons, a looser and a stricter likelihood cut.

1. Pion selection

- $LH(\pi) > LH(K), LH(p), LH(e)$
- $\frac{LH(\pi)}{LH(bg)} > 2$ (looser cut)
- $\frac{LH(\pi)}{LH(bg)} > 3$ (stricter cut)

2. Electron selection

- $LH(e) > LH(\pi), LH(K), LH(p)$
- $\frac{LH(e)}{LH(bg)} > 2$ (looser cut)
- $\frac{LH(e)}{LH(bg)} > 3$ (stricter cut)

The number of electrons (positrons) and negative (positive) pions of the real data in the momentum region 3-8 GeV/c, using the event number after radiative corrections, are summarized in Table 7. In the negative case, the fraction of electrons in the real sample range from 0.099 to 0.09, depending on the likelihood cuts. The electron fraction from the MC simulation is 0.086. The difference between real data and Monte Carlo it is only 13%. Given the overall small size of this correction, it is reasonable to use the Monte Carlo sample to calculate the electron contamination in the momentum region of the analysis, where the electron identification cannot be provided by the RICH detector. The systematic uncertainty is estimated by the difference of the electron fraction coming from the data and the MC simulation. The fraction of electron contamination in the hadron and pion sample in the momentum range between 12-40 GeV/c obtained from Monte Carlo alone is shown in Figure 99 for unidentified hadrons and in Figure 100 for the charged pions. The correction has a strong z dependence: with low z the electron correction reaches its maximum (in some bins, up to 8%).

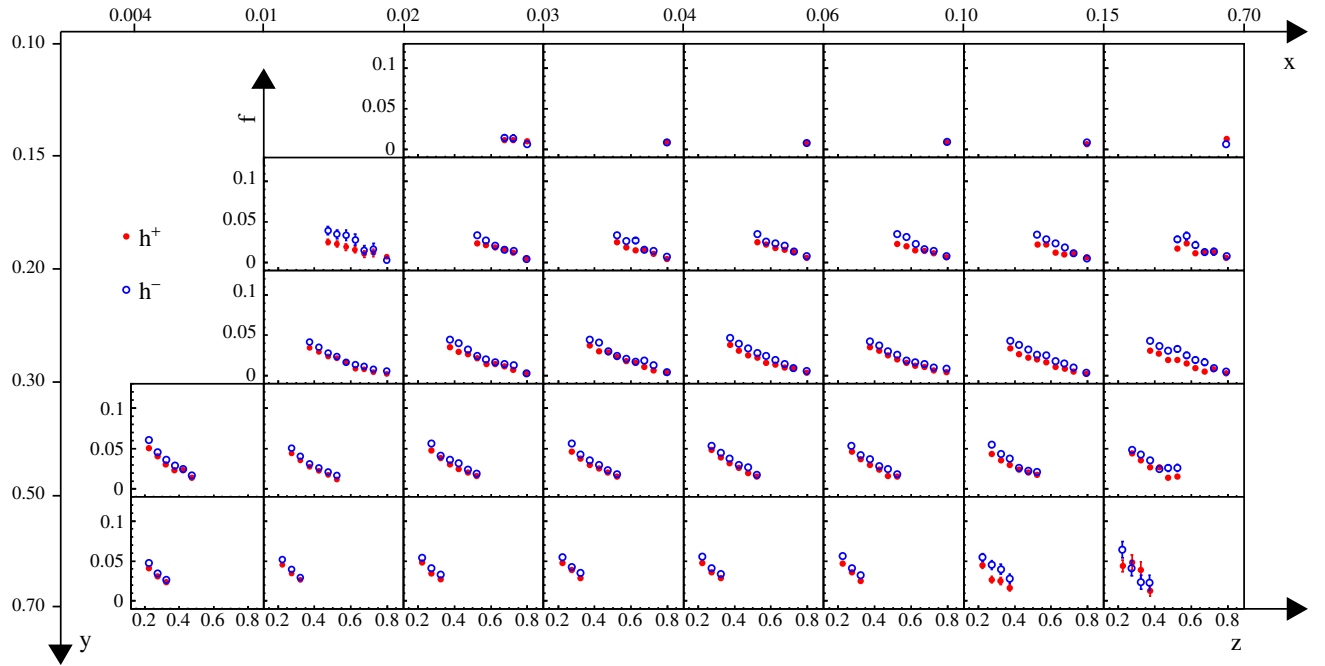


Figure 99: Fraction of electron contamination in the hadron sample in x , y , and z bins. The red markers correspond to positive hadrons and the blue markers to negative hadrons.

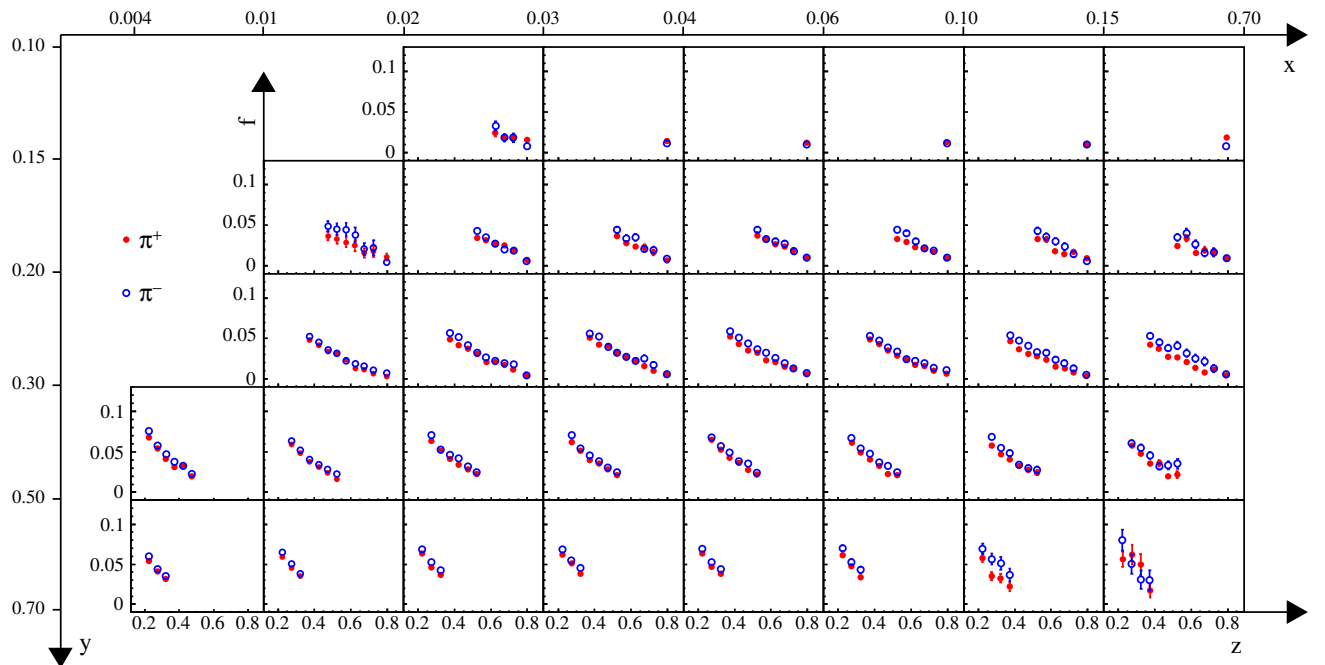


Figure 100: Fraction of electron contamination in the pion sample in x , y , and z bins. The red markers correspond to positive pions and the blue markers to negative pions.

8.4 CONTAMINATION OF EXCLUSIVE VECTOR MESONS

The muon-nucleon scattering can result in diffractively produced vector mesons, which decay in lighter mesons such as π or kaons. It can be described by the Vector Meson Dominance model (VMD) [96]. It is assumed that the virtual photon fluctuates into a $q\bar{q}$ -pair. The cross-section of the process is roughly proportional to $1/Q^6$. At COMPASS kinematics, the dominant channels are the diffractively production of ρ^0 -mesons and ϕ -mesons:

$$\begin{aligned}\gamma^* p &\rightarrow \rho^0 p \rightarrow p\pi^+\pi^- \\ \gamma^* p &\rightarrow \phi p \rightarrow pK^+K^-\end{aligned}$$

The two reactions are exclusive, but in some cases (roughly 20%), a diffractive dissociation of the target nucleon occurs. Figure 101 shows a process diagram for the exclusive, diffractive ρ production in comparison to the SIDIS process, where a pion is produced during the hadronisation of the struck quark. In the exclusive ρ^0 production, the contribution could be quantified by detecting the two pions (π_1 and π_2). The sum of two hadron momentum fractions should add up to $z_1 + z_2 = 1$. But there are events in which one of the pions is not reconstructed. The remaining pion is then wrongly taken into account, when calculating the hadron multiplicities. This contribution can only be estimated by using MC simulations. A multiplicative correction factor $B^h(x, y, z)$ is calculated with two MC data samples, each using a different event generator. The first sample is a DIS sample with standard LEPTO event generator. The second one uses HEPGEN² [97], an event generator specialised for exclusive high energy processes, to create a sample with diffractively produced vector mesons. The idea is to compare the number of mesons from the diffractive vector mesons with the number of vector mesons in the DIS sample.

In the first step, the fraction of pions and kaons coming from the diffractive vector mesons production is determined:

$$f_{\rho^0}^{\pi}(x, y, z) = \frac{N_{\text{HEPGEN}}^{\pi}(x, y, z)}{N_{\text{LEPTO}}^{\pi}(x, y, z) + N_{\text{HEPGEN}}^{\pi}(x, y, z)} \quad (75)$$

$$f_{\phi}^K(x, y, z) = \frac{N_{\text{HEPGEN}}^K(x, y, z)}{N_{\text{LEPTO}}^K(x, y, z) + N_{\text{HEPGEN}}^K(x, y, z)} \quad (76)$$

The number of reconstructed pions (kaons) in the LEPTO sample $N_{\text{LEPTO}}^{\pi(K)}(x, y, z)$ and in the HEPGEN sample $N_{\text{HEPGEN}}^{\pi(K)}(x, y, z)$ are normalised by the corresponding MC luminosity. The luminosity depends on the event weighting and the process cross-section. In the second step, one takes into account the contribution of diffractive events to the selected DIS sample.

$$f_{DIS}^{\rho^0} = \frac{N_{\rho^0}^{DIS}(x, y, z)}{N_{\text{LEPTO}}^{DIS}(x, y, z)} \quad \text{and} \quad f_{DIS}^{\phi} = \frac{N_{\phi}^{DIS}(x, y, z)}{N_{\text{LEPTO}}^{DIS}(x, y, z)} \quad (77)$$

The sum of $f_{DIS}^{\rho^0}$ and f_{DIS}^{ϕ} is taken as the contribution of vector mesons to the DIS sample $f_{DIS}^{VM}(x, y, z)$. Further contribution of vector mesons, *e.g.* ρ and ω , are small and not taken into account here. The final correction factor for multiplicities is given by Equations (78), (79) and (80) for unidentified hadrons, pions and kaons.

$$B^h(x, y, z) = \frac{\frac{N^{\pi(x,y,z)}}{N^h(x,y,z)} \left(1 - f_{\rho^0}^{\pi}(x, y, z)\right) + \frac{N^K(x,y,z)}{N^h(x,y,z)} \left(1 - f_{\phi}^K(x, y, z)\right) + \frac{N^p(x,y,z)}{N^h(x,y,z)}}{1 - f_{DIS}^{VM}(x, y, z)} \quad (78)$$

² <http://project-gpd-full-chain-mc.web.cern.ch/project-gpd-full-chain-mc/hepgen/>

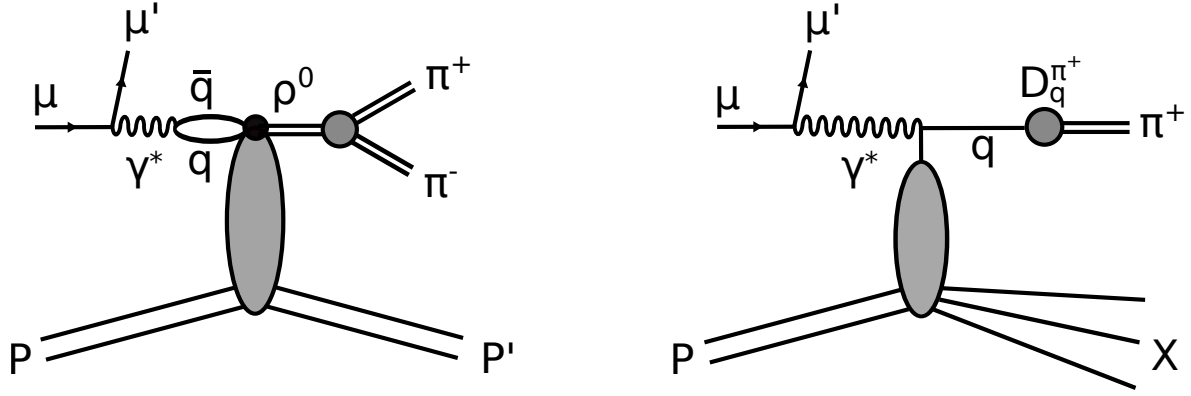


Figure 101: Comparison of mesons coming from diffractive ρ^0 production (left) and from semi-inclusive deep inelastic scattering (right).

$$B^\pi(x, y, z) = \frac{1 - f_{\rho^0}^\pi(x, y, z)}{1 - f_{DIS}^{VM}(x, y, z)} \quad (79)$$

$$B^K(x, y, z) = \frac{1 - f_\phi^K(x, y, z)}{1 - f_{DIS}^{VM}(x, y, z)} \quad (80)$$

Figure 102 and Figure 103 show the correction factors in the multiplicity binning in x , y and z for unidentified hadrons and pions. Bins which are excluded by the LEPTO extrapolation (Section 8.5) are not shown here. In the $y > 0.3$ region, which corresponds to higher Q^2 values, the contribution by vector mesons is rather small, so the multiplicative correction factor $B(x, y, z)$ is around one. In the region of lower x and y ($0.15 < x$ and $0.3 < y$), the correction factor shows a clear z dependence. With increasing z , the correction factor decreases to 0.5. The z dependence is similar for unidentified hadrons and the charged pions. Bins with large VM correction correspond to bins in which the multiplicities are very small, so that the contribution of the correction $B(x, y, z)$ is small.

The systematic uncertainty is small. In HEPGEN, the cross-section for exclusive vector meson production is normalized to the GPD model of Goloskokov and Kroll [98]. The theoretical uncertainty on the predicted cross-section close to COMPASS kinematics is around 30%. Propagating this uncertainty leads to a maximum uncertainty below 12% for the correction factor B in the low x and low y bins. This also includes other VMs and excited VMs.

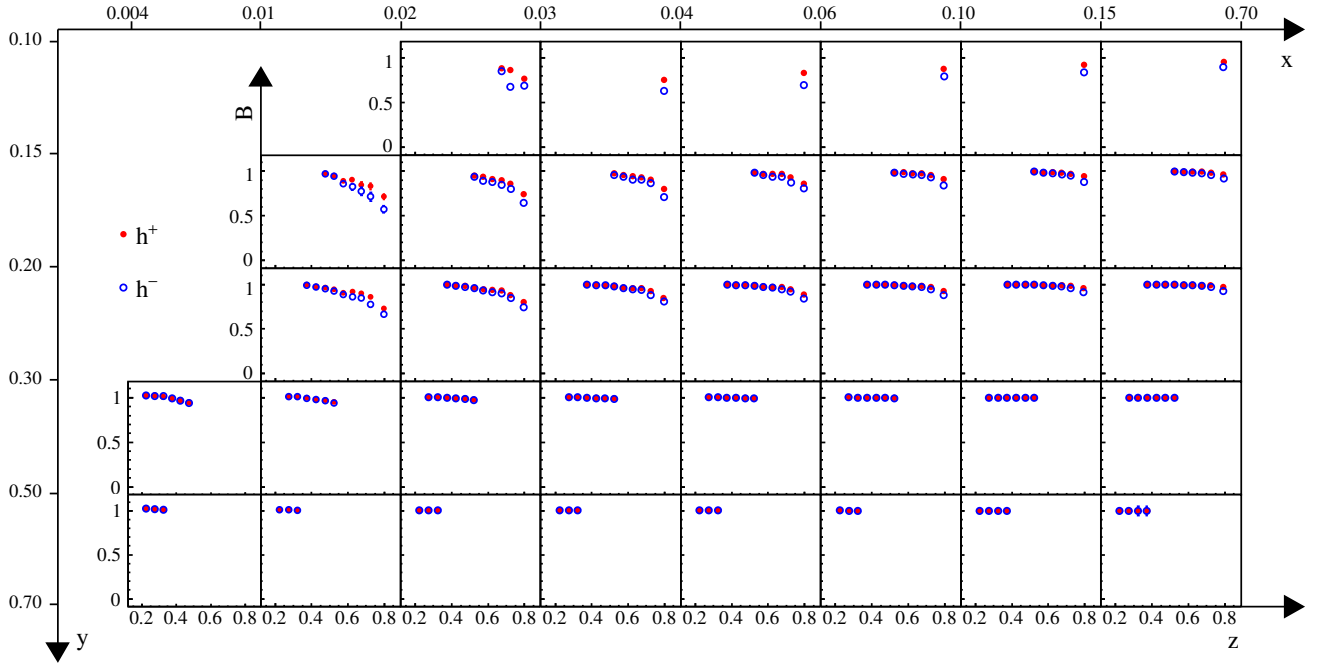


Figure 102: Correction factor B^h for the ρ^0 and ϕ as a function of z for (x, y) bins. The red markers correspond to positive hadrons and the blue markers to negative hadrons.

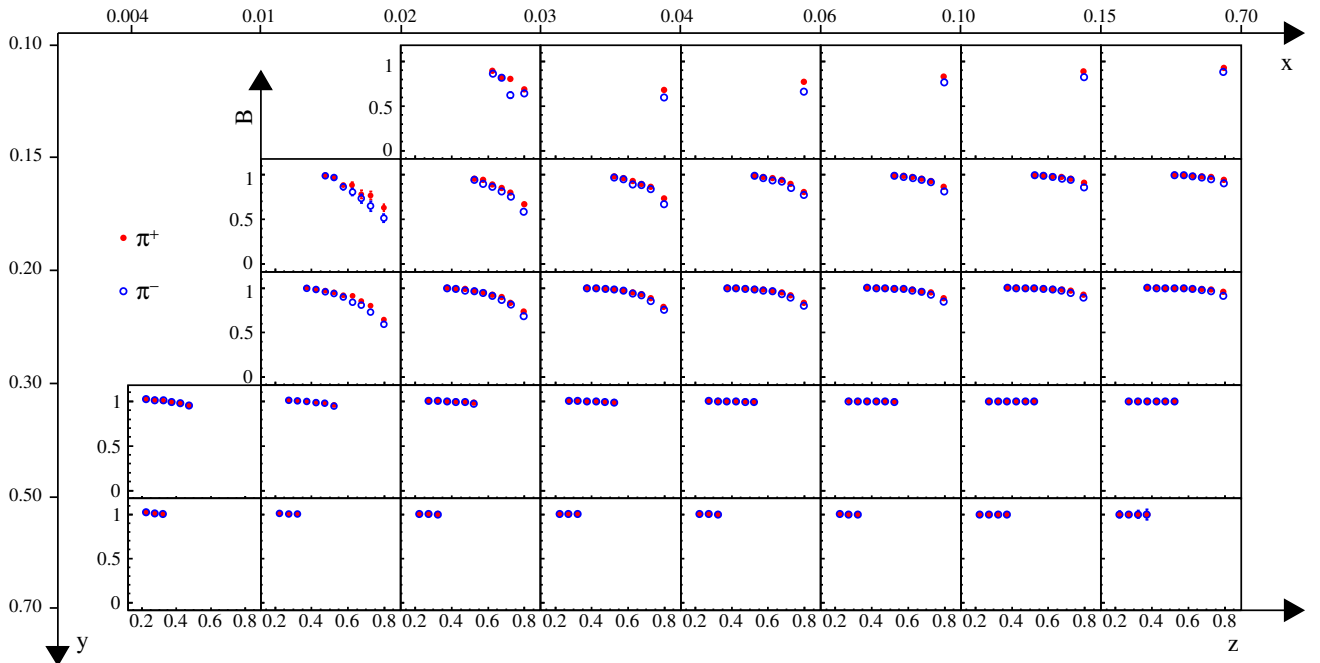


Figure 103: Correction factor B^π for the ρ^0 as a function of z for (x, y) bins. The red markers correspond to positive pions and the blue markers to negative pions.

8.5 LEPTO EXTRAPOLATION

The COMPASS data is truncated in several kinematic variables, which can be considered by theoreticians, except for the cut on the hadron momentum p_h . Due to the hadron momentum cut p_h , done to improve the particle identification, the measured data is cut off. This is nicely observable in the previous chapters in Figures 86, 87 and 88, exposing the raw hadron multiplicities. The z range in one bin corresponds to a p_h region. In some bins in the multiplicities, hadrons are not taken into account due to the p_h cut. Nevertheless, the corresponding DIS events are counted, which leads to smaller multiplicities. A model of multiplicities is added to obtain a result over the full hadron momentum range. The multiplicity of this non-measured range is calculated with the generated MC data set. For the model, the LEPTO parametrisation with JETSET is used. The generated multiplicities in the range between $0 \text{ GeV}/c < p_h < 12 \text{ GeV}/c$ and $40 \text{ GeV}/c < p_h < 180 \text{ GeV}/c$ are extracted. The difference of these calculated multiplicities ($M_{\text{gen}}^{0-180}(x, y, z)$ and $M_{\text{gen}}^{12-40}(x, y, z)$) is the LEPTO contribution in the non-measured range, which is then added to the measured multiplicities. The LEPTO contribution $M_{\text{gen}}^{\text{LEPTO}}(x, y, z)$ is given by

$$M_{\text{gen}}^{\text{LEPTO}}(x, y, z) = M_{\text{gen}}^{0-180}(x, y, z) - M_{\text{gen}}^{12-40}(x, y, z) \quad (81)$$

in x , y and z binning. Figure 104 shows in red (blue) the measured unidentified hadron multiplicities $M^{h^+}(x, y, z)$ ($M^{h^-}(x, y, z)$) in the familiar three-dimensional binning, corrected for the RICH efficiency, radiative correction, electron contribution, vector meson contribution and acceptance. Namely, all corrections, except the LEPTO extrapolation, are applied. In black (orange), the LEPTO extrapolation of the non-measured range is shown for positive (negative) unidentified hadrons. The error bars are not shown here, mainly due to the fact that the errors from the LEPTO extrapolation are absorbed into the systematic uncertainties. Also, the plot with already four quantities would appear unclear and the error bars would be smaller than the markers. The sum of the measured multiplicities and the multiplicities coming from the LEPTO models are the final multiplicities over the full momentum range (0 to 180 GeV/c). But as seen in the Figure, the contribution coming from the model may be very large in the low z region.

The contribution L from the LEPTO extrapolation to the measured multiplicities is given by

$$L = \frac{M^{\text{RD}}}{M^{\text{LEPTO}} + M^{\text{RD}}} \quad (82)$$

with the measured multiplicities M^{RD} and the MC multiplicities of the non-measured momentum range M^{LEPTO} . To be less dependent on the LEPTO model, bins where the contribution L is larger than 10% are taken out of the analysis. Figure 105 shows the contribution according to Equation 82 in the three-dimensional binning, in red (blue) for positive (negative) unidentified hadrons. The dashed line shows the $\pm 10\%$ limit. In the low y region, the contribution of the LEPTO extrapolation is very large, so that only one z bin of twelve remains.

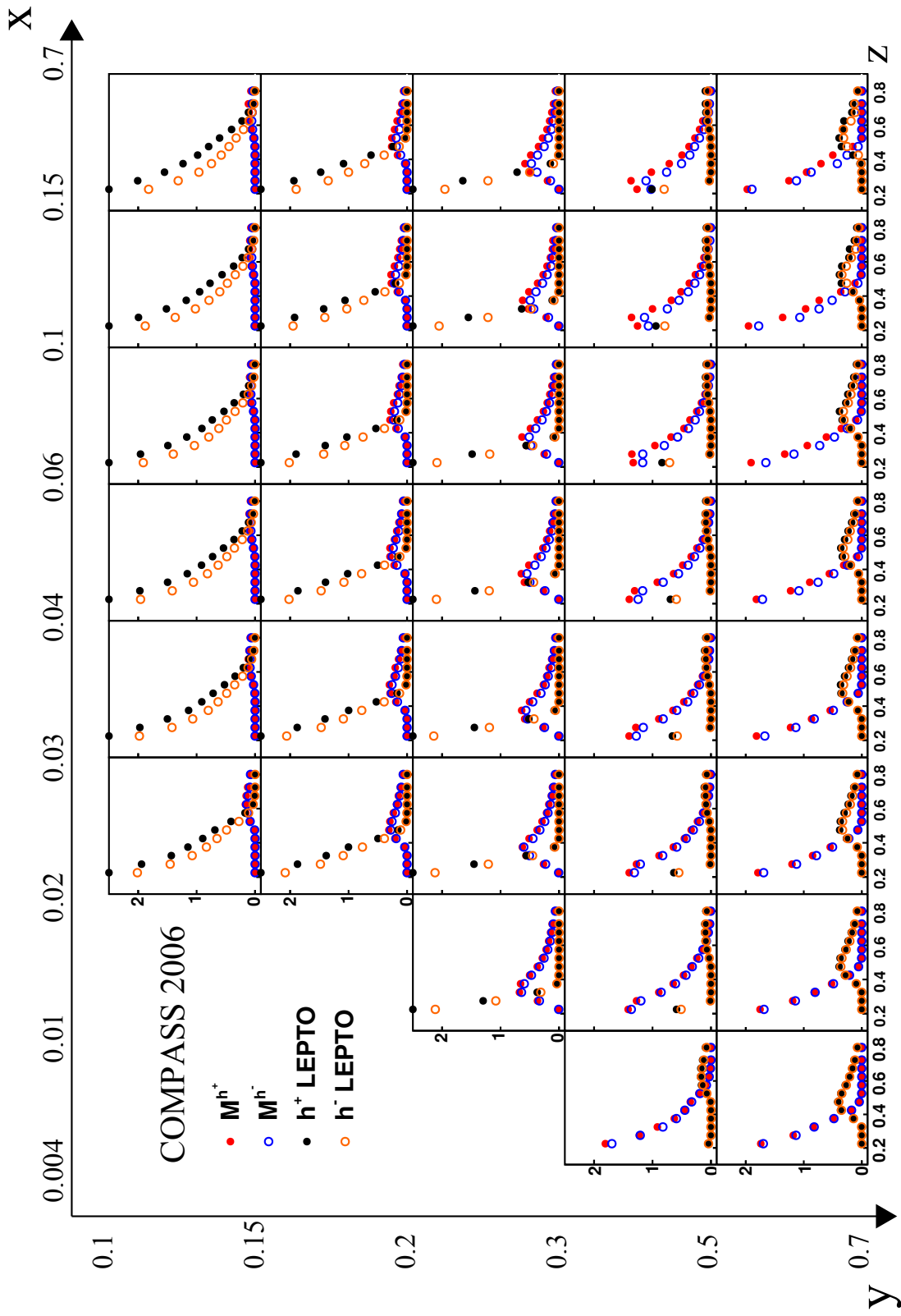


Figure 104: The measured unidentified hadron multiplicities M^{h^\pm} are shown together with the multiplicities from LEPTO in the non-measured range.

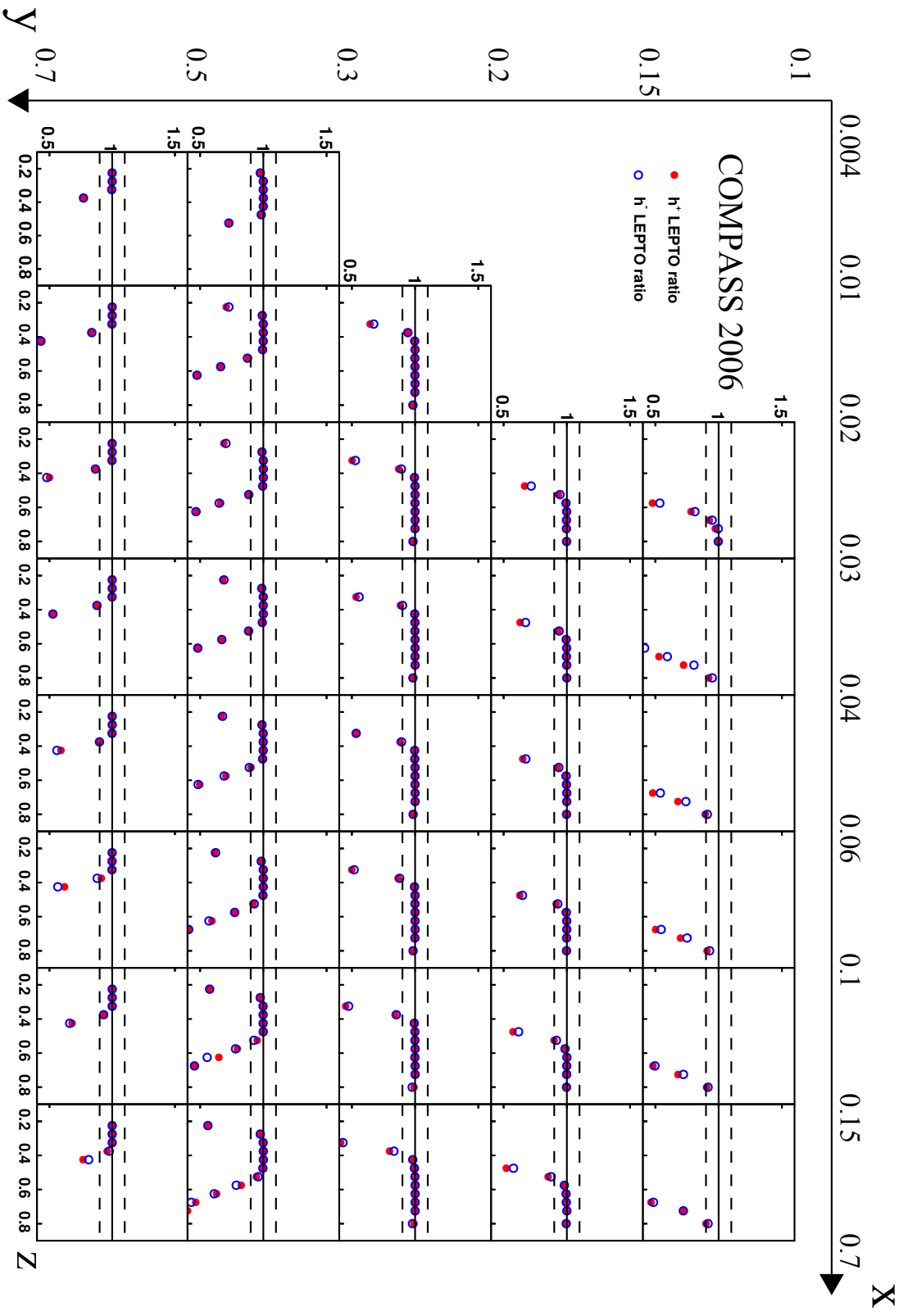


Figure 105: The ratio L of the measured hadron multiplicities and the multiplicities corrected by the LEPTO model are shown in the three-dimensional binning, here for unidentified hadrons. The dashed lines indicate the $\pm 10\%$ range.

FINAL CHARGED HADRON MULTIPLICITIES

The final multiplicities for unidentified hadrons, charged pions and charged kaons are obtained after implementing all correction factors mentioned in Chapter 8. The multiplicities contain corrections for the RICH efficiency, radiative corrections, acceptance, electron contamination and the contribution from diffractive meson production. The non-measured momentum range is filled up with a LEPTO model and bins in which the contribution of the LEPTO extrapolation exceeds 10% are excluded. Before the final result is shown, the systematics uncertainties are summarised. In addition, a preliminary look on the charged kaon multiplicities is presented. An updated version of the pion and unidentified hadron multiplicities and the COMPASS LO extraction of fragmentation function will be published in due time [99].

9.1 SUMMARY OF THE SYSTEMATIC STUDIES

The largest contribution to the final multiplicities comes from the determination of the spectrometer acceptance, the performance of the RICH detector, the correction for the electron contamination and the correction of the diffractive ρ^0 contribution.

The acceptance was determined with a set of Monte Carlo data. The MC simulation uses a LEPTO parametrisation for DIS events, JETSET for the hadronisation and a MSTW08 parametrisation for the parton distribution functions. The determination of the systematic uncertainty for the MC was done by comparing different sets of MC data: one with the default JETSET settings and one with the “high p_t tuning” (used in this analysis) [100]. In addition, different parametrisations of the parton distribution functions were tested. The uncertainty on the acceptance calculation of at most 5% was evaluated.

The systematic uncertainty of the extrapolation to the unmeasured kinematic region, whose contribution is limited to 10%, was estimated by varying the LEPTO parameters and was found to be below 1%.

To estimate the uncertainty linked to the RICH identification and unfolding procedure, different RICH tables were built by varying the matrix elements within their statistical error. The difference on the resulting multiplicities versus the original ones gives an estimate of the uncertainty. In the low hadron momentum region ($z < 0.4$), the uncertainty is below 1% and reaches 2% at high z . No time dependence was observed by comparing the results obtained from data taken over 6 different weeks.

For the electron contamination, an uncertainty of 50% of the correction was estimated on the basis of the data and MC comparison for momenta below 8 GeV/c. As the correction itself is small, the associated uncertainty on the multiplicities is small.

The cross-section for exclusive production of ρ^0 calculated in HEPGEN is normalized to the GPD model of Goloskokov and Kroll [101]. The theoretical uncertainty on the predicted cross-section close to COMPASS kinematics is around 30%. This results in a maximal uncertainty of 30% on the diffractive ρ^0 correction factor, depending on the kinematic range.

The semi-inclusive radiative correction is only used as a function of x and y . The z dependence of the semi-inclusive radiative corrections was calculated with a Monte Carlo simula-

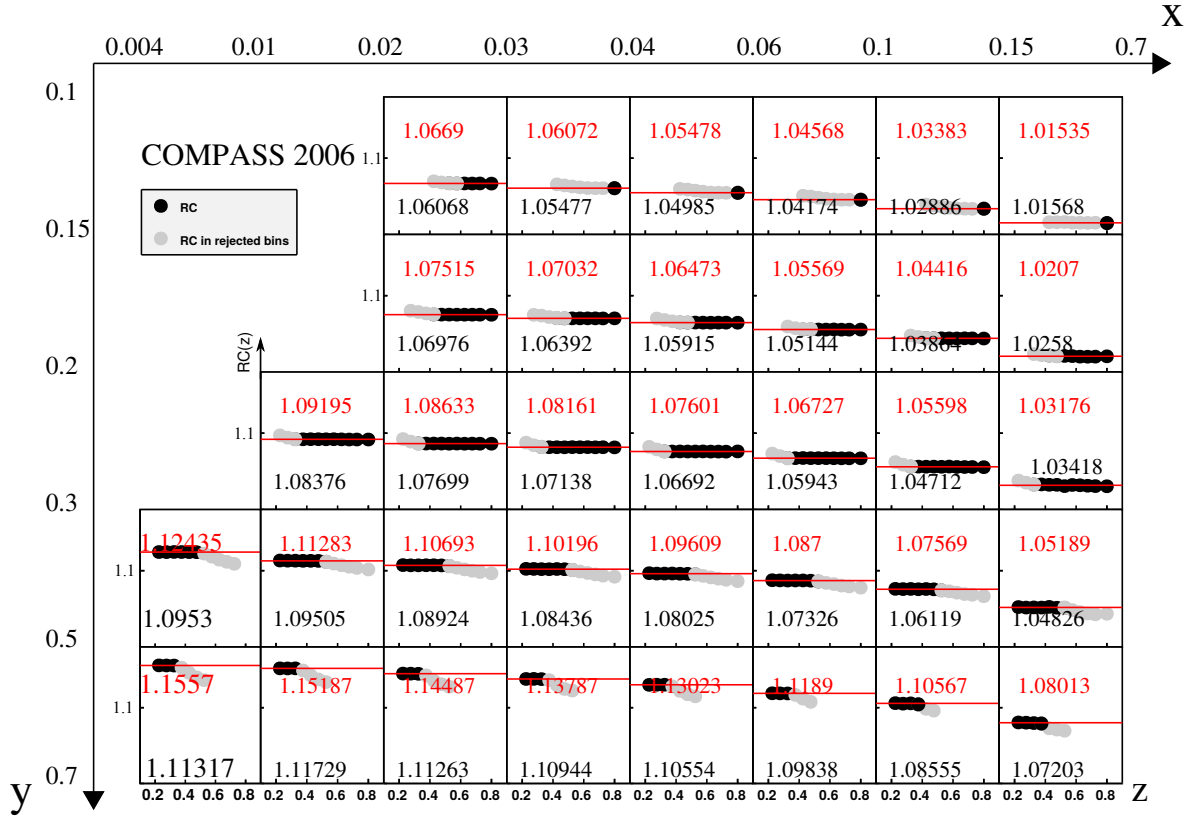


Figure 106: The x , y and z dependence of the semi-inclusive radiative correction extracted from MC data (RADGEN). The black points are used for the analysis while the grey points are rejected due to the LEPTO extrapolation. The black numbers are the RC from TERAD, the red numbers indicated the average of the used z bins. The y -axis of the small histograms ranges from 1.0 to 1.18

tion (RADGEN [102]) and is shown in Figure 106 in the typical three-dimensional binning of the multiplicity analysis (x , y and z). In this Figure, the semi-inclusive correction is drawn in black with the average over z as the red number. The average is determined with a linear fit over the radiative correction. The grey points are the bins excluded by the LEPTO extrapolation and are not taken into account for the determination of the average. The black numbers indicate the radiative correction in this x, y bin from TERAD. The y -axis of the histogram ranges from 1 to 1.18. In most bins, the two numbers agree very well and the z dependence is negligible in the used range of the analysis. The uncertainties of the radiative corrections are small ($<1\%$) compared to the other uncertainties and are neglected.

9.2 FINAL MULTIPLICITIES (H^\pm , π^\pm AND K^\pm)

Figures 107, 108 and 109 show the final result of the unidentified charged hadron multiplicities $M^h(x, y, z)$, the charged pion multiplicities $M^\pi(x, y, z)$ and the preliminary charged kaon multiplicities $M^K(x, y, z)$ in three-dimensional binning with all corrections applied. Negative (positive) hadrons are shown in blue (red). All contributions to the systematic uncertainties were added in quadrature. The total systematic uncertainty varies between 1% and 10%. The systematic uncertainties for the unidentified hadron and the charged pion multiplicities are shown as small bands. For the charged kaon multiplicities, the uncertainties are not shown, as further investigations are ongoing. In all three plots, the prevalent z dependence, a small

but expected x dependence and charge asymmetry between positive and negative hadrons are seen.

The main result of this thesis is the charged pion multiplicity, which looks very similar to the unidentified hadron multiplicity. This is because 70% of all measured hadrons in the kinematic range of COMPASS are in fact charged pions. In both cases (h, π), the statistical error is smaller than the marker and smaller than the systematic uncertainties. The value for each point of the pion multiplicities is shown in the Appendix B with the corresponding statistical and systematic uncertainties. The pion multiplicities are used to determine the favoured and the unfavoured fragmentation functions directly from Equation 43 and with a leading-order fit. A slightly modified result of the hadron and pion multiplicities will be published soon [99] to contribute to the world data fit on fragmentation function. The differences of the newer analysis for the paper and the analysis here presented, are discussed in the summary of the thesis.

The charged kaon multiplicities M^{K^\pm} are currently under further investigation, but a first glimpse is shown in Figure 109. As the previous results on unidentified hadrons and charged hadrons, the kaon multiplicities are corrected for acceptance, radiative correction, RICH efficiency, electron contamination and the diffractive vector mesons ($\phi \rightarrow K^+K^+$). The kinematic dependences are similar to the charged hadron and charged pion multiplicities, but the absolute values of the multiplicities are smaller. The number of measured kaons is smaller, which also leads to larger statistical error bars. The charge asymmetry is visible, the positive kaon multiplicity is always larger than the negative kaon multiplicity. The asymmetry increases with increasing x .

9.3 CHARGE ASYMMETRY

As mentioned above, all measured hadron multiplicities $M^h(x, y, z)$ (with $h = h^\pm, \pi^\pm$ and K^\pm) have an asymmetry with increasing x (in the higher y region). The multiplicities of positive hadrons (red in the Figures) tend to be larger than the negative ones. This effect stems from the quark contents of the measured hadrons, the valence and sea quark content of the struck nucleon in the target:

$$\pi^+ = \left\{ \begin{array}{c} u \\ \bar{d} \end{array} \right\}, \quad \pi^- = \left\{ \begin{array}{c} d \\ \bar{u} \end{array} \right\}, \quad K^+ = \left\{ \begin{array}{c} u \\ \bar{s} \end{array} \right\} \quad \text{and} \quad K^- = \left\{ \begin{array}{c} s \\ \bar{u} \end{array} \right\}. \quad (83)$$

The isoscalar LiD target contains the same amount of u and d quarks ($p = uud$ and $n = udd$). In the pion multiplicities, the positive hadrons exceed the negative ones with increasing x . This is explained by the u -quark dominance. The DIS cross section, in terms of the structure function F_2 (Equations (13) and (16)), depends on the squared charge e_q^2 of the struck quark. In the case of the u -quark, the cross section is therefore elevated in comparison to the d -quark. The struck u -quark hadronises with a higher probability into a positive pion with the favoured fragmentation. The charge asymmetry decreases with decreasing x as the PDF for sea quarks and valence get closer in the small x region.

With larger x , the positive kaon multiplicity M^K is larger than the negative counterpart. This asymmetry is explained by the quark content of the struck target and the quark content of the charged kaons. The positive kaon-meson K^+ contains an u -quark and can be created directly from a struck valence u -quark of the target. The according fragmentation function $D_u^{K^+}$ is a favoured fragmentation. The negative kaon-meson K^- can only be created from a struck sea quark (\bar{u} or s) or via the unfavoured fragmentation.

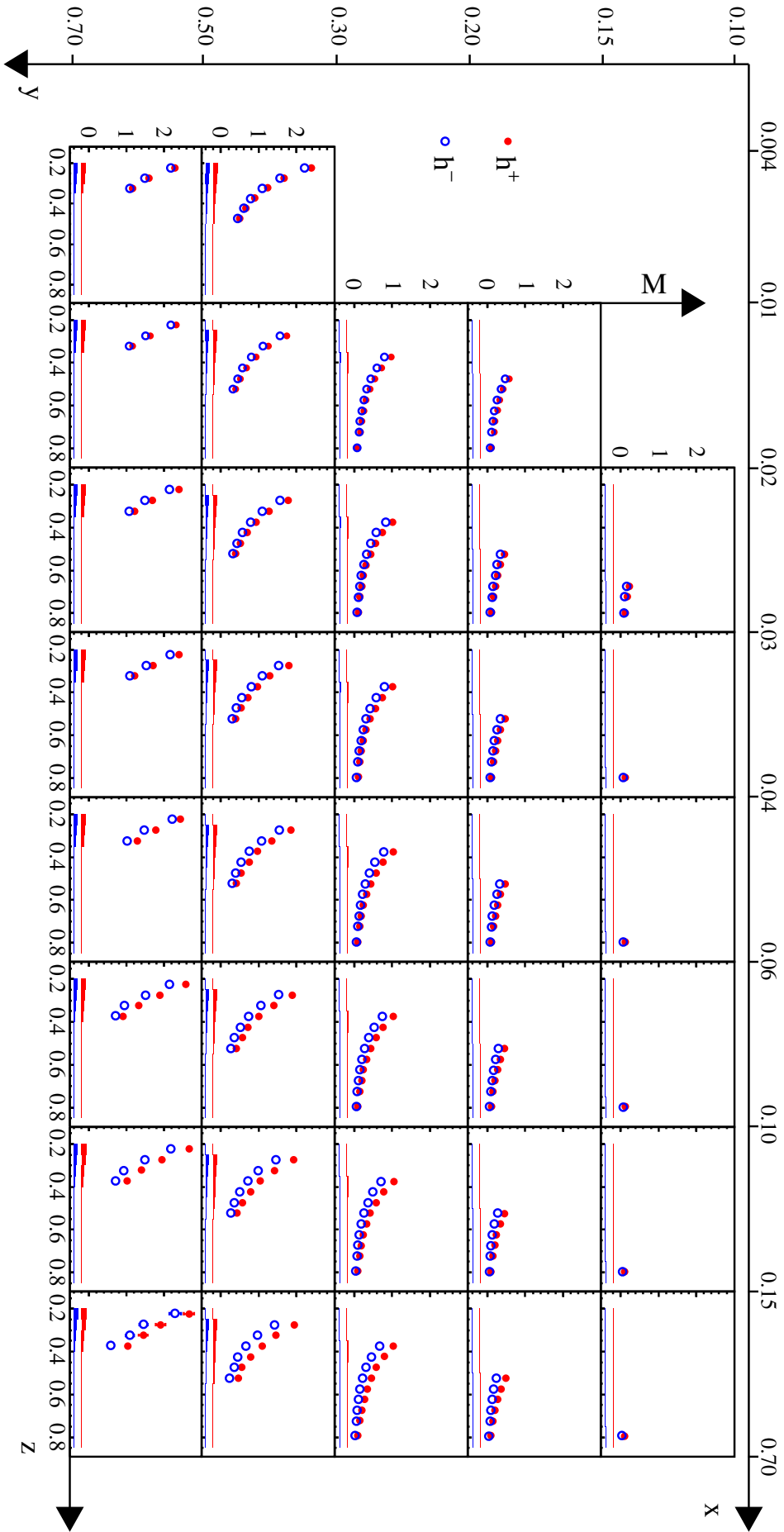


Figure 107: Unidentified hadron multiplicities with vector-meson corrections in x , y and z bin for the 6 weeks of the 2006 data taking. Each column corresponds to an x bin and each row to an y bin. The red markers correspond to positive hadrons and the blue markers to negative hadrons. The systematic errors are shown as error bands below the histograms in the corresponding colour.

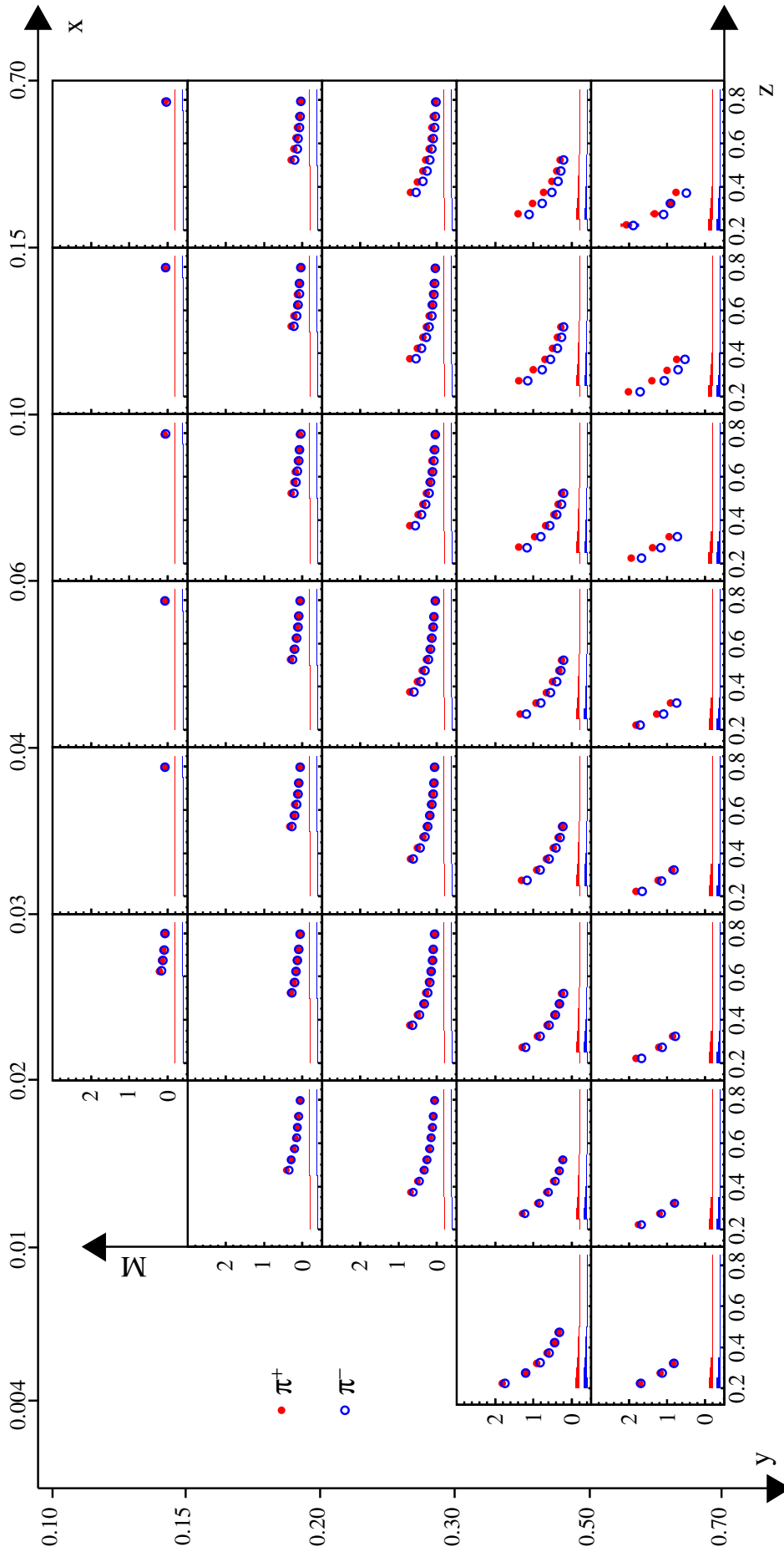


Figure 108: Final pion multiplicities with vector-meson corrections in x , y and z bin for the 6 weeks of the 2006 data taking. Each column corresponds to an x bin and each row to an y bin. The red markers correspond to positive pions and the blue markers to negative pions. The systematic errors are shown as error bands below the histograms in the corresponding colour.

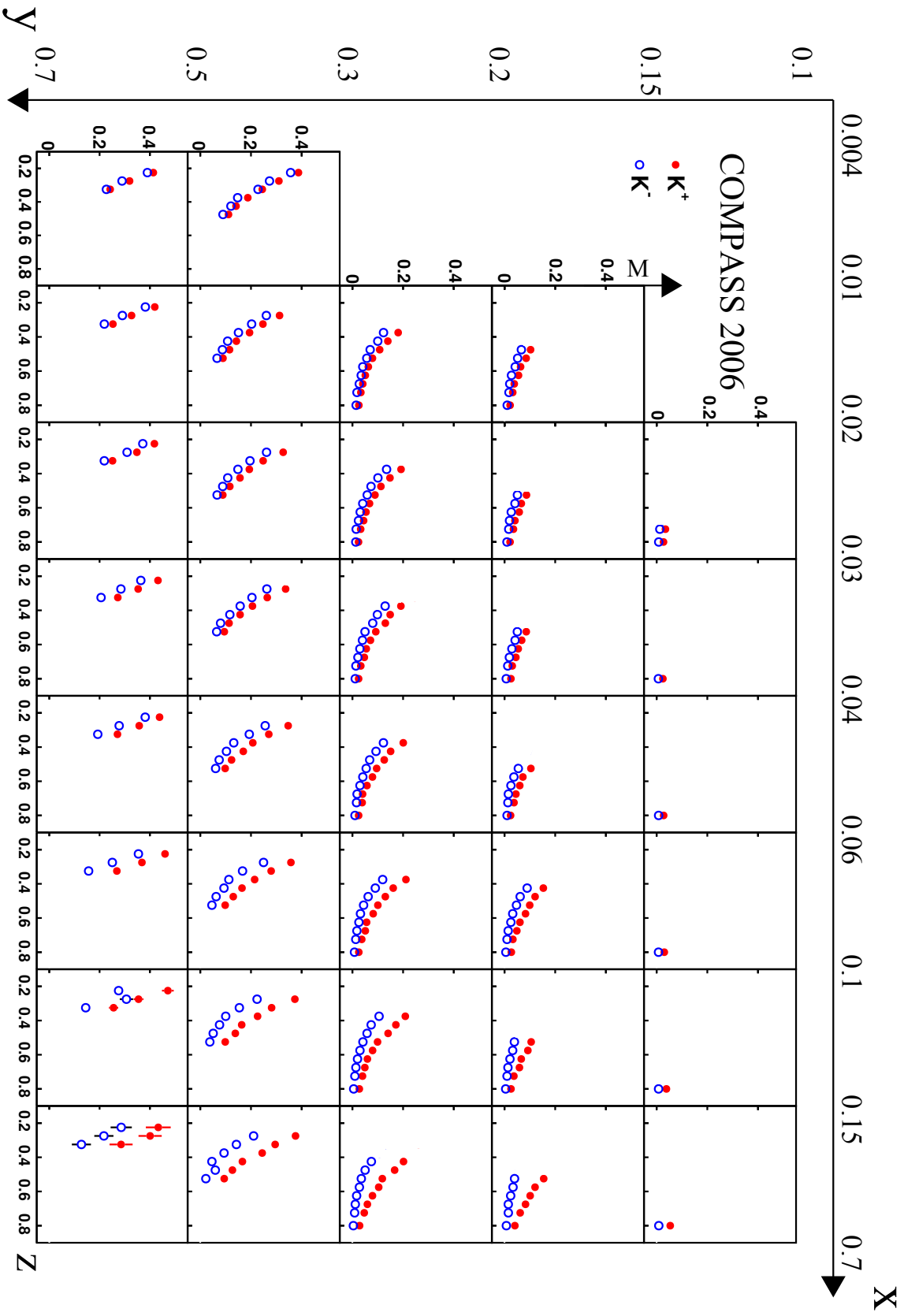


Figure 109: Preliminary kaon multiplicities with vector-meson corrections in x , y and z bin for the 6 weeks of the 2006 data taking. Each column corresponds to an x bin and each row to an y bin. The red markers correspond to positive kaons and the blue markers to negative kaons. The systematic uncertainties are under investigation.

DETERMINATION OF QUARK FRAGMENTATION FUNCTIONS

The measured multiplicities are used to determine the quark fragmentation functions for kaons and pions. In NLO order, this task is performed by a number of theoretical groups like DSS [26], HKNS [103], KRETZER [24] etc... Leading-order extractions are less involved and are performed inside the COMPASS collaboration. As an example, the LO extraction of quark FFs into charged pions is discussed here, using two different approaches. The first one is the direct extraction and the second one is based a LO pQCD [104] fit.

10.1 DIRECT EXTRACTION OF FRAGMENTATION FUNCTIONS

The z -dependent multiplicities and the fragmentation functions are linked in LO by the parton distribution functions $q(x, Q^2)$ of a quark of flavour q and the wanted fragmentation functions D_q^h

$$\frac{dM^h(x, z, Q^2)}{dz} = \frac{d^3\sigma^h(x, z, Q^2)/dxdQ^2dz}{d^2\sigma^{\text{DIS}}(x, Q^2)/dxdQ^2} \stackrel{\text{LO}}{=} \frac{\sum_q e_q^2 q(x, Q^2) D_q^h(z, Q^2)}{\sum_q e_q^2 q(x, Q^2)} \quad (84)$$

For simplification, the kinematic dependence of the PDF ($q \equiv q(x, Q^2)$) and the fragmentation function ($D_q^h(z, Q^2) \equiv D_q^h$) are dropped in the following. The multiplicities for charged hadrons and an isoscalar target can be written as:

$$M^{h^+} = \frac{4(uD_u^{h^+} + \bar{u}D_{\bar{u}}^{h^+}) + (dD_d^{h^+} + \bar{d}D_{\bar{d}}^{h^+}) + (sD_s^{h^+} + \bar{s}D_{\bar{s}}^{h^+})}{5Q + 2S} \quad (85)$$

$$M^{h^-} = \frac{4(uD_u^{h^-} + \bar{u}D_{\bar{u}}^{h^-}) + (dD_d^{h^-} + \bar{d}D_{\bar{d}}^{h^-}) + (sD_s^{h^-} + \bar{s}D_{\bar{s}}^{h^-})}{5Q + 2S},$$

with the sum over the light quark-antiquarks $Q = Q(x, Q^2) = (u(x, Q^2) + \bar{d}(x, Q^2) + u(x, Q^2) + \bar{d}(x, Q^2))$ and the sum over the strange quarks $S = S(x, Q^2) = (s(x, Q^2) + \bar{s}(x, Q^2))$. The quark content of charged pions consists of up, down and the corresponding anti-quark: $\pi^+ = u\bar{d}$ and $\pi^- = d\bar{u}$. For the pion fragmentation functions, twelve FFs remain: $D_u^{\pi^+}$, $D_{\bar{d}}^{\pi^+}$, $D_{\bar{u}}^{\pi^+}$, $D_d^{\pi^+}$, $D_s^{\pi^+}$, $D_{\bar{s}}^{\pi^+}$, $D_u^{\pi^-}$, $D_{\bar{d}}^{\pi^-}$, $D_{\bar{u}}^{\pi^-}$, $D_d^{\pi^-}$, $D_s^{\pi^-}$ and $D_{\bar{s}}^{\pi^-}$, only assuming up, down and strange quarks to contribute. With the charge conjugation ($D_q^{h^+} \equiv D_{\bar{q}}^{h^-}$), six fragmentation functions remain in Equation 85. A further reduction of the number of fragmentation is done with the introduction of the favoured (unfavoured) fragmentation function D_{fav}^π (D_{unf}^π). The hadronisation of a quark q into a hadron h , which contains the quark q , is called *favoured*. If the final hadron does not contain the fragmenting quark q , the fragmentation function is called *unfavoured*. As the charged pions do not contain any strangeness, the s quark fragmentation is considered as unfavoured. In this approach, it is assumed that all favoured FFs are equal and that favoured FFs are larger than the unfavoured ones

$$D_{\text{fav}}^\pi = D_u^{\pi^+} \equiv D_{\bar{d}}^{\pi^+} \equiv D_d^{\pi^-} \equiv D_{\bar{u}}^{\pi^-} \quad (86)$$

$$D_{\text{unf}}^\pi = D_{\bar{d}}^{\pi^+} \equiv D_{\bar{u}}^{\pi^+} \equiv D_s^{\pi^+} \equiv D_{\bar{s}}^{\pi^+} \equiv D_{\bar{d}}^{\pi^-} \equiv D_u^{\pi^-} \equiv D_s^{\pi^-} \equiv D_{\bar{s}}^{\pi^-}$$

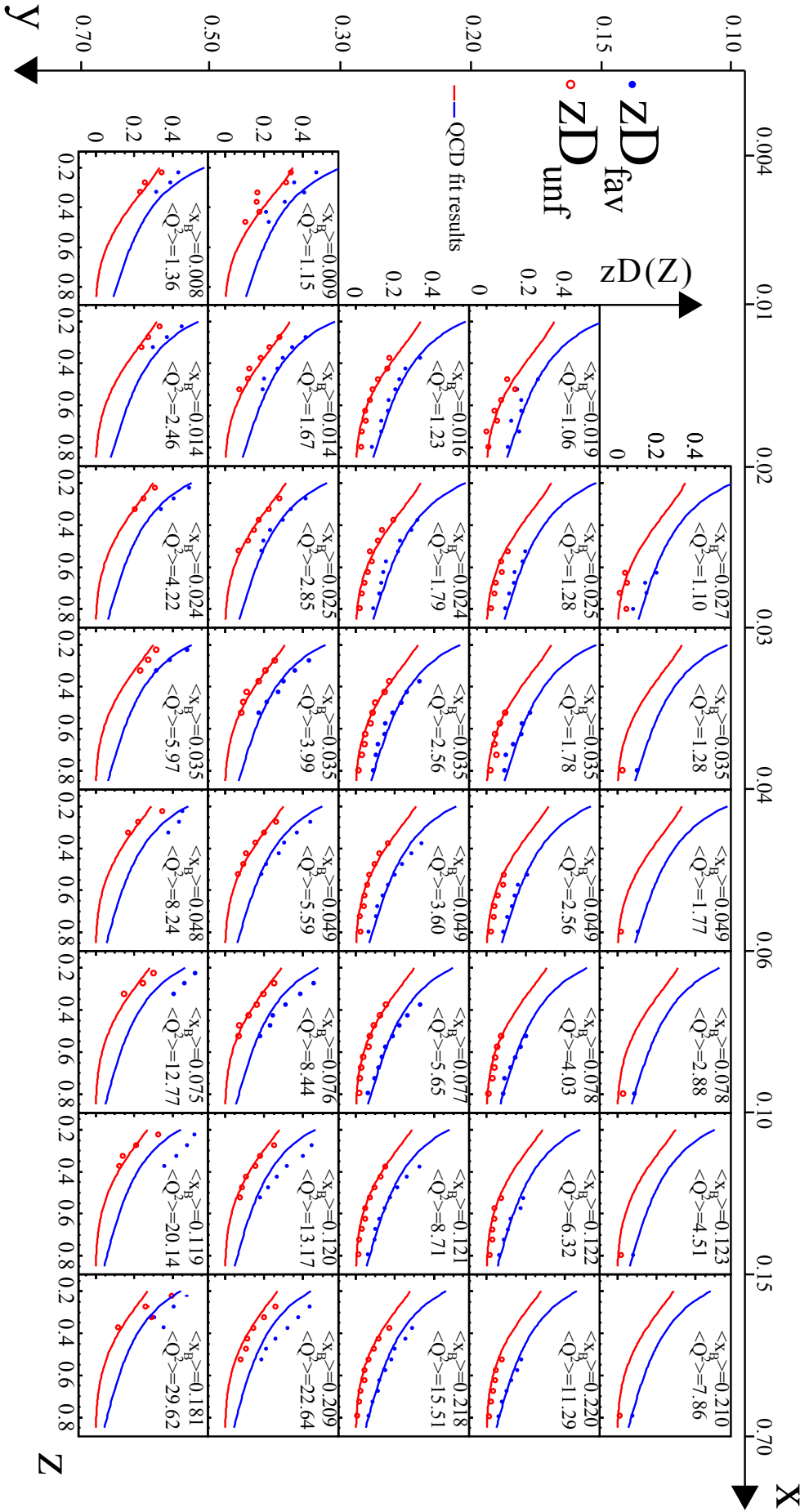


Figure 110: Direct determination of the pion fragmentation function in the three-dimensional binning: the favoured and the unfavoured fragmentation functions (zD_{fav}^{π} and zD_{unf}^{π}) extracted from pions are shown here.

With ?? and the assumptions made in Equation 86, the charged pion multiplicities can be rewritten in terms of the two fragmentation functions and the PDFs:

$$\begin{aligned} M^{\pi^+} &= \frac{4[(u+d) + \bar{u} + \bar{d}]D_{\text{fav}}^{\pi} + [u+d + 4(\bar{u} + \bar{d}) + 2s + 2\bar{s}]D_{\text{unf}}^{\pi}}{5Q + 2S}, \\ M^{\pi^-} &= \frac{4[(\bar{u} + \bar{d}) + u + d]D_{\text{fav}}^{\pi} + [4(u+d) + \bar{u} + \bar{d} + 2s + 2\bar{s}]D_{\text{unf}}^{\pi}}{5Q + 2S}. \end{aligned} \quad (87)$$

The linear equation system can be written in terms of matrices

$$\begin{pmatrix} M^{\pi^+} \\ M^{\pi^-} \end{pmatrix} = \begin{pmatrix} \frac{4[(u+d) + \bar{u} + \bar{d}]}{5Q+2S} & \frac{[u+d+4(\bar{u} + \bar{d}) + 2s + 2\bar{s}]}{5Q+2S} \\ \frac{4[(\bar{u} + \bar{d}) + u + d]}{5Q+2S} & \frac{[4(u+d) + \bar{u} + \bar{d} + 2s + 2\bar{s}]}{5Q+2S} \end{pmatrix} \begin{pmatrix} D_{\text{fav}}^{\pi} \\ D_{\text{unf}}^{\pi} \end{pmatrix} \rightarrow \vec{M} = B \cdot \vec{D} \quad (88)$$

and is solved by inverting the matrix B to calculate \vec{D} , the unknown fragmentation functions D_{fav}^{π} and D_{unf}^{π} . For each data point (x, y, z) of the measured π^{\pm} multiplicities, the favoured and the unfavoured fragmentation functions are calculated by solving Equation 88. The parton distribution functions ($u, d, \bar{u}, \bar{d}, s$ and \bar{s}) are first calculated for each x bin center and the corresponding average Q^2 , using the code from hepforge¹, and make use of the recent MSTW08 parametrisation [16] (note that the program output is $xq(x, Q^2)$). The PDFs are visualised in Figure 8. The result of this analysis is shown in Figure 110, in the same binning as the measured multiplicities. The favoured fragmentation functions (zD_{fav}^{π}) is shown in blue and the unfavoured one (zD_{unf}^{π}) in red. In addition, the LO COMPASS fit result, which is discussed right below, is shown in the same Figure. The LO fit results are calculated in a grid of Q^2 and the closest value to the average $\langle Q^2 \rangle$ is used for the comparison.

In Figure 111, the charged pion multiplicities are displayed in an alternative way. For the eight x bins, the z and the y dependence of the multiplicities M^{π} are shown in a staggered way with the average Q^2 . The y bins are colour-coded and staggered by the addition of α (between 0 and 1.00) for a better comparison of the z -slope of the multiplicities. Only the statistical uncertainties are shown. The lines correspond to the global LO fit of positive and negative pion multiplicities used to extract pion FFs. It illustrates the good coverage in z of the COMPASS measurement when averaging over y . This allows for a QCD fit to the data extracting parametrisations of the FFs.

10.2 COMPASS LEADING-ORDER FIT

In addition to the direct extraction, a LO pQCD fit on the measured pion multiplicities is performed by the COMPASS collaboration [105]. For the combined analysis of π^+ and π^- multiplicities, isospin and charge symmetry are imposed as in the direct extraction in Equation 86, leading to the two pion fragmentation functions D_{fav}^{π} and D_{unf}^{π} . The aim is to extract a z -dependent parametrisation for the two FFs. The DGLAP code [106] is used for the Q^2 evolution for each data point. Even in LO, this evolution involves the additional gluon fragmentation functions with $D_{\text{g}}^{\pi} = D_{\text{g}}^{\pi^{\pm}}$. For the parton distribution functions $q(x)$, the leading-order MSTW08 parametrisation is used. The functional form

$$D_i(z, Q_0^2) = N_i z^{\alpha_i} (1-z)^{\beta_i} \quad (89)$$

¹ <https://mstwpdf.hepforge.org/code/code.html>

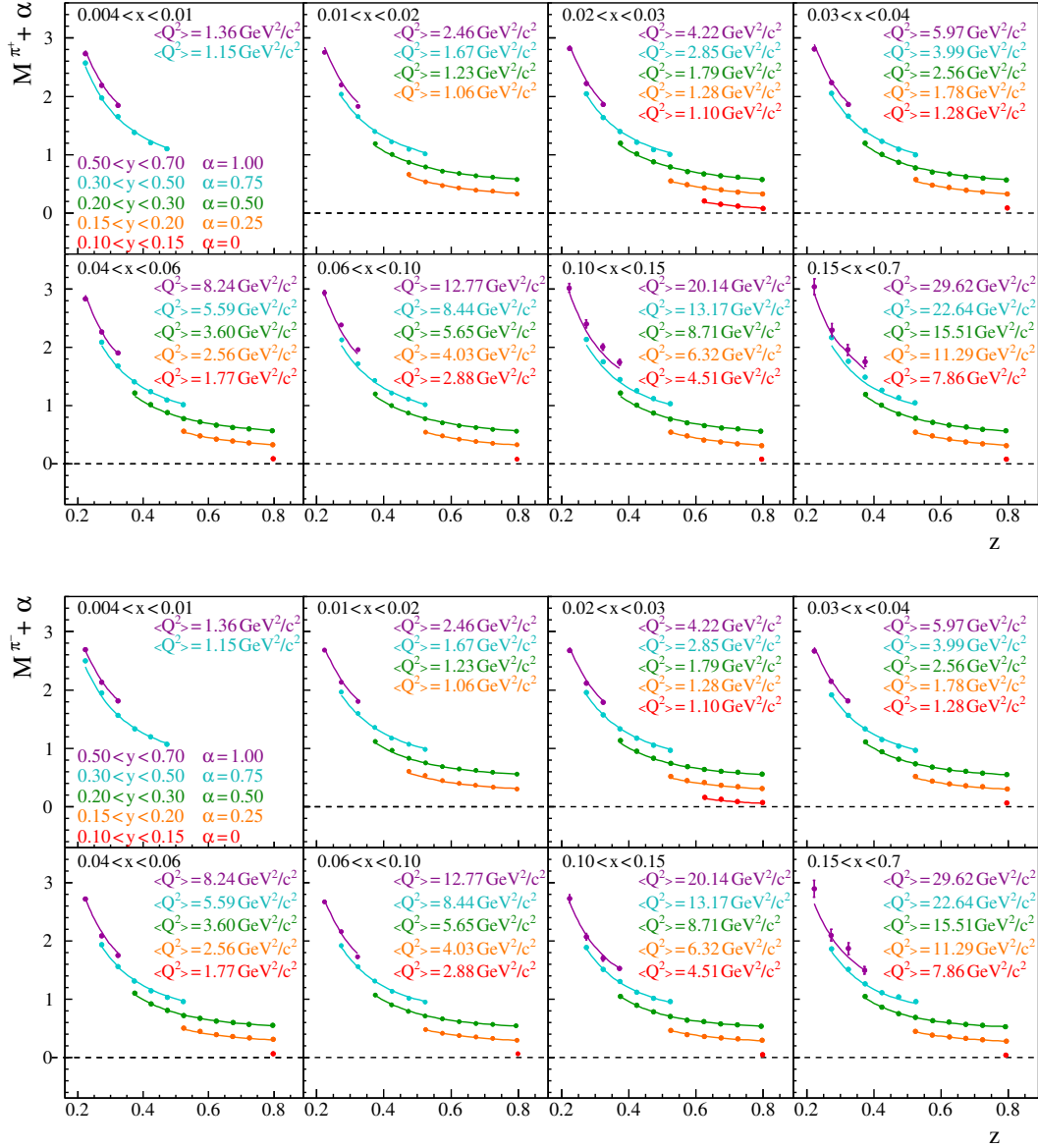


Figure 111: Charged pion multiplicities as a function of z for 8 x and 5 y bins. The different y bins are shown in a staggered way and are colour-coded. The curves correspond to the LO COMPASS fit for the according Q^2 .

is used to describe the z dependence of the FFs, calculated at a reference scale $Q_0^2 = 1 \text{ GeV}/c^2$ for $i=\text{fav, unfav, g}$. To take into account the limited z -range, the normalisation of the parametrisation is modified according to

$$D_i(z, Q_0^2) = N_i \frac{z^{\alpha_i} (1-z)^{\beta_i}}{\int_{0.2}^{0.85} z^{\alpha_i} (1-z)^{\beta_i} dz}. \quad (90)$$

Then, a standard χ^2 minimisation procedure is applied:

$$\chi^2 = \sum_{j=1}^N \left[\left(\frac{\sum_q e_q^2 q(x_j, Q_j^2) D_q^{\pi^\pm}(z_j, Q_j^2)}{\sum_q e_q^2 q(x_j, Q_j^2)} - M_{\text{exp}}^{\pi^\pm}(x_j, Q_j^2, z_j) \right) / \Delta_j \right]^2 \quad (91)$$

with the measured multiplicities $M_{\text{exp}}^{\pi^\pm}(x_j, Q_j^2, z_j)$ and the quadratic sum of the statistical and uncorrelated systematic uncertainties, Δ_j^2 . The number of data points is denoted as N .

For the fit, the C++ framework ROOT MINUIT² is used for the minimisation. For each data point, the FFs are evolved to the corresponding Q^2 , the multiplicities are calculated according to Equation 84 and compared with the measured multiplicities.

The uncertainties of the extracted FFs are determined with the bootstrap method [107]. For that, a number of resamples of the original multiplicity dataset is generated. This is done by adding noise to each data point of the original dataset. The noise is randomly generated from a zero-centered Gaussian distribution with the width of the data points error. For each resample the FFs are extracted using the fit procedure from Equation 91. The error bands are determined as the mean value and the root mean square of the extracted FFs from the resamples. For the current analysis, 100 resamples are used. Error bands for statistical and systematical errors are calculated with the assumption that the systematic errors are correlated. For a resample, each systematic error is weighted by the same randomly determined value. For both error bands (the statistical and systematical), the statistical errors are used for the calculation of the χ^2 sum.

The result of the fragmentation function $zD_{\text{fav}}^{\pi^+}$ ($zD_{\text{unf}}^{\pi^-}$), determined with the COMPASS fit, is shown in Figure 112 in blue (red) for $Q^2 = 3 \text{ GeV}^2/c$. The solid blue and red lines are the result from the unmodified multiplicity data set. Two error bands are shown in the corresponding color: the darker ones for the statistical uncertainty (barely visible) and the systematical uncertainty as a lighter band. In grey, the ratio of the FFs is shown with the according statistical error band, most of the systematics cancel. As expected, the favoured FF is larger than the unfavoured one. The ratio the two fragmentation functions decreases with higher z . In the favoured case, for example, an u quark makes the transition to a $\pi^+ = u\bar{d}$, but to create positive pions from d -quarks (unfavoured fragmentation D_{unf}), an intermediate step is needed. An additional quark (\bar{u} or a \bar{d}) is needed. In this case, the probability that the hadron holds a large portion of the photon energy is smaller, as further more hadrons have to be created.

² <http://hep.fi.infn.it/minuit.pdf>

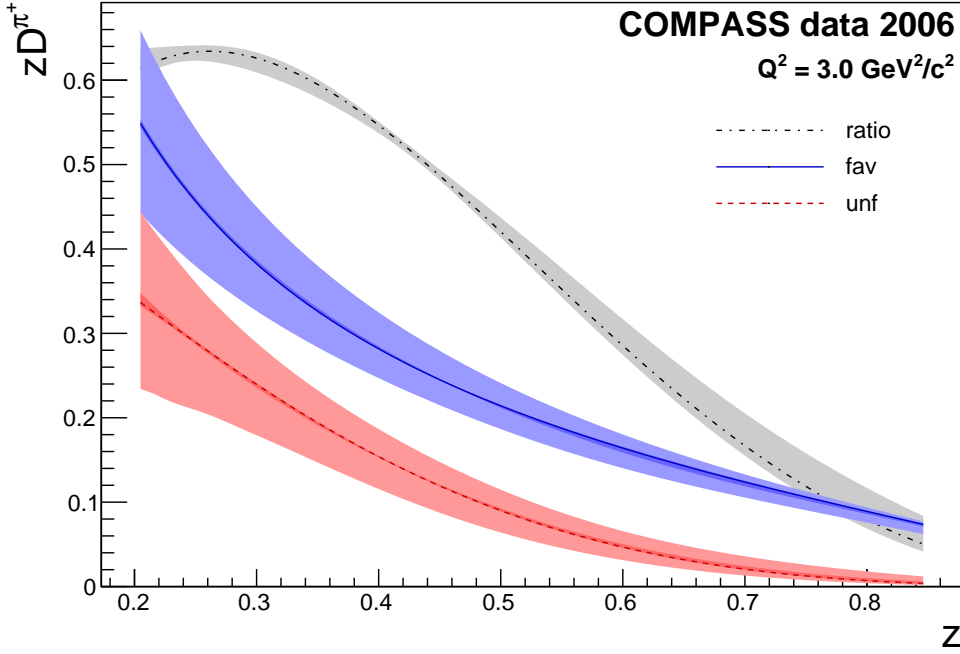


Figure 112: The LO fit result of the favoured (blue), unfavoured fragmentation function (red) and the ratio (grey) including the error bands for statistics and systematics uncertainties. Calculated for $Q^2 = 3 \text{ GeV}^2/c^2$.

10.3 LO AND NLO PARAMETRISATIONS

Experimental results on multiplicities were used by several theory groups to extract FFs. As an example, the DSS and HKNS parametrisations are briefly described. All theory groups use similar assumptions on fragmentation functions such as the isospin symmetry and the momentum conservation. Perturbative QCD fits are used to extract the fragmentation functions in LO and NLO, but the focus lays nowadays on the NLO FFs. The differences between the different groups are due to different analysis methods, different data set and further assumptions.

DSS [108]: D. de Florian, M. Stratmann and R. Sassot performed a fit to extract the FF for charged kaons (K^\pm), pions (π^\pm) and protons (p/\bar{p}). The data sets used in this fit include e^+e^- data from CERN-LEP and SLAC [109]. For pp collisions, data from the BRAHMS [110], PHENIX [111] and STAR [112] experiments at RHIC [113] are used. Results from semi-inclusive deep inelastic scattering is considered from the HERMES experiment [36] at HERA and from the EMC [34] experiment. Also, preliminary results from the COMPASS experiments have been included [100]. In the global analysis, the individual fragmentation functions for all partons are determined by fitting the following functions at a starting scale Q_0^2 to the charged hadron multiplicities:

$$D_i^h(z, Q_0^2) = \frac{N_i z^{\alpha_i} (1-z)^{\beta_i} [1 + \gamma_i (1-z)^{\delta_i}]}{B[2 + \alpha_i, \beta_i + 1] + \gamma_i B[2 + \alpha_i, \beta_i + \delta_i + 1]}. \quad (92)$$

Here, $B[a, b]$ is the Euler Beta-function and N_i represents the contribution of D_i^h in the momentum sum rule. Isospin symmetry for the sea and valence quarks, ($D_u^{\pi^+} = D_d^{\pi^+}$) is imposed. In addition, it is assumed for strange quarks that

$$D_s^{\pi^+} = D_{\bar{s}}^{\pi^+} = N' D_u^{\pi^+}, \quad (93)$$

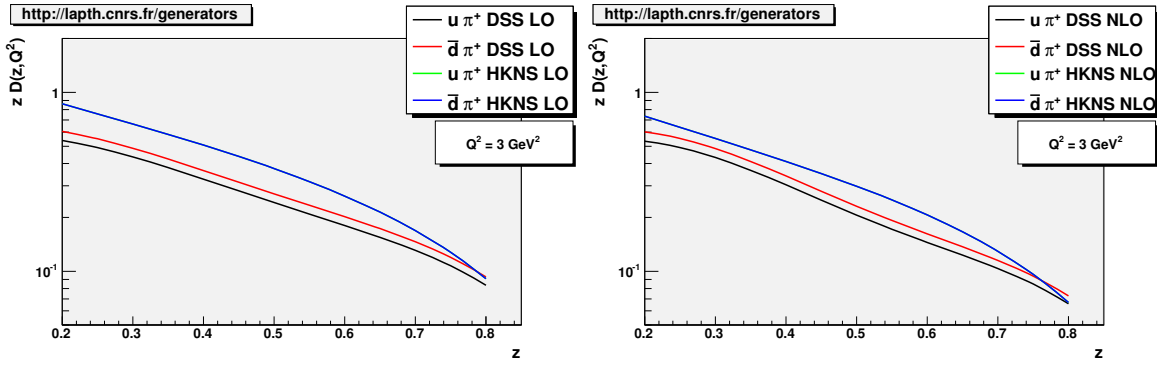


Figure 113: Fragmentation of u and \bar{d} quark in positive pions as an example for the favoured fragmentation, in leading order (left) and next-to-leading order (right).

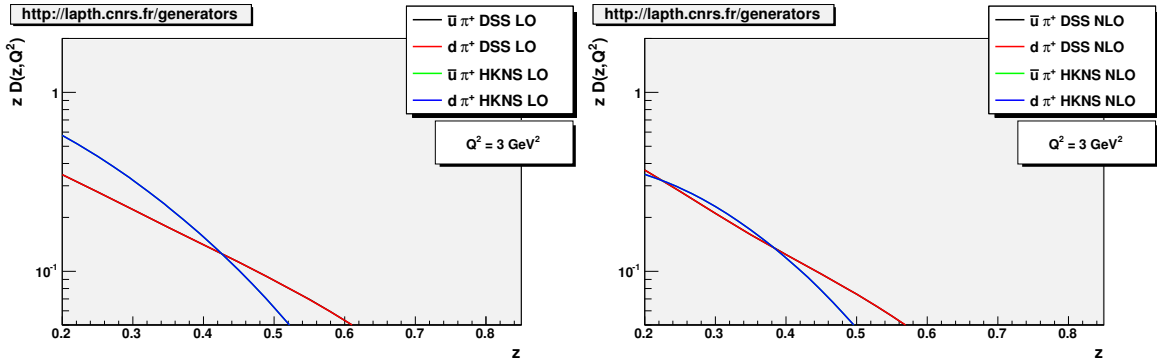


Figure 114: Fragmentation of d and \bar{u} quark in positive pions as an example for the unfavoured fragmentation, in leading order (left) and next-to-leading order (right).

where N' is a normalisation factor, independent of z .

For the unfavoured kaon fragmentation, it is assumed that all distributions have the same functional form and cannot be distinguished between flavours:

$$D_{\bar{u}}^{K^+} = D_s^{K^+} = D_d^{K^+} = D_{\bar{d}}^{K^+}. \quad (94)$$

HKNS [103]: The parametrisation of fragmentation functions from M. Hirai, S. Kumano, T.-H. Nagai, and K. Sudoh is based on data coming from e^+e^- collisions (for instance TASSO [114], TOPAZ [115], DELPHI [116]) with identified final-state hadrons. The data with unidentified hadrons is disregarded to avoid contamination. The following functional form

$$D_i^h = N_i^h z^{\alpha_i^h} (1-z)^{\beta_i^h} \quad (95)$$

is fitted at an initial scale of $Q_0^2 = 1 \text{ GeV}^2/c^2$. The function has 14 fit parameters. The main assumption is the equality of all favoured fragmentation functions and the fixing of the gluon parameters.

Kretzer [24]: Similar to HKNS, Kretzer uses data from e^+e^- annihilation with hadrons in the final state (ALEPH [117], TPC [118], SLD [119]). Also, the same functional form used for the fit (see Equation 95). The aim of the Kretzer parametrisation is the determination of FF to pions and kaons and unidentified hadrons. The major Ansatz and the difference to HKNS is power-like suppressions of the unfavoured fragmentation with

$$D_u^{\pi^+} = D_{\bar{d}}^{\pi^+}, D_{\bar{u}}^{\pi^+} = (1-z)D_u^{\pi^+}, D_u^{K^+} = (1-z)D_s^{K^+}, D_{\bar{u}}^{K^+} = (1-z)^2D_s^{K^+}. \quad (96)$$

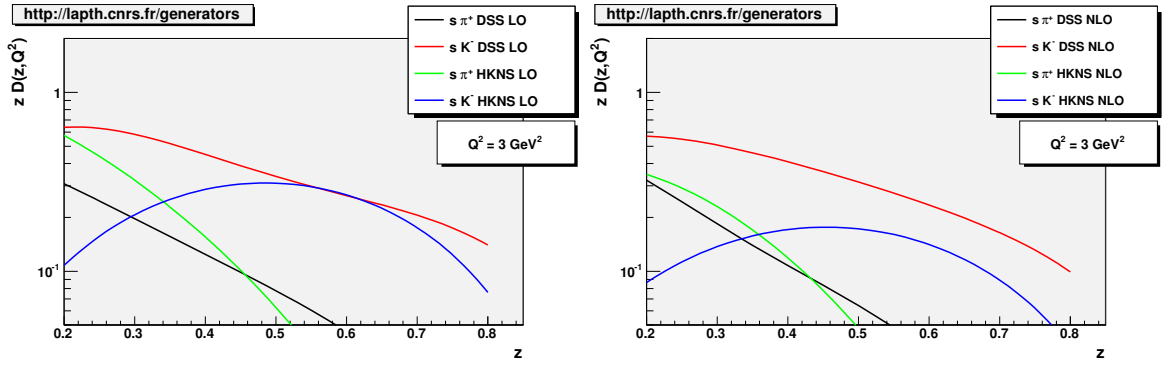


Figure 115: Fragmentation of a strange quark s into π^+ and K^- , in leading order (left) and next-to-leading order (right).

The following symmetries and hierarchy are assumed using charge conjugation and the valence structure of pions and kaons and strangeness suppression:

$$\begin{aligned}
 D_q^{h^+, h^-} &= D_{\bar{q}}^{h^-, h^+} \\
 D_d^{\pi^+} &= D_{s, \bar{s}}^{\pi^+} < D_u^{\pi^+} = D_{\bar{d}}^{\pi^+} \\
 D_{\bar{u}}^{K^+} &= D_{d, \bar{d}}^{K^+} < D_u^{K^+} < D_{\bar{s}}^{K^+}
 \end{aligned} \tag{97}$$

Figures 113, 114 and 115 show various fragmentation functions zD_q^h as a function of z within the range used in the COMPASS analysis ($0.2 < z < 0.85$). Both, leading and next-to-leading orders are shown for two of the introduced parametrisations (DSS and HKNS). All plots are shown for $Q^2 = 3 \text{ GeV}^2/c^2$ and are taken from <http://laphth.cnrs.fr/ffgenerator>.

First, as an example for the favoured fragmentation function, the transitions $u \rightarrow \pi^+$ and $\bar{d} \rightarrow \pi^+$ are shown. In the case of HKNS, these two FFs are identical due to the assumptions made in the calculation. In the case of DSS, they differ by a small amount (0.15 to 0.2). The HKNS parametrisation is systematically larger than the DSS one by roughly 30%. This difference is smaller in the NLO analysis. But overall, the plots show the expected decrease and the typical slope of the fragmentation functions with increasing z .

For the unfavoured one, the fragmentation functions $zD_{\bar{u}}^{\pi^+}$ and $D_{\bar{d}}^{\pi^+}$ are chosen as an example. As expected, the unfavoured FF is smaller than the favoured one. Again, some lines are overlapping in the Figure due to the assumption that all unfavoured FFs are equal.

Figure 115 shows the fragmentation function of strange quarks s into π^+ and K^- . The DSS strange FF decreases with increasing z . In the case of HKNS, the FF $zD_s^{K^-}$ starts with a low value of 0.1 and has a maximum at $z = 0.5$, then the FF decreases. The NLO results show similar behaviours. The kaon fragmentation functions of the two groups differs up to a factor of 4. This displays the difficulty to extract the kaon FFs.

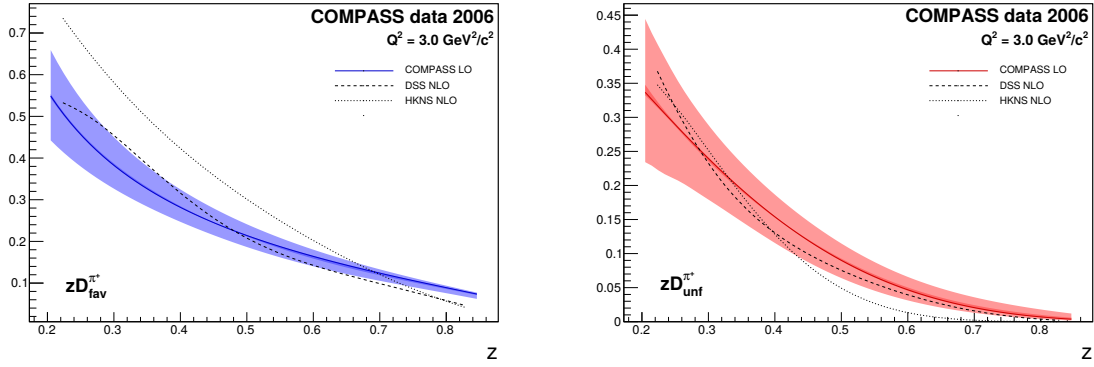


Figure 116: Left: LO COMPASS fragmentation function compared with the NLO parametrisation of DSS and HKNS. Calculated for $Q^2 = 3 \text{ GeV}^2/c^2$.

The two obtained FFs from the LO fit at COMPASS are compared in Figure 116 with the NLO parametrisation from HKNS and DSS. The comparison with LO parametrisation would lead to larger differences.

In the favoured case and up to $z = 0.7$, the HKNS parametrisation in NLO is systematically larger than the COMPASS result. Above $z = 0.7$, the slope is much steeper than the COMPASS one. The HKNS slope does not match well the COMPASS one. On the other hand, the COMPASS fit on FFs agrees well with the parametrisation from DSS and are over a large z range in the systematic uncertainty of the COMPASS fit. In the unfavoured case, the differences between the three parametrisation are not as large. But still, the DSS one seems to agree better to the COMPASS results. Over the full z range, the DSS curves is within the systematical uncertainty in the LO parametrisation.

The large difference to HKNS may stem from the fact that they only use data from e^+e^- annihilation. Here, only the sum of fragmentation is determined and for the separation of favoured and unfavoured FFs assumptions are necessary. The well matching result of the COMPASS fragmentation functions and the NLO result from DSS show that, with the current set-up and analysis method, COMPASS is well prepared for the extraction of kaon FFs.

SUMMARY AND OUTLOOK

A study on the quark fragmentation functions D_q^h has been carried out by measuring charged hadron multiplicities in semi-inclusive deep inelastic scattering ($\mu + N \rightarrow \mu' + h + X$). The measurement was performed in 2006 by the COMPASS experiment at the M2 beam line of the Super Proton Synchrotron at CERN, using a 160 GeV/c muon beam impinging on an isoscalar lithium-deuterid target. The data was collected using a trigger system for scattered muons coming from the target region.

The trigger system mainly consists of pairs of scintillator hodoscopes. For stable data taking, the performance of the trigger is checked with online methods. The online monitoring comprises *e.g.* rate stability, check of expected hit patterns and the observation of the trigger time resolution. The typical time resolution of a muon trigger is $\delta t \sim 1$ ns. An offline method to determine the hodoscope and trigger efficiency is introduced using reconstructed data selected by the Calorimeter Trigger. The hodoscope efficiency reaches up to 99.9 %, while the trigger efficiency is about 90 %.

For the COMPASS II phase, a new trigger system for muons with large scattering angles was needed. The Large Angle Spectrometer Trigger was realised in 2010 with the implementation of the hodoscopes H1 and H2 in the first COMPASS spectrometer part. The functionality, the stability and the time resolution ($\delta t \sim 0.9$ ns) are comparable to the already existing trigger system. This system is able to trigger on four-momentum transfer Q^2 up to 100 GeV²/c² and thus enlarging the kinematic acceptance for scattered muons.

In a fixed target experiment, the luminosity is given by the target density and the integrated particle flux. Two different methods for the flux determination are presented, by counting beam tracks using a true random trigger (Random Trigger method) and by counting hits in the scintillating fibre station of the beam telescope (Scaler method). Both methods were studied in details for the 2009 data taking and agree well, resulting in a luminosity of 3.86 pb⁻¹. Systematic studies shows that the uncertainty of the Random Trigger method is below 5 %, allowing a precise determination of the muon flux. The systematic uncertainty of the Scaler method was studied and ranges from 10 to 15 %. This method can be used for a fast determination of the flux or when larger systematic uncertainties are acceptable. In addition, the luminosity of the 2006 data set, used for the multiplicity analysis, is determined with the Scaler method. The result is 0.54 fb⁻¹.

The hadron multiplicities M^h are given by the number of hadrons of the type h per deep inelastic scattering event. They are determined for unidentified hadrons h^\pm , charged pions π^\pm and charged kaons K^\pm in a three-dimensional binning of the Bjorken scaling x , the relative photon energy y and hadron energy fraction z . Several correction factors are taken into account to obtain the final results of the charged multiplicities. They include corrections for radiative effects (inclusive and semi-inclusive ones), correction for the hadron identification procedure. The measured multiplicities are corrected for the spectrometer acceptance, contribution of diffractive vector meson production and contamination of electrons and positrons. The previous corrections are obtained with detailed studies on Monte Carlo simulations. In addition, the measured multiplicities are extrapolated towards the non-measured hadron momentum range using a Monte Carlo model. The final charged hadron multiplicities show the expected strong z dependence. Due to the large amount of collected data, the statistical

uncertainties for the unidentified hadron and the pion multiplicities are small. The main contributions to the systematic uncertainties are coming from the hadron identification and the acceptance correction. The measured π^+ and π^- multiplicities are used to determine the pion fragmentation functions in LO with two different methods. The favoured and unfavoured fragmentation functions are obtained by a direct extraction (point-by-point) and by a LO pQCD fit with a parametrisation for the fragmentation functions. The fragmentation functions shows a strong z dependence as expected from current parametrisations. The favoured FF is larger than the unfavoured one, especially in the high z region. The results are compared with existing NLO parametrisations from DSS and HKNS and the fitted COMPASS fragmentation agree well to the DSS parametrisation. The next step is the determination of the kaon fragmentation functions.

The analysis presented in this thesis and the results of the multiplicities, which will be published [99], differ in some points. A new x binning is used for $0.004 < x < 0.4$ and new cut on the virtual photon energy ν is introduced, replacing the LEPTO extrapolation. In addition, bins in which the hadron acceptance is smaller than 30 % are not included in the new analysis. These changes further improved the quality of the measured charged hadron multiplicities. The future COMPASS physics program includes the DVCS measurement with a 2.5 m long liquid hydrogen target and a muon beam with a momentum of 160 GeV/c. The measurements are expected to take place in 2016 and 2017. In parallel, the measurement of semi-inclusive deep inelastic scattering will be done. Already in 2012, a successful DVCS test measurement took place and the analysis for the determination of the multiplicities on a proton target has already started.

III

APPENDIX

APPENDIX A

This Appendix contains supporting technical Figures and Tables.

Figure 117 shows all elements in the M2 beam line, from the production target T6 to the second spectrometer magnet SM2 in the COMPASS experiment.

Figures 118 - 120 are technical drawings for the most common light guides used in H1 and H2. The design is loosely based on existing light guides in the COMPASS experiment and scaled/modified for the specific needs.

The voltage dividers for the XP2982 of the H1 hodoscope were designed by the colleagues of the Warsaw University of Technology and the circuit design is shown in Figure 121.

Figure 122 is a picture of the hodoscope H1, before the installation in the experiment. The different groups, cased by the ROHACELL/fibre glass sandwich, are visible and the attachment of the soft iron shielding on the frame. The central hole in the ROHACELL construction indicates the position of the air light guides.

Figure 123 shows the hodoscope H2 during installation. The aluminium structure, the patch panel cabling and the layout of the scintillator slabs are visible.

Figure 124 and 125 show the stability simulation for the two new hodoscopes H1 and H2. Table 8 summarises all scintillator trigger elements. The position, size, number of slabs and the PMTs used are shown.

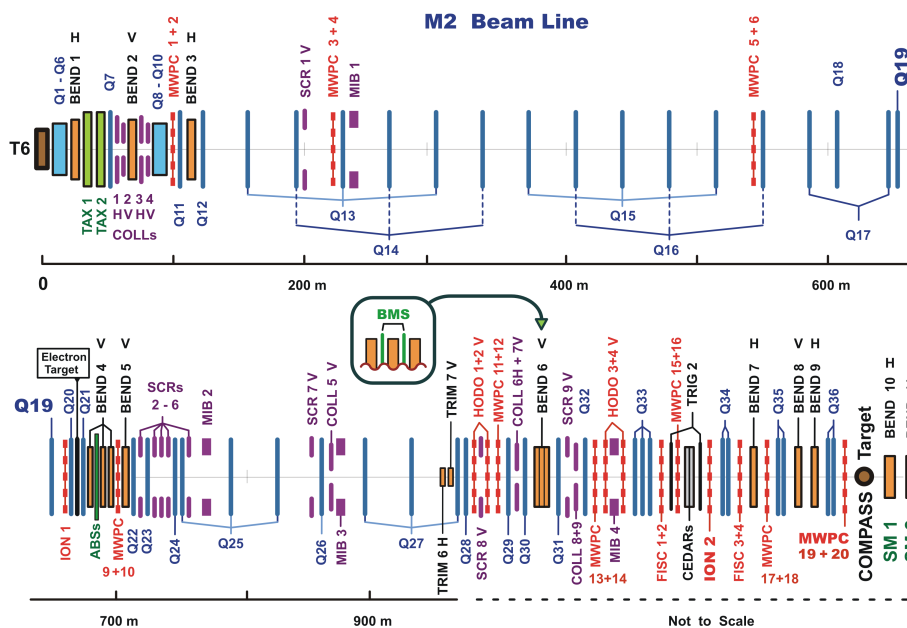


Figure 117: The M2 beam line with all elements.

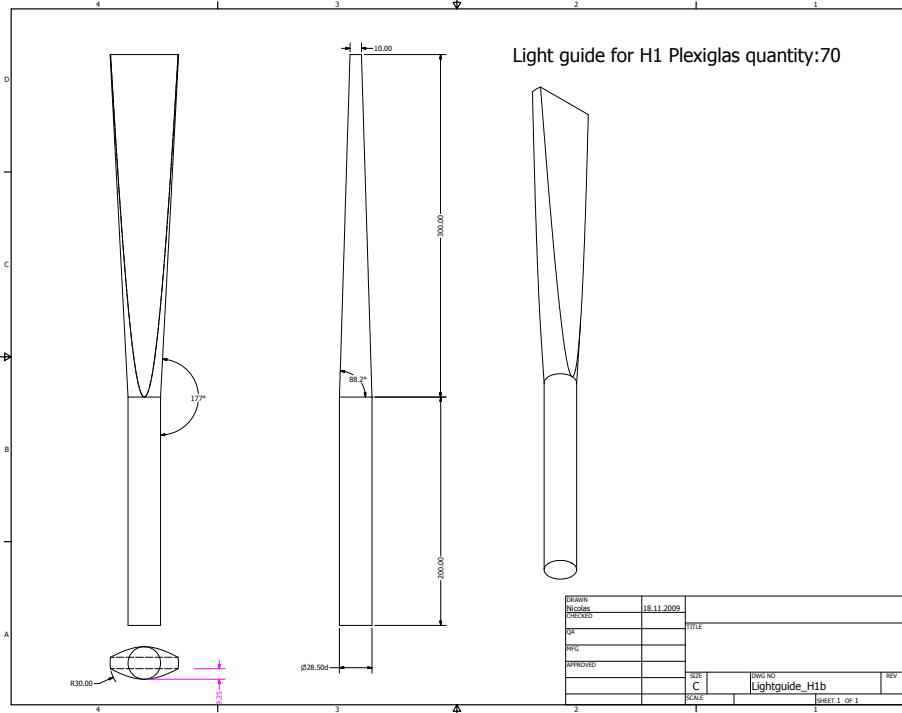


Figure 118: The standard light guide used in H1, made of PMMA.

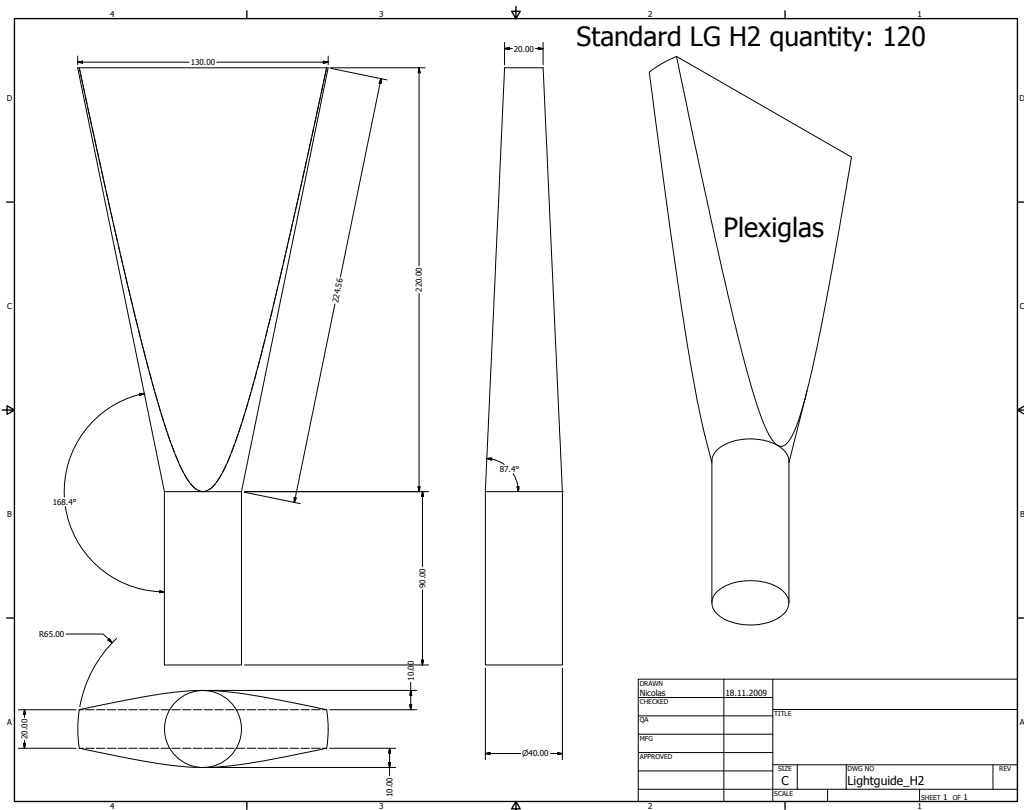


Figure 119: The standard light guide used in H2, made of PMMA.

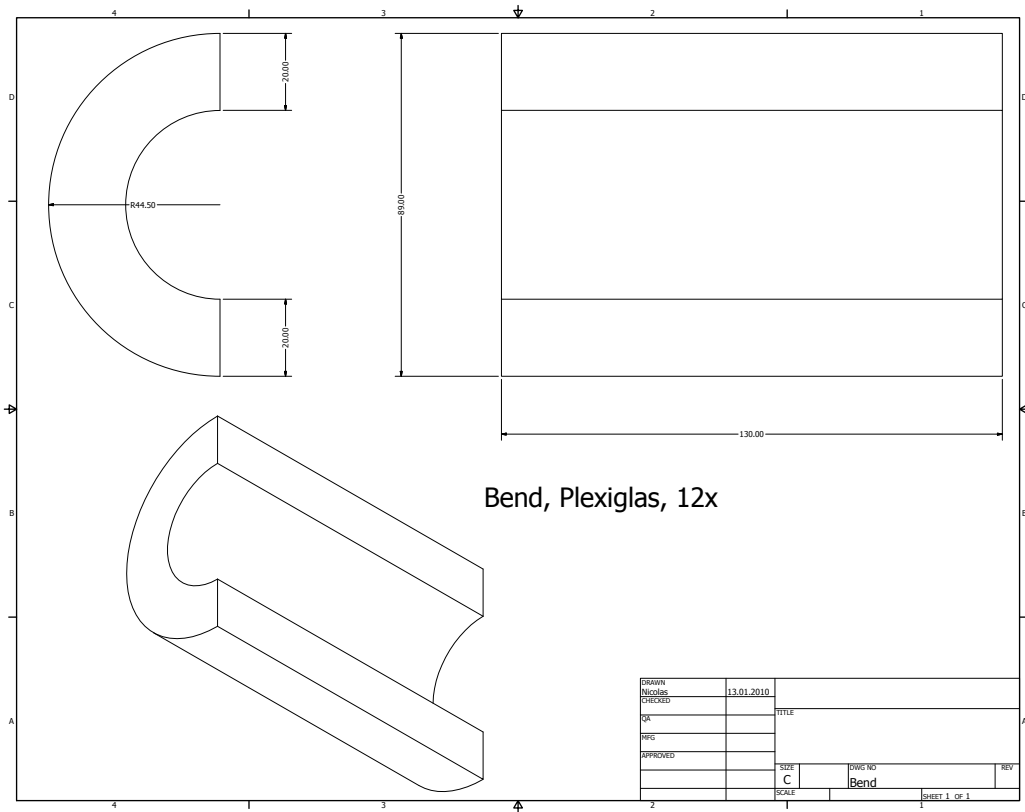


Figure 120: Bent light guide of the central H2 slabs.

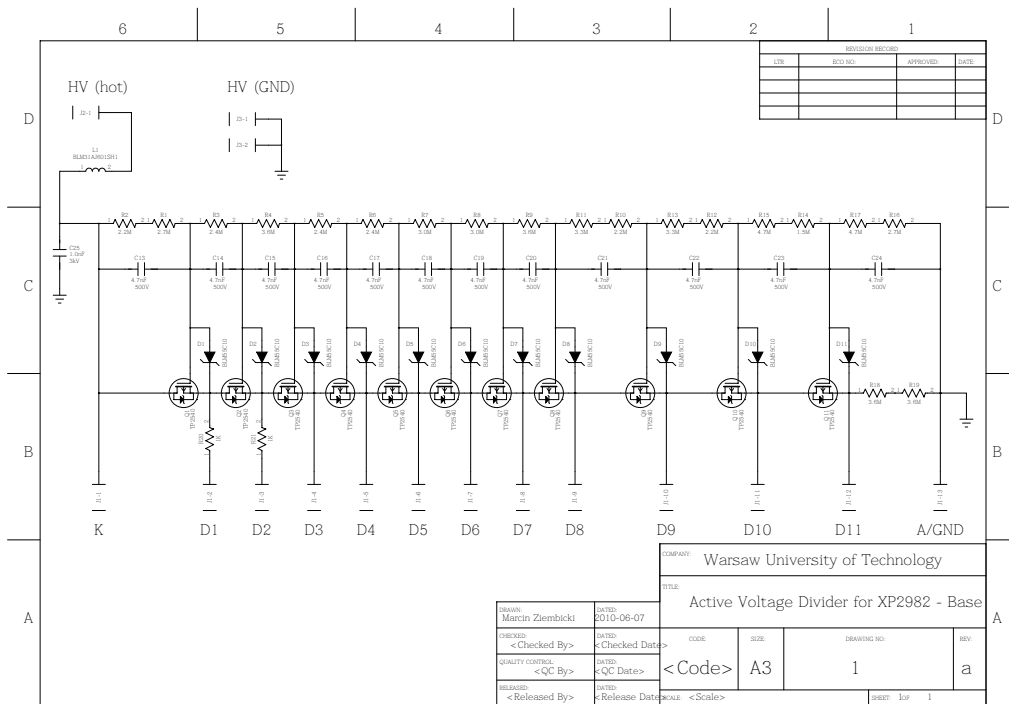


Figure 121: Circuit plan of the H1 voltage divider. It fits to XP 2982 PMTs.



Figure 122: Picture of H1 during construction, attached to the mounting frame with wheels.



Figure 123: Picture of H2 during installation in 2010.

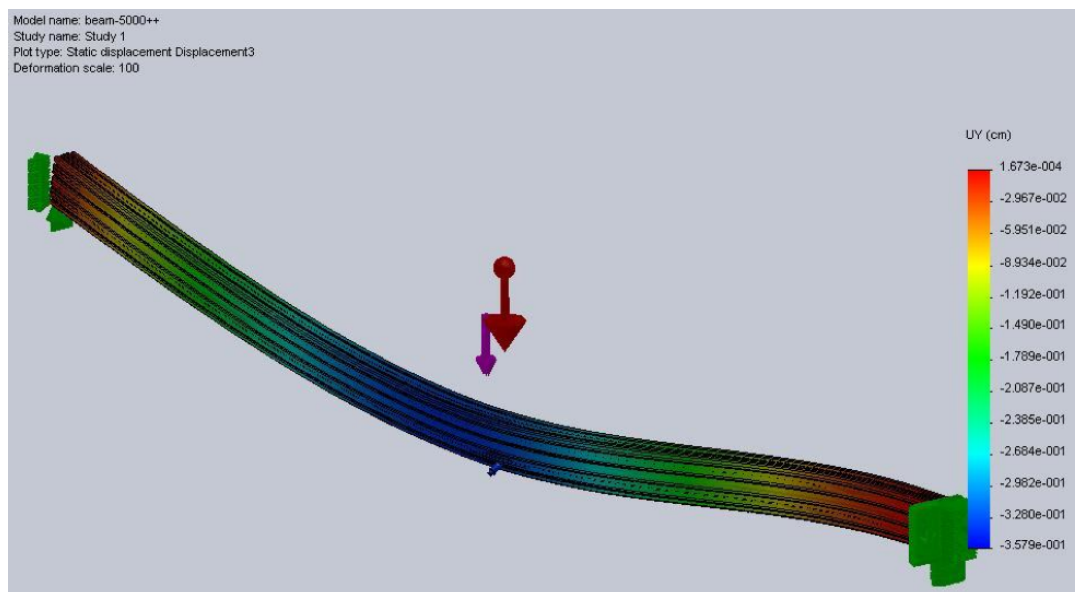


Figure 124: Simulation of the H1 frame stability. The deformation is colour-coded.

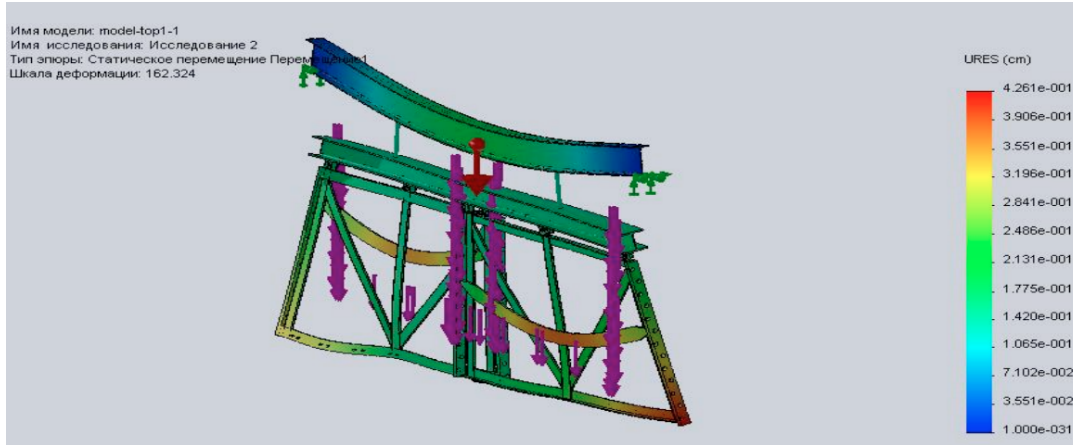


Figure 125: Stability of the H2 frame. the deformation coming from the weight of the detector and the magnetic force between SM2 and the soft iron shielding are shown.

System	Hodoscope	No. of strips	Width (mm)	z-Pos. (m)	Area ($x \times y$) (cm^2)	PMT type
Inner	H4I (up)	32	6	32	17.34×32	R7400
	H4I (dn)	32	6	32		R7400
	H5I (up)	32	12	51	35.3×51	XP2900
	H5I (dn)	32	12	51		XP2900
Ladder	H4L	32	22-57	40.65	128.2×40	XP2900 2090,2020
	H5L	32	27-87	48.05	168.2×47.5	XP2900 2090,2020
Middle	HM4X (up)	20	62	40.3	120×102	XP2072B
	HM4X (dn)	20	62	40.3		XP2072B
	HM4Y	32	21.5-25	40.4		XP2900
	HM5X (up)	20	77	47.7	150×120	EMI9954B
	HM5X (dn)	20	77	47.7		EMI9954B
	HM5Y	32	25-30	47.8		XP2900
Outer	HO3	16	70	23	200×100	9813/XP2020
	H04	32	150	40	480×225	9813/XP2020
LAS	H1	32	60	5.8	230×192	XP2900/2982
	H2	32	136	16	500×420	9813KB

Table 8: Table with all trigger hodoscopes, their relevant dimensions and the photomultiplier tube types.

APPENDIX B

In the following Table, the hadron multiplicities for positive and for negative pions are summarised. All corrections discussed in Chapter 7 and 8 are applied. Only bins remaining after the LEPTO extrapolation requirement are shown. The multiplicities are calculated in a 3-dimensional binning of 8 x bins, 5 y bins and 12 z bins:

- x : {0.004, 0.01, 0.02, 0.03, 0.04, 0.06, 0.1, 0.15, 0.7}
- y : {0.1, 0.15, 0.2, 0.3, 0.5, 0.7}
- z : {0.2, 0.25, 0.3, 0.35, 0.4, 0.45, 0.5, 0.55, 0.6, 0.65, 0.7, 0.75, 0.85}.

The numbers denote the lower boundary of the bin. In addition, the average value for x, y, z and Q^2 is given. The statistical and the systematical uncertainties are given separately.

x bin	y bin	z bin	$\langle x \rangle$	$\langle y \rangle$	$\langle Q^2 \rangle$	$\langle z \rangle$	M^{π^+}	$\Delta^{\text{stat}} M^{\pi^+}$	$\Delta^{\text{sys}} M^{\pi^+}$	M^{π^-}	$\Delta^{\text{stat}} M^{\pi^-}$	$\Delta^{\text{sys}} M^{\pi^-}$
0.004	0.3	0.2	0.0088	0.4386	1.1474	0.2233	1.8193	0.0158	0.0899	0.2235	1.7499	0.0865
0.004	0.3	0.25	0.0088	0.4386	1.1474	0.2734	1.2248	0.0135	0.0615	0.2732	1.2026	0.0603
0.004	0.3	0.3	0.0088	0.4386	1.1474	0.3232	0.9051	0.0121	0.0454	0.3234	0.8121	0.0407
0.004	0.3	0.35	0.0088	0.4386	1.1474	0.3734	0.6352	0.0104	0.032	0.3738	0.5883	0.0296
0.004	0.3	0.4	0.0088	0.4386	1.1474	0.4234	0.4599	0.0093	0.0235	0.4231	0.4506	0.023
0.004	0.3	0.45	0.0088	0.4386	1.1474	0.4729	0.3556	0.0086	0.0186	0.4729	0.3233	0.017
0.004	0.5	0.2	0.0075	0.6083	1.36	0.223	1.7324	0.0102	0.0871	0.2231	1.6882	0.0849
0.004	0.5	0.25	0.0075	0.6083	1.36	0.2732	1.1858	0.009	0.0594	0.273	1.1311	0.0567
0.004	0.5	0.3	0.0075	0.6083	1.36	0.323	0.8471	0.0081	0.0424	0.3228	0.8173	0.041
0.01	0.15	0.45	0.0188	0.188	1.0647	0.4745	0.412	0.0163	0.0207	0.4741	0.3556	0.018
0.01	0.15	0.5	0.0188	0.188	1.0647	0.5242	0.2896	0.014	0.0148	0.5235	0.2888	0.0148
0.01	0.15	0.55	0.0188	0.188	1.0647	0.574	0.223	0.0125	0.0135	0.5745	0.1993	0.0128
0.01	0.15	0.6	0.0188	0.188	1.0647	0.623	0.1864	0.0115	0.0114	0.6243	0.1481	0.0113
0.01	0.15	0.65	0.0188	0.188	1.0647	0.6745	0.1393	0.0108	0.0113	0.6735	0.1215	0.0112
0.01	0.15	0.7	0.0188	0.188	1.0647	0.7247	0.1269	0.0102	0.0107	0.7252	0.0899	0.0102
0.01	0.15	0.75	0.0188	0.188	1.0647	0.7971	0.0818	0.0062	0.0096	0.7959	0.0588	0.0087
0.01	0.2	0.35	0.0162	0.2545	1.226	0.3743	0.6914	0.0071	0.0333	0.3742	0.621	0.03
0.01	0.2	0.4	0.0162	0.2545	1.226	0.4238	0.5034	0.0063	0.0254	0.4237	0.4653	0.0235
0.01	0.2	0.45	0.0162	0.2545	1.226	0.4738	0.3708	0.0055	0.019	0.4737	0.3318	0.0172
0.01	0.2	0.5	0.0162	0.2545	1.226	0.524	0.2885	0.005	0.0152	0.5241	0.2506	0.0136
0.01	0.2	0.55	0.0162	0.2545	1.226	0.5743	0.2187	0.0044	0.0123	0.574	0.1908	0.0112
0.01	0.2	0.6	0.0162	0.2545	1.226	0.6242	0.1805	0.004	0.0103	0.6239	0.1504	0.0103
0.01	0.2	0.65	0.0162	0.2545	1.226	0.6741	0.1407	0.0038	0.0093	0.6743	0.1217	0.0092
0.01	0.2	0.7	0.0162	0.2545	1.226	0.7244	0.1186	0.0036	0.0091	0.7242	0.0962	0.0091
0.01	0.2	0.75	0.0162	0.2545	1.226	0.7961	0.0727	0.0021	0.0083	0.7967	0.0611	0.0078

x bin	y bin	z bin	$\langle x \rangle$	$\langle y \rangle$	$\langle Q^2 \rangle$	$\langle z \rangle$	M^{π^+}	$\Delta^{\text{stat}} M^{\pi^+}$	$\Delta^{\text{sys}} M^{\pi^+}$	M^{π^-}	$\Delta^{\text{stat}} M^{\pi^-}$	$\Delta^{\text{sys}} M^{\pi^-}$
0.01	0.3	0.25	0.0143	0.3935	1.67	0.2735	1.2864	0.0069	0.0641	0.2734	1.2128	0.0604
0.01	0.3	0.3	0.0143	0.3935	1.67	0.3234	0.9	0.0059	0.045	0.3234	0.8447	0.0423
0.01	0.3	0.35	0.0143	0.3935	1.67	0.3735	0.6483	0.0051	0.0325	0.3735	0.6052	0.0303
0.01	0.3	0.4	0.0143	0.3935	1.67	0.4234	0.4758	0.0045	0.0239	0.4235	0.425	0.0214
0.01	0.3	0.45	0.0143	0.3935	1.67	0.4736	0.3455	0.0039	0.0175	0.4737	0.3189	0.0161
0.01	0.3	0.5	0.0143	0.3935	1.67	0.5231	0.2657	0.0035	0.0128	0.5229	0.2294	0.0113
0.01	0.5	0.2	0.014	0.5919	2.4624	0.223	1.7578	0.0104	0.088	0.2231	1.6826	0.0843
0.01	0.5	0.25	0.014	0.5919	2.4624	0.2731	1.195	0.0089	0.0598	0.273	1.1361	0.0569
0.01	0.5	0.3	0.014	0.5919	2.4624	0.3229	0.8327	0.0077	0.0418	0.3231	0.8039	0.0402
0.02	0.1	0.6	0.0272	0.1358	1.1048	0.6249	0.2096	0.007	0.0113	0.6258	0.1581	0.0092
0.02	0.1	0.65	0.0272	0.1358	1.1048	0.6739	0.1539	0.0064	0.011	0.6752	0.1261	0.0092
0.02	0.1	0.7	0.0272	0.1358	1.1048	0.7241	0.1237	0.006	0.0095	0.7236	0.0884	0.0106
0.02	0.1	0.75	0.0272	0.1358	1.1048	0.7991	0.0832	0.0037	0.0086	0.7986	0.0742	0.0085
0.02	0.15	0.5	0.0247	0.1741	1.2789	0.5242	0.3053	0.0058	0.0157	0.5248	0.2705	0.0142
0.02	0.15	0.55	0.0247	0.1741	1.2789	0.5739	0.2375	0.0051	0.0126	0.5738	0.2019	0.0119
0.02	0.15	0.6	0.0247	0.1741	1.2789	0.6243	0.1841	0.0047	0.0111	0.6242	0.166	0.0107
0.02	0.15	0.65	0.0247	0.1741	1.2789	0.6745	0.1503	0.0043	0.0101	0.674	0.1221	0.0091
0.02	0.15	0.7	0.0247	0.1741	1.2789	0.7241	0.1142	0.0039	0.0088	0.7246	0.0947	0.0083
0.02	0.15	0.75	0.0247	0.1741	1.2789	0.7979	0.0787	0.0024	0.0085	0.7972	0.0622	0.0081
0.02	0.2	0.35	0.0245	0.2453	1.7893	0.3746	0.7002	0.0075	0.0321	0.3746	0.6388	0.0294
0.02	0.2	0.4	0.0245	0.2453	1.7893	0.4237	0.5168	0.0068	0.0259	0.4238	0.4505	0.0226
0.02	0.2	0.45	0.0245	0.2453	1.7893	0.4737	0.3764	0.0058	0.0189	0.4739	0.329	0.0167
0.02	0.2	0.5	0.0245	0.2453	1.7893	0.5239	0.2932	0.0052	0.015	0.5244	0.2427	0.0125
0.02	0.2	0.55	0.0245	0.2453	1.7893	0.5744	0.2142	0.0045	0.0112	0.5742	0.1908	0.0101
0.02	0.2	0.6	0.0245	0.2453	1.7893	0.6238	0.1711	0.0042	0.0094	0.6244	0.144	0.0082

x bin	y bin	z bin	$\langle x \rangle$	$\langle y \rangle$	$\langle Q^2 \rangle$	$\langle z \rangle$	M^{π^+}	$\Delta^{\text{stat}} M^{\pi^+}$	$\Delta^{\text{sys}} M^{\pi^+}$	M^{π^-}	$\Delta^{\text{stat}} M^{\pi^-}$	$\Delta^{\text{sys}} M^{\pi^-}$
0.02	0.2	0.65	0.0245	0.2453	1.7893	0.6739	0.1375	0.0038	0.008	0.6744	0.1119	0.0072
0.02	0.2	0.7	0.0245	0.2453	1.7893	0.724	0.1125	0.0037	0.0079	0.7244	0.0883	0.0066
0.02	0.2	0.75	0.0245	0.2453	1.7893	0.7962	0.0764	0.0022	0.007	0.7964	0.0599	0.0063
0.02	0.3	0.25	0.0245	0.3896	2.8477	0.2736	1.2923	0.0096	0.0642	0.2735	1.2055	0.0598
0.02	0.3	0.3	0.0245	0.3896	2.8477	0.3237	0.8908	0.0081	0.0446	0.3234	0.8214	0.0411
0.02	0.3	0.35	0.0245	0.3896	2.8477	0.3736	0.6469	0.0069	0.0324	0.3735	0.5856	0.0293
0.02	0.3	0.4	0.0245	0.3896	2.8477	0.4235	0.4625	0.006	0.0232	0.4233	0.4245	0.0213
0.02	0.3	0.45	0.0245	0.3896	2.8477	0.473	0.3405	0.0052	0.0171	0.4734	0.3087	0.0155
0.02	0.3	0.5	0.0245	0.3896	2.8477	0.5226	0.255	0.0045	0.012	0.5229	0.2144	0.0101
0.02	0.5	0.2	0.0243	0.5832	4.2244	0.2231	1.8207	0.0174	0.0911	0.2231	1.675	0.0838
0.02	0.5	0.25	0.0243	0.5832	4.2244	0.2732	1.2235	0.0147	0.0612	0.2735	1.1173	0.0559
0.02	0.5	0.3	0.0243	0.5832	4.2244	0.323	0.8627	0.0128	0.0432	0.323	0.7861	0.0393
0.03	0.1	0.75	0.0348	0.1233	1.2799	0.7974	0.0869	0.0025	0.009	0.7964	0.0658	0.0083
0.03	0.15	0.5	0.0346	0.1729	1.781	0.5245	0.3241	0.0076	0.016	0.5241	0.271	0.0135
0.03	0.15	0.55	0.0346	0.1729	1.781	0.5739	0.2334	0.0066	0.012	0.5742	0.1911	0.0101
0.03	0.15	0.6	0.0346	0.1729	1.781	0.6244	0.1903	0.006	0.0103	0.625	0.1458	0.0087
0.03	0.15	0.65	0.0346	0.1729	1.781	0.6744	0.1451	0.0053	0.0085	0.6738	0.1121	0.0069
0.03	0.15	0.7	0.0346	0.1729	1.781	0.7232	0.11	0.0047	0.0071	0.724	0.0955	0.0066
0.03	0.15	0.75	0.0346	0.1729	1.781	0.7966	0.0777	0.0031	0.0072	0.7968	0.0582	0.0064
0.03	0.2	0.35	0.0347	0.2475	2.5617	0.3744	0.6994	0.009	0.032	0.3745	0.6133	0.028
0.03	0.2	0.4	0.0347	0.2475	2.5617	0.4241	0.5056	0.0081	0.0253	0.4234	0.4468	0.0224
0.03	0.2	0.45	0.0347	0.2475	2.5617	0.4741	0.3749	0.007	0.0188	0.4743	0.3131	0.0157
0.03	0.2	0.5	0.0347	0.2475	2.5617	0.5241	0.2755	0.006	0.0139	0.5239	0.2345	0.0118
0.03	0.2	0.55	0.0347	0.2475	2.5617	0.5739	0.2074	0.0052	0.0106	0.574	0.1782	0.0091
0.03	0.2	0.6	0.0347	0.2475	2.5617	0.6245	0.1701	0.005	0.0089	0.6245	0.1348	0.0072

x bin	y bin	z bin	$\langle x \rangle$	$\langle y \rangle$	$\langle Q^2 \rangle$	$\langle z \rangle$	M^{π^+}	$\Delta^{\text{stat}} M^{\pi^+}$	$\Delta^{\text{sys}} M^{\pi^+}$	M^{π^-}	$\Delta^{\text{stat}} M^{\pi^-}$	$\Delta^{\text{sys}} M^{\pi^-}$
0.03	0.2	0.65	0.0347	0.2475	2.5617	0.6736	0.1244	0.0043	0.0068	0.6737	0.1043	0.0058
0.03	0.2	0.7	0.0347	0.2475	2.5617	0.7251	0.0994	0.0039	0.0061	0.7236	0.0782	0.0053
0.03	0.2	0.75	0.0347	0.2475	2.5617	0.7948	0.0713	0.0026	0.0057	0.7965	0.0506	0.0044
0.03	0.3	0.25	0.0346	0.3865	3.9911	0.2735	1.3016	0.0122	0.0646	0.2737	1.1692	0.058
0.03	0.3	0.3	0.0346	0.3865	3.9911	0.3232	0.9108	0.0103	0.0455	0.3236	0.8164	0.0408
0.03	0.3	0.35	0.0346	0.3865	3.9911	0.3738	0.6629	0.0089	0.0332	0.3734	0.5884	0.0294
0.03	0.3	0.4	0.0346	0.3865	3.9911	0.4237	0.4798	0.0076	0.024	0.4232	0.3979	0.0199
0.03	0.3	0.45	0.0346	0.3865	3.9911	0.4735	0.3465	0.0066	0.0173	0.4733	0.2905	0.0145
0.03	0.3	0.5	0.0346	0.3865	3.9911	0.5233	0.2518	0.0056	0.0119	0.5232	0.2186	0.0103
0.03	0.5	0.2	0.0345	0.5796	5.9687	0.223	1.8073	0.0239	0.0904	0.2228	1.6658	0.0833
0.03	0.5	0.25	0.0345	0.5796	5.9687	0.2733	1.2386	0.0205	0.062	0.2729	1.1451	0.0573
0.03	0.5	0.3	0.0345	0.5796	5.9687	0.3232	0.8599	0.0171	0.0431	0.3229	0.8124	0.0406
0.04	0.1	0.75	0.0487	0.1219	1.7719	0.7973	0.0871	0.0022	0.0071	0.7978	0.0609	0.0067
0.04	0.15	0.5	0.0494	0.1741	2.56	0.5239	0.305	0.0064	0.0149	0.524	0.2512	0.0123
0.04	0.15	0.55	0.0494	0.1741	2.56	0.5742	0.2263	0.0056	0.0115	0.574	0.1944	0.01
0.04	0.15	0.6	0.0494	0.1741	2.56	0.624	0.1748	0.0048	0.009	0.6246	0.1426	0.0076
0.04	0.15	0.65	0.0494	0.1741	2.56	0.6738	0.14	0.0044	0.0074	0.674	0.1065	0.0059
0.04	0.15	0.7	0.0494	0.1741	2.56	0.7238	0.1081	0.0039	0.0064	0.7247	0.0859	0.0058
0.04	0.15	0.75	0.0494	0.1741	2.56	0.7964	0.0744	0.0025	0.0057	0.7975	0.0558	0.0047
0.04	0.2	0.35	0.0491	0.2461	3.6029	0.3747	0.712	0.0077	0.0326	0.374	0.6053	0.0277
0.04	0.2	0.4	0.0491	0.2461	3.6029	0.4236	0.5138	0.0069	0.0257	0.4237	0.4205	0.021
0.04	0.2	0.45	0.0491	0.2461	3.6029	0.4739	0.3781	0.0059	0.0189	0.4737	0.3069	0.0154
0.04	0.2	0.5	0.0491	0.2461	3.6029	0.5239	0.2768	0.005	0.0139	0.5243	0.2193	0.011
0.04	0.2	0.55	0.0491	0.2461	3.6029	0.5737	0.2139	0.0044	0.0108	0.5736	0.1678	0.0085
0.04	0.2	0.6	0.0491	0.2461	3.6029	0.6236	0.158	0.0039	0.0081	0.6236	0.1236	0.0064

x bin	y bin	z bin	$\langle x \rangle$	$\langle y \rangle$	$\langle Q^2 \rangle$	$\langle z \rangle$	M^{π^+}	$\Delta^{\text{stat}} M^{\pi^+}$	$\Delta^{\text{sys}} M^{\pi^+}$	M^{π^-}	$\Delta^{\text{stat}} M^{\pi^-}$	$\Delta^{\text{sys}} M^{\pi^-}$
0.04	0.2	0.65	0.0491	0.2461	3.6029	0.6743	0.1226	0.0034	0.0064	0.6749	0.1	0.0054
0.04	0.2	0.7	0.0491	0.2461	3.6029	0.7232	0.0977	0.0033	0.0055	0.7243	0.0693	0.0041
0.04	0.2	0.75	0.0491	0.2461	3.6029	0.7948	0.0616	0.0019	0.0044	0.7959	0.0495	0.0038
0.04	0.3	0.25	0.0489	0.3838	5.5931	0.2735	1.3374	0.0114	0.0664	0.2733	1.1836	0.0587
0.04	0.3	0.3	0.0489	0.3838	5.5931	0.3234	0.9304	0.0095	0.0465	0.3232	0.8068	0.0403
0.04	0.3	0.35	0.0489	0.3838	5.5931	0.3733	0.6525	0.0079	0.0326	0.3735	0.5562	0.0278
0.04	0.3	0.4	0.0489	0.3838	5.5931	0.4232	0.4862	0.0069	0.0243	0.4237	0.3944	0.0198
0.04	0.3	0.45	0.0489	0.3838	5.5931	0.4732	0.3408	0.0058	0.0171	0.4736	0.2811	0.0141
0.04	0.3	0.5	0.0489	0.3838	5.5931	0.5232	0.2611	0.0051	0.0123	0.5229	0.2057	0.0096
0.04	0.5	0.2	0.0481	0.5741	8.2391	0.2234	1.83	0.0256	0.0915	0.2232	1.7149	0.0858
0.04	0.5	0.25	0.0481	0.5741	8.2391	0.2734	1.2637	0.0214	0.0632	0.2728	1.0838	0.0542
0.04	0.5	0.3	0.0481	0.5741	8.2391	0.323	0.8993	0.0189	0.0451	0.3234	0.7539	0.0378
0.06	0.1	0.75	0.0783	0.1235	2.8802	0.7961	0.0808	0.002	0.0056	0.7987	0.059	0.0049
0.06	0.15	0.5	0.0779	0.1737	4.03	0.5242	0.292	0.0055	0.0142	0.5242	0.2242	0.0109
0.06	0.15	0.55	0.0779	0.1737	4.03	0.5741	0.2249	0.0048	0.0113	0.5742	0.1635	0.0083
0.06	0.15	0.6	0.0779	0.1737	4.03	0.6241	0.1733	0.0043	0.0088	0.6243	0.1272	0.0065
0.06	0.15	0.65	0.0779	0.1737	4.03	0.6738	0.1351	0.0039	0.007	0.6742	0.0993	0.0052
0.06	0.15	0.7	0.0779	0.1737	4.03	0.7244	0.0964	0.0033	0.0052	0.7242	0.0724	0.0041
0.06	0.15	0.75	0.0779	0.1737	4.03	0.7958	0.0729	0.0021	0.0047	0.7965	0.0454	0.0034
0.06	0.2	0.35	0.0775	0.2448	5.6518	0.3747	0.6975	0.0073	0.0319	0.3744	0.5677	0.0258
0.06	0.2	0.4	0.0775	0.2448	5.6518	0.4236	0.4988	0.0063	0.0249	0.4235	0.4052	0.0202
0.06	0.2	0.45	0.0775	0.2448	5.6518	0.4734	0.3691	0.0055	0.0185	0.4736	0.2909	0.0146
0.06	0.2	0.5	0.0775	0.2448	5.6518	0.5235	0.2731	0.0047	0.0137	0.5234	0.2091	0.0105
0.06	0.2	0.55	0.0775	0.2448	5.6518	0.574	0.2051	0.004	0.0103	0.5739	0.1628	0.0082
0.06	0.2	0.6	0.0775	0.2448	5.6518	0.6237	0.1565	0.0036	0.0079	0.6241	0.112	0.0057

x bin	y bin	z bin	$\langle x \rangle$	$\langle y \rangle$	$\langle Q^2 \rangle$	$\langle z \rangle$	M^{π^+}	$\Delta^{\text{stat}} M^{\pi^+}$	$\Delta^{\text{sys}} M^{\pi^+}$	M^{π^-}	$\Delta^{\text{stat}} M^{\pi^-}$	$\Delta^{\text{sys}} M^{\pi^-}$
0.06	0.2	0.65	0.0775	0.2448	5.6518	0.6739	0.1233	0.0033	0.0063	0.6736	0.084	0.0044
0.06	0.2	0.7	0.0775	0.2448	5.6518	0.724	0.0921	0.0028	0.0048	0.7239	0.062	0.0034
0.06	0.2	0.75	0.0775	0.2448	5.6518	0.7945	0.0579	0.0017	0.0035	0.7939	0.0418	0.0028
0.06	0.3	0.25	0.0757	0.374	8.442	0.2737	1.3763	0.0127	0.0683	0.2733	1.1721	0.0581
0.06	0.3	0.3	0.0757	0.374	8.442	0.3236	0.9693	0.0107	0.0485	0.3234	0.806	0.0403
0.06	0.3	0.35	0.0757	0.374	8.442	0.3734	0.678	0.0089	0.0339	0.3733	0.5631	0.0282
0.06	0.3	0.4	0.0757	0.374	8.442	0.4235	0.4645	0.0073	0.0233	0.4237	0.3839	0.0192
0.06	0.3	0.45	0.0757	0.374	8.442	0.4732	0.3592	0.0065	0.018	0.4738	0.2661	0.0134
0.06	0.3	0.5	0.0757	0.374	8.442	0.5228	0.2633	0.0054	0.0125	0.5232	0.2026	0.0097
0.06	0.5	0.2	0.0747	0.5725	12.7659	0.2231	1.9345	0.0362	0.0969	0.2232	1.6689	0.0835
0.06	0.5	0.25	0.0747	0.5725	12.7659	0.2733	1.3827	0.031	0.0692	0.2734	1.1598	0.058
0.06	0.5	0.3	0.0747	0.5725	12.7659	0.3232	0.9564	0.0266	0.048	0.322	0.7257	0.0364
0.1	0.1	0.75	0.1228	0.1231	4.5079	0.795	0.0761	0.0024	0.0045	0.798	0.0478	0.0034
0.1	0.15	0.5	0.1223	0.1732	6.3189	0.5241	0.2878	0.0069	0.014	0.5242	0.2119	0.0103
0.1	0.15	0.55	0.1223	0.1732	6.3189	0.5739	0.2238	0.0062	0.0112	0.5733	0.141	0.0071
0.1	0.15	0.6	0.1223	0.1732	6.3189	0.6227	0.1535	0.0049	0.0077	0.6241	0.106	0.0054
0.1	0.15	0.65	0.1223	0.1732	6.3189	0.6737	0.1232	0.0045	0.0062	0.6741	0.0802	0.0041
0.1	0.15	0.7	0.1223	0.1732	6.3189	0.7238	0.093	0.0039	0.0048	0.724	0.0644	0.0034
0.1	0.15	0.75	0.1223	0.1732	6.3189	0.7961	0.0615	0.0023	0.0035	0.7962	0.0396	0.0026
0.1	0.2	0.35	0.1209	0.2415	8.7067	0.3747	0.7138	0.0104	0.0325	0.3745	0.5487	0.0249
0.1	0.2	0.4	0.1209	0.2415	8.7067	0.4236	0.5098	0.0089	0.0255	0.4235	0.3953	0.0198
0.1	0.2	0.45	0.1209	0.2415	8.7067	0.4736	0.3672	0.0075	0.0184	0.4737	0.2818	0.0141
0.1	0.2	0.5	0.1209	0.2415	8.7067	0.5238	0.2695	0.0062	0.0135	0.5236	0.1976	0.0099
0.1	0.2	0.55	0.1209	0.2415	8.7067	0.574	0.2021	0.0054	0.0101	0.5737	0.1367	0.0069
0.1	0.2	0.6	0.1209	0.2415	8.7067	0.6241	0.1516	0.0047	0.0076	0.624	0.1098	0.0055

x bin	y bin	z bin	$\langle x \rangle$	$\langle y \rangle$	$\langle Q^2 \rangle$	$\langle z \rangle$	M^{π^+}	$\Delta^{\text{stat}} M^{\pi^+}$	$\Delta^{\text{sys}} M^{\pi^+}$	M^{π^-}	$\Delta^{\text{stat}} M^{\pi^-}$	$\Delta^{\text{sys}} M^{\pi^-}$
0.1	0.2	0.65	0.1209	0.2415	8.7067	0.6754	0.1146	0.0041	0.0058	0.6736	0.0771	0.0039
0.1	0.2	0.7	0.1209	0.2415	8.7067	0.7246	0.0966	0.0039	0.005	0.7239	0.0557	0.003
0.1	0.2	0.75	0.1209	0.2415	8.7067	0.7933	0.0557	0.0022	0.0031	0.7936	0.0344	0.0021
0.1	0.3	0.25	0.1197	0.3685	13.1708	0.2738	1.3807	0.0209	0.0685	0.2736	1.1367	0.0564
0.1	0.3	0.3	0.1197	0.3685	13.1708	0.3233	1.0029	0.0183	0.0501	0.3234	0.7613	0.0381
0.1	0.3	0.35	0.1197	0.3685	13.1708	0.3733	0.699	0.0146	0.035	0.3735	0.5482	0.0274
0.1	0.3	0.4	0.1197	0.3685	13.1708	0.4238	0.5037	0.0127	0.0252	0.4234	0.3716	0.0187
0.1	0.3	0.45	0.1197	0.3685	13.1708	0.474	0.3679	0.0108	0.0187	0.4737	0.2661	0.0135
0.1	0.3	0.5	0.1197	0.3685	13.1708	0.5233	0.2778	0.0092	0.0134	0.5233	0.2047	0.01
0.1	0.5	0.2	0.1192	0.566	20.1373	0.2223	2.0164	0.0669	0.1008	0.2233	1.7262	0.0864
0.1	0.5	0.25	0.1192	0.566	20.1373	0.2729	1.4017	0.0577	0.0702	0.2735	1.0705	0.0536
0.1	0.5	0.3	0.1192	0.566	20.1373	0.3225	1.0036	0.0485	0.0507	0.3231	0.7006	0.0353
0.1	0.5	0.35	0.1192	0.566	20.1373	0.3723	0.7454	0.0433	0.035	0.3722	0.5234	0.0275
0.15	0.1	0.75	0.2096	0.1246	7.857	0.7952	0.0734	0.0032	0.004	0.7925	0.0374	0.0023
0.15	0.15	0.5	0.2203	0.1718	11.294	0.5238	0.2878	0.0085	0.014	0.5242	0.1982	0.0096
0.15	0.15	0.55	0.2203	0.1718	11.294	0.5738	0.2243	0.0076	0.0112	0.5744	0.1337	0.0067
0.15	0.15	0.6	0.2203	0.1718	11.294	0.6247	0.1676	0.0065	0.0084	0.6244	0.1022	0.0051
0.15	0.15	0.65	0.2203	0.1718	11.294	0.6739	0.1217	0.0055	0.0061	0.6741	0.0752	0.0038
0.15	0.15	0.7	0.2203	0.1718	11.294	0.7242	0.0893	0.0047	0.0045	0.7241	0.0536	0.0028
0.15	0.15	0.75	0.2203	0.1718	11.294	0.794	0.0605	0.0027	0.0032	0.7946	0.0313	0.0018
0.15	0.2	0.35	0.2177	0.2388	15.5089	0.375	0.6916	0.0126	0.0313	0.3741	0.5422	0.0245
0.15	0.2	0.4	0.2177	0.2388	15.5089	0.423	0.5077	0.0112	0.0254	0.4237	0.36	0.018
0.15	0.2	0.45	0.2177	0.2388	15.5089	0.4737	0.3559	0.0092	0.0178	0.474	0.2527	0.0126
0.15	0.2	0.5	0.2177	0.2388	15.5089	0.5232	0.2856	0.0081	0.0143	0.5231	0.1821	0.0091
0.15	0.2	0.55	0.2177	0.2388	15.5089	0.5747	0.2112	0.0069	0.0106	0.5748	0.1261	0.0063

x bin	y bin	z bin	$\langle x \rangle$	$\langle y \rangle$	$\langle Q^2 \rangle$	$\langle z \rangle$	M^{π^+}	$\Delta^{\text{stat}} M^{\pi^+}$	$\Delta^{\text{sys}} M^{\pi^+}$	M^{π^-}	$\Delta^{\text{stat}} M^{\pi^-}$	$\Delta^{\text{sys}} M^{\pi^-}$
0.15	0.2	0.6	0.2177	0.2388	15.5089	0.6242	0.1584	0.006	0.0079	0.6231	0.1026	0.0052
0.15	0.2	0.65	0.2177	0.2388	15.5089	0.6748	0.1296	0.0054	0.0065	0.6735	0.0687	0.0035
0.15	0.2	0.7	0.2177	0.2388	15.5089	0.7238	0.0934	0.0047	0.0047	0.7236	0.0498	0.0026
0.15	0.2	0.75	0.2177	0.2388	15.5089	0.7929	0.0621	0.0028	0.0034	0.7923	0.0286	0.0017
0.15	0.3	0.25	0.2086	0.3652	22.6374	0.274	1.4132	0.0278	0.0701	0.2737	1.1149	0.0553
0.15	0.3	0.3	0.2086	0.3652	22.6374	0.3235	1.0106	0.0236	0.0505	0.3237	0.7636	0.0382
0.15	0.3	0.35	0.2086	0.3652	22.6374	0.3738	0.7339	0.0196	0.0367	0.3732	0.5136	0.0257
0.15	0.3	0.4	0.2086	0.3652	22.6374	0.4238	0.5104	0.0163	0.0256	0.4238	0.3597	0.0181
0.15	0.3	0.45	0.2086	0.3652	22.6374	0.4735	0.3802	0.0145	0.0194	0.4739	0.2865	0.0145
0.15	0.3	0.5	0.2086	0.3652	22.6374	0.523	0.2992	0.0126	0.015	0.5249	0.2041	0.0101
0.15	0.5	0.2	0.1805	0.5494	29.6216	0.223	2.0378	0.119	0.1021	0.2222	1.8945	0.0948
0.15	0.5	0.25	0.1805	0.5494	29.6216	0.275	1.2944	0.0955	0.0649	0.2728	1.0966	0.0549
0.15	0.5	0.3	0.1805	0.5494	29.6216	0.3217	0.955	0.0828	0.0481	0.3243	0.8673	0.0437
0.15	0.5	0.35	0.1805	0.5494	29.6216	0.3744	0.7518	0.0709	0.0357	0.3719	0.4923	0.0225

BIBLIOGRAPHY

- [1] H. Geiger and E. Marsden. The Laws of Deflexion of α Particles through Large Angles. *Phil.Mag.*, 25:604–623, 1913. (Cited on page 1.)
- [2] E. Rutherford. The scattering of alpha and beta particles by matter and the structure of the atom. *Phil.Mag.*, 21:669–688, 1911. (Cited on page 1.)
- [3] Martin Breidenbach, Jerome I. Friedman, Henry W. Kendall, Elliott D. Bloom, D. H. Coward, H. C. DeStaebler, J. Drees, Luke W. Mo, and Richard E. Taylor. Observed Behavior of Highly Inelastic electron-Proton Scattering. *Phys. Rev. Lett.*, 23:935–939, 1969. (Cited on pages 1 and 8.)
- [4] Murray Gell-Mann. A Schematic Model of Baryons and Mesons. *Phys. Lett.*, 8:214–215, 1964. (Cited on page 1.)
- [5] G. Zweig. An SU(3) model for strong interaction symmetry and its breaking. Version 1. 1964. (Cited on pages 1 and 9.)
- [6] Richard P. Feynman. Very high-energy collisions of hadrons. *Phys. Rev. Lett.*, 23:1415–1417, 1969. (Cited on page 1.)
- [7] R. Brandelik et al. Evidence for Planar Events in $e^+ e^-$ Annihilation at High-Energies. *Phys. Lett.*, B86:243, 1979. (Cited on page 1.)
- [8] J. Beringer et al. Review of Particle Physics (RPP). *Phys.Rev.*, D86:010001, 2012. (Cited on pages 1, 12, 13, 33, and 90.)
- [9] S. Stein, W. B. Atwood, Elliott D. Bloom, R. Leslie Cottrell, H. C. DeStaebler, C. L. Jordan, H. Piel, C. Y. Prescott, R. Siemann, and Richard E. Taylor. Electron Scattering at 4-Degrees with Energies of 4.5-GeV - 20-GeV. *Phys. Rev.*, D12:1884, 1975. (Cited on page 6.)
- [10] B. Povh, K. Rith, C. Scholz, and F. Zetsche. *Teilchen und Kerne - Eine Einführung in die physikalischen Konzepte*. Springer, 7. edition edition, 2006. (Cited on page 9.)
- [11] Jr. Callan, Curtis G. and David J. Gross. High-energy electroproduction and the constitution of the electric current. *Phys.Rev.Lett.*, 22:156–159, 1969. (Cited on page 9.)
- [12] Richard P. Feynman. Very high-energy collisions of hadrons. *Phys. Rev. Lett.*, 23:1415–1417, 1969. (Cited on pages 9 and 17.)
- [13] J. D. Bjorken and Emmanuel A. Paschos. Inelastic Electron Proton and gamma Proton Scattering, and the Structure of the Nucleon. *Phys. Rev.*, 185:1975–1982, 1969. (Cited on page 9.)
- [14] R. Devenish and A. Cooper-Sarkar. *Deep Inelastic Scattering*. Oxford, 2011. (Cited on page 15.)
- [15] G. Altarelli and G. Parisi. Asymptotic Freedom in Parton Language. *Nucl.Phys.*, B126: 298, 1977. (Cited on page 15.)

- [16] A.D. Martin, W.J. Stirling, R.S. Thorne, and G. Watt. Parton distributions for the LHC. *Eur.Phys.J.*, C63:189–285, 2009, 0901.0002. (Cited on pages 15, 114, and 139.)
- [17] J. Ashman et al. A Measurement of the Spin Asymmetry and Determination of the Structure Function $g(1)$ in Deep Inelastic Muon-Proton Scattering. *Phys. Lett.*, B206:364, 1988. (Cited on page 16.)
- [18] M.G. Alekseev et al. The Spin-dependent Structure Function of the Proton g_1^p and a Test of the Bjorken Sum Rule. *Phys.Lett.*, B690:466–472, 2010, 1001.4654. (Cited on page 16.)
- [19] C. Adolph et al. Leading and Next-to-Leading Order Gluon Polarization in the Nucleon and Longitudinal Double Spin Asymmetries from Open Charm Muoproduction. *Phys. Rev.*, D87(5):052018, 2013, 1211.6849. (Cited on page 16.)
- [20] J. Ashman et al. A Measurement of the Spin Asymmetry and Determination of the Structure Function $g(1)$ in Deep Inelastic Muon-Proton Scattering. *Phys. Lett.*, B206:364, 1988. (Cited on page 16.)
- [21] K. V. Dharmawardane et al. Measurement of the x - and Q^2 -dependence of the asymmetry $A(1)$ on the nucleon. *Phys. Lett.*, B641:11–17, 2006, nucl-ex/0605028. (Cited on page 16.)
- [22] Roland Windmolders. Quark helicity distributions from longitudinal spin asymmetries in muon-proton and muon-deuteron scattering. *J. Phys. Conf. Ser.*, 295:012069, 2011. (Cited on page 19.)
- [23] M. Alekseev et al. Flavour Separation of Helicity Distributions from Deep Inelastic Muon-Deuteron Scattering. *Phys. Lett.*, B680:217–224, 2009, 0905.2828. (Cited on page 19.)
- [24] S. Kretzer. Fragmentation functions from flavor inclusive and flavor tagged $e^+ e^-$ annihilations. *Phys.Rev.*, D62:054001, 2000, hep-ph/0003177. (Cited on pages 20, 137, and 143.)
- [25] M. Arneodo et al. Measurements of the u Valence Quark Distribution Function in the Proton and u Quark Fragmentation Functions. *Nucl. Phys.*, B321:541, 1989. (Cited on page 20.)
- [26] Daniel de Florian, Rodolfo Sassot, and Marco Stratmann. Global analysis of fragmentation functions for pions and kaons and their uncertainties. *Phys. Rev. D*, 75:114010, Jun 2007. URL <http://link.aps.org/doi/10.1103/PhysRevD.75.114010>. (Cited on pages 20 and 137.)
- [27] Frank E. Paige, Serban D. Proto pescu, Howard Baer, and Xerxes Tata. ISAJET 7.40: A Monte Carlo event generator for $p p$, anti- $p p$, and $e^+ e^-$ reactions. 1998, hep-ph/9810440. (Cited on page 20.)
- [28] T. Sjostrand. High-energy physics event generation with PYTHIA 5.7 and JETSET 7.4. *Comput.Phys.Commun.*, 82:74–90, 1994. (Cited on page 20.)
- [29] G. Marchesini, B.R. Webber, G. Abbiendi, I.G. Knowles, M.H. Seymour, et al. HERWIG: A Monte Carlo event generator for simulating hadron emission reactions with interfering gluons. Version 5.1 - April 1991. *Comput.Phys.Commun.*, 67:465–508, 1992. (Cited on page 20.)

- [30] R.D. Field and R.P. Feynman. A Parametrization of the Properties of Quark Jets. *Nucl.Phys.*, B136:1, 1978. (Cited on pages 20 and 21.)
- [31] Bo Andersson, G. Gustafson, G. Ingelman, and T. Sjostrand. Parton Fragmentation and String Dynamics. *Phys.Rept.*, 97:31–145, 1983. (Cited on page 22.)
- [32] Various Authors. *EMC seminar 28.10.1982 - 03.03.1983*, 1983. (Cited on page 22.)
- [33] Torbjorn Sjostrand, Patrik Eden, Christer Friberg, Leif Lonnblad, Gabriela Miu, et al. High-energy physics event generation with PYTHIA 6.1. *Comput.Phys.Commun.*, 135:238–259, 2001, hep-ph/0010017. (Cited on page 23.)
- [34] J. Ashman et al. Forward produced hadrons in mu p and mu d scattering and investigation of the charge structure of the nucleon. *Z. Phys.*, C52:361–388, 1991. (Cited on pages 26, 27, and 142.)
- [35] J.-F. Rajotte. *Hadron muoproduction at the COMPASS experiment*. PhD thesis, Ludwig-Maximilians-Universität München, 2010. (Cited on pages 26 and 116.)
- [36] K. Ackerstaff et al. The HERMES spectrometer. *Nucl.Instrum.Meth.*, A417:230–265, 1998, hep-ex/9806008. (Cited on pages 27 and 142.)
- [37] A. Airapetian et al. Multiplicities of charged pions and kaons from semi-inclusive deep-inelastic scattering by the proton and the deuteron. *Phys. Rev.*, D87:074029, 2013, 1212.5407. (Cited on page 27.)
- [38] G.K. Mallot et al. The COMPASS spectrometer at CERN. *Nucl.Instrum.Meth.*, A518:121–124, 2004. (Cited on page 31.)
- [39] F. Gautheron et al. COMPASS-II Proposal. 2010. (Cited on page 31.)
- [40] Ph. Abbon et al. The COMPASS Setup for Physics with Hadron Beams. *CERN-PH-EP-2014-247*, 2014. (Cited on pages 31 and 32.)
- [41] L. Gatignon, 2006. URL <http://sba.web.cern.ch/sba/BeamsAndAreas/M2/M2-OperatorCourse.pdf>. (Cited on page 32.)
- [42] M. Barnes, 2009. URL <http://cas.web.cern.ch/cas/Belgium-2009/Lectures/PDFs/Barnes-1.pdf>. (Cited on page 32.)
- [43] M. von Hodenberg. *First measurement of the gluon polarisation in the nucleon using hadron pairs with high transverse momentum at COMPASS*. PhD thesis, Physikalisches Institut, Albert-Ludwigs-Universität Freiburg, 2005. (Cited on page 35.)
- [44] I. Abt, S. Masciocchi, B. Moshous, T. Perschke, K. Riechmann, et al. Double-sided microstrip detectors for the high radiation environment in the HERA-B experiment. *Nucl.Instrum.Meth.*, A439:442–450, 2000. (Cited on page 35.)
- [45] H. Angerer, R. De Masi, A. Esposito, J. Friedrich, S. Gerassimov, et al. Present status of silicon detectors in COMPASS. *Nucl.Instrum.Meth.*, 512:229–238, 2003. (Cited on page 35.)
- [46] A. Abragam. *The principles of Nuclear Magnetism*. Oxford University Press, 1961. (Cited on page 36.)

- [47] Yu Kiselev, N. Doshita, S. Goertz, K. Kondo, W. Meyer, G. Reicherz, Günter Baum, Fabrice Gautheron, J. Ball, and A. Magnon. Features of dynamic nuclear polarization in irradiated lid target material. pages 816–819, 2004. (Cited on page 36.)
- [48] J. Bernhard. *Aufbau des inneren Rings eines Recoildetektors am COMPASS-Experiment*. Diploma thesis, Institut für Kernphysik, Johannes Gutenberg-Universität Mainz, 2007. (Cited on page 37.)
- [49] J. Bernhard. *Exclusive Vector Meson Production in pp Collisions at the COMPASS Experiment*. PhD thesis, Institut für Kernphysik, Johannes Gutenberg-Universität Mainz, 2014. (Cited on page 37.)
- [50] F. Sauli. GEM: A new concept for electron amplification in gas detectors. *Nucl.Instrum.Meth.*, A386:531–534, 1997. (Cited on page 38.)
- [51] F. Kunne, P. Abbon, J. Ball, Y. Bedfer, C. Bernet, et al. The gaseous microstrip detector Micromegas for the COMPASS experiment at CERN. *Nucl.Phys.*, A721:1087–1090, 2003. (Cited on page 38.)
- [52] B. Grube. *The Trigger Control System and the Common GEM and Silicon Readout for the COMPASS Experiment*. Diploma thesis, Technische Universität München, 2001. (Cited on page 43.)
- [53] G. Braun, H. Fischer, J. Franz, A. Grunemaier, F.H. Heinsius, et al. TDC chip and read-out driver developments for COMPASS and LHC experiments. 1998, hep-ex/9810048. (Cited on page 43.)
- [54] H. Fischer, J. Franz, A. Grunemaier, F.H. Heinsius, L. Hennig, et al. Implementation of the dead time free F1 TDC in the COMPASS detector readout. *Nucl.Instrum.Meth.*, A461:507–510, 2001, hep-ex/0010065. (Cited on page 44.)
- [55] M. J. French et al. Design and results from the APV25, a deep sub-micron CMOS front-end chip for the CMS tracker. *Nucl. Instrum. Meth.*, A466:359–365, 2001. (Cited on page 44.)
- [56] C. Bernet et al. The COMPASS trigger system for muon scattering. *Nucl.Instrum.Meth.*, A550:217–240, 2005. (Cited on page 47.)
- [57] M. Leberig. *Das COMPASS Triggersystem zur Messung des Gluonbeitrags ΔG zum Protonspin*. PhD thesis, Institut für Kernphysik, Johannes Gutenberg-Universität Mainz, 2002. (Cited on page 47.)
- [58] Gerald R. Lynch and Orin I. Dahl. Approximations to multiple Coulomb scattering. *Nucl. Instrum. Meth.*, B58:6–10, 1991. (Cited on page 48.)
- [59] G. Audi, O. Bersillon, J. Blachot, and A.H. Wapstra. The nubase evaluation of nuclear and decay properties. *Nuclear Physics A*, 729(1):3 – 128, 2003. ISSN 0375-9474. The 2003 [NUBASE] and Atomic Mass Evaluations. (Cited on page 49.)
- [60] W. R. Leo. *Techniques for Nuclear and Particle Physics Experiments*. Springer, 1994. (Cited on pages 51 and 70.)
- [61] Einstein, A. Über einen die Erzeugung und Verwandlung des Lichtes betreffenden heuristischen Gesichtspunkt. *Annalen der Physik*, 322(6):132–148, 1905. ISSN 1521-3889. URL <http://dx.doi.org/10.1002/andp.19053220607>. (Cited on page 51.)

- [62] A.R. Baldwin and R. Madey. An analog mean-timer circuit for use with large-volume scintillation counters. *Nuclear Instruments and Methods*, 171(1):149–152, 1980. ISSN 0029-554X. (Cited on page 58.)
- [63] O. Freyermuth. *Development of a Dead Time Measurement System for the Compass Experiment using FPGA Technology*. Diploma thesis, Physikalisches Institut, Universität Bonn, 2012. (Cited on page 60.)
- [64] J. Pretz. *Veto dead time & beam duty factor*. COMPASS Note, November 2010. (Cited on page 60.)
- [65] C. Adolph et al. A high-statistics measurement of transverse spin effects in dihadron production from muon-proton semi-inclusive deep-inelastic scattering. *Phys. Lett.*, B736: 124–131, 2014, 1401.7873. (Cited on page 61.)
- [66] A. Zimmermann. *Design und Test von Szintillationszählern mit Luftlichtleitern für das Triggersystem des COMPASS Experiments*. Diploma thesis, Institut für Kernphysik, Johannes Gutenberg-Universität Mainz, 2010. (Cited on page 63.)
- [67] C. Seiffert. *Aufbau und Charakterisierung eines Triggerhodoskops für das COMPASS Experiment*. Diploma thesis, Institut für Kernphysik, Johannes Gutenberg-Universität Mainz, 2010. (Cited on page 63.)
- [68] Dudder, A. *Umbau des Large Angle Triggersystems des COMPASS Experiments*. Diploma thesis, Institut für Kernphysik, Johannes Gutenberg-Universität Mainz, 2012. (Cited on page 63.)
- [69] S. Bartknecht et al. Development of a 1-GS/s High-Resolution Sampling ADC System. *Nucl.Instrum.Meth.*, A623:507–509, 2010. (Cited on page 68.)
- [70] S. Bartknecht et al. Development and Performance Verification of the GANDALF High-Resolution Transient Recorder System. *IEEE Trans.Nucl.Sci.*, 58:1456–1459, 2011, 1112.4281. (Cited on page 68.)
- [71] J. Bieling. *Entwicklung eines ungetakteten 64-Kanal-Meantimers und einer Koinzidenzschaltung auf einem FPGA*. Diploma thesis, Physikalisches Institut, Rheinische Friedrich-Wilhelms-Universität Bonn, 2010. (Cited on page 68.)
- [72] J. Bieling et al. Implementation of mean-timing and subsequent logic functions on an FPGA. *Nucl.Instrum.Meth.*, A672:13–20, 2012, 1109.4735. (Cited on page 68.)
- [73] P. Clark Souers. *Hydrogen Properties for Fusion Energy*. University of California Press, 1986. (Cited on page 82.)
- [74] H. Wollny. *Bestimmung des Myonenflusses am COMPASS-Experiment*. Diploma thesis, Physikalisches Institut, Albert-Ludwigs-Universität Freiburg, 2007. (Cited on page 83.)
- [75] C. Höppner. *First Measurement of the Cross Section for the Production of Hadrons with High Transverse Momenta at COMPASS, and Developments for Particle Tracking in High-Rate Experiments*. PhD thesis, Technische Universität München, 2012. (Cited on page 86.)
- [76] C. Höppner et al. *Luminosity (2004W28-W31 and F_2^d Comparison with Literature)*. COMPASS Release Note, August 2010. (Cited on page 86.)
- [77] R.P. Mount. The Measurement of Intense Particle Beams. *Nucl.Instrum.Meth.*, 187:401–405, 1981. (Cited on page 86.)

- [78] R. J. Barlow. *Statistics: A Guide to the Use of Statistical Methods in the Physical Sciences*. Wiley, 1989. (Cited on page 100.)
- [79] P. Schiavon. *Particle Identification in COMPASS RICH 1*. COMPASS Note, September 2001. (Cited on page 100.)
- [80] O. Ullaland. Fluid systems for RICH detectors. *Nucl.Instrum.Meth.*, A553:107–113, 2005. (Cited on page 100.)
- [81] A. Nappi. A Pitfall in the use of extended likelihood for fitting fractions of pure samples in mixed samples. *Comput. Phys. Commun.*, 180:269–275, 2009, 0803.2711. (Cited on page 101.)
- [82] M. Lefebvre et al. Propagation of errors for matrix inversion. *Nucl.Instrum.Meth.*, A451:520–528, 2000, hep-ex/9909031. (Cited on page 102.)
- [83] Q. Curiel. *Measurement of Hadron Multiplicities in Deep Inelastic Scattering and Extraction of Quark Fragmentation Functions*. PhD thesis, Institut de Recherche sur les lois Fondamentales de l'Univers, CEA Saclay, 2014. (Cited on page 103.)
- [84] L.C. Maximon. Comments on radiative corrections. *Rev.Mod.Phys.*, 41:193–204, 1969. (Cited on page 107.)
- [85] Arif A. Akhundov, Dmitri Yu. Bardin, Lida Kalinovskaya, and Tord Riemann. Model independent QED corrections to the process $e p \rightarrow e X$. *Fortsch.Phys.*, 44:373–482, 1996, hep-ph/9407266. (Cited on page 107.)
- [86] A.A. Akhundov, D. Yu. Bardin, and N.M. Shumeiko. Electromagnetic Corrections to Elastic Radiative Tail in Deep Inelastic Lepton - Nucleon Scattering. *Sov.J.Nucl.Phys.*, 44:988, 1986. (Cited on page 107.)
- [87] D. Yu. Bardin and N.M. Shumeiko. On the Weak Neutral Current and Electromagnetic Correction Effects on the Quantities Measured in Deep Inelastic Lepton+- n Scattering. *Sov.J.Nucl.Phys.*, 29:499, 1979. (Cited on page 107.)
- [88] B. Badelek, Dmitri Yu. Bardin, K. Kurek, and C. Scholz. Radiative correction schemes in deep inelastic muon scattering. *Z. Phys.*, C66:591–600, 1995, hep-ph/9403238. (Cited on page 107.)
- [89] H. Bethe. Theory of the passage of fast corpuscular rays through matter. *Annalen Phys.*, 5:325–400, 1930. (Cited on page 113.)
- [90] M. Arneodo et al. Measurement of the proton and deuteron structure functions, $F_2(p)$ and $F_2(d)$, and of the ratio σ_L / σ_T . *Nucl.Phys.*, B483:3–43, 1997, hep-ph/9610231. (Cited on page 114.)
- [91] C. Adolph et al. Leading order determination of the gluon polarisation from DIS events with high- p_T hadron pairs. *Phys.Lett.*, B718:922–930, 2013, 1202.4064. (Cited on page 114.)
- [92] T. Böhlen et al. The FLUKA Code: Developments and Challenges for High Energy and Medical Applications. *Nuclear Data Sheets*, 120:211–214, 2014. (Cited on page 114.)
- [93] Alfredo Ferrari, Paola R. Sala, Alberto Fasso, and Johannes Ranft. FLUKA: A multi-particle transport code (Program version 2005). 2005. (Cited on page 114.)

- [94] C. Adolph et al. Hadron Transverse Momentum Distributions in Muon Deep Inelastic Scattering at 160 GeV/c. *Eur. Phys. J.*, C73(8):2531, 2013, 1305.7317. [Erratum: *Eur. Phys. J.*, C75,no.2,94(2015)]. (Cited on page 116.)
- [95] T. Ernst. Diploma thesis, Physikalisches Institut, Albert-Ludwigs-Universität Freiburg, 1985. (Cited on page 117.)
- [96] Maurice Benayoun, Heath Bland O'Connell, and Anthony Gordon Williams. Vector meson dominance and the ρ meson. *Phys.Rev.*, D59:074020, 1999, hep-ph/9807537. (Cited on page 125.)
- [97] A. Sandacz and P. Sznajder. HEPGEN - generator for hard exclusive lepton production. 2012, 1207.0333. (Cited on page 125.)
- [98] S. V. Goloskokov and P. Kroll. The Role of the quark and gluon GPDs in hard vector-meson electroproduction. *Eur. Phys. J.*, C53:367–384, 2008, 0708.3569. (Cited on page 126.)
- [99] C. Adolph et al. Multiplicities of charged pions and unidentified charged hadrons from semi-inclusive deep-inelastic scattering of muons on an isoscalar target. 2015 (to be submitted to Phys Rev D). (Cited on pages 131, 133, and 148.)
- [100] N. Makke. *Measurement of the polarization of strange quarks in the nucleon and determination of quark fragmentation functions into hadrons*. PhD thesis, Institut de Recherche sur les lois Fondamentales de l'Univers, CEA Saclay, 2011. (Cited on pages 131 and 142.)
- [101] S. V. Goloskokov and P. Kroll. Transversity in hard exclusive electroproduction of pseudoscalar mesons. *Eur. Phys. J.*, A47:112, 2011, 1106.4897. (Cited on page 131.)
- [102] I. Akushevich et al. RADGEN 1.0: Monte Carlo generator for radiative events in DIS on polarized and unpolarized targets. 1998, hep-ph/9906408. (Cited on page 132.)
- [103] M. Hirai, S. Kumano, T.-H. Nagai, and K. Sudoh. Determination of fragmentation functions and their uncertainties. *Phys.Rev.*, D75:094009, 2007, hep-ph/0702250. (Cited on pages 137 and 143.)
- [104] John C. Collins and Davison E. Soper. The Theorems of Perturbative QCD. *Ann. Rev. Nucl. Part. Sci.*, 37:383–409, 1987. (Cited on page 137.)
- [105] D. Hahne. *Extraction of Quark Fragmentation Functions in Leading Order*. PhD thesis, Physikalisches Institut, Rheinische Friedrich-Wilhelms-Universität Bonn, to be submitted. (Cited on page 139.)
- [106] R. Brun, M. Caillat, M. Maire, G.N. Patrick, and L. Urban. THE GEANT3 ELECTROMAGNETIC SHOWER PROGRAM AND A COMPARISON WITH THE EGS3 CODE. 1985. (Cited on page 139.)
- [107] A. Airapetian et al. Measurement of Parton Distributions of Strange Quarks in the Nucleon from Charged-Kaon Production in Deep-Inelastic Scattering on the Deuteron. *Phys.Lett.*, B666:446–450, 2008, 0803.2993. (Cited on page 141.)
- [108] D. de Florian and R.J. Hernandez-Pinto. Extracting the fragmentation functions with global analyses. *J.Phys.Conf.Ser.*, 485:012056, 2014. (Cited on page 142.)
- [109] K. Abe et al. Production of π^+ , K^+ , K^0 , K^{*0} , ϕ , p and Λ^0 in hadronic Z^0 decays. *Phys.Rev.*, D59:052001, 1999, hep-ex/9805029. (Cited on page 142.)

- [110] I. Arsene et al. Production of mesons and baryons at high rapidity and high $P(T)$ in proton-proton collisions at $\sqrt{s} = 200$ -GeV. *Phys. Rev. Lett.*, 98:252001, 2007, hep-ex/0701041. (Cited on page 142.)
- [111] K. Adcox et al. PHENIX detector overview. *Nucl. Instrum. Meth.*, A499:469–479, 2003. (Cited on page 142.)
- [112] K. H. Ackermann et al. STAR detector overview. *Nucl. Instrum. Meth.*, A499:624–632, 2003. (Cited on page 142.)
- [113] M. Harrison, T. Ludlam, and S. Ozaki. RHIC project overview. *Nucl. Instrum. Meth.*, A499:235–244, 2003. (Cited on page 142.)
- [114] R. Brandelik et al. Evidence for Planar Events in e^+e^- Annihilation at High-Energies. *Phys. Lett.*, B86:243, 1979. (Cited on page 143.)
- [115] R. Itoh et al. Measurement of inclusive particle spectra and test of MLLA prediction in e^+e^- annihilation at $\sqrt{s} = 58$ -GeV. *Phys. Lett.*, B345:335–342, 1995, hep-ex/9412015. (Cited on page 143.)
- [116] P. Abreu et al. π^+ , K^+ , p and anti- p production in $Z^0 \rightarrow q \text{ anti-}q$, $Z^0 \rightarrow b \text{ anti-}b$, $Z^0 \rightarrow u \text{ anti-}u$, $d \text{ anti-}d$, $s \text{ anti-}s$. *Eur. Phys. J.*, C5:585–620, 1998. (Cited on page 143.)
- [117] D. Buskulic et al. Measurement of the effective b quark fragmentation function at the Z resonance. *Phys. Lett.*, B357:699–714, 1995. (Cited on page 143.)
- [118] H. Aihara et al. Charged hadron inclusive cross-sections and fractions in e^+e^- annihilation $\sqrt{s} = 29$ GeV. *Phys. Rev. Lett.*, 61:1263, 1988. (Cited on page 143.)
- [119] K. Abe et al. Production of π^+ , K^+ , K^0 , K^{*0} , ϕ , p and Λ^0 in hadronic Z^0 decays. *Phys. Rev.*, D59:052001, 1999, hep-ex/9805029. (Cited on page 143.)

ABBREVIATIONS

BMS	Beam Momentum Station
CERN	Conseil Européen pour la Recherche Nucléaire
CFD	Constant Fraction Discriminator
CM	Center of Mass
COMGEANT	COMPASS GEANT
COOL	COmpass Online toOL
COMPASS	COmmon Muon and Proton Apparatus for Structure and Spectroscopy
CORAL	COmpass Reconstruction ALgorithm
CT	Calorimeter Trigger
DAQ	Data AcQuisition
DC	Drift Chambers
DGLAP	Dokshitzer-Gribov-Lipatov-Parisi
DIS	Deep Inelastic Scattering
DVCS	Deep Virtual Compton Scattering
DY	Drell-Yan
ECAL	Electromagnetic CALorimeter
EMC	European Muon Collaboration
FI	scintillating FIBre detector
FF	Fragmentation Function
GEM	Gaseous ElectronMultiplier
GPD	Generalised Parton Distribution
LAS	Large Angle Spectrometer
LEP	Large Electron-Positron collider
LED	Leading Edge Discriminator
LINAC	LINear ACcelerator
LO	Leading Order
MAPMT	Multi-Anode PhotoMultiplier Tubes
MC	Monte Carlo
MF	Muon Filter
MIP	Minimum Ionising Particle
MM	MicroMega
MSTW	Martin-Stirling-Thorne-Watt
MT	Middle Trigger

MWPC	Multi Wire Proportional Chamber
NLO	Next-to-Leading Order
OT	Outer Trigger
PDF	Parton Distribution Function
PDG	Particle Data Group
PETRA	Positron-Elektron-Tandem-Ring-Anlage
PHAST	PHysics Analysis Software Tool
PMT	PhotoMultiplier Tubes
pQCD	perturbative Quantum ChromoDynamics
QCD	Quantum ChromoDynamics
QED	Quantum ElectroDynamics
QPM	Quark Parton Model
RICH	Ring Imaging CHerenkov
RT	Random Trigger
SAS	Small Angle Spectrometer
SIDIS	Semi-Inclusive Deep Inelastic Scattering
SLAC	Stanford Linear Accelerator Center
SM	Spectrometer Magnet
SPS	Super Proton Synchrotron

LIST OF FIGURES

Figure 1	Deep inelastic scattering process	5
Figure 2	Nucleon resonances	7
Figure 3	First F_2 indication at SLAC	9
Figure 4	DIS in the quark-parton model	10
Figure 5	Structure function F_2^p	12
Figure 6	Structure function F_2^d	13
Figure 7	Scaling and splitting functions	14
Figure 8	MSTW2008 parton distribution functions	15
Figure 9	Semi-inclusive deep inelastic scattering process	17
Figure 10	Polarised PDFs at COMPASS	20
Figure 11	Independent hadronisation	21
Figure 12	Flux tube from $q\bar{q}$	22
Figure 13	Quark tunnelling in the Lund model	23
Figure 14	Comparison of the hadronisation models	24
Figure 15	Fragmentation functions from ee and pp collision	24
Figure 16	Factorisation in SIDIS	26
Figure 17	HERMES and EMC results on multiplicities	27
Figure 18	Isometric view of the COMPASS experiment	31
Figure 19	Beam line	32
Figure 20	Beam momentum parameters	33
Figure 21	Beam profile in X and Y	34
Figure 22	The polarised target	36
Figure 23	The liquid hydrogen target	37
Figure 24	Tracking detector principles: micro pattern	39
Figure 25	Tracking detector principles: wire	39
Figure 26	RICH detector	42
Figure 27	Data acquisition overview	44
Figure 28	Principle of target pointing triggers	48
Figure 29	Principle of energy loss triggers	49
Figure 30	The true random trigger set-up	50
Figure 31	Light output of BC408 and wavelength acceptance of a PMT	52
Figure 32	Example for a scintillator counter	52
Figure 33	Energy levels in scintillator	53
Figure 34	Trigger element overview	54
Figure 35	Hodoscope overview	56
Figure 36	Kinematic range of the COMPASS trigger	56
Figure 37	Inclusive kinematics per trigger	57
Figure 38	Trigger electronic overview	58
Figure 39	Veto dead time and duty factor	59
Figure 40	LAST in the spectrometer	61
Figure 41	H1 technical drawing	62
Figure 42	H1 read-out	64
Figure 43	H2 technical drawing	66
Figure 44	H2 read-out	68

Figure 45	Interconnection of the different devices of the LAS-Trigger	69
Figure 46	LAST: Hit result and analogue signal of LAST	71
Figure 47	LAST: Timing of one slab of H1 and H2	71
Figure 48	LAST: kinematic distribution	71
Figure 49	Scaler display 2010	72
Figure 50	COMPASS data flow	73
Figure 51	Reconstructed event with CORAL	74
Figure 52	Extrapolated position and hits on HO04_Y1 (2006)	77
Figure 53	Hodoscope efficiency of HO04_Y1 (2006)	77
Figure 54	Trigger efficiency of HO04_Y1 (2006)	78
Figure 55	Hodoscope and trigger efficiency of HM05X_d (2006)	80
Figure 56	Primary vertex distribution in XY and Z	82
Figure 57	Primary vertex distribution in XY and Z	82
Figure 58	Scalers 2006 and 2009	83
Figure 59	Uncorrected scalers 2006 and 2009	84
Figure 60	Geometric correction for 2006	84
Figure 61	Geometric correction factor for 2006 and 2009	85
Figure 62	Scaler result 2006 and 2009	85
Figure 63	Random Trigger attempts	86
Figure 64	Tracktime per spill and event	88
Figure 65	Statistics reduction of RT beam tracks	89
Figure 66	Data quality check for W38 (vertices)	89
Figure 67	Quality checks for W38	90
Figure 68	K^0 fit	90
Figure 69	K^0 mass for W38	91
Figure 70	K^0 mass for W40	91
Figure 71	Systematic: Target density W38	92
Figure 72	Systematic: Target density W40	92
Figure 73	Systematic: Track time symmetry W38	94
Figure 74	Systematic: Track time symmetry W40	94
Figure 75	Systematic: Momentum reconstruction W38	95
Figure 76	Systematic: Momentum reconstruction W40	95
Figure 77	Random Trigger Flux 2009	96
Figure 78	Cherenkov angles in the RICH	100
Figure 79	RICH likelihoods and RICH rings	101
Figure 80	RICH matrices for positive hadrons	104
Figure 81	Kinematics 2006: W , Q^2 , x and y	105
Figure 82	Kinematics 2006: p_h , z , p_t and θ_h	106
Figure 83	Radiative effects	106
Figure 84	Inclusive and semi-inclusive radiative correction	108
Figure 85	Kinematics 2006: x versus y	108
Figure 86	Raw unidentified hadron multiplicities	111
Figure 87	Raw charged pion multiplicities	112
Figure 88	Raw charged kaon multiplicities	112
Figure 89	Chart of MC data production	113
Figure 90	Comparison MC/RD inclusive	116
Figure 91	Comparison MC/RD semi-inclusive	117
Figure 92	Single ratio acceptance: unidentified hadrons	118
Figure 93	Single ratio acceptance: charged pions	118
Figure 94	Single ratio acceptance: charged kaons	119

Figure 95	Double ratio acceptance: unidentified hadrons	120
Figure 96	Double ratio acceptance: charged pions	120
Figure 97	Double ratio acceptance: charged kaons	121
Figure 98	Comparison of single and double ratio acceptance	122
Figure 99	Electron correction for unidentified hadrons	124
Figure 100	Electron correction for pions	124
Figure 101	Diffractive meson production and DIS	126
Figure 102	Vector meson correction for unidentified hadrons	127
Figure 103	Vector meson correction for pions	127
Figure 104	LEPTO extrapolation and multiplicities	129
Figure 105	LEPTO extrapolation bin rejection	130
Figure 106	z dependence of the radiative correction	132
Figure 107	Final corrected unidentified hadron multiplicities	134
Figure 108	Final corrected charged pion multiplicities	135
Figure 109	Preliminary corrected charged kaon multiplicities	136
Figure 110	Direct determination of the pion fragmentation function	138
Figure 111	COMPASS staggered pion multiplicities	140
Figure 112	COMPASS fragmentation function in LO	142
Figure 113	Favoured pion fragmentation (DSS, HKNS)	143
Figure 114	Unfavoured pion fragmentation (DSS, HKNS)	143
Figure 115	Strange fragmentation into pions and kaons	144
Figure 116	COMPASS fragmentation and comparison	145
Figure 117	Beam line details	151
Figure 118	H1 light guides	152
Figure 119	H2 light guides	152
Figure 120	Bent light guide	153
Figure 121	Voltage divider XP 2982	153
Figure 122	Picture of H1	154
Figure 123	Picture of H2	155
Figure 124	Frame stability of H1	155
Figure 125	Frame stability of H2	156

PUBLICATIONS

Some ideas and figures have appeared previously in the following publications:

- “Technical Summary Of The Large Angle Spectrometer Trigger”
COMPASS internal note (2011-5)
- “Technical Release: Flux Determination for 2009 DVCS Data”, March 2012
COMPASS internal release note
- “DVCS at COMPASS and Luminosity Determination”
SPIN-Praha-2012 conference proceeding, not published yet
- “Flux Determination for 2009 DVCS Data”, September 2012
COMPASS internal release note
- “ Release Note on hadron multiplicities from 2004 and 2006 muon DIS on isoscalar target”, April 2013
COMPASS internal release note
- “ Modification of H1”
COMPASS internal note (2013-6)
- “HADRON MULTIPLICITIES AND QUARK FRAGMENTATION FUNCTIONS AT COMPASS”
DSPIN-2013 conference proceeding
- “Hadron Multiplicities at COMPASS”
DIS2014 conference proceeding
- “ Pion and unidentified hadron multiplicities from muon deep inelastic scattering on ${}^6\text{LiD}$ (2006 COMPASS data)”, November 2014
COMPASS internal release note
- “Trigger Modification For Drell-Yan”
COMPASS internal note (2015-4)
- “Multiplicities of charged and unidentified charged hadrons from semi-inclusive deep-inelastic scattering of muons on an isoscalar target”
from the COMPASS collaboration, to be submitted to Phys. Rev. D

PRESENTATIONS

The status and the results of this thesis have been presented at several conferences:

- “Large Angle Spectrometer Trigger at COMPASS”
DPG-Frühjahrstagung, Münster, Germany, March 21 - 25, 2011
- “Luminosity Determination at COMPASS”
DPG-Frühjahrstagung, Mainz, Germany, March 19 - 23, 2012
- “DVCS and Flux Determination at COMPASS”
Advanced Studies Institute: Symmetries and Spin (SPIN-Praha-2012), Prague, Czech Republic, July 1 - 8, 2012
- “GPD Measurement at COMPASS II”
DPG-Frühjahrstagung, Dresden, Germany, March 4 - 8, 2013
- “Pion and Kaon Multiplicities in Muon-Nucleon Scattering”
XV WORKSHOP ON HIGH ENERGY SPIN PHYSICS (DSPIN-13), Dubna, Russia, October 8 - 12, 2013
- “Pion and Kaon Multiplicities in Muon-Nucleon Scattering”
DPG-Frühjahrstagung, Frankfurt, Germany, March 17 - 21, 2014
- “Hadron Multiplicities at COMPASS ”
XXII. International Workshop on Deep-Inelastic Scattering and Related Subjects (DIS2104), Warsaw, Poland, 28 April - 2 May, 2014
- “Extraction of Quark Fragmentation Functions in Leading Order at COMPASS”
DPG-Frühjahrstagung, Heidelberg, Germany, March 23 - 27, 2014

ACKNOWLEDGEMENTS

The completion of this dissertation was a big and exciting challenge. All on my own, I would not have managed. So, I am grateful to a lot of people who accompanied and supported me along the way.

First of all I have to thank my supervisor Eva-Maria Kabuß. She gave me the opportunity for the extended stay at CERN. Those years were very important for my personal development. I am grateful for her patience, her support and her knowledge. She always took her time to motivate me and, in times of stress, she found the right words to calm me down.

A large thank is reserved to my colleague and above all my friend, Johannes Bernhard. Without him, I would not have found my way to COMPASS. With him, the office was not only a place for work but also for fun. I enjoyed his advice in professional and private matters.

Many thanks to my colleagues of the COMPASS group Mainz/Bonn. Anytime I had a stupid question, I could rely on Jens Barth, Dietrich von Harrach, Moritz Veit, Tobias Weisrock and Malte Wilfert.

Thanks to all members of the COMPASS collaboration. It was a great experience to be accepted in this large community. Unfortunately there are way too many members to mention them personally. But nonetheless I would like to acknowledge my Gentner program supervisor Gerhard Mallot and the kind and helpful Anne Lissajoux. Lots of thanks go to our engineer Vladimir Anosov, who together with our technician Didier Cotte took supported the trigger group in all matters.

I would like to thank the people involved (KPH Mainz, Institut für Physik Bonn, INFN Torino and Trieste) in the construction of H1 and H2, specially Fulvio Tassarotto.

I deeply thank my family, particularly my parents Michel and Gabriele du Fresne von Hohenesche. They always supported me, not only during this phase of life. Last but definitely not least, a very special thanks goes out to my lovely Wanessa. She gave me stability and joy during the hard times. She had to stand my moods, but as reward she was allowed to proof-read my whole thesis:)

LEBENS LAUF

Nicolas du Fresne von Hohenesche
Hochheimer Straße 11
55252 Mainz-Kastel

geboren am 10. August 1982 in Frankfurt am Main



NATIONALITÄT

deutsch und schweizerisch

SCHULE

09/1987 - 07/1990 Lycée Français de Duesseldorf
09/1990 - 06/1991 Grundschule Mainz-Laubenheim
08/1991 - 07/2001 Gymnasium am Kurfürstlichem Schloß zu Mainz
Juli 2001 Abitur mit Durchschnittsnote 2.5

WEHRDIENST

11/2001 - 08/2002 Fernmelderegiment 920 in Kastelaun
Dienstgrad: Obergefreiter

STUDIUM

09/2002 - 04/2008 Studium der Physik an der Johannes Gutenberg-Universität Mainz
04/2008 - 04/2009 Diplomarbeit: Charakterisierung von Sitall an der ultrakalten Neutronenquelle am TRIGA-Reaktor Mainz
April 2009 Diplom mit Gesamtnote "gut"
09/2009 - 06/2016 Promotion in Physik an der Johannes Gutenberg-Universität Mainz
Abschluß mit "magna cum laude"
03/2010 - 02/2013 Deutsches Technisches Doktorandenprogramm am CERN (Wolfgang-Gentner-Stipendium)

VERSICHERUNG

Hiermit versichere ich gemäß §12 Abs. 3e der Promotionsordnung des Fachbereichs 08, Physik, Mathematik und Informatik der Johannes Gutenberg-Universität Mainz vom 02.12.2013:

- a) Ich habe die jetzt als Dissertation vorgelegte Arbeit selbstständig verfasst. Es wurden ausschließlich die angegebenen Quellen und Hilfsmittel verwendet. Von der Ordnung zur Sicherung guter wissenschaftlicher Praxis in Forschung und Lehre und vom Verfahren zum Umgang mit wissenschaftlichem Fehlverhalten habe ich zur Kenntnis genommen.
- b) Ich habe oder hatte die jetzt als Dissertation vorgelegte Arbeit nicht schon als Prüfungsarbeit für eine andere Prüfung eingereicht.
- c) Ich hatte weder die jetzt als Dissertation vorgelegte Arbeit noch Teile davon an einer anderen Stelle als Dissertation eingereicht.

Mainz, den 15. November

Nicolas du Fresne von Hohenesche

